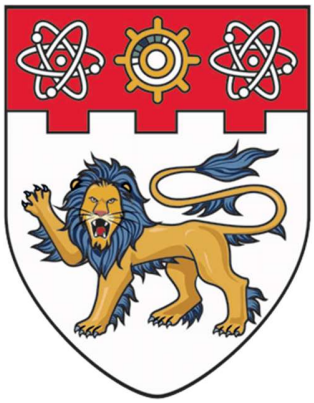

NANYANG TECHNOLOGICAL UNIVERSITY
SINGAPORE

EFFECTS OF HIGH TEMPERATURES ON ROCKS

Li Zhihuan

School of Civil and Environmental Engineering

2018

EFFECTS OF HIGH TEMPERATURES ON ROCKS

Li Zhihuan

School of Civil and Environmental Engineering

A thesis submitted to

Nanyang Technological University

in partial fulfilment of the requirements for the degree of

Doctor of Philosophy

2018

TABLE OF CONTENT

Acknowledgement

I would like to show my appreciation to my supervisors, Assoc. Prof. Louis Wong (supervisor from August 2013 to July 2015, co-supervisor from July 2015 to March 2018) and Assoc. Prof. Teh Cee Ing (co-supervisor from July 2015 to March 2018), for their guidance and invaluable help throughout my candidature.

I would also like to thank Mr. Cheng Weng Kong from the Protective Engineering and Construction Technology Laboratory, as well as Mr. Eugene Tan, Mr. Vincent Heng and Mr. Andy Koh from the Geotechnics, Transport and Geospatial Laboratory for their help in conducting the experiments mentioned in this thesis.

In addition, I would like to express my gratitude to Mr. Kang Hyeongmin for his help in performing the dynamic compressive tests and the analysis of the data found in chapter 5.

Summary

Due to competition for usable space, underground construction is an increasingly attractive option. However, the effects of a fire on the integrity and stability of underground rock structures need to be studied further to understand the potential ramification of a fire hazard within an underground rock structure.

In this thesis, Brazilian tensile tests are conducted on Bukit Timah Granite specimens after exposure to different heating temperature. The variation of Brazilian tensile strength with respect to heating temperature and cooling rate of the specimens is explored and linked to the color changes of the specimens after heating. A MATLAB script is written to segmentate the specimen from the background of a photo and analyse it for its color values in the CIEL*a*b* color space. A relationship between the heating temperature and the Brazilian tensile strength of the specimens was found, as did a relationship between the color changes and the heating temperature of the specimens.

The dynamic compressive strength test was also performed on both heated Bukit Timah Granite and Carrara marble specimens. An increase in heating temperature was found to reduce the dynamic compressive strength of both Carrara marble and Bukit Timah Granite, although the extent of the degradation in dynamic compressive strength is different for both materials. This is most likely due to the difference in the material of the specimens. Stress shadowing was also observed for Carrara marble. The presence of stress shadowing is influenced by the amount of energy used to compress the marble specimen as well as the heating temperature.

Following this, microscopic observations of heated Bukit Timah Granite Brazilian tensile test specimens are presented. Comparisons were made between specimens that underwent a combination of heating and mechanical loading. The cumulative microcrack length, microcrack length distribution and microcrack orientation were analysed. The median microcrack length was found to similar despite the different thermal and mechanical loading. The mineralogical texture was also found to influence the length of the microcracks.

Note

Chapter 4 contains content from the paper:

- Li, Z., Wong, L. N. Y., & Teh, C. I. (2017). Low cost colorimetry for assessment of fire damage in rock. Engineering Geology, 228, 50-60.

Chapter 5 contains content from the papers:

- Wong, L. N. Y., Li, Z., Kang, H. M., & Teh, C. I. (2017). Dynamic loading of Carrara marble in a heated state. Rock Mechanics and Rock Engineering, 50(6), 1487-1505
- Li, Z., Wong, N. Y. L., Kang, H. M., & Teh, C. I. (2016). Dynamic loading of Carrara marble in a heated state. Proceedings of the International Geotechnics Symposium cum International Meeting of CSRME 14th Biennial National Congress, Hong Kong, 14-17 Dec, 2016
- Wong, L. N. Y., Li, Z., Kang, H. M., & Teh, C. I. (2018). Dynamic loading of Bukit Timah Granite in a heated state. (Submitted to Rock Mechanics and Rock Engineering)

Chapter 6 contains content from the paper:

- Li, Z., Wong, L. N. Y., & Teh, C. I. (2018). Influences on thermal and mechanical loading on development of microcracks in granite. (Submitted to Rock Mechanics and Rock Engineering)

LIST OF FIGURES

LIST OF TABLES

Chapter 1 Introduction

1.1. Motivation and objectives

As the world's population increases, competition for natural resources also increases exponentially. Natural resources, in this case, refer not only to tangible items such as food and water, but also to the inputs that is required to create these, such as land. Viable land is at a premium due to its myriad of usages, such as water catchment areas for constructing reservoirs, or for agriculture. One method to meet the demand for land is to construct and use underground structures. Underground spaces are generally non-viable for activities such as agriculture, or non-preferred for recreational purposes.

It is well known that exposure to high temperatures, such as a fire caused by traffic accidents, damages rocks. Such incidents include the Mont Blanc Tunnel fire of 1999, where a fire burned for more than 50 hours (BBC, 1999), and the St Gotthard Tunnel fire of 2001, where the duration of the fire was up to 24 hours (New York Times, 2001).

Deeper knowledge of how rocks are weakened by high temperatures and the behaviour of thermally weakened rocks in various situations can help bring about a greater standard of safety for underground rock structures. Even though it is common for underground rock structures to be reinforced with rock bolts and shotcrete, this only mitigates the impact of a fire on the rock hosting the structure and does not eliminate it completely. Rock bolts can conduct heat and create localised hot spots within the rock mass, while shotcrete can spall during a fire leading to increased conduction of heat into the rock (Caner et al., 2005; Erdakov and Khokhryachkin, 2005; Larsson, 2006; Nordlund et al., 2015).

Fig. 1.1 Occurrence of spalling in Mont Blanc tunnel fire (Promat, 2017a)

Besides understanding the characteristics of thermally weakened rock, a quick and reliable method of quantifying the degree of damage of thermally weakened rocks is also useful for practical applications. By reliably estimating the degree of damage of the thermally weakened rocks, a cost-benefit analysis can be carried out with regards as to whether a salvage operation is feasible and viable.

By performing a systematic study on the exposure of rocks to high temperatures, this thesis aims at investigating the mechanisms behind the weakening of rocks, and to formulate a method of estimating damage done to an underground rock structure. Different scenarios based on the different phases of a fire will be simulated. Phases when an underground rock structure is most vulnerable would be dynamic loading, such as those caused by explosions during a fire, as well as quasi-static loading after the fire has been extinguished.

Numerical simulations were also conducted to assess the evolution of thermally induced damage to the rock with respect to the increasing temperature that the rock is exposed to. The ability to assess the degree of damage and the preference for point of microcrack initiation will enable us to monitor the specimen for damage in real time.

1.2 Approach

This thesis comprises both laboratory experiments and numerical simulations using the Particle Flow Code 2D (PFC2D) program developed by Itasca Consulting Group. For the laboratory experiments, quasi-static tests were conducted on Bukit Timah Granite as it is the most suitable rock for underground construction locally. Dynamic tests were conducted on both Carrara marble and Bukit Timah Granite to gain a better understanding on how dynamic loading interacts with the presence of thermally induced microcracks within a heated specimen.

Various steps were taken in this study. More detailed information will be provided in **Chapter 3.**

- **Specimen preparation**
- Brazilian tensile test specimens were prepared from Bukit Timah Granite rock cores using a diamond cutting saw. Split Hopkinson Pressure Bar (SHPB) dynamic compression test specimens were prepared from both Bukit Timah Granite and Carrara marble using a diamond cutting saw and an OMAX 2626 Waterjet respectively. Thermal treatment of specimens was performed either with a Nabertherm furnace or a customised oven designed to fit around the Split Hopkinson Pressure Bar setup.
- **Color analysis**

  A MATLAB script was written to analyse the color of Bukit Timah Granite specimens. The color space used was the CIEL*a*b*. The color of the specimens was then quantified for easy comparison after heating. The benefit of color analysis is that it can be completed in a fast and economical manner. If color changes can be accurately correlated to the temperature that a rock mass was exposed to, a post incident assessment of an underground structure can be conducted in a fast and cost effective manner.
- **Brazilian tensile test**

  Brazilian tensile tests were conducted with a MTS 815 testing machine equipped with indirect tensile test accessories to examine the effects of thermal treatment on the indirect tensile strength of the specimens. The tensile strength data

collected was also used to correlate color changes of Bukit Timah Granite with the heating temperature.

- **Dynamic compression test**

  Dynamic compression tests were conducted using the SHPB setup on both Bukit Timah Granite and Carrara marble specimens. A three wave analysis of the collected data was performed to investigate the strain rate effect of thermally treated specimens. A dry sieve analysis of the residual fragments was conducted to link the thermal treatment with the residual fragment size distribution.

- **Microscopic examination**

  The microscopic characteristics of generated microcracks were analysed through the vacuum impregnation of specimens with fluorescent epoxy after the Brazilian tensile test. Buehler epothin 2 epoxy was used as it was specifically formulated for vacuum impregnation of specimens. Through excitation of the fluorescent dye with light of the appropriate wavelength, the generated microcracks would be highlighted. Valuable data regarding the microcrack length and orientation was obtained.

- **Numerical simulation**

  A numerical simulation using the PFC2D program from Itasca Consulting Group was also conducted. The PFC2D program utilises the Discrete Element Method (DEM). It is a numerical method that utilises a large collection of small particles to model geomaterials. The advantages of the DEM include being able to model brittle material past the point of the first crack initiation. The model used in this simulation is a four mineral bonded particle grain based model (GBM).

1.3 Organization of thesis

The thesis consists of 8 chapters. The approaches and objectives mentioned in the above sections will be further elaborated upon in the following 7 chapters:

- **Chapter 2** conducts a comprehensive literature review on the several topics, including Linear Elastic Fracture Mechanics (LEFM) theory, tensile tests used to analyse brittle materials and microcrack generation within rock materials.
- **Chapter 3** describes the experimental methodology, which includes the specimen preparation, experimental details, and the analysis methods used.

- **Chapter 4** details the results of the Brazilian tensile tests performed with the MTS 815 machine. A method of correlating color changes of the Bukit Timah Granite specimens with the heating temperature that the rock was exposed to will also be explained. This demonstrates a relationship between the residual tensile strength of the thermally treated rock and its color changes. This chapter simulates the effects of a quasi-static load, such as the normal design loads that an underground rock structure is expected to withstand, after the fire has been extinguished.
- **Chapter 5** details the dynamic compression tests conducted with the SHPB setup. The three wave analysis method was used to obtain the stress-strain curve and dry sieving was performed to obtain the particle size distribution curve for the fragments. Metrics such as the energy absorbed by the specimen was calculated for an in-depth understanding of the effects of heating on the dynamic compressive strength of Bukit Timah Granite and Carrara marble specimens. This chapter simulates the effects of a dynamic load, such as those imparted by explosions or vehicular collisions, while the fire is ongoing.
- **Chapter 6** illustrates the results of the microscopic observations. As the compressive strength of brittle materials such as ceramics or rocks are normally several times higher than its tensile strength, it is extremely likely that tension plays an important part in the collapse of underground rock structures. The microcrack distribution and characteristics of the thermally treated Brazilian tensile test specimens were analysed for a better understanding of the mechanisms behind the collapse of underground rock structures.
- **Chapter 7** explores the possibility of using a four mineral GBM approach in PFC2D, and its use in simulating Bukit Timah Granite, as well as the effects of exposure to high temperature on Bukit Timah Granite.
- **Chapter 8** summarises the conclusions drawn from the study in the context of a fire in an underground rock structure. Some ideas regarding any future work that may build upon the current study are also listed.

Chapter 2 Literature review

2.1. Introduction

The literature review in this chapter is split into a few parts, mainly:

- Linear Elastic Fracture Mechanics (LEFM) theory
- Testing methods (dynamic compression, Brazilian tensile test, fluorescent dye impregnation)
- Effects of high temperatures on rocks
- Discrete Element Method (DEM)

2.2. Strength of materials theory

In material science, the strength of materials approach is conventionally used to quantify the ability of a material to resist load. In this approach, an item made from the same material with the same geometry will have the same strength, and will fail at the same amount of applied stress. In the 17th century, Galileo conducted rudimentary tensile and bending tests on columns and bars and observed that for a bar made of a certain material, its tensile strength is proportionate to its cross sectional area and independent of its length. Following this, Hooke made significant contributions to this area, in the form of his works regarding the elastic properties of materials (Timoshenko, 1953).

2.3. Linear Elastic Fracture Mechanics

In the early 20th century, Griffith (1921) conducted experiments on glass rods and noticed that the tensile strength of glass rods that were scratched failed at an applied stress that were below their theoretical tensile strength. He reasoned that since the energy from the applied stress was not sufficient to overcome the intermolecular forces of attraction between glass molecules, the presence of scratches, or microcracks, must somehow affect the tensile strength of the glass rods.

He also inferred, and later proved experimentally, that the strength of a bundle of thin glass fibers having the same cross sectional area of a single, thick, glass fiber would be stronger, the reason being that the size of each individual thin glass fiber would impose a restriction on the size of flaws that may be present in the fibers.

The thermodynamics approach taken by Griffith was later complemented by Irwin (1956, 1957). Irwin built upon Griffith's work and introduced a variable meant to take into account plastic deformation at the crack tip. He also developed a method of quantifying the energy available for crack propagation in terms of the crack geometry and loading conditions, the stress intensity factor, K.

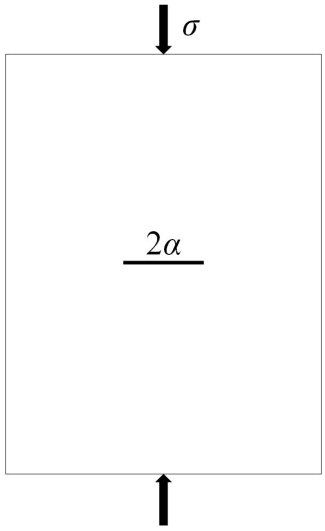

Fig. 2.1 Plate of infinite width with a single crack of length 2α, being loaded with a stress of σ

For a single mode I crack on an infinite plane (Fig. 2.1), the critical stress intensity factor is as follows:

$$K_{IC} = \sigma\sqrt{\pi\alpha} \tag{2.1}$$

where K_{IC} is the critical stress intensity factor for a mode I crack
σ is the stress applied
2α is the length of the crack

This was significantly easier to use as compared to the thermodynamics approach taken by Griffith, as the loading conditions (stress) and crack geometry (orientation and length) is easier to measure and quantify than the thermodynamic free energy of a system.

Irwin (1956, 1957) framed the problem of fracture mechanics in terms of a stress intensity factor, K (equation 2.1), which was further subdivided into three different types of stress intensity factor corresponding to the three different modes of crack surface displacement, as shown in Fig. 2.2.

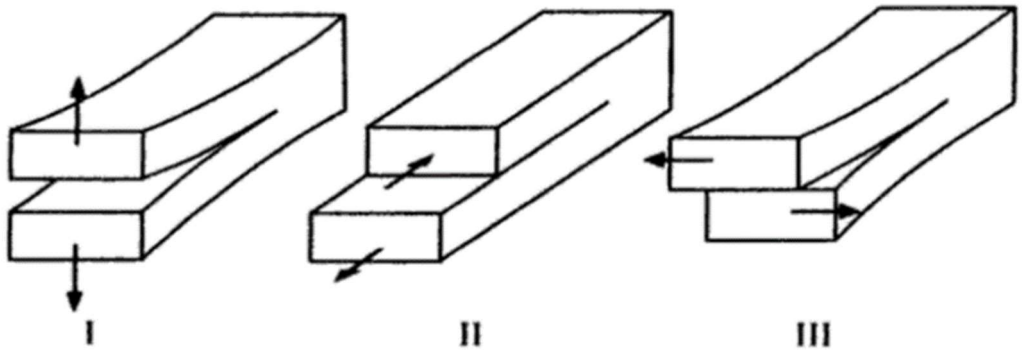

Fig. 2.2 The three modes of crack loading, type I (opening), type II (in place shear) and type III (out of plane shear) (Lawn, 1993)

Out of these three fracture modes, type I and II is of particular concern, as the type III fracture mode is insignificant for plane stress problems, such as those assumed by the Brazilian tensile test.

It has also been found that for multiple microcracks within an area of interest, the microcrack density also plays a part in influencing the strength of the material as the microcracks would interact with each other (Lockner et al., 1992; Ning et al, 2010; Paliwal and Ramesh, 2008). This is significant as during the heating process it is not possible to control the amount of microcracks formed, the location in which the microcracks appear or the length of microcracks that will appear.

Other than the size and shape of the microcrack, the location at which the microcrack is present is also important. Theoretically, the critical stress intensity factor is calculated via the balance between the increase in surface free energy and the work done to the specimen (Leckie and Dal Bello, 2008). With this approach, microcracks on the surface or near the surface of the specimen will be more critical as they would fail first. This is because to create a new surface along the surface of a specimen requires lesser energy than creating a new surface inside of a solid. For a microcrack of the same size and shape, a surface microcrack will propagate earlier than a microcrack that is inside of a solid.

2.4. Testing methods

Due to the difficulties in conducting direct tensile and dynamic compressive tests on brittle materials, a large variety of tests was developed to experimentally test brittle materials. However, each test or variation has its own pros and cons.

2.4.1 Direct tensile test

The direct tensile test was first used to determine the tensile strength of steel. A steel specimen was machined in the shape of a “dog bone” or “dumbbell” and was held in place via clamps on each end. The steel specimen was then loaded via a testing machine to failure. The stress and strain of the specimen were then recorded and used to plot a stress-strain curve of the material being tested. However, there are unique drawbacks that make this test unsuitable for use on brittle material, such as rocks.

Brittle materials are very hard to machine into a “dog bone” or “dumbbell” shape, such as the concrete specimens in Fig. 2.3. This greatly increases the cost and difficulty of performing the direct tensile test. Even if specimens were machined into those shapes, microcracking near the edges and corners of the specimen would form stress concentrations and increase the likelihood of specimens failing near the machined section, invalidating the test.

To overcome this problem, a direct tensile test specifically for brittle materials was developed (ISRM, 1978). Specially manufactured end caps were produced as an interface between the testing machine and the specimens. The end caps were glued to the specimen via the application of epoxy before being attached to the testing machine (Fig. 2.4). A successful test will be one where the specimen fails, whereas an invalid test will be one where the epoxy fails and the specimen is separated from the end cap with no fracture of the specimen taking place. The epoxy for the test must be chosen carefully to fulfil several criteria, such as: fast curing time, high bond strength, low elongation under tension and low sensitivity to environmental conditions. Furthermore, for the end caps to be reused, the epoxy needs to be cleanly removed after every test. As the epoxy was chosen due to its strength, the removal of the epoxy is very difficult and time consuming.

Fig. 2.3 "Dog bone" shaped concrete specimens (Hassan et al., 2012)

Fig. 2.4 Photo of direct tensile test

2.4.2. Brazilian tensile test

The more popular method of tensile strength determination is the indirect tensile test, also known as the Brazilian tensile test. The Brazilian tensile test is performed by compressing a short cylindrical specimen, or a disc specimen, along its diametrical line. This induces tensile stresses within the specimen. The suggested formula for calculating the tensile strength of the specimen is:

$$\sigma = \frac{2P}{\pi D t} \tag{2}$$

Where σ is tensile strength (Pa)

P is load at failure (N)

D is diameter (m)

t is thickness of specimen (m)

The Brazilian tensile test was invented by Professor Fernando L. L. B. Carneiro in the 1940s, when he was testing the strength of concrete rollers. He noticed that most of the time, the concrete failed in a vertical plane connecting the line of contact

between the cylindrical specimen and the compression platens. From this observation he developed a method to test for the tensile strength of brittle materials (Fairbairn and Ulm, 2002).

The specimen can be loaded by flat platens, with cushioning material or with curved loading jaws as shown in Fig 2.5.

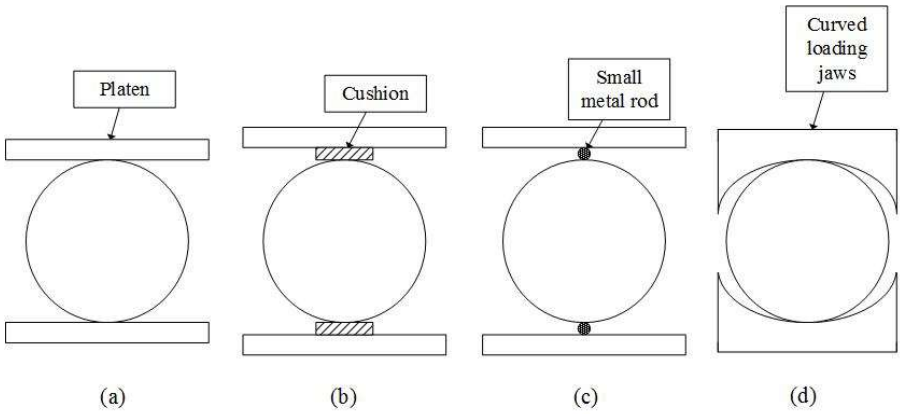

Fig. 2.5 Brazilian tensile test platens (Li and Wong, 2013)

There are a few assumptions made about the Brazilian tensile test. The Brazilian tensile test is idealized as a plane stress problem as it is assumed that the intermediate principal stress has no influence on the disc fracture (Fairhurst, 1964), and the specimen used is thin. Also, the specimen is assumed to be homogeneous, isotropic and linearly elastic before brittle failure occurs (Mellor and Hawkes, 1971). This poses a problem, as most rocks are polymineralic, which would make it heterogeneous.

The effects of anisotropy within a Brazilian tensile test specimen have been explored by several researchers. Wang et al. (2018) conducted a numerical study on a jointed rock specimen, and concluded that although both the inclination angle and the joint spacing affects the Brazilian tensile strength, the inclination angle has a more dominant effect. Dan et al. (2013) investigated the effects of joint inclination angle with respect to loading direction and specimen axis on gneiss and slate specimens, and found that even the joint inclination angle with respect to specimen axis can have a large influence on a specimen's Brazilian tensile strength (25% decrease). The effects of joint inclination angle on the elastic constants of a sandstone specimen are much subtler (Chen et al., 1998).

ASTM (2008a) addresses the heterogeneity problem by specifying that the minimum diameter of the specimen shall be at least 10 times greater than the largest mineral grain constituent. This ensures that the specimen shall be of a large enough size to be considered a Representative Volume Element (RVE).
According to ASTM (2008a), a Brazilian tensile test specimen need to fulfill the following requirements:

- A thickness-to-diameter ratio of between 0.2 to 0.75.
- The circumferential surface of the specimen be smooth and straight to 0.5mm.
- The ends of the specimen not deviate perpendicularly from the core axis by more than 0.5˚.
- Furthermore, the experimental setup shall have a curved bearing surface with a surface contact arc of not more than 15˚ or a contact width of not more than D/6 where D is the diameter of the specimen. If one is not available, a flat bearing surface may be used provided that the surface is cushioned with bearing strips made from soft material such as cardboard or plywood. One of the bearing surfaces shall be rigid and the other shall have a spherical seating.

The effects of tangential frictional stresses have been found to have an effect on the result of the Brazilian tensile test and the stress field within the specimen itself. Friction at the platen-specimen interface have been found to change the stress field near the edge of the specimen, which may fail the specimen by compression instead of tension (Markides et al., 2011, Markides and Kourkolis, 2012).

This is also noted by Fairhurst (1964), who wrote that frictional restraint at the platen-specimen interface produces some out of plane compressive stresses, which may lead to minor spalling at the point of loading and does not affect the validity of the test. Although the spalling causes flaws in the specimen which act as stress concentrators, the specimen may still fail by tension if the compressive strength of the specimen is significantly higher than the tensile strength of the specimen.

Tangential frictional forces may also lead to an inaccurate test result, as Lanaro et al. (2009) found through numerical modeling. Friction at the platen-specimen interface

may lead to an underestimation of the tensile strength by about 50%, and the specimen still experiences tensile failure, but at a lower applied force. This can be seen as the position of the crack initiation is still the same although the crack pattern at failure is different due to different friction conditions.

To determine whether or not the Brazilian tensile test conducted is a valid one, it is important to determine whether the failure is a compressive failure or a tensile failure. This can be achieved via the use of a high speed camera. High speed camera footage can be analyzed to determine the point of crack initiation and observe crack behavior (Wong and Jong, 2014; Wong et al., 2014, 2015; Zou and Wong, 2016a, 2016b; Zou et al., 2016). Cracks initiated somewhere on the face of the specimen indicates a tensile failure while cracks initiated under the points of loading indicates a compressive failure. However, this is assuming that the point of fracture initiation lies on the surface of the specimen and not within the specimen.

According to numerical modeling, the position of the maximum tensile stress is on the surface of a specimen (Yu et al., 2006; Yu et al., 2009), and as stated earlier, a surface microcrack would fail earlier than an internal microcrack, thus, it is likely that whenever a specimen fails, the point of crack initiation is always on the surface of the specimen instead of within a specimen.

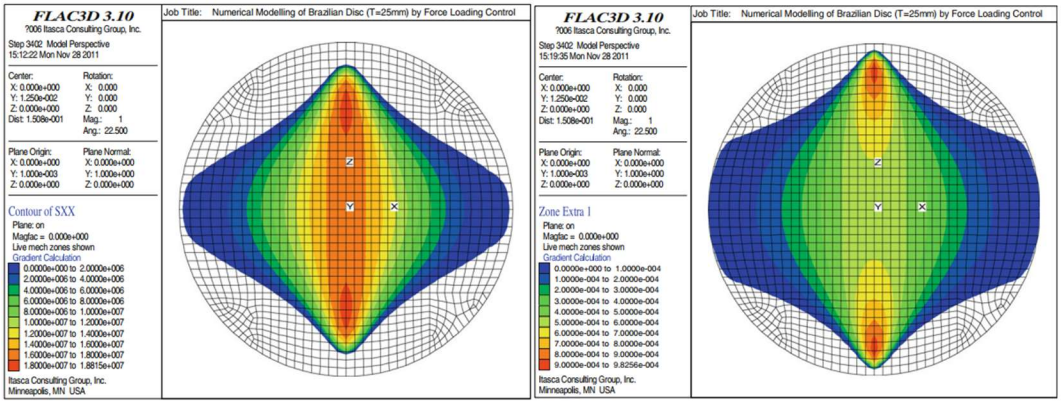

Fig. 2.6 FEM simulation of the surface of a Brazilian tensile test specimen, tensile stress (left) and tensile strain (right) (Li and Wong, 2013)

Recent research shows that the point of crack initiation may not initiate from the central regions. Fig. 2.6 shows that for the surface of a Brazilian tensile test specimen loaded with a vertical distributed load, the areas of maximum tensile stress and

maximum tensile strain is somewhere in between the point of loading and the center region of the specimen.

Previous analytical solutions would assume either a plane stress or a plane strain scenario (Fairhurst, 1964; Hondros, 1959), neither of which strictly conforms to an actual Brazilian tensile test specimen. The inner part of the specimen was found to conform to the analytical solution and exhibit a tensile zone right in the middle of the specimen, so it is likely that the deviance from the analytical solution is due to the 3D nature of the numerical simulation.

2.4.3. Dynamic compressive test

It has long been known that the strain rate of a test affects the observations made about a material being tested. As such, different types of tests have been conducted on materials at a variety of strain rates. These tests are characterized into two main types, quasi-static tests, used to emulate long term stresses on materials, such as the dead load of a building, or geological stresses on underground rocks; and dynamic tests, used to simulate short term loading, such as earthquakes or explosions. Fig 2.7 shows the strain rates and testing apparatus commonly used in quasi-static and dynamic tests.

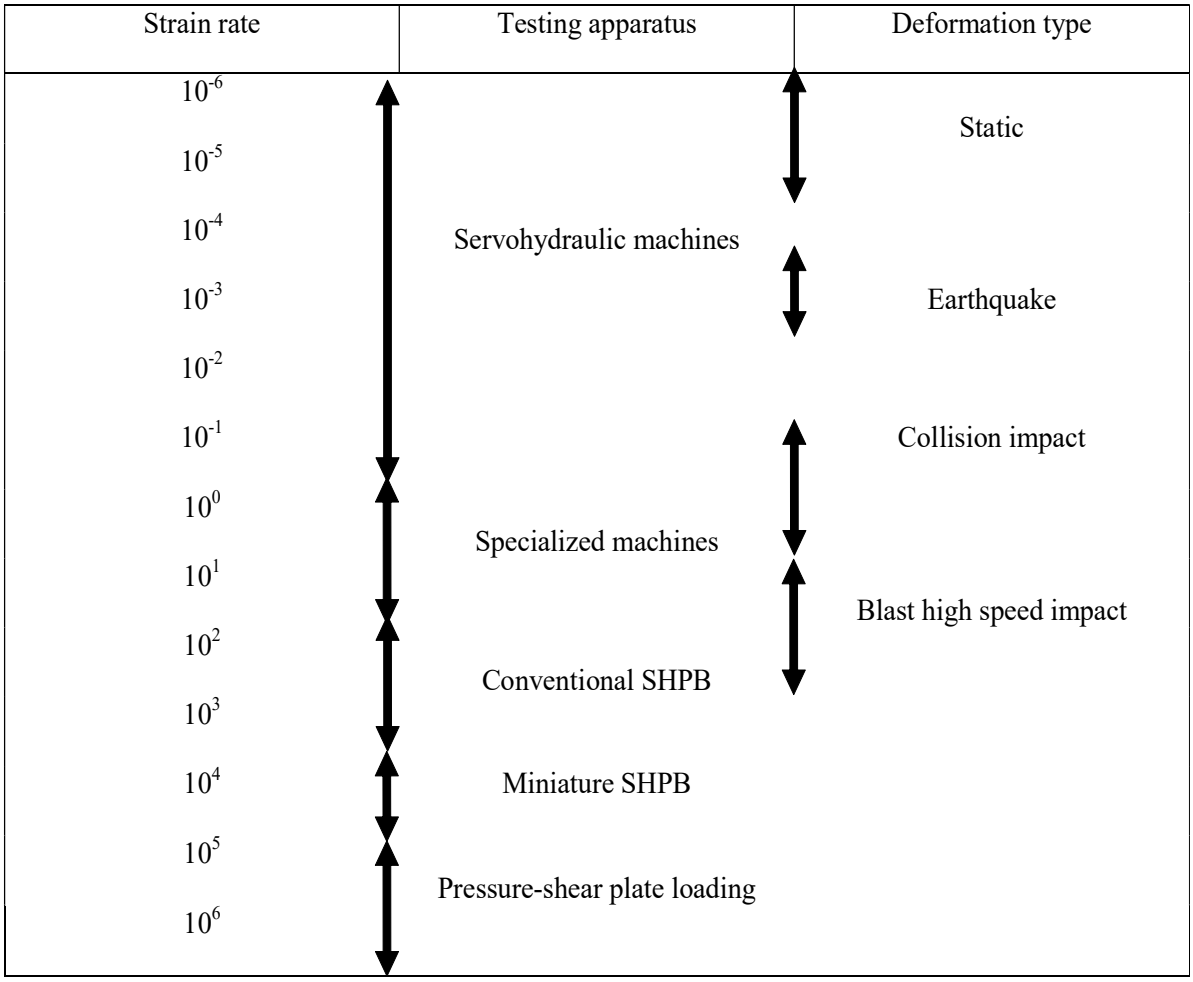

Fig. 2.7 Testing apparatus used for different tests at different strain rates (Ramesh, 2008; Chen et al., 2015)

For this study, a SHPB setup was used to perform dynamic compressive tests. The SHPB setup consists of two long bars made of a material of known properties, the input bar and the output bar. It is important that the input and output bar has a higher yield strength than the specimen tested to ensure elastic wave propagation within the bars, as such, it is common for the bars to be made out of materials such as high strength stainless steel. As seen in Fig 2.8, strain gauges are placed in the middle of the input and output bars to capture:

- The incident wave generated, ε_I (input bar)
- The reflected wave from the interface between the input bar and the specimen, ε_R (input bar)
- The transmitted wave, ε_T (output bar)

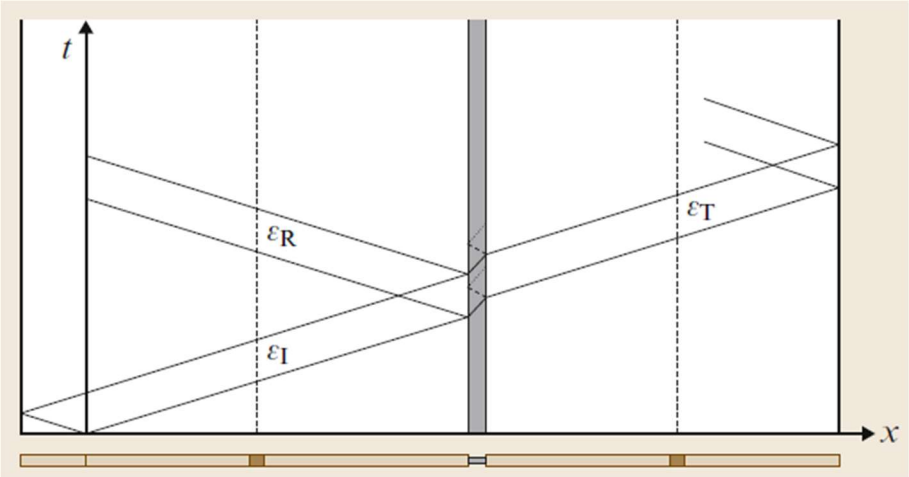

Fig. 2.8 Diagram showing the propagation of stress wave along the SHPB setup, x, with respect to time, t (Ramesh, 2008).

The use of the SHPB setup in dynamic compressive tests is based on some assumptions. These assumptions are that one dimensional (1D) elastic wave propagation is present in the bars and that the specimen being tested deforms homogeneously (Dai et al., 2010). To ensure that these assumptions are valid, experiments involving the SHPB are usually designed with 3 design parameters in mind: the bar length to diameter ratio, bar diameter to specimen diameter ratio and the specimen length to diameter ratio (Ramesh, 2008).

A problem specific to the testing of brittle materials is the short rise time of the loading pulse as well as the presence of Pochammer-Chree (PC) oscillations created by the short rise time (Xia and Yao, 2015). As Liu et al. (1996) stated, the smaller moduli of elasticity of rocks as compared to metals causes more serious PC oscillations, making the control of PC oscillations even more important for testing of brittle materials. The high levels of PC oscillations make it difficult for a dynamic stress equilibrium state to be achieved within the specimen, furthermore, the short rise time of the loading pulse may cause the specimen to fail in a non-uniform manner.

The problem of PC oscillations led to the later development of pulse shaping techniques. There are two main ways of shaping the incident pulse, namely, through the use of a shaped striker bar (Christensen et al., 1972; Frantz et al., 1984; Li et al., 2000; Liu et al., 1996; Zhou et al., 2012), or through the use of a pulse shaper attached to the input bar (Frew et al., 2001, 2002). Pulse shaping allows for a balance of forces

on both sides of the specimen tested and ensures that the specimen tested fails homogeneously.

Another improvement to the standard SHPB system is the use of a momentum trap. Without the use of a momentum trap, the output bar will rebound upon impact with the end of the SHPB system and apply additional loading to the specimen (Nemat-Nasser et al., 1991; Nemat-Nasser and Isaacs, 1997; Song and Chen, 2004; Xia et al, 2008). Even though the time needed for the rebounding output bar to strike the specimen again is longer than the time needed for the specimen to fail, and would not affect the analysis and calculation of the dynamic stress strain curve, the additional loading complicates cases where the specimen does not fail and is supposed to be recovered for further analysis.

After collecting the elastic wave data, there are a few different types of analysis that can be used to construct the dynamic stress strain curve. These methods are the one wave analysis (Gray, 2000; Mohr et al., 2010), two wave analysis (Gray, 2000; Gray and Blumenthal, 2000), three wave analysis (Gray, 2000; Mohr et al., 2010), direct estimate (Mohr et al., 2010), foot shifting method (Mohr et al., 2010), hybrid analysis (Perkins et al., 1970; Shan et al., 2000; Gilat et al., 2009), and inverse analysis (Zhao and Gary, 1996; Peirs et al., 2011; Pierron and Forquin, 2012). As a larger than normal dynamic compressive specimen is needed for rocks to obtain a RVE, a SHPB with a larger bar diameter is needed.

Lok et al. (2001) stated that for a large diameter SHPB, the travel time of the stress wave in the specimen will be longer. In addition, the rise time of the loading pulse is very short. Uniform stress within the specimen cannot be assumed during the initial deformation phase of the specimen. To reduce the test error in this case, a three wave analysis is preferred, as it averages the force applied by using the incident, reflected and transmitted waves. The three wave analysis coupled with the pulse shaper used in this study to modify the rise time and shape of the loading pulse greatly enhances the reliability of the test data.

The equations used for the three wave analysis are as follows:

$$\sigma(t) = \frac{A_e E_e}{2A_s}[\varepsilon_I(t) + \varepsilon_T(t) + \varepsilon_R(t)] \tag{2.2}$$

$$\varepsilon(t) = \frac{C_e}{L_s}\int_0^t [\varepsilon_I(t) - \varepsilon_T(t) - \varepsilon_R(t)]dt \quad (2.3)$$

$$\frac{d\varepsilon(t)}{dt} = \frac{C_e}{L_s}[\varepsilon_I(t) - \varepsilon_T(t) - \varepsilon_R(t)] \quad (2.4)$$

Where σ(t) is the stress at time t

ε(t) is the strain at time t

A_e is the cross sectional area of the input and output bars

E_e is the Young's modulus of the input and output bars

A_s is the cross sectional area of the specimen

L_s is the thickness of the specimen

C_e is the elastic wave velocity of the input and output bars

$\varepsilon_I(t)$ is the incident stress wave

$\varepsilon_R(t)$ is the reflected stress wave

$\varepsilon_T(t)$ is the transmitted stress wave

2.4.4. Microcrack observation techniques

Microcrack quantification techniques can be subdivided into two categories: indirect and direct observation. Indirect observation techniques attempt to quantify microcracks through the use of other correlating specimen properties, such as P-wave velocity measurements (Wei et al., 2013; Siegesmund et al., 1991; Zinke, 1999), nitrogen gas adsorption method (Glover et al., 1995), and the measurement of porosity changes (Freire-Lista & Fort, 2017; Heap et al., 2014).

The other type of observation techniques is the direct measurement of micro-cracks. Some popular techniques include Scanning Electron Microscopy (SEM) (Akcaoglu, 2017; Amelinckx, 2008a; Cooper et al., 2017; Knapek et al., 2016; Stutzman, 1990; Wang et al., 2005) , transmitted light microscopy (Amelinckx, 2008b; John, 1990), X-Ray computer tomography (CT) (Guo et al., 2017; Jia et al., 2013a; Jia et al., 2013b) and the use of fluorescent substances to highlight micro-cracks (Cheng and Wong, 2017; Freire-Lista et al., 2015, 2016; Freire-Lista and Fort, 2017; Lim et al.,

2012; Onishi and Shimizu, 2005; Postiglione et al., 2017; Song et al., 2016; Zunino et al., 2015).

The key advantage of direct observation techniques over indirect observation techniques is that the amount of microcracks is observed directly and quantified. The increase in the number of microcracks are not disputable. Indirect observation techniques take advantage of correlations between microcrack density and physical properties such as P-wave velocity measurements to provide a fast gauge of the degree of microcracking. However, any change in such properties may also be due to other factors, such as chemical changes within the constituent minerals of the rock.

Another advantage of direct observation techniques is that it provides more comprehensive information of the micro-cracks. Information such as the orientation of the micro-cracks and the modal micro-crack length cannot be inferred from indirect observation techniques. Such information is valuable from an engineering perspective, as it may indicate any possible anisotropy of the rock in question.

Even though direct observation techniques offer many advantages, not all direct observation techniques are ideal for microcrack analysis. For example, it is difficult for transmitted light microscopy to identify microcracks that are developed, as such microcracks may be obscured by other types of microstructures such as grain boundaries, especially since microcracks may develop at grain boundaries as well.

Although conventional SEM techniques are more powerful and are able to reveal microcracks and allow for observation in great detail, it is cumbersome and large sections of specimens are not able to be analysed. As conventional SEM techniques requires the specimen being observed to be within a vacuum, specimens that are too large are unable to fit within the vacuum chamber. An alternative is the Environmental Scanning Electron Microscopy (ESEM), which does not require a vacuum for the specimen chamber. This allows for observation of living microorganisms (Swift and Brown, 1970).

Another disadvantage of conventional SEM is that the specimens being observed needs to be coated with a thin layer of conductive metal, such as gold or osmium (Suzuki, 2002). This increases the cost and difficulty of producing SEM specimens

as the coating metal and specialized machines needed adds to the cost. ESEM does not require the surface of the specimen to be conductive (Hortolà, 2005).

However, compared to SEM, ESEM has its own disadvantages such as “frequent specimen damage or difficulty in specimen handling” and “loss of practical resolution” (Danilatos, 2009).

In contrast, fluorescent microscopy only requires fluorescent dye added to low viscosity epoxy, a vacuum chamber and a vacuum pump. This greatly reduces the cost and difficulty of creating fluorescent microscopy specimens. Fluorescent microscopy can also offer excellent visibility of cracked region as well as ease of detection of exact crack position (Song et al., 2012, 2016). This offers advantages in qualitative and quantitative analysis of microcrack density and microcrack patterns, as subtle microcracks are more easily revealed (Akesson et al., 2004; Kim and McCarter, 1998; Kusuda et al., 1995).

The fluorescent dye used must be carefully chosen, as each dye is excited by a light with a specific wavelength. The wavelength of the light used for the excitation of the fluorescent dye should be carefully chosen to avoid any autofluorescence of the minerals within the rock. For example, certain common minerals exhibit fluorescence when in the presence of ultraviolet light (Robbins, 1994; Sweet, 1961; Warren, 1995). In this case, the fluorescent dye used for vacuum impregnation of rocks containing these minerals should not be excited by ultraviolet light, as the autofluorescence of the minerals will reduce the contrast between the epoxy filled microcracks and the rock. Microcracks with a smaller aperture that fluorescence at a dimmer magnitude will be harder to observe.

2.4.5. P-wave velocity

The correlation of P-wave velocity of rocks with its physical properties such as tensile strength, porosity and elastic modulus have been investigated for different types of rocks (Kahraman and Yeken, 2008; Khandelwal, 2013; Karakul and Ulusay, 2013; Yagiz, 2011). The P-wave velocity has a correlation with the strength of a rock specimen because the P-wave velocity is influenced by variables such as the density and porosity of the rock specimen (Blum, 1997), which also influences the strength

of a rock specimen. ASTM (2009) gives the formula for estimating P-wave velocity, V, in concrete as follows:

$$V = \sqrt{\frac{E-E\mu}{\rho(1-\mu-2\mu^2)}} \tag{2.5}$$

where E is the dynamic modulus of elasticity

μ is the dynamic Poisson's ratio

ρ is the density of the rock specimen

From equation 2.5, we can see that the P-wave velocity of a rock specimen is a function of its dynamic modulus of elasticity, its dynamic Poisson's ratio and its density.

The dynamic modulus of elasticity, E, is given by ASTM (2008b) as a function of the geometry of the specimen, its mass, and its resonant frequency. Since the geometry and the mass of a specimen would not be affected by heating, assuming no chemical changes, the dynamic modulus of elasticity of a specimen treated thermally can be regarded to depend predominantly on the resonant frequency of the specimen. The resonant frequency of a rock specimen containing microcracks has been found to decrease as the amount of microcracks in the specimen increases (Lyakhovsky et al., 2009).

The dynamic Poisson's ratio is dependent on the constituent mineral composition and the type and amount of cracks in the rock specimen, as well as being correlated to the static Poisson's ratio (Zhang and Bentley, 2005). The static Poisson's ratio of a rock specimen with microcracks filled with water is expected to be higher than when the microcracks are dry (O'Connell and Budiansky, 1974).

While there is a huge elastic modulus change of 45% to 65% for different types of granite heated to 600 ˚C (Goudie et al., 1992), the permanent strain in Inada granite heated to 600 ˚C at a slow rate is only about 1%, followed by a drop in the P-wave velocity of the specimen (Lin, 2002). As the permanent strain is small, we can assume that the change in density of the rock specimen is negligible.

From this we can infer that the dominant factors influencing the P-wave velocity of a rock specimen is the dynamic elastic modulus and the dynamic Poisson's ratio of the rock specimen, both of which are influenced by the presence of microcracks in the specimen. Thus, the measurement of the P-wave velocity of a rock can be used to indicate the degree of microcracking present.

Another factor that can influence the P-wave velocity of a rock specimen is the degree of saturation. Yagiz (2011) showed that there is an inversely proportionate relationship between the P-wave velocity and the degree of saturation of a rock specimen. A more comprehensive study conducted by Karakul and Ulusay (2013) showed that the relationship between the degree of saturation and the P-wave velocity of rocks varied across different types of rocks. It is important to have a similar degree of saturation when measurements of the rock specimens are being taken. As it is very hard to control the degree of saturation when the rock specimen is unsaturated, a more feasible way would be to either test completely saturated specimens or oven-dried specimens.

ASTM (2000) provides a few criteria for an accurate determination of the travel time of the P-wave through the rock specimen.

- The transmitter should be able to generate wavelengths of at least 3 times the average grain size of the rock.
- The thickness to diameter ratio of the test specimen should be less than 5, as shown in Fig. 2.9.

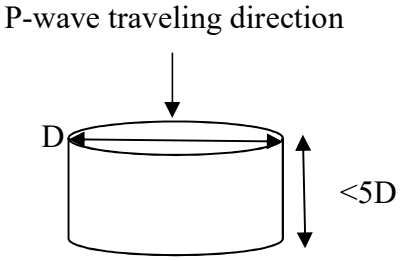

Fig. 2.9 Specimen dimensions, D is the specimen diameter

- The travel distance of the P-wave should be at least 10 times the average grain size of the rock.

- The ratio of the diameter of the specimen to the wavelength of the P-wave should at least be 5.

2.4.6. Colorimetry

The color of the individual minerals in rocks is dictated by the chemical composition and the physical structure of the mineral. When light strikes the surface of a rock, part of the light penetrates the rock while the rest is reflected. The selective reflection and absorption of certain wavelengths in the light gives a mineral its particular color.

Color is a key property of rocks that changes when exposed to high temperatures. Some of these color changes are due to chemical reactions that take place during heating and may occur earlier than any noticeable loss of strength. Some examples of color changes caused by chemical reactions are the thermal decomposition of carbonate compounds and the subsequent formation of Portlandite (white to yellowish or greenish white) (Hajpal, 2002) and the dehydration of iron compounds within sandstone (brown to reddish brown) (Chakrabarti et al., 1996). The discoloration of iron-containing sandstone is known to start from 250 ˚C due to oxidation of the iron compounds (Ingham, 2009).

It is likely that the strength and hence, load bearing capacity of rocks are affected when its constituent minerals undergo chemical changes as a result to exposure to high temperatures. Ingham (2009) reasoned that by examining the discoloration of concrete in a structure, the temperature that the concrete has been exposed to can be estimated. Similarly, if we can quantify the color changes of thermally treated local rocks, it may be possible to estimate the temperature an area of rock was exposed to, and the damage developed in that area due to a fire.

The use of colorimetry have been explored in the field of fire safety regarding concrete structures as well as other purposes such as quantifying soil colors. The instruments used ranged from low cost digital cameras (Colombo and Felicetti, 2007), phone cameras (Gomez-Robledo et al., 2013) and flatbed scanners (Annarel and Taerwe, 2011; Hager, 2014) to expensive spectrometers (Annarel and Taerwe, 2009) and spectrophotometers (Annarel and Taerwe, 2011). The instruments used were as simple as lamps to provide lighting and a tripod to hold the imaging device (Oestmo, 2013), to custom built boxes and frames designed to hold specimens and provide

consistent lighting by fixing the positions of lamps relative to the specimens (Gomez-Robledo et al., 2013; Leon et al., 2006).

Similar to other brittle materials such as concrete, microcrack generation in rocks during exposure to high temperatures causes physical deterioration in rocks. The strength and load bearing capacity of rocks could also be affected when its constituent minerals undergo chemical changes due to exposure to high temperatures. Both microcrack generation and chemical changes are dependent on the magnitude of temperature increase. Both the physical and chemical changes could alter the color of the rocks. It seems plausible to estimate the cumulative damage done to the rock through measuring the color changes of the rocks. For this to work, it is necessary to develop a repeatable and objective way of measuring color (and color changes) and its relationship to the integrity of the rock.

2.4.6.1 Color spaces

Qualitative description of color and color changes may be sufficient to describe large changes in color after rocks have been heated up to high temperatures. However, changes in the color of rocks may be subtle and hard to describe despite a difference in color being visually identifiable. Moreover, qualitative description of color of rocks may be subjective to different people.

There are a few ways to quantify the color of an object by computer image analysis such as the HSL and HSV system (Joblove and Greenberg, 1978), the Munsell color system (Landa and Fairchild, 2005), the CIE XYZ system (Kerr, 2010) and an improved version, the CIE L*a*b* system (Hoffman, 2013). Although the Munsell color system is commonly used to classify soil color (Lynn and Pearson, 2000), it is associated with a few problems. Firstly, unlike soil, rock is an aggregate of minerals whereby different minerals retain their individual color. This makes it hard to use the Munsell color system to classify rock colors. Secondly, the Munsell color system requires human observation and judgement to classify the rocks. This introduces a degree of subjectivity, and for large amounts of rock specimens, it will be very time consuming.

For computer analysis of colors, a more suitable system to use would be the CIE L*a*b* system. The CIE L*a*b* system has been used in other fields of research such as food colorimetry (Afshari-Jouybari and Farahnaky, 2011; Leon et al., 2006). Some of the advantages of the usage of this system for the comparison of color include being device independent, which means that the same values will be obtained even when using different machines to process the data (Yam and Papadakis, 2004), and being widely available, as the CIE L*a*b* system is integrated into commercial software such as Adobe Photoshop (Adobe Online Photoshop Manual, 2014) and MATLAB (The Mathworks Inc., 2014) which makes the usage of this system convenient. A repeatable and objective way of measuring color and color changes is essential in correlating color changes with the effects of exposing rocks to high temperatures.

The CIE L*a*b* system is made up of 3 different color values. The L* value is an indicator of where the specimen lies on a scale of pure white to pure black, and is on a scale of 0-100. The a* value is an indicator of where the specimen lies on a scale of red to green. The b* value is an indicator of where the specimen lies on a scale of blue to yellow. Both the a* and the b* scales are infinite, but are most commonly limited to a scale of -128 to 127. This is because although the CIE L*a*b* system can theoretically display colors that are imaginary due to an infinite range, most colors that can be found in nature and displayed by computers fall within this range of -128 to 127.

2.4.6.2 Lumen depreciation

The colorimetry process is dependent on many factors, one of which is the lighting conditions. The lighting conditions needs to be bright enough for a suitable photo of the rock in question to be taken, and would often require additional light sources.

Current light sources have a rated lifetime. Incandescent bulbs can last for about 1000 hours, while Light Emitting Diode bulbs can last up to 25000 hours. During its rated lifetime, most light sources would be subjected to lumen depreciation, which is a phenomenon where light sources become progressively dimmer (Fig. 2.10).

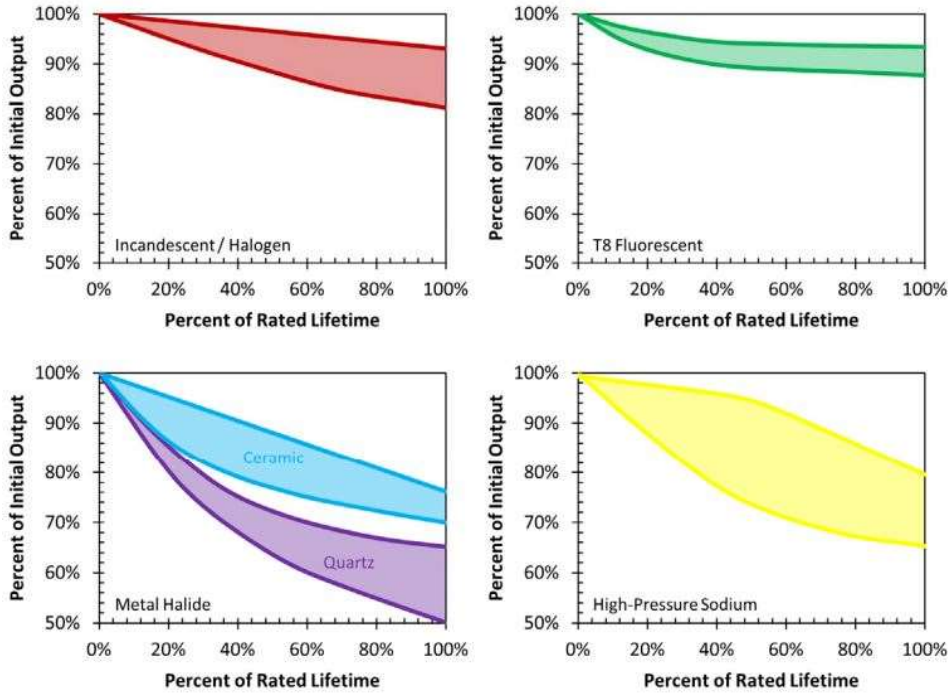

Fig. 2.10 Chart of lumen depreciation for various types of light sources against rated lifetime (US Department of Energy, 2013)

Even though the colorimetry process may use the same equipment in an effect to duplicate the exact same conditions as before, there will still be variation in the brightness of the light sources due to lumen depreciation. As such, a method to correct for lumen depreciation may be needed.

2.4.6.3 Light scattering

Another likely reason for color changes to occur in rocks that have been exposed to high temperatures could be the generation of microcracks within the minerals and along the mineral grain boundaries of the rock. The physical structure of the rock also affects the color as impurities, microcracks, or microvoids within the rock can cause scattering and refraction, which influences the color of the rock (Kennard and Howell, 1941). Microcracks generated within materials are known to cause color changes, such as in polymers which turn from transparent to white due to the formation of microcracks (Ashby et al., 2009; Ashby et al., 2013).

In the case of brittle materials, subsurface scattering of laser beams has been used as a non-destructive testing tool for the detection of microcracks within translucent

optical glass (Wang et al., 2011). Yuryeva and Yuryev (2014) noted that for blue-green glass beads tested with a spectroscope, areas containing cracks exhibit a transition of color from blue-green to brownish-green, and suggested that the color change was most likely due to Reyleigh scattering of light.

Reyleigh scattering occurs when the direction of propagation of light and other electromagnetic waves are altered by particles or microstructures smaller than the wavelength of the electromagnetic waves that are present within the medium of propagation. In this case, it is possible that damage done to rocks in the form of mechanical loading or heating generates microcracks of appropriate lengths for subsurface Reyleigh scattering to take place. As the wavelength of light is on the nanometer scale, microcracks that are of appropriate lengths will also be on the nanometer scale (Yuryeva and Yuryev, 2014).

Such cracks are hard to observe as they are smaller than the wavelength of visible light, as such, Scanning Electron Microscopy (SEM) techniques are necessary for the observation of these microcracks. Various researchers have confirmed the existence of nanometer scale microcracks within rocks using SEM techniques (Cheng et al., 2016; Dengler, 1976; Hao et al., 2017; Lee et al., 2006; Mamtani et al., 2012; Přikryl et al., 2003; Sprunt and Brace, 1974; Tapponnier and Brace, 1976; Wong and Einstein, 2009b; Zhu et al., 2008)

2.5. Factors influencing the strength of rocks

2.5.1. Exposure to high temperatures

Exposure to high temperatures will reduce the strength of rocks (Bauer and Handin, 1983; Richter and Simmons, 1974). This includes not only compressive but also yield strength and shear strength (Griggs et al., 1960; Odedra et al., 2001).

Different rocks will experience a different loss in strength, as some rocks will only experience mechanical effects from the thermal loading whereas some rocks may experience both mechanical and chemical effects from the thermal loading.

2.5.1.1 Chemical changes

An increase of thermal energy has been known to increase the rate of reaction of chemical reactions by providing enough energy to reach the activation energy for a

specific chemical reaction. This suggests that besides exposure to high temperature, chemically reactive components need to be present as well for chemical reactions to occur. This is implied by Atkinson and Meredith (1987) when they found out that exposure to high temperature amplifies the effects of stress corrosion, and by Tullis and Yund (1980) who found that a combination of moisture with heat decreases the strength of rocks more effectively than simply heating alone.

Besides speeding up chemical reactions that weaken the rocks, another way whereby chemical reactions weaken rocks can also be an alteration of their physical properties through mineralogical changes. Examples of this would be the transformation of smectite to illite (Kolarikova et al., 2005), the transformation of gypsum into bassinite (Brantut et al., 2011) and the transformation of aragonite into calcite (Yoshioka and Kitano, 1985).

2.5.1.2 Physical changes

A mechanical effect of thermal loading on rocks can also be related to the production of microcracks within a rock specimen. Due to a difference in the coefficient of thermal expansion of different mineral grains within a rock, microcracks can be generated within a rock specimen even when the rock is uniformly heated and not subjected to thermal shock (Devore, 1969).

Microcracks within a rock specimen can also be generated due to volumetric expansion of a certain mineral due to the reorganization of its internal crystalline structure during a phase change (Glover et al., 1995). This was shown by monitoring the acoustic emissions emitted by a rock specimen as it undergoes thermal loading, the generation of microcracks was confirmed with scanning electron microscope micrographs and an increase in porosity as confirmed by the nitrogen adsorption method. A sharp increase in the amount of acoustic emissions was detected when the temperature rose to 573 ˚C, which happens to be the phase change temperature for quartz to change from α-quartz to a bulkier β-quartz.

It has also been found that the type of microcracking that occurs is also temperature dependent. When Remiremont granite is heated to a temperature less than 600 ˚C, intergranular microcracks form at a higher rate, while the pace of intragranular

microcrack generation is slower. When the temperature is above 600 ˚C, the intragranular microcrack generation rate is higher than that of intergranular microcracks (Homand-Etienne and Houpert, 1989). This observation was also made by Hajpal and Torok (2004), who noted that in sandstone, intergranular microcracks form at lower temperatures of about 600 ˚C, as compared to intragranular microcracks in the quartz and feldspar grains, which appear at 750 ˚C.

Appendix I summarizes the previous experimental studies on the effects of high temperatures on rocks, separated into whether the specimens are tested while being held at high temperatures, or tested after the specimens has cooled down.

Rock types that were tested includes igneous rocks (pumice, basalt, gabbro, andesite and granite), sedimentary rocks (limestone, gypsum, dolomite and sandstone) and metamorphic rocks (marble, slate and schist). The temperatures tested range from -140 °C to 1200 °C. A variety of heating methods were employed, including heating via different types of furnaces, heating via heating elements wrapped around the specimen or even through an open fire. Tests performed include triaxial compressive tests, triaxial tensile tests, UCS tests, acoustic emissions and scanning electron microscopy.

Although most studies observed strength decreases and loss of integrity of rock specimens after heating, some studies observed an increase in strength due to various reasons such as evaporation of water, or a reduction in porosity due to expansion of minerals. Appendix II summarizes previous experimental studies where strength increases were observed after heating.

The strength increase is observed for all types of rocks, igneous (granite), sedimentary (sandstone) and metamorphic (marble). The heating methods used were less diverse and mostly consist of ovens and furnaces. Tests performed were similarly more limited, consisting mainly of Brazilian tensile tests and UCS tests

2.5.2. Rate of heating and cooling

So far the thermal effects on the rocks mentioned mostly deal with effects of thermal loading on the microscopic scale. Another effect of thermal loading and unloading on rocks on a larger scale is thermal shock. Thermal shock happens when one area of the rock has a higher temperature than another part. The difference in expansion or contraction of the area of rock generates stresses within the rock. However, there exists a critical temperature gradient which must be present before thermal shock takes place (Hasselman, 1969).

Rocks appear to have a threshold temperature, under which, microcracks do not appear, regardless of heating rate. For example, for Westerly granite, it has been found that acoustic emissions indicating the generation of microcracks only appears once rocks have been heated to about 80 ˚C at a pressure of 7 atm but not below the threshold temperature of 80 ˚C (Wang et al., 1989).

Another important factor that may influence the strength degradation of the rocks is the rate of heating of the rocks during the thermal loading process. A high rate of heating, which induces a high thermal gradient within the rocks, may lead to thermal shock. This leads to an uneven expansion between the core and the surface of the rocks. Richter and Simmons (1974) found that at a relatively low temperature of less than 250 ˚C, if the heating rate of a 50 mm long rock cylinder with 10 mm diameter is kept to less than 2 ˚C per minute, no permanent strain can be detected.

Todd (1973) stated that 2 ˚C per minute is the threshold, beyond which, acoustic emissions that implies the formation of microcracks begin to occur in Westerly granite, while no acoustic emissions were detected at a heating rate of less than 2 ˚C per minute, even though his specimens were heated to 300 ˚C. However, his conclusion was later disputed by Yong and Wang (1980), who found that acoustic emissions that implies the formation of microcracks appear after the specimen (19.1 mm diameter, 38.1 mm long cylinder) has been heated to 60-70 ˚C with a heating rate from as low as 0.4 ˚C per minute to as high as 12.5 ˚C per minute. One possible reason given by the authors to account for this is that their equipment used is much more sensitive than the one used by Todd (1973).

Other than the heating duration and rate, another attribute of a temperature gradient induced within the rock specimens is related to the cooling down period. Although Bauer and Handin (1983) claim that microcracking mostly forms during the heating period and almost none during the cooling period, Chakrabarti et al. (1996) are of the opinion that due to the low thermal diffusivity of rocks, steep temperature gradients can form during rapid cooling, which will induce stresses in the rocks.

2.5.3. Heating duration

Homand-Etienne and Troalen (1984) suggested that the time spent at the maximum temperature experienced by the rock specimen also plays a part in the formation of microcracks in a rock specimen. However, there seems to be a limit, after which further heating of rocks causes only minor additional changes in physical properties of rocks (Yavuz et al., 2010). Even though the time spent at maximum temperature does play a part, the difference in heating time that was able to cause significant changes in the rock properties is in the scale of hours. The P-wave velocity of rock tested decreased by only several percent after an additional 19 hours of heating following an initial period of 5 hours (Homand-Etienne and Troalen, 1984); or a decrease of about 50% after 12 hours of heating at 500 °C; and almost no change after 100 hours of heating at 100 °C (Yavuz et al., 2010).

2.5.4. Water content

Water content can reduce the strength of rocks through a relatively long term physical weathering processes such as the freeze-thaw cycle, or through chemical weathering processes such as the dissolution of soluble minerals within a rock. It can also directly reduce the mechanical strength of rocks through mechanisms such as the weakening of phyllosilicates bonds which are commonly present in granodiorites (Rossana and Paola, 2012).

Studies are unable to agree on the exact effects of water content on the strength of rocks, with some researchers finding that it reduces compressive strength and tensile strength by an equal amount (Vasarhelyi, 2005), and some researchers finding that, for sandstone, it has a larger effect on the tensile strength of rocks (50 % decrease) as compared to the compressive strength of rocks (20 % to 25 % decrease) (Ojo and

Brook, 1990). A comprehensive metastudy conducted by Wong et al. (2016) showed that sandstones are most susceptible to strength loss from an increase of moisture content, with a modal UCS loss of 20 % to 30 %.

It has also been shown that even a small change of 1% in the moisture content of a rock can lead to a nearly 50% change in the compressive strength of sandstones (Vasarhelyi and Van, 2006). As such, the control of the moisture content of the rocks used in our experiment is very important.

An interesting theory for the reduction in strength of water-saturated rocks is the Rehbinder effect (Iphar & Goktan, 2003). The Rehbinder effect explains the decrease in mechanical strength of saturated rocks through thermodynamics, similar to the method that Griffith (1921) used. The Rehbinder effect states that for a saturated rock, cracks are more likely to be generated due to a lower surface free energy due to the adsorption of the water molecules on the surfaces of the rocks. As the surface free energy is lower as compared to that of dry rocks, a loading of the same magnitude is able to create a larger surface area, or cracks, as compared to that of a dry rock.

2.5.5. Rate of heat release

As stated in sections 2.5.1 and 2.5.2, both the heating rate and heating duration of a fire in a rock tunnel can influence the residual strength of the rock mass after a fire. As it is hard to estimate the heating rate of any random fire, various tests were conducted in both real, disused tunnels and laboratories to examine the likely rate of heat release for fuel sources commonly feeding accidental fires. Such materials include hydrocarbons and cellulose. Data collected from these tests were compiled (Fig. 2.11) to give an indication of the rate of temperature increase of a fire, as well as the maximum temperature reached.

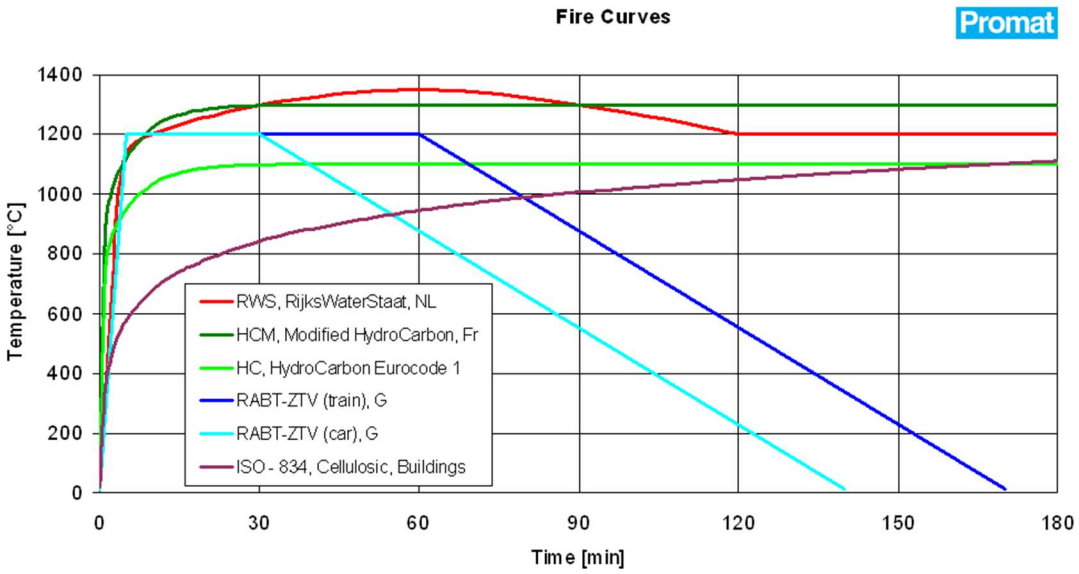

Fig. 2.11 Various fire curves developed (Promat, 2017b). Legend shows the standards that the curves were extracted from. NL means Netherlands, Fr means France and G means Germany.

The duration of a fire is dependent mostly on fire-fighting efforts as well as the availability of flammable materials within the affected zone, whereas the rate of temperature increase and maximum temperature reached is dependent on the nature of the flammable material feeding the fire. Local projects such as the Kallang-Paya Lebar Expressway adopted the RWS fire curve (Fig. 2.11, red) as its standard (Promat, 2017b).

The RWS curve was developed during a collaboration between the Efectis Group and the Dutch Ministry of Infrastructure and the Environment, with most of the temperature increase happening within the first 5 minutes (Breunese et al, 2008).

Besides the nature of the flammable material fueling the fire, factors such as the geometry and the ventilation of the tunnel also affects the rate of heat release of the fire. Wider tunnels have been found to have a slower heat release as compared to narrower tunnels, however, the effects of ventilation have a more dramatic influence of the rate of heat release of a fire (Carvel et al., 2004).

In a local context, this will increase the rate of heat release of a fire, as local guidelines recommend maintaining mechanical ventilation during a fire for smoke control purposes (SCDF, 2012). To better understand the actual conditions during a fire, the

heating scheme used in this study will encompass a scenario where rapid heating takes place, as well as a slower heating in cases of rocks being of a further distance from the fire.

2.5.6. Kaiser effect

As the rocks will be dried in an oven, the specimens may possibly be exposed to temperatures in the oven that are sufficiently high to cause microcracking. However, Yong and Wang (1980) found that after Westerly granite was heated up to a high temperature and then cooled, further heating did not produce acoustic emissions that may indicate the generation of microcracks as long as the temperature did not exceed the previous temperature reached.

Since the theorized mechanism for the thermal weakening of the rocks is via the generation of microcracks, we can say that thermal loading is somewhat similar to mechanical loading. It is likely that this lack of acoustic emission during heating at a lower temperature is a form of the Kaiser effect, similar to that seen in cases of mechanical loading.

The Kaiser effect is a phenomenon observed during repeated loading of brittle materials, and has been used in various ways such as the damage assessment of reinforced concrete structures (Vidya Sagar et al., 2014), and the estimation of in-situ stresses on rocks (Kojima and Matsuki, 1994; Lehtonen et al., 2012). For a brittle material, such as limestone (Lavrov, 2001), granite (Yuan and Li, 2008) and even bulk metallic glasses (Bakai et al., 2007), there is a form of memory of the previous stress level reached by the loading. Unloading and loading of the material to a level lower than the previous loading produces little or no acoustic emissions which indicate damage done to the material. A model suggested for the Kaiser effect is the reversible Griffith crack model (Lavrov, 2003). In this model, a microcrack can exist in two states, the opened state and the closed state. In the opened state, the microcrack is assumed to have no strength, while in the closed state, it is modeled as partially healed. As the specimen is loaded, energy is used to open the crack again. This increases the elastic energy stored in the crack. As the loading reaches its previous level, the length of the crack remains constant, but once the loading goes past the

previous level, energy is used to propagate the crack, which produces additional acoustic emissions (Holcomb and Stevens, 1980).

2.5.7. Stress waves and stress shadowing

The SHPB dynamic compression test works on the assumption that when the striker bar hits the input bar, the amplitude of the stress wave within both the input bar and the output bar will be smaller than the yield stress of these steel bars. However, as the specimen is known to fail during the course of the experiment, it is clear that we can assume an elastic stress wave within the input and output bars, but not within the specimen itself. There have been two schools of thought regarding the nature of plastic stress waves. The first states that plastic stress wave propagation within a medium is strain rate independent, whereas the second school of thought states that the strain rate is a variable in plastic stress wave propagation (Kolsky, 1964).

As a stress wave is a form of P-wave, the P-wave velocity formula (equation 2.5), which describes the relationship between the P-wave velocity and material properties, can help us understand stress wave propagation within the SHPB bars.

In elastic wave propagation, E is a function of both the stress σ, and the strain ϵ. However, researchers have found that the dynamic stress-strain curve of certain materials showed that the elastic modulus also varies with strain rates (Alter and Curtis, 1956; Bell, 1956; Sternglass and Stuart, 1953). This led to a strain rate dependent theory for plastic wave propagation in which the elastic modulus, E, is dependent on stress σ, strain ϵ, and the strain rate $\frac{d\epsilon}{dt}$ (Kolsky and Douch, 1962; Lubliner, 1964).

As a stress wave passes through a brittle medium, flaws within that medium may fail due to local stress amplification, hence creating cracks that propagate outwards. The crack that extends outwards creates a shielded zone behind it that reduces the probability of crack initiation from flaws within the shielded zone (Doan and Billi, 2011; Doan and d'Hour, 2012; Hild et al., 2003). This phenomenon has been noted in the oil and gas industry, where it affects the effectiveness of hydraulic fracturing, as well as with regards to high strain rate deformation during earthquakes. (Bunger and Cardella, 2015; Taghichian, 2014; Zangeneh et al., 2015). Stress shadowing leads

to the formation of relatively large flaw-containing fragments without initiated cracks within the shielded zone. The stress shadowing phenomenon assumes that the plastic wave velocity is lower than the crack propagation velocity within the medium. If the plastic wave velocity is higher than the crack propagation velocity, the plastic wave would cause crack initiation at every flaw that fulfills the crack initiation criterion, as the plastic wave would have passed the shielded zone before the cracks have sufficient time to propagate outward to form the shielded zone.

2.6. Bukit Timah Granite

Singapore Bukit Timah Granite rock cores are examined in this study. It is one of the two major rock formations in Singapore, the other being the Jurong formation that is of sedimentary origin (Lee and Zhou, 2009). Studies on Bukit Timah Granite are especially useful as it has already been identified as a suitable host rock for underground structure construction and it is widespread in Singapore (Fig. 2.12). An example is the Singapore Armed Forces underground ammunition storage facility in the Mandai area, which is hosted within Bukit Timah Granite (DSO National Laboratories, 2016).

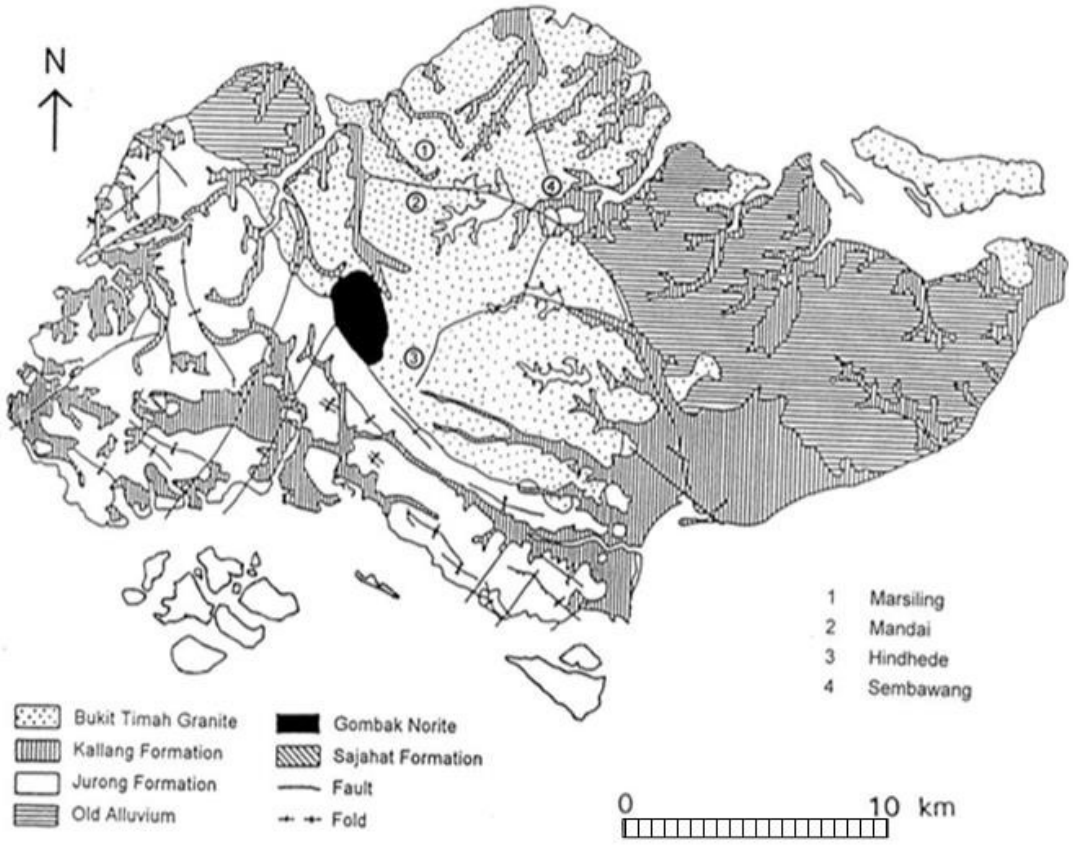

Fig. 2.12 Geological map of Singapore (modified from Zhao, 1998)

According to the lithological classification system outlined by Wong and Maruvanchery (2016), there exists seven different types of Bukit Timah Granite. They each differ in physical appearance, mineral composition, as well as engineering properties.

The rock cores used in this study are of the A+ type out of a total of seven types of Bukit Timah Granite. It is a light grey, coarse grained and equigranular granodiorite, with its mineral content listed in Table 2.1. The minerals of Bukit Timah Granite which has a holocrystalline, hypidiomorphic granular texture, can be distinguished easily by the naked eye. The average grain size is estimated to be around 2 mm (Fig. 2.13a, 2.13b). The major constituents of A+ type Bukit Timah Granite are either subhedral (plagioclase and alkali feldspar) or anhedral (quartz) (Fig. 2.13c).

Table 2.1. Mineral content of A+ Bukit Timah Granite used in this study

Mineral	Alkali feldspar	Quartz	Plagioclase	Biotite	Sphene	Apatite	Zircon	Opaque
Mineral content by volume (%)	22.1	30.1	36.2	10.6	0.2	0.2	0.2	0.4

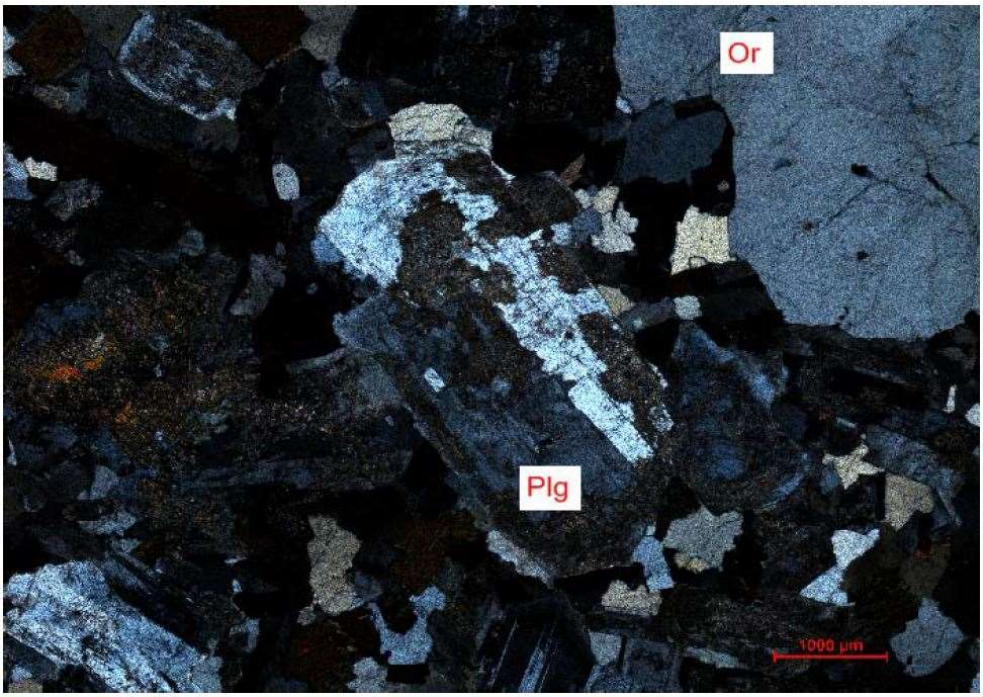

(a)

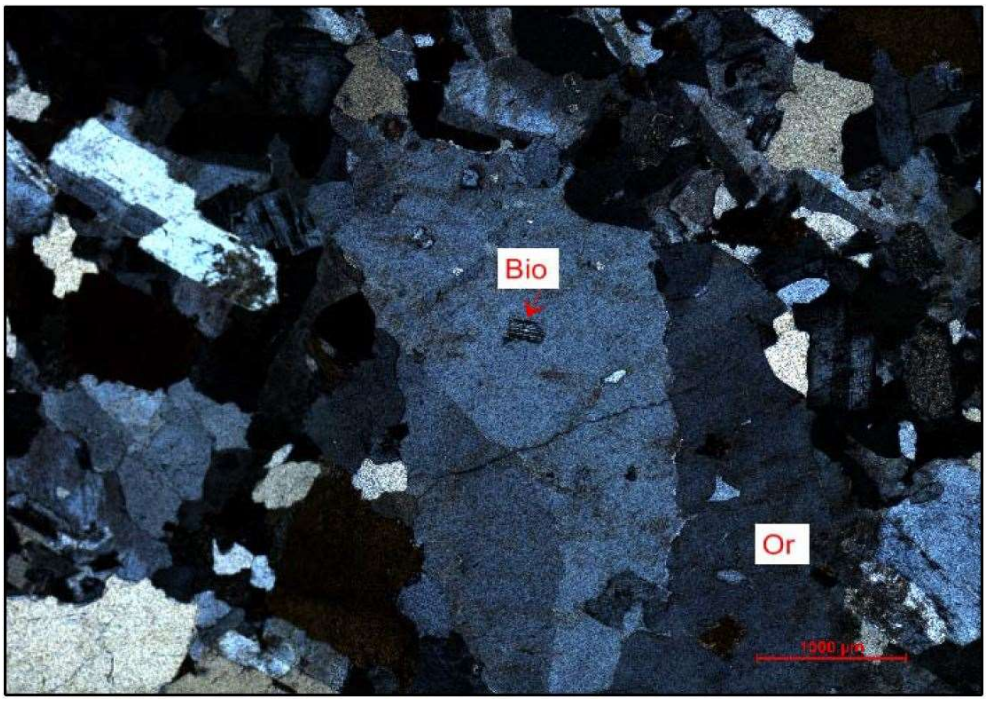

(b)

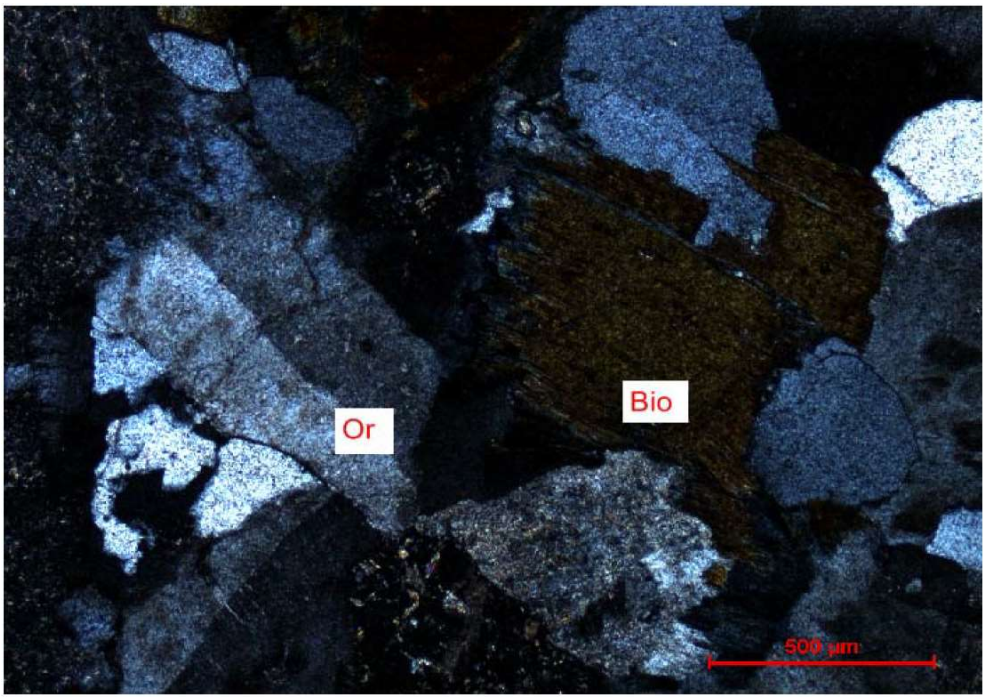

(c)

Fig. 2.13 Thin section study of Bukit Timah Granite showing (a) average grain sizes of plagioclase (Plg) and alkali feldspar (Or), (b) biotite inclusions within other grains, (c) subhedral alkali feldspar (Or) and anhedral biotite (Bio).

2.7. Effects of rock texture on rock strength

Different rocks with very similar mineral constituents but different grain sizes are known to have vastly different strengths. Researchers have found that the strength of a rock either correlates linearly with the grain size (Hugman and Friedman, 1979; Onodera and Asoka Kumara, 1980), or with the square root of the grain size (Fredrich et al., 1990; Haney and Shakoor, 1994; Hatzor and Palchik, 1997; Olsson, 1974; Wong et al., 1996).

The texture of the rocks may also play a part in determining the strength of the rocks (Kolay and Baser, 2017). A dimensionless "Texture Coefficient" (TC) comprising of grain circularity, grain elongation, grain orientation and degree of grain packing was proposed (Howarth and Rowlands, 1986, 1987). Although the TC was shown to be correlated to rock strength, it was argued that the TC was not comprehensive enough as it does not take into account various parameters such as the average grain size and the porosity. It is merely an empirical correlation rather than a mechanistic explanation of the effects of rock texture (Prikryl, 2006).

Case et al. (1980) determined that the crack initiation of uniformly heated ceramics is dependent on the grain size as well as other material properties. Hasselman (1969) also concluded that the crack initiation of ceramics subjected to thermal shock does not occur until a certain threshold temperature has been reached.

Homand-Etienne and Houpert (1989) also found that for the modal crack lengths of Remiremont granite with subhedral plagioclase, "no matter what the intensity of the thermal treatment is, the distribution of crack lengths is almost the same. In fact, crack lengths depend only upon the initial material structure and, in particular, the shape and dimensions of the crystals."

2.8 Summary

The effects of exposure to elevated temperatures on the properties of rocks have been studied extensively for the past century. However, most of these studies focused on the effects of slow heating commonly found in tectonic events, or heating due to radioactive isotopes in the form of the natural geothermal gradient or storage of nuclear waste. By contrast, the effects of a faster heating rate, such as those found in

an accidental fire, are less well studied. This presents a research gap that needs to be addressed so as to improve underground construction safety.

Another research gap that was identified is the lack of studies utilising local rocks, such as Bukit Timah Granite. As a host rock, Bukit Timah Granite is suitable for underground construction due to its inherently high strength, as well as its widespread availability (Fig. 2.12). As many different factors influence the mechanical properties of rocks, such as rock texture, grain size and chemical composition, the lack of data concerning the effects of thermal exposure of Bukit Timah Granite would add a degree of uncertainty in underground construction.

Finally, most of the testing conducted by previous studies involves destructive testing such as the UCS test, or the Brazilian tensile test. In practical usage, destructive testing is costly and time-consuming. Non-destructive testing would be more useful in assessing the residual strength of fire-damaged rock. Non-destructive testing can be used as a preliminary assessment of whether repair work will be economically feasible, as well as generate a map of potential weak zones for workers to avoid.

Chapter 3 Material and experiment methodology

3.1 Introduction

The conditions that an underground structure experiences in a fire changes with respect to the phase of the fire. For example, the rock mass may have different behaviours during the course of the fire and after the fire was put out. Also, the type of loading that we should be concerned with also changes during the course of the fire. While the fire is raging, it is likely that flammable substances may explode. This would impart a dynamic loading on the rock mass while it is still at an elevated temperature. After the fire has been put out, we should be more concerned with the effects of long term static loading on the fire-weakened rock mass at room temperature.

This study simulates the effects of a fire on an underground rock structure, as such, it is split into a few parts. This chapter will give an overview on the methods and equipment used in this study.

3.2 Specimen preparation

This study used both Bukit Timah Granite (BTG) and Carrara Marble (CM). BTG was chosen as it is one of the most commonly available rock locally. It is also extremely suitable for construction due to its strength. Structures such as an underground ammunition facility has already been built from BTG (MINDEF, 2010). A greater understanding of the response of BTG under different conditions will be useful in predicting the behaviour of local underground rock structures.

CM was chosen as it is a classic material that was extensively studied (Atkinson, 1979; Covey-Crump, 1997; Ree et al., 2014; Sassoni et al., 2017; Wong and Einstein, 2006, 2007, 2008, 2009a, 2009b, 2009c, 2009d; Wong et al., 2014). It is a monomineralic rock that is also extremely pure and shows an almost homogenous fabric. This reduces the natural variation present in the specimens and accentuates the effects on the different heating and loading conditions.

In this study, Brazilian tensile test specimens were produced using BTG and dynamic compression tests specimens were produced from both BTG and CM.

3.3 Brazilian tensile test specimens

The specimens used in the present study were cut from rock core samples of coarse grained, light grey granodiorite obtained from the Mandai area by the Defence Science and Technology Agency (DSTA) (Fig. 3.1). The samples are mainly composed of quartz, feldspar, mica and hornblende. It is estimated that the mineral contents are 75% felsic and 25% mafic.

Fig. 3.1 Rock cores obtained from DSTA

The rock core samples were first cut into the discs with a Buehler Auto Chop 2216 Delta Automatic Abrasive Cutter, as shown in Fig. 3.2, with a feed rate of 0.8 mm per second. However, even though the feed rate is carefully selected undesirable chipping often occurs along the edges of the specimens. The specimen would then be grinded with a Chiao Bang CB-3060ASD rock grinding machine, as shown in Fig. 3.3, to remove the chips and to obtain smooth end faces.

Fig. 3.2 Buehler Auto Chop 2216 Delta Automatic Abrasive Cutter

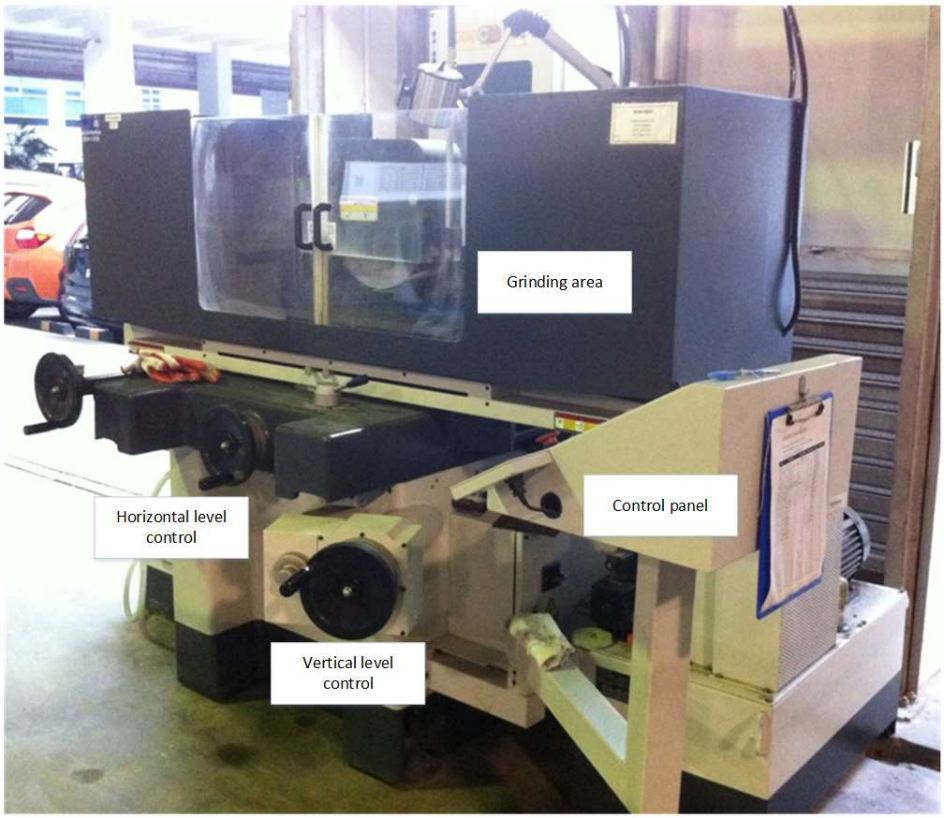

Fig. 3.3 Chiao Bang CB-3060ASD rock grinding machine

The diameter of the Brazilian tensile test specimens was around 50 mm, and the thickness of the specimens were around 25 mm to give a thickness-to-diameter ratio

of around 0.5. Besides using the grinder to remove chips along the rim of the specimens, the grinder also used precision-made placeholders to secure the specimens, ensuring parallelism of the specimen faces.

All specimens were prepared in the Geotechnics Workshop at the Nanyang Technological University, in general accordance with the ASTM (2008) and were kept in an oven maintained at 40 °C so as to remove water from the specimens.

3.4 Dynamic compressive tests

For the dynamic compressive tests, CM discs (Fig. 3.4) were cut from CM slabs. As only CM slabs instead of rock cores or cylinders were available, an abrasive waterjet machine (Fig. 3.5) was used to cut discs from the slabs. As the slabs were made for commercial use, one side is rough while the other side was smooth. Both sides were then polished with the rock grinding machine (Fig. 3.3) to ensure equal smoothness and to remove minor chipping around the rims of the specimen. As the dynamic compressive test using the SHPB setup relies on the transmission of stress waves through the specimen, it is necessary for the specimen to have smooth faces so as to reduce the impedance mismatch. Care was taken to ensure that the diameter of the specimens remained smaller than the diameter of the input and output bars of the SHPB setup even after thermal expansion from the heating process. This is so that the assumption of one dimensional wave propagation is still valid. The marble specimens were about 48 mm in diameter and 26 mm thick to give an average thickness to diameter ratio for of 0.54.

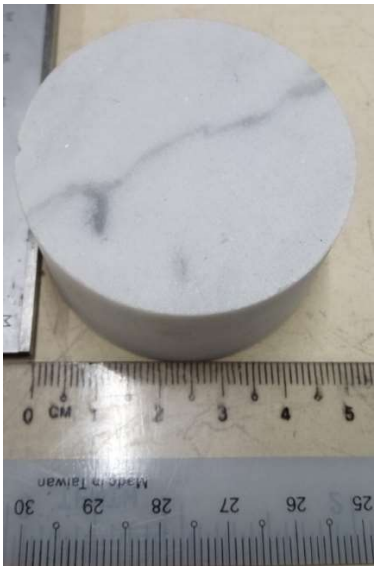

Fig. 3.4 Carrara marble specimen (around 48 mm in diameter, around 26 mm in thickness)

Fig. 3.5 OMAX abrasive waterjet machine

Dynamic compressive tests on BTG were also conducted. Fabrication of BTG dynamic compressive specimens was more difficult as only rock cores were available. Dynamic compressive test specimens cut from the available 50 mm diameter rock cores tended to have a larger diameter than the input and output bars of the SHPB system after thermal expansion. As such, after 40 mm thick BTG discs were cut from the rock cores, they were polished using the rock grinding machine to ensure a flat surface. The abrasive waterjet machine was then used to cut 40 mm diameter discs from the 50 mm diameter discs. After this, the rock grinding machine was used to grind the 48 mm thick BTG discs to a thickness of around 26 mm.

3.5 Vacuum impregnation

Epoxy filled specimens were also produced through the use of vacuum impregnation. Brazilian tensile test specimens as specified in section 3.2.1 were produced. After the specimens were thermally treated, a low viscosity mixture of Buehler epothin 2 resin and epothin 2 hardener was prepared according to the manufacturer's specifications. The chosen epoxy, which was specially designed for the impregnation of micropores and microcracks, has low viscosity as well as low shrinkage. A yellow fluorescent dye was added to the mixture. The yellow fluorescent dye used in this study is excited

by blue light and emits green light. The above method was adapted from Nishiyama and Kusuda (1994, 1996).

The yellow fluorescent dye was chosen instead of Buehler's Epoblue fluorescent dye. Even though Epoblue is excited by ultraviolet light which is invisible and does not light up the specimen, it was found that the use of ultraviolet light causes autofluorescence of minerals within BTG. Autofluorescence is a phenomenon where minerals within the rock absorbs ultraviolet light and releases it in the form of visible light (section 2.4.4). The autofluorescence of these minerals are sufficiently bright to obscure the finer microcracks generated within the specimens.

Fig. 3.6 Specimens coated with fluorescent epoxy (50 mm diameter)

After the fluorescent low viscosity mixture was prepared, a small amount was poured into an aluminium foil container and the thermally treated specimen was placed on it, so as to have a layer of low viscosity fluorescent epoxy covering the bottom surface of the specimen (Fig. 3.6). The container and specimen were then placed within Buehler's Cast N' Vac vacuum chamber and attached to a vacuum source. The specimens were then left to cure overnight.

During the curing process, heat is generated, which may lead to shrinkage of the epoxy upon cooling. Depending on the degree of bonding between the microcrack faces and the epoxy, the effects can range from additional stress being applied to the microcracks, or debonding from the faces of the microcracks. In both cases, the potential complications that may arise would have minimal effect on the observation of microcracks. Epoxy that has debonded from the faces of the microcracks would be held in place as the microcracks are neither completely smooth, nor completely straight. The degree of epoxy shrinkage is too small to cause the solidified epoxy to

entirely lose contact with the microcrack or be removed from the microcrack, as the epoxy was specially formulated for impregnation of micropores and microcracks.

After the curing process, the specimens were removed and cut into sections, as shown in Fig. 3.7, to give 25 mm thick pieces. The surface area of each section observed is about 245.44 mm^2. The wavy red line represents the failure plane, or the main crack.

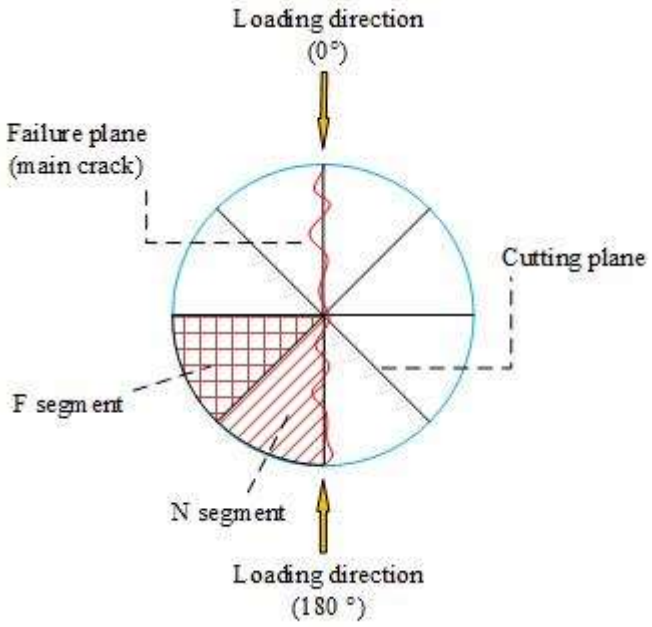

Fig. 3.7 Sectioning of specimen after vacuum impregnation of fluorescent epoxy

The expected damage to the specimen during the sectioning process is expected to be minimum, as the low viscosity fluorescent epoxy would have reinforced the specimen and reduced the amount of microcracks formed during the process. Any microcracks that do form during the process will not show up during the microscopic observation process later as they will not be filled by the solidified fluorescent epoxy.

After the sectioning process, pieces were selected and placed in Buehler epoxy specimen cups that were coated with a silicon based release agent beforehand. The selected segments were chosen on the basis of the least damage caused during the sectioning process by visual inspection. The pieces were then completely encapsulated within a layer of clear epoxy to support the specimen during the polishing process. After the second layer of epoxy has finished curing, the specimens were demolded and placed within a polishing machine. The machine then polished

the specimen with 320 grit sandpaper until both the clear and fluorescent epoxy layer was removed.

3.6 Brazilian tensile test

Brazilian tensile tests were conducted in conjunction with the colorimetric tests. All specimens that underwent the Brazilian tensile test were tested in a cooled state. To correlate the change in color values with the change in Brazilian tensile strength. The Brazilian tensile tests were conducted with an MTS 815 machine (Fig. 3.8) with the indirect tensile test apparatus equipped. The loading rate used for the tests was 0.1 kN/sec, so as to achieve a quasi-static loading to finish the loading test in a reasonable amount of time (ASTM, 2008).

Fig. 3.8 MTS 815 with indirect tensile test apparatus

Various researchers have suggested using cushions or loading jaws to increase the contact area between the platen and the specimen. This would increase the chances of the specimen failing under tensile stress instead of compressive stress as well as increase the accuracy of the test (ASTM, 2008, Andreev, 1991, Fairhurst, 1964). For this experiment, curved loading jaws were used as it was more convenient than using strips of cushioning material. This is because the cushioning material will have to be

replaced after every test as the cushioning would be deformed from the compression. Also, as the metal loading jaws are smoother than the masking tape or cardboard used as loading strips, there will be lesser friction that acts along the edge of the specimen.

For the specimens that experienced minor chipping at the edges during the heating process, special care was taken to orientate the chips at a 45˚ angle from the horizontal, as shown in Fig. 3.9. This is to minimize the effect that the chip in the specimen on the stress field induced in the specimen during the loading test.

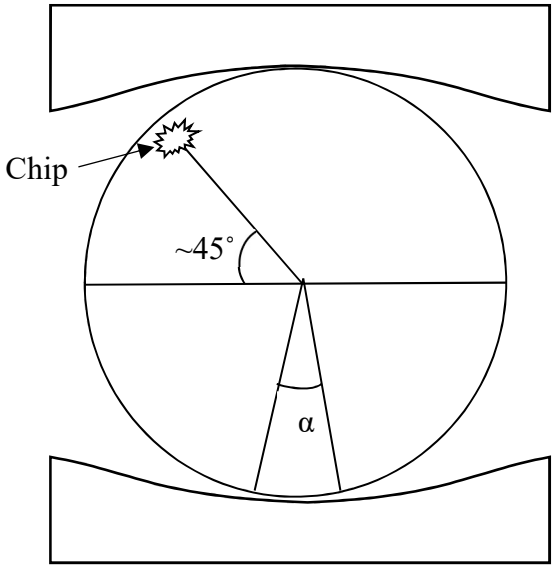

Fig. 3.9 Orientation of specimen during Brazilian tensile test, with arc of contact, α

Due to the fact that the Brazilian tensile test induces both compressive and tensile stresses within the specimen as compared to a uniaxial tensile test which dominantly induces a tensile stress within the specimen, there is a chance that the specimen may undergo compressive failure, particularly adjacent to the loading points, instead. To determine the validity of a test, we need to differentiate between the compressive failure and the tensile failure of a specimen, which can be achieved through the use of a high speed camera. By examining the high speed camera footage of the experiment at the point of failure, we can visually inspect the specimen for the location of the crack initiation, assuming that the crack initiates on the face of the specimen that is being recorded, which would indicate whether the specimen failed by compressive or tensile failure. The high speed camera footage may also give us additional information such as the cracking pattern of the specimen, as well as the

speed of crack propagation. For this experiment, a Phantom v310 high speed camera was used to capture images at a rate 20000 frames per second. A lower frame rate was chosen so as to increase the exposure time for each frame of a particular video footage, which will lead to brighter images for an easier crack identification.

After each test the high speed camera footage was reviewed to check if the test conducted is a valid one, where the crack initiates from the middle of the specimen.

3.7 Heating schemes

In this study, two different types of heating schemes were used. The two different heating schemes differed in the rate of heating. The first heating scheme had a high heating rate, which is meant to simulate the effects of an uncontrolled fire on an underground rock structure. The second heating scheme has a heating rate of 2 °C as recommended by Todd (1973), which is meant to prevent the occurrance of thermal shock.

3.7.1. First heating scheme

The first heating scheme is to simply heat the rock specimens being prepared for 30 minutes as fast as possible. A standardized time for heating of the specimens was used as it was suggested that the time spent at the maximum temperature experienced by the rock specimen also plays a part in the formation of microcracks in a rock specimen (Homand-Etienne and Troalen, 1984). To ensure that the specimen is homogenously heated, a MATLAB script using the finite difference method was written to simulate the heating process and to see how much time is needed for the entire specimen to be homogenously heated. The MATLAB script required several variables, such as the coefficient of thermal conduction of granite and the coefficient of convection within the furnace.

Firstly, dummy rock specimens were heated to the target temperatures using the same programming on the furnace so as to obtain the heating curve of the furnace. This process was repeated for each target temperature as the furnace may heat up at different rates depending on the target temperature set.

To emulate the rapidly rising temperature of a fire, the furnace was programmed to reach the target temperature as soon as possible. The heating curve of the furnace was

then obtained by taking the air temperature inside the furnace at 30 second intervals using the integrated thermometer. The temperature of the dummy specimen being heated was taken immediately with an infrared thermometer (Fig. 3.10) after the target temperature was reached, whilst the specimen was still in the oven. This is so that we will have a data point to match the actual temperature reached by the dummy specimen with the numerical modeling of the heat treatment done afterward.

Fig 3.10 Omega OS425-LS non-contact infrared thermometer

Once we know the heating curve of the air inside the oven, it can be plotted out in Microsoft Excel and the best-fit polynomial equation of the heating curve was determined, as shown in Fig. 3.11. This polynomial equation can then be used in the MATLAB simulation to model the heating environment of the specimen.

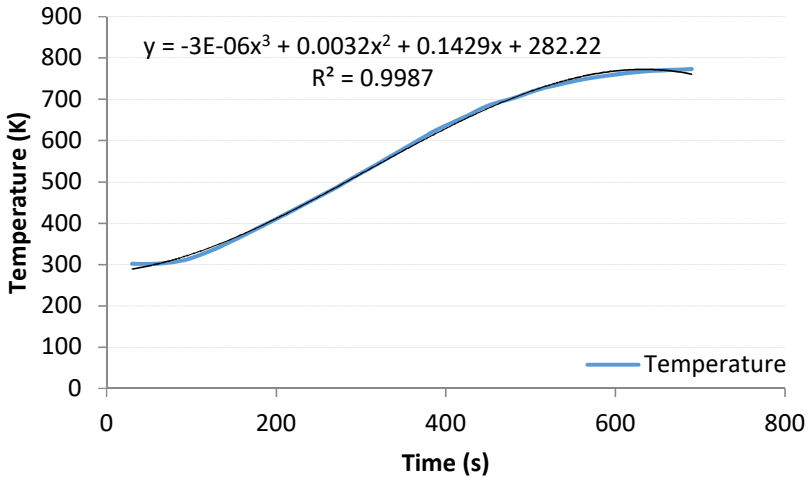

Fig. 3.11 Heating curve of test specimen heated to 500 ˚C

A model of a granite disc with dimensions of 50 mm diameter and 30 mm thickness was then developed in MATLAB. Using the finite difference method, the specimen was heated up in the simulation in accordance with the equation created from the data collected from the actual heating on the dummy specimen. This simulation is affected by an unknown variable, the convective heat transfer coefficient between air and the specimen, which is dependent on several other variables such as the condition of the air flow within the furnace and the temperature of the air within the furnace. As the convective heat transfer coefficient is normally treated as an empirical coefficient (Osczevski, 1995), the applicable convective heat transfer coefficient in the simulation was found through a series of trial and error, and checked by matching the surface temperature of the model with the actual surface temperature of the dummy specimen. The actual convective heat transfer coefficient is expected to be lower than the value used in the simulation, as this method of determining the convective heat transfer coefficient would include the radiative heat transfer as well. However, since the purpose of this simulation is to determine the time needed for heating the specimen, the inclusion of the radiative heat transfer is expected to improve the accuracy of the modeling. The simulation is considered accurate only if the surface temperature of the model is the same as the surface temperature of the dummy specimen in the test heating.

Using this convective heat transfer coefficient, the simulation, as seen in Fig. 3.12, was run once again to determine the time needed to equalize the temperature between the surface and the core of the specimen. This is so as to ensure the temperature within the specimen is as uniform as possible. The core and surface temperature is treated as being uniform once the difference between the two temperatures is less than 3 ˚C. After considering the time needed to equalize the temperature between the core and the surface of the specimen, it was decided set the heating time at 30 minutes.

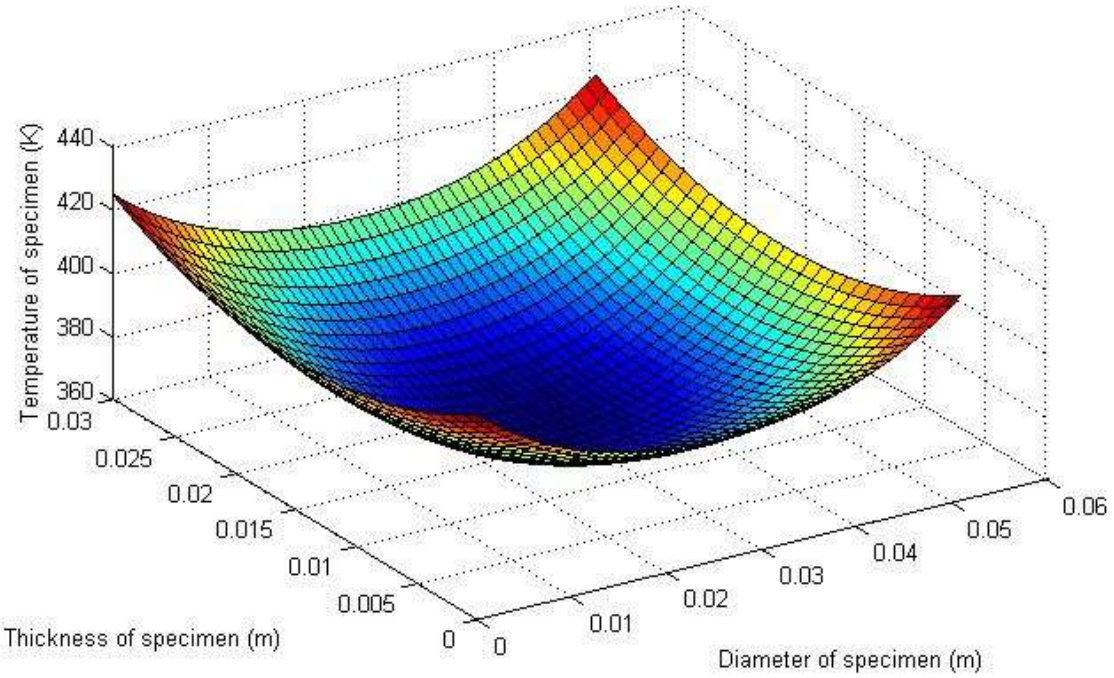

Fig. 3.12 Simulation of specimen heating to determine heating time (50 mm diameter, 30 mm thickness)

For the specimens undergoing the colorimetric process, the effects of the cooling rate on the color change was also explored. The cooling rate of the specimens were varied using different methods. The exact rate of cooling is hard to control as it depends on many factors, thus 3 rates of cooling in different environments that significantly differ from each other were used.

Slow cooling was achieved by leaving the specimens in the oven after heating while leaving the door of the oven open. Residual heat from the heating elements of the oven ensures a low cooling rate. A normal cooling rate was achieved by removing

the specimens from the oven and leaving it to cool in a place with no airflow. A high cooling rate was achieved as compared to the specimens undergoing slow cooling as the temperature difference between the surroundings and the specimen is larger. For fast cooling, the specimens were rapidly cooled to room temperature with an electric fan, in the same area as the specimens that underwent normal cooling. This creates an airflow which increases the convective heat transfer coefficient of the specimen.

In the case of normal cooling and fast cooling, there is a problem associated with controlling the cooling rate of the specimen after being removed from the furnace. As the specimens come into contact with the workbench, the conduction heat loss of the specimen is a lot higher than the convective heat loss. This makes it hard to control the cooling rate of the specimen as the different methods used to control the cooling rate only affects the convective heat loss of the specimen, which is negligable compared to the conductive heat loss. To solve this problem, a piece of silica aerogel was used to insulate the specimens from the workbench and reduce the amount of heat loss through conduction. Silica aerogel has a conductivity of 0.03 W/(mK), which is comparable to the conductivity of air, which is 0.0262 W/(mK) (Lide, 2005). Another precaution taken to minimize conductive thermal loss is to lay the heated specimens on its rim. This minimizes the surface area in contact with the aerogel, as seen in Fig. 3.13. A combination of these two precautions aims at reducing the conduction heat loss to a negligible amount.

Fig. 3.13 Cooling configuration used to reduce conduction heat loss (Specimen diameter is 50 mm, thickness is 25 mm)

3.7.2. Second heating scheme

The second heating scheme, used in the dynamic compression tests, heats the specimen at a rate of 2 °C per minute. This heating rate is specifically chosen to avoid thermal shock in the specimen and has been used as a limit by other researchers to determine the effects of heating on rock mechanics (Richter and Simmons, 1974; Todd, 1973; Batzle et al., 1980; Yatsu, 1988; Hall and Hall, 1991; Hall, 1997, 1999). Even though this heating scheme keeps the heating rate under the 2 °C per minute limit, it means that for different target temperatures, the specimens will spend different amounts of time being heated, which may affect the amount and type of microcracks being generated. At the end of the temperature increase phase, the specimen is held at the target heating temperature for an additional 30 minutes to ensure a homogenous temperature throughout the specimen.

3.8 Colorimetry

Colorimetry was performed on two different types of specimens. All specimens that underwent colorimetry was photographed in a cooled state. The first group are simply specimens that were heated with the first heating scheme. The photos of these specimens were taken before and after the heating process and subjected to the colorimetry process described below.

The second group of specimens analyzed with colorimetry was heated with the first heating scheme, before having high temperature grease smeared onto one flat side of the heated specimen (Fig. 3.14). The purpose for doing so is to simulate the effects of smoke and soot on the surface of the rock.

As soot and smoke are carbon particles suspended within partially unburnt hydrocarbons, they tend to be black in color and greasy. The high temperature grease used to simulate smoke and soot damage consists of tungsten disulfide powder suspended within a high viscosity synthetic base oil. Once applied to the specimens, it is black in color and greasy, similar to actual smoke and soot.

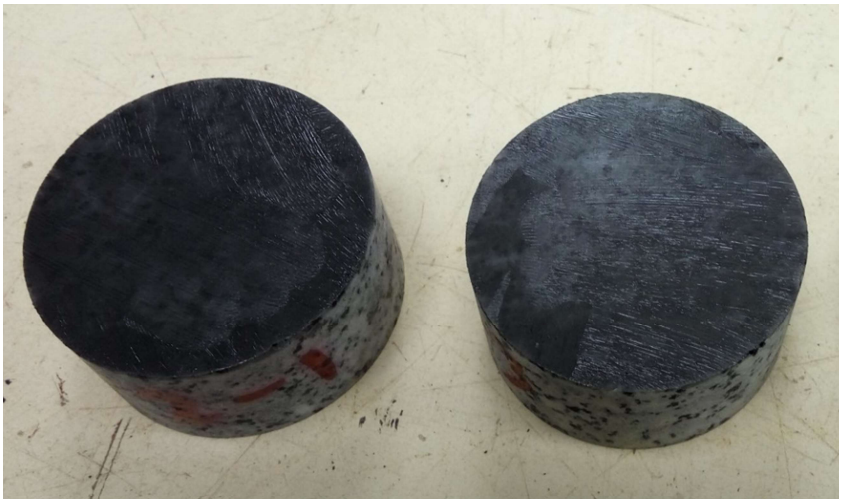

Fig. 3.14 Granite specimens (50 mm diameter, thickness of around 25 mm) coated with high temperature grease to simulate soot and smoke damage.

As the presence of smoke and soot can influence the accuracy of colorimetry, it is important to determine the remnant effects, if any, of smoke and soot being removed on the effects of the color of the specimen. After the high temperature grease was applied to the specimens, the coated specimens were left in a 40 °C oven for 24 hours. Afterwards, the grease was removed by scrubbing the specimens with a scouring pad and isopropyl alcohol before completing the colorimetry process.

The photo taking process used to obtain images for the colorimetry process is as follows:

1. Arrange the specimens on a red background in a well-lit room.
2. Place two Dedocool lights at equidistance from the specimen, in a way that the specimen will be illuminated at a 45 degree angle. Use the Dedocool lights at its highest setting, producing a light with a color temperature of 3300 °K.
3. Use a DSLR camera mounted on a tripod to take photos of the specimens. Ensure that the DSLR camera is in manual mode, with the same values for settings such as color correction, ISO, and shutter speed. The setup is shown in Fig. 3.15.

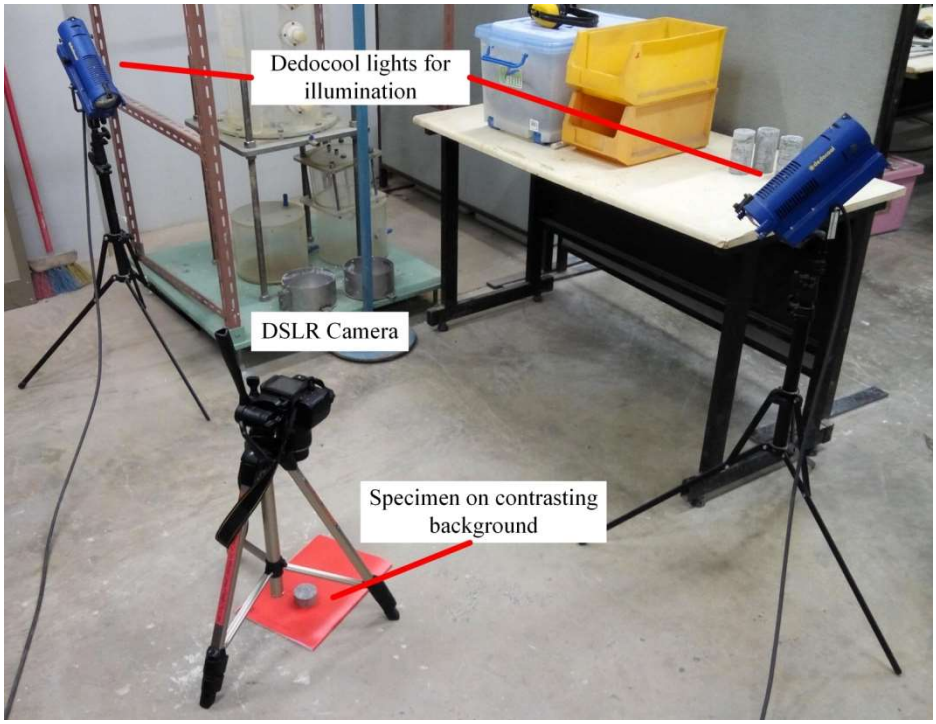

Fig. 3.15 Setup used to take photos for the colorimetry process

After the "before" and "after" images of the specimens were obtained, the images were fed into the MATLAB script for the colorimetry process. The actual colorimetry process itself uses the MATLAB script to segmentate the image based on two points that are manually selected by the user as a reference for the background and the specimen. The image of the specimen was then converted into the CIE L*a*b* color scheme. Details regarding the CIE L*a*b* color scheme can be found in section 2.4.6.1. Following that, each pixel in the image of the specimen was analyzed to determine its L*, a* and b* values. Average L*, a* and b* values of the image were then calculated. To account for minute changes in the lighting conditions for each photo taking session, the color values of the specimens were calibrated using the background. As the background used is the same for all photos, the color of the background was analyzed for all photos to obtain a correction factor for all three color values separately. The respective correction factor was then applied to adjust the color values for the specimens after heating. This would attenuate the effects of lumen depreciation. An example of the segmentation process is shown in Fig. 3.16.

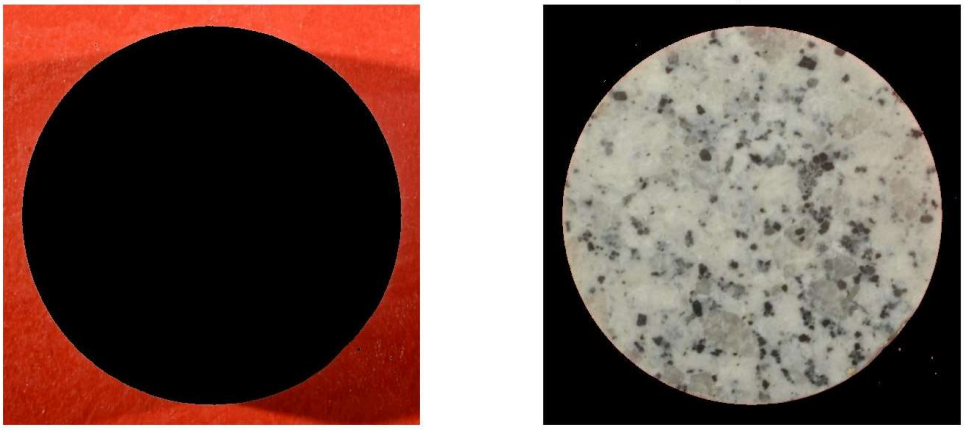

Fig. 3.16 Segmentation of background (left) and specimen (right) after image processing, specimen has a diameter of 50 mm

Some specimens were coated with high temperature grease on one side. These specimens were coated with the high temperature grease after the heating was completed. Coating the specimen with the high temperature grease before heating would have caused the high temperature grease to act as a thermal insulator and cause uneven heating. After the heating process was completed, the high temperature grease was applied to the specimen before the specimen cooled down. The heated specimen will cause the synthetic grease base in the high temperature grease to be partially burnt, mimicking the conditions in an actual underground rock structure fire. The high temperature grease was first applied onto one of two metal bars and pressed against the heated specimen. The changes in L*, a* and b* values for all tests were then plotted against each other and in a 3D plot to find any correlation with each other.

3.9 Dynamic compressive tests

All dynamic compressive tests were performed with the Split Hopkinson Pressure Bar (SHPB) setup in the Construction Technology Laboratory of the Nanyang Technological University. The SHPB setup has a striker bar driven by a gas gun that is powered by nitrogen gas cylinders. As it is hard to precisely control the speed at which the striker bar is launched, the amount of pressure that the gas gun is charged with is used to control the amount of force applied to the specimen. The SHPB gas

gun was charged with three different levels of pressures so as to vary the velocity of the striker bar, and thus varying the strain rate on the specimen.

Even though the gas pressure used to charge the gas gun can be controlled, to accurately analyze the data from the dynamic compressive test, the exact speed of the striker bar needs to be known. This data is obtained from two sets of photogates stationed at the mouth of the gas gun and just in front of the input bar. As the distance between the photogates are known, the speed of the striker bar can simply be found by dividing the distance with the time obtained from a timer triggered by the photogates.

A copper pulse shaper of diameter 22 mm and thickness 2 mm was placed between the striker bar and the input bar to shape the incident stress wave and prevent Pochhammer-Chree oscillations (Frew et al. 2002). The copper pulse shaper also leads to a longer rise time and allows more time for the specimen to reach stress equilibrium (Frantz et al. 1984). This method was chosen over using a shaped striker bar as copper pulse shapers are easier to machine and shaped striker bars may not reliably trigger the photogates and may lead to inaccurate velocities being recorded.

As the tests were designed to investigate the effects of heating on the dynamic properties of rocks, the SHPB setup was outfitted with a custom made oven (Fig. 3.17)

Fig. 3.17 Custom made SHPB oven

The oven, which is rated for 800 °C, is designed to fit over the input and output bars during the test, so as to contain any fragments that may be generated from the impact. It also allows for minimal handling of the specimen after heating, which would help in maintaining the specimen at a temperature as close to the target temperature as possible.

During the heating process, the opening of the oven was covered with asbestos plugs to ensure an even heating rate, as heated air will be unable to escape from the oven. The specimen was also placed on a concave asbestos holder, meant to insulate the specimen from the metal grate protecting the heating element. The concave shape of the holder also helps to reduce the surface area in contact with the specimen and ensure maximum exposure of the specimen to the heated air.

After the heating process is complete, the end surfaces of the input and output bars in contact with the marble specimen were coated with high temperature grease. The grease, rated for temperatures between -20 °C and 800 °C, was to ensure good transmission of the stress wave between the SHPB bars and the specimen. The input and output bars were only brought into contact with the heated specimen just before the striker bar was launched. This, together with the high temperature grease as an insulator, reduces any heating of the input and output bars which may lead to inaccurate calculations due to a change in the elastic wave velocity of the bars.

After the striker bar was launched, the elastic stress waves within the input and output bars were obtained via strain gauges attached to the center of the respective bars. The recorded stress waves were then separated into the incident wave, transmitted wave and reflected wave. The respective waves then underwent smoothing via the adjacent averaging method.

3.9.1. 3 wave analysis

The gathered data was analyzed using the 3 wave analysis method. The strain rate of the specimen was calculated from the part of the curve between the first 10% and the last 10% of the curve before the peak stress. This has been found to correspond to the elastic stage of the loading as stated by Wang et al. (2015). This method is preferred as it provides a more accurate analysis for brittle material of a large diameter, such as

the specimens used in this study (Lok et al., 2001). Furthermore, it was found that, when compared to the 1 wave analysis method, the 3 wave analysis method is able to produce the stress strain curve after peak stress. This allows for the determination of specific energy absorbed for specimens that remained intact after the dynamic compression test. It also allows for the differentiation between class I and class II failure modes (Wawersik and Fairhurst, 1970) for each specimen. The equations used in this study are equations 2.2, 2.3 and 2.4 (section 2.4.3).

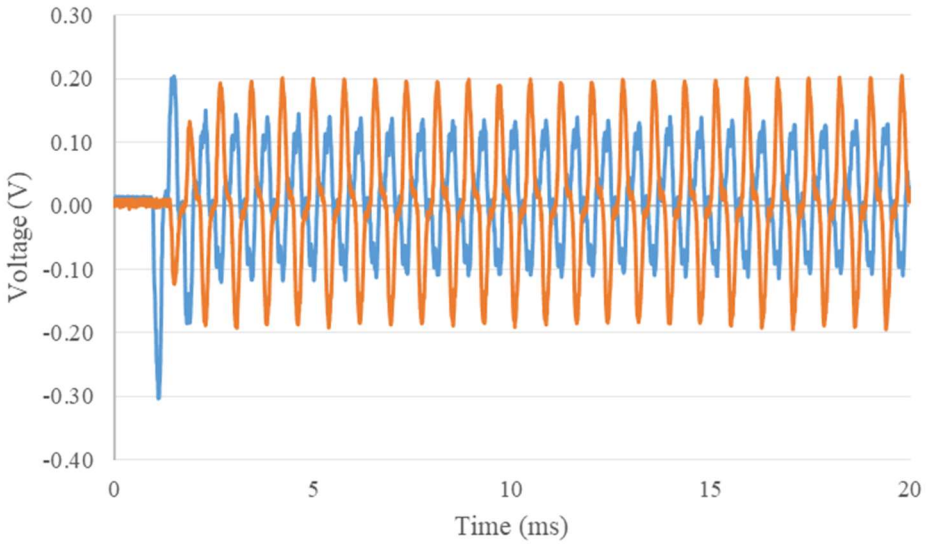

Fig. 3.18 Example of raw data collected

Before the 3 wave analysis was conducted, the raw data (Fig. 3.18) was first treated to separate the incident, transmitted and reflected wave. The waves then underwent smoothing using the adjacent averaging method.

3.9.2. Sieve analysis

After the dynamic compression test, if the specimen exhibited axial splitting or comminution, the specimen fragments were collected for further analysis. The oven was left to cool down for one day before the fragments of the specimen were collected and stored in individually marked Ziploc bags (Fig. 3.19).

Fig. 3.19 Collected residual marble fragment after dynamic compression test.

The fragmented remains were then subjected to sieve analysis in the Geotechnics Laboratory to obtain the particle size distribution in general accordance with American Society for Testing and Materials (ASTM) D2487 (2011) with some modifications as per ASTM D6913 (2009) due to the friable nature of the heat treated marble fragments. The collected fragments were sieved and separated with a mechanical shaker (Fig. 3.20) for a duration of 2.5 minutes. The masses retained on each individual sieve were recorded to the nearest 0.1 g. Particle size distribution curves were then plotted with respect to the testing pressures and heating temperatures used. Intact specimens and specimens that underwent axial splitting did not undergo the sieve analysis. The criteria for axial splitting is that the specimen did not split into more than 3 pieces.

Fig. 3.20 Mechanical dry sieving shaker

3.10 Microscopic observation

The epoxy specimens mentioned in section 3.2.3 were used in the microscopic observation part of this study. A Nikon H550L microscope with a PLAN Fluor 4x magnification lens was used. Digital photos of the pieces were taken using the NIS Elements Basic Research program and stitched together to form a macro-image. Their length, as well as the accompanying orientation was recorded by the program using data from the points specified. Cracks that deviate less than 10 degrees over its entire length was counted as the same crack, while cracks that deviate more than 10 degrees over its length were broken down into sections as individual cracks, as it is more likely that it was formed as a result of the coalescence of two or more micro-cracks.

The gathered data was pre-processed with data binning for easier handling. The orientation of the individual microcracks were binned in intervals of 5°. The length of the individual microcracks were similarly binned in intervals of 5 μm. All microcracks that fall within each 5° sector are then summed. The cumulative microcrack length data are also calculated using the pre-processed crack length.

The specimens tested was cut into different sections as shown in Fig. 3.7. This allows us to examine the effects of thermal treatment, mechanical loading, as well as the

effects of both with respect to distance from the point of loading of the specimen. Table 3.1 shows the treatment regime that the specimens were subjected to.

Table 3.1. Treatment regime that the specimens were subjected to

	Group 1	Group 2
	Loaded	Unloaded
Unheated	U025	L025
Heated at 200 °C	U200	L200
Heated at 350 °C	U350	L350
Heated at 500 °C	U500	L500

3.11 P-wave velocity

P-wave velocity measurements were taken for specimens undergoing colorimetry tests. The purpose of these measurements were to show that even though color change in specimens undergoing heating may be due to chemical reactions, it could also be due to increased light scattering caused by increased microcracking within the specimen. As P-wave velocity has been shown to be correlated to the degree of microcracking (section 2.4.5), it is a useful and easy to obtain measurement of the degree of microcracking present in a specimen.

The specimens were tested with a PUNDIT lab plus tester (Fig. 3.21) with transducers operating at 54 kHz. The tester was first calibrated with a plastic rod of a known P-wave velocity before use.

Fig. 3.21 PUNDIT lab plus ultrasonic tester

The 50 mm diameter Brazilian tensile test specimens had their P-wave velocity measurements taken before and after heating. Before the measurement, the specimens to be measured were kept in an oven maintained at 40 °C so as to have a consistent moisture content, which would affect the P-wave velocity measurements. During the measurements, saline gel was spread on the transducers before the transducers were pressed against the specimen to ensure good contact. The specimens were wiped with a piece of wet cloth after the measurements were taken to remove the saline gel, and returned to the oven afterwards. Consecutive readings of the specimen were taken at least one day apart as wiping off the ultrasonic gel with a piece of moist cloth may affect the moisture content of the rock specimen which in turn may affect the P-wave velocity measurement.

Multiple readings were taken of each specimen and were found to be consistent. This proves that random error is not present. As we are only interested in the relative changes in the P-wave velocity of each specimen and not the absolute P-wave velocity value of the specimens, any systematic error present is irrelevant as it will be cancelled out when the ‘after’ value is subtracted from the ‘before’ value.

Chapter 4 Color change of Bukit Timah Granite with respect to heating temperature

4.1 Introduction

It has been known for a long time that exposure to high temperatures causes a decrease in the integrity of rocks. This is especially crucial in underground structures, where rock failure can cause cave-ins. Unsafe sections of an underground opening exposed to high temperatures can be determined if the rock exhibits visible damage, such as spalling. However, rocks that are exposed to intermediate temperatures of between 200 ˚C to 500 ˚C, may not exhibit visible signs of damage even though they have been weakened.

Even though visible signs of damage may not be present, it can be clearly seen from the color of the rocks that there are changes (Oestmo, 2013). Furthermore, the same phenomenon was observed in other brittle materials such as concrete (Colombo and Felicetti, 2007; Annarel and Taerwe, 2009, 2011). The use of colorimetry can potentially be a cost effective and efficient way of characterizing damage done to rocks in the form of thermal loading.

Most researchers focused on the mechanisms behind damage done to rocks by thermal loading, and work regarding the quantification of thermal damage to rocks are lacking. Research into quantifying damage done to rock will gain in importance in the future, as stiff competition for usage of limited land will lead to increased usage of underground spaces. Even though most underground spaces will be lined with shotcrete, in the event of a fire, shotcrete will exhibit spalling. Also, rock bolts meant to reinforce the rock mass can also conduct heat and create localized hotspots (Larsson, 2006).

This chapter focuses on the possible failure of rocks via tension after a fire. A cost effective and efficient way of performing colorimetry to estimate the temperatures that the rocks have been exposed to is also shown in this chapter. This will be useful in estimating the remaining strength in rocks after a fire has been put out.

4.2 Color changes of specimen

This part of the thesis deals with the color changes of the specimen. Section 4.1 has shown that color changes do occur in some rocks after heating. However, a quantitative measurement of the color and color change of rocks is desired, as it will allow us to correlate the degree of color change to the heating temperature.

The changes in the color values of the individual specimens were adjusted with the correction factor (section 3.5) and the average values were plotted out. The error bars represent 1 standard deviation. The photographs were taken in accordance to the method outlined in section 3.8.

4.2.1 Color changes of specimen with respect to cooling rate

Fig. 4.1 shows the color changes of the specimens plotted against the different cooling rates used. The rocks were cooled at a high rate, by increasing the convective heat loss with a fan; at a normal rate, by resting the specimens on a piece of aerogel, without a fan; and at a low rate, by leaving the specimen in a powered down furnace after the heating phase, with residual heat radiating from the heating elements. Details can be found in section 3.7.1.

The purpose is to reveal if the different cooling rates used will have any effects on the color changes of the rocks. By also determining how the cooling rate used will affect the tensile strength of the rocks, we can assess the reliability of using color changes of the rocks as a means of estimating the strength of rocks after a fire.

Through naked eye observation, there indeed seems to be a noticeable change in the color of specimens heated only at 350˚C and above. The MATLAB program, however, detected a change in the color of all specimens, even those heated at 200 ˚C.

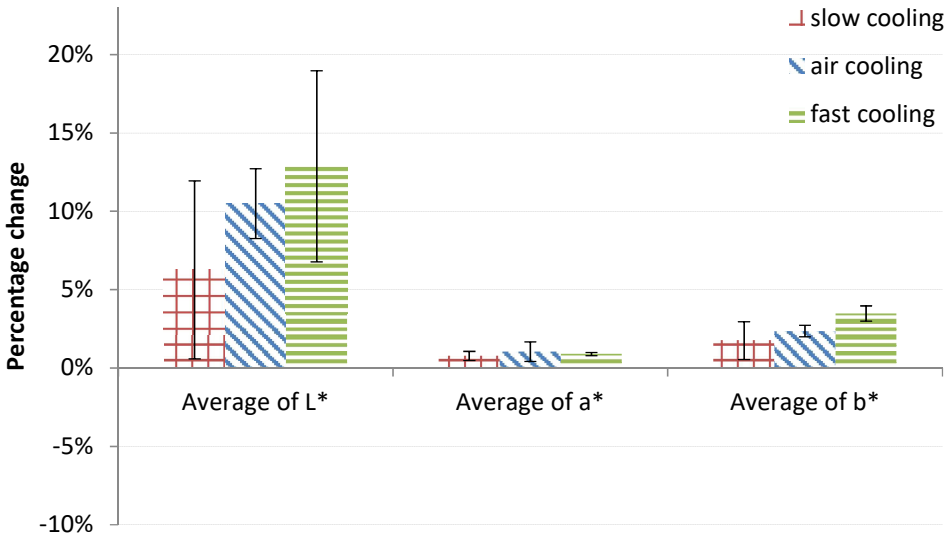
slow cooling
air cooling
fast cooling
20%
15%
10%
5%
0%
-5%
-10%
Percentage change
Average of L*
Average of a*
Average of b*

(a)

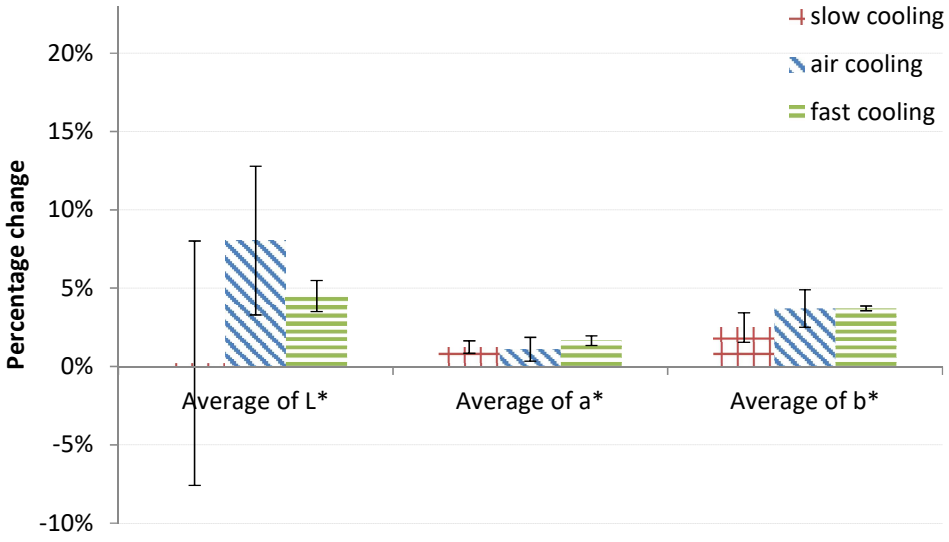
slow cooling
air cooling
fast cooling
20%
15%
10%
5%
0%
-5%
-10%
Percentage change
Average of L*
Average of a*
Average of b*

(b)

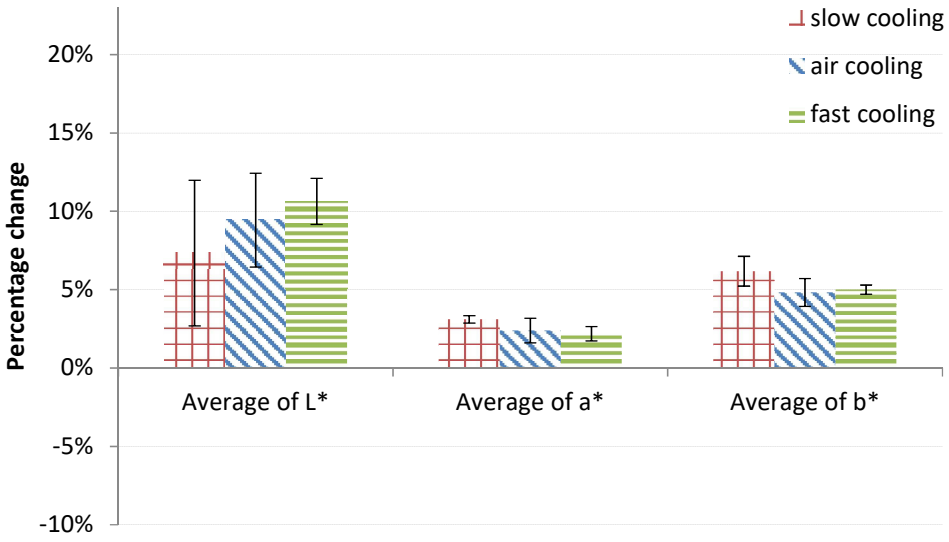

(c)

Fig. 4.1 Color changes against cooling rate for specimens heated up to (a) 200 ˚C, (b) 350 ˚C and (c) 500 ˚C, error bars indicate 1 standard deviation, 3 specimens tested per cooling rate at each temperature

The rate of cooling that the specimens undergo seems to have no significant effect on the color changes of the specimen. For example, in Fig. 4.1 (a) and (b), we can see that both the a* and b* values show an increasing trend with respect to rate of cooling, but this does not hold true for Fig. 4.1(c). Similarly, for Fig. 4.1 (a) and (c) we can see that there is an increasing trend for the L* value, which correlates with a higher cooling rate, but this does not hold true for Fig. 4.1 (b). The color changes seem to fluctuate about an average level based on the temperature that they have been heated to. It can be seen that for all cases, the changes in the L* value is the most prominent, followed by a moderate change in the b* value, and lastly, the a* value.

4.2.2 Color changes of specimen versus heating temperature

The other variable being explored in this chapter is the heating temperature of the specimens. The figure below shows the color changes of the specimens with respect to the heating temperature, with the cooling rate that the specimens were exposed to being held constant.

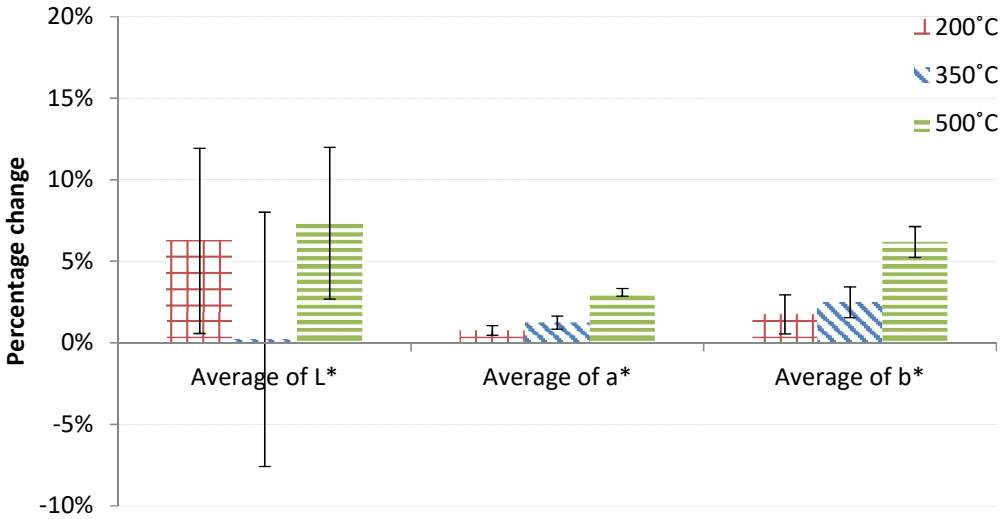
20%
15%
10%
5%
0%
-5%
-10%
Percentage change
200˚C
350˚C
500˚C
Average of L*
Average of a*
Average of b*

(a)

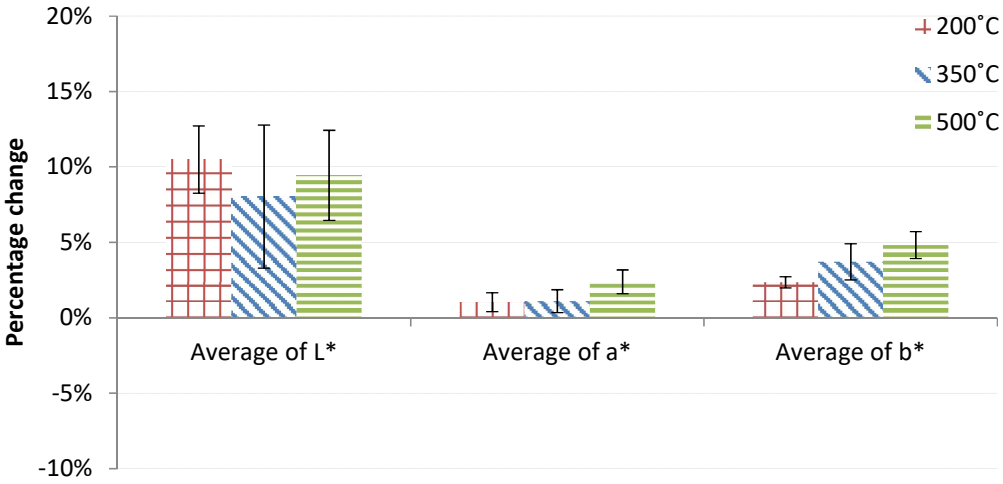
20%
15%
10%
5%
0%
-5%
-10%
Percentage change
200˚C
350˚C
500˚C
Average of L*
Average of a*
Average of b*

(b)

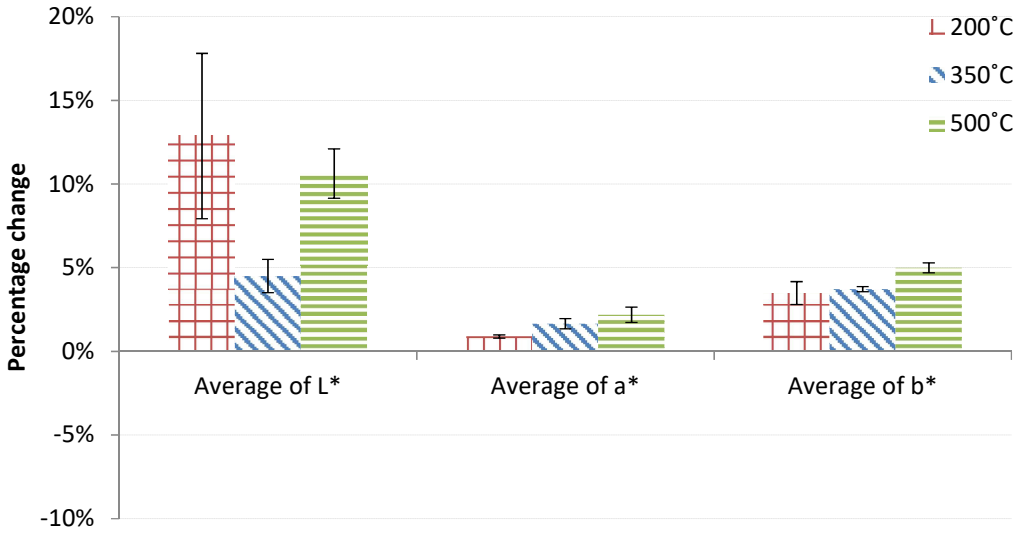

(c)

Fig. 4.2 Color changes against heating temperature, for specimens exposed to (a) slow cooling, (b) air cooling and (c) fast cooling, error bars indicate 1 standard deviation, 3 specimens tested per cooling rate at each temperature

We can see that in Fig. 4.2, for all cooling rates, there is a trend of increasing color changes with respect to the temperature that the specimens are heated to. Moreover, the cooling rate of the specimens seemed not to significantly affect the degree of the color change. It also seems that the a* value changes more gradually and linearly when compared to the b* value of the specimens.

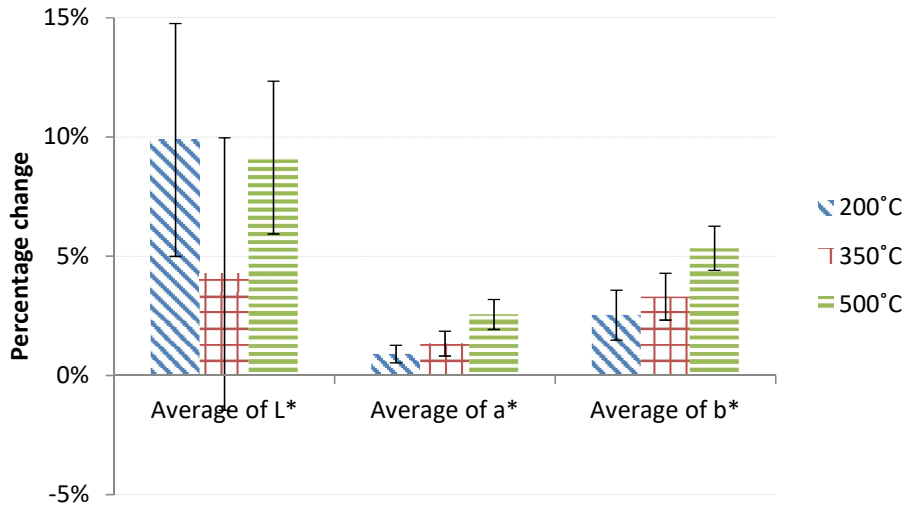

(a)

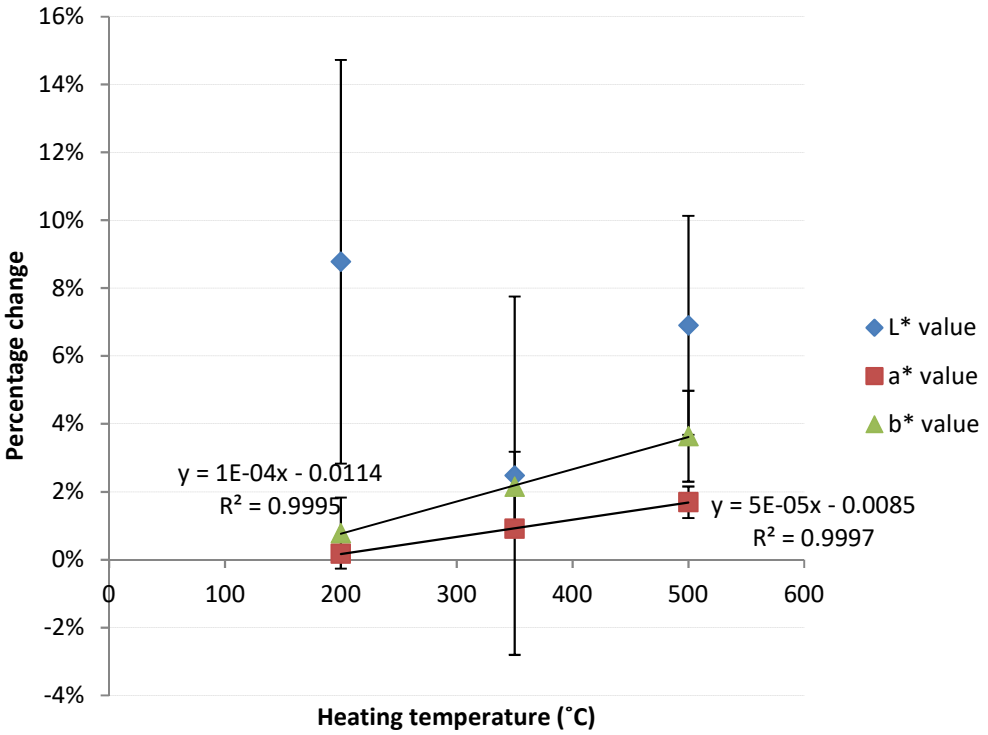

(b)

Fig. 4.3 Color changes vs heating temperature plotted as (a) a bar chart and (b) scatter plot with best fit equation for a* and b* values, error bars indicate 1 standard deviation

Since the positive correlation between the a* value, b* value and heating temperature is similarly observed for all the cooling rates, and the cooling rate of the specimen seems to have no significant effect on the specimens, we can group and analyze the data of color changes of the specimen according to the temperature that they are heated to regardless of the cooling rate (Fig. 4.3). The trend of increasing color change can be seen more clearly in this way. With a larger sample size of 9 in each group as compared to 3 in each group when the specimens were still divided according to cooling rate, data scattering can be reduced.

From Fig. 4.3, it seems that the L* value change with temperature still has no definite trend, while the a* value and b* value changes increase linearly with temperature. This could be due to the L* value being strongly sensitive to the lighting conditions, where a brighter light source would increase the L* value significantly. For the a*

value, the color change increases by 0.7% to 0.8% with every 150˚C increase in temperature, while for the b* value, there is a 1.3% to 1.5% increase with every 150˚C increase in temperature. While the a* value change is more consistent than the b* value change, its magnitude is lower as compared to the changes in the b*. This would mean that if we are interested in using the a* value to measure damage caused to the rocks, the equipment used must be more sensitive than if we were to measure the change in the b* value.

4.2.3 a* against b* value with respect to heating temperature

Although the a* and b* has been shown to have a correlation with the heating temperature of the specimens, the color change values are more meaningful when plotted against each other, as a linear relationship can be seen in the changes of the a* and b* values (Fig. 4.4c).

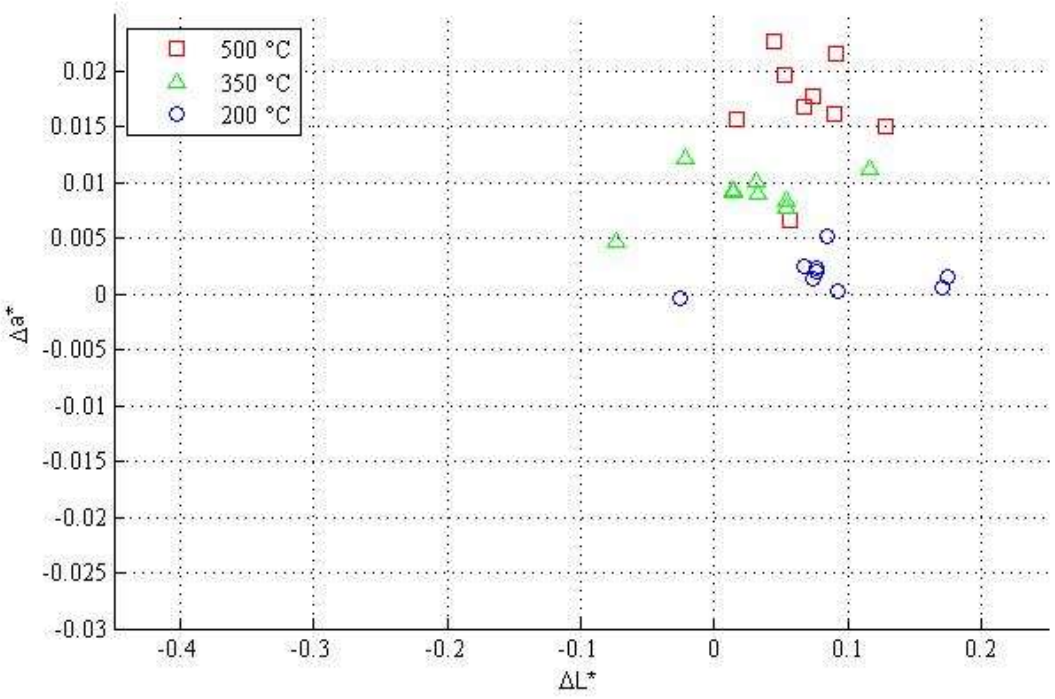

(a)

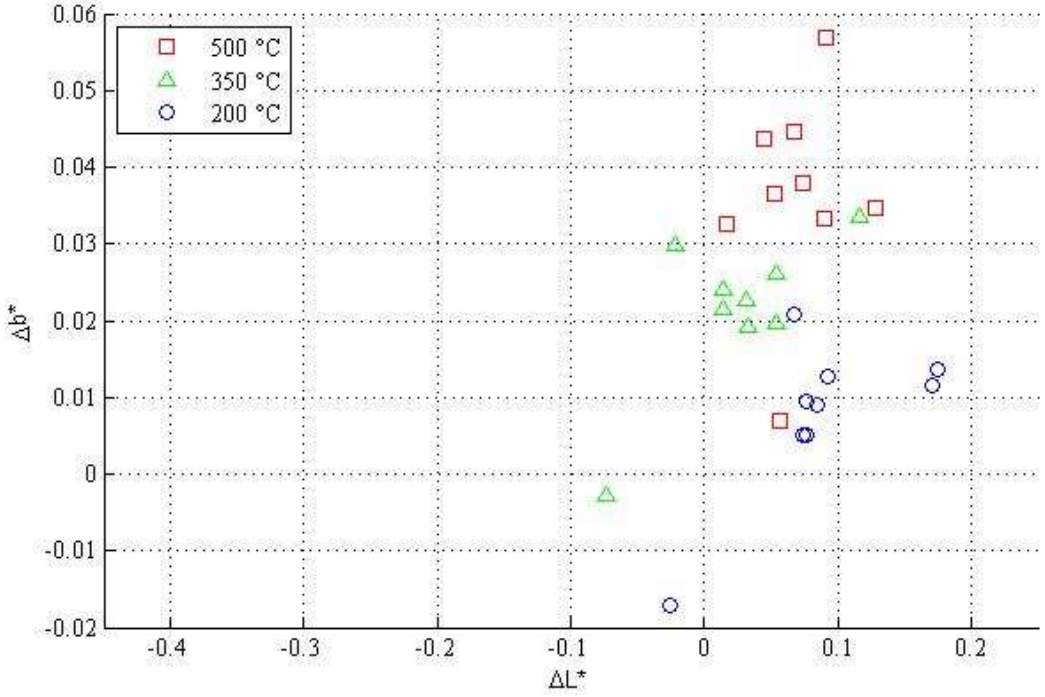
500 °C
350 °C
200 °C
Δb*
ΔL*
0.06
0.05
0.04
0.03
0.02
0.01
0
-0.01
-0.02
-0.4
-0.3
-0.2
-0.1
0
0.1
0.2

(b)

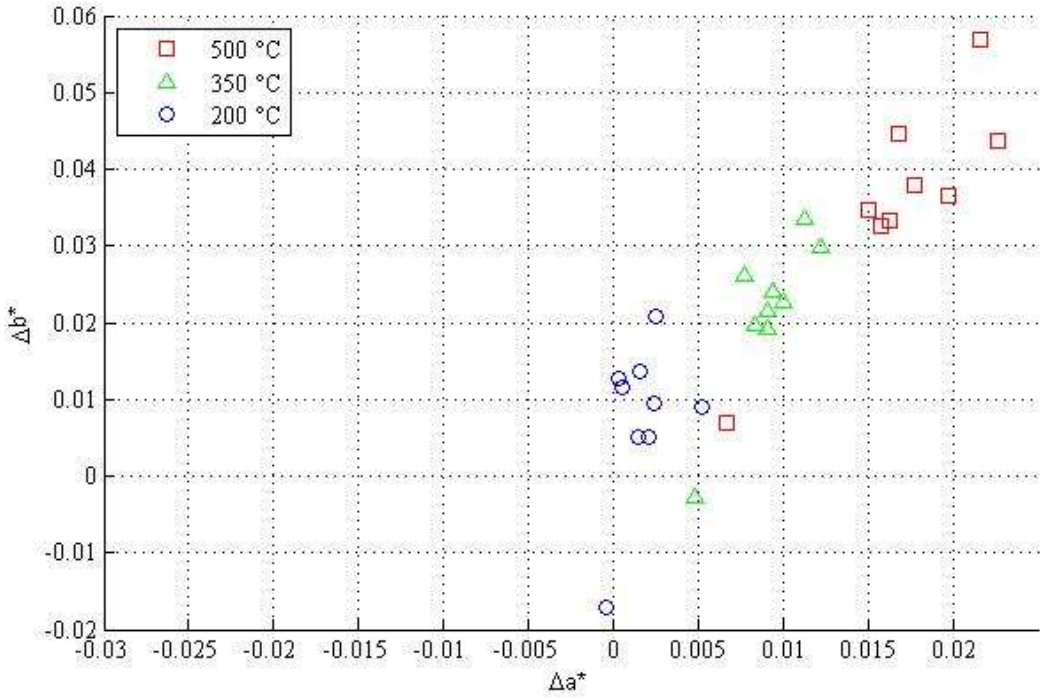
500 °C
350 °C
200 °C
Δb*
Δa*
0.06
0.05
0.04
0.03
0.02
0.01
0
-0.01
-0.02
-0.03
-0.025
-0.02
-0.015
-0.01
-0.005
0
0.005
0.01
0.015
0.02

(c)

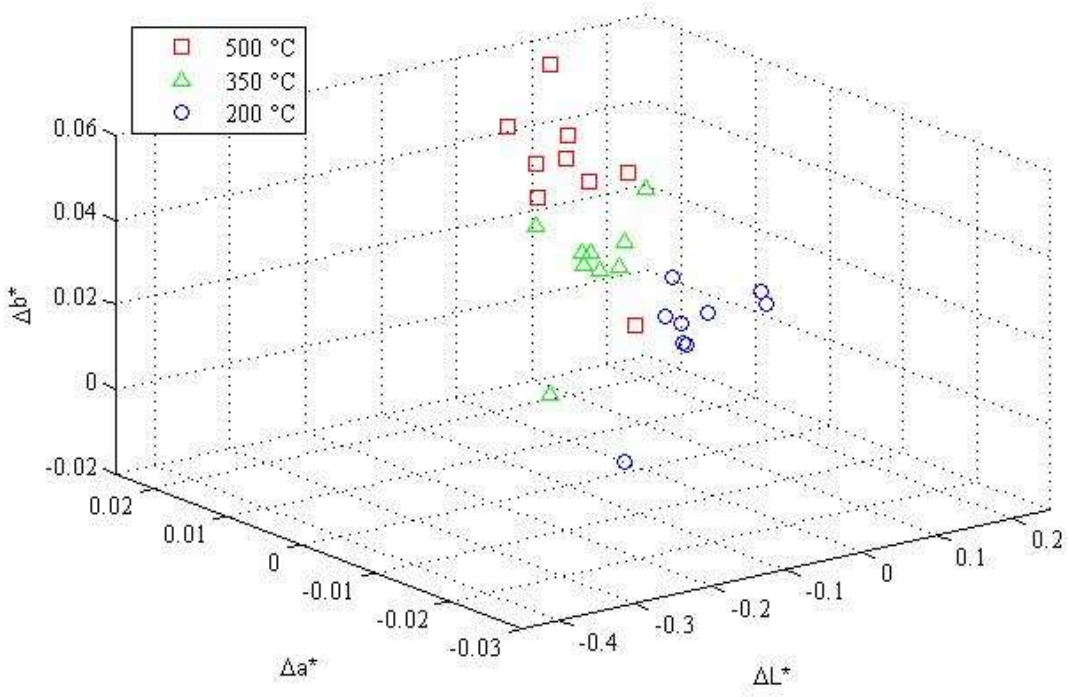

(d)

Fig. 4.4 Color changes (Δ) versus heating temperature of the uncoated granite specimens for (a) ΔL* against Δa*, (b) ΔL* against Δb*, (c) Δa* against Δb*, (d) 3D plot of ΔL*, Δa* and Δb*

With a clear linear relationship between the a* and b* value changes with respect to heating temperature, we can use this linear relationship to enhance the reliability of the colorimetry process. As the a* and b* value change ratio will stay within a certain range, we can conclude that analyzed photos that show a large deviation from this ratio needs to be retaken due to problems with the lighting conditions or photo taking process.

4.2.4 Tensile strength versus heating temperature

Fig. 4.5 shows the relationship between the Brazilian tensile strength of the rock specimens with respect to the heating temperature. As Fig. 4.5 shows, the Brazilian tensile strength of the rock specimens decreases with the heating temperature. In the Brazilian tensile test (section 3.6), the tensile strength of the rock specimen is calculated from the compressive force applied on the specimen. As the tensile stress

in the center of the specimen reaches the critical value, the specimen starts to fail as microcracks coalesce and propagate in an unstable manner.

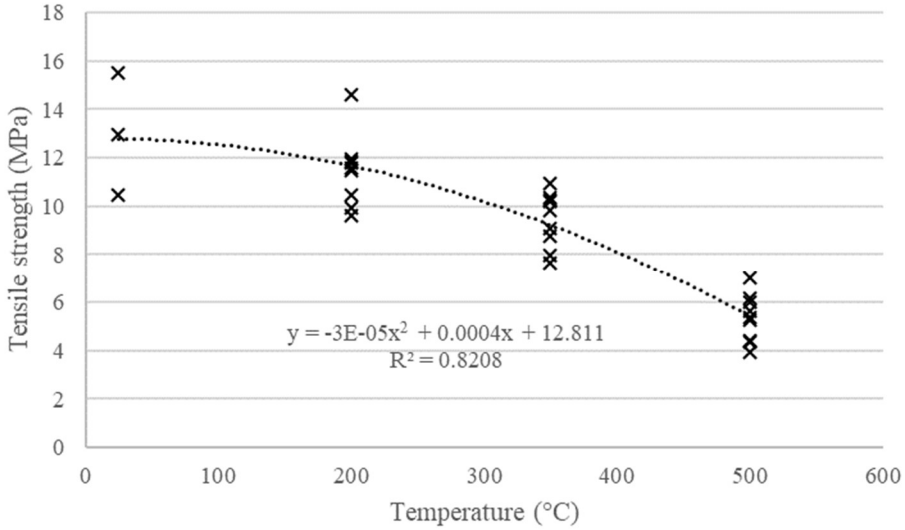

Fig. 4.5 Brazilian tensile strength of rock specimens versus heating temperature

The critical value in this case, is conceptually determined by the critical stress intensity, which is influenced by microcrack density within the area of interest (section 2.3). Hence, the more numerous microcracks generated by a higher heating temperature would at least partially account for the reduced strength seen in the heated specimens.

As the heating temperature increases, more microcracks would be formed, which will increase the microcrack density. The increase in microcrack density leads to more significant crack-crack interaction during loading and reduces the tensile strength. The probability of finding sufficiently long microcracks within the area experiencing tensile stress also increases, as microcracks can also link up to form a longer microcrack.

As seen in equation 2.1 (section 2.3), a longer microcrack means that the same stress intensity factor can be reached with a lower stress applied. This causes the failure of the rock specimen to happen at a lower tensile stress, demonstrated by Fig. 4.6, as the chances of longer microcracks, microcracks orientated more favorably appearing within the tensile stress zone (dashed line) increases. The increase in microcrack density also contributes to the strength degradation.

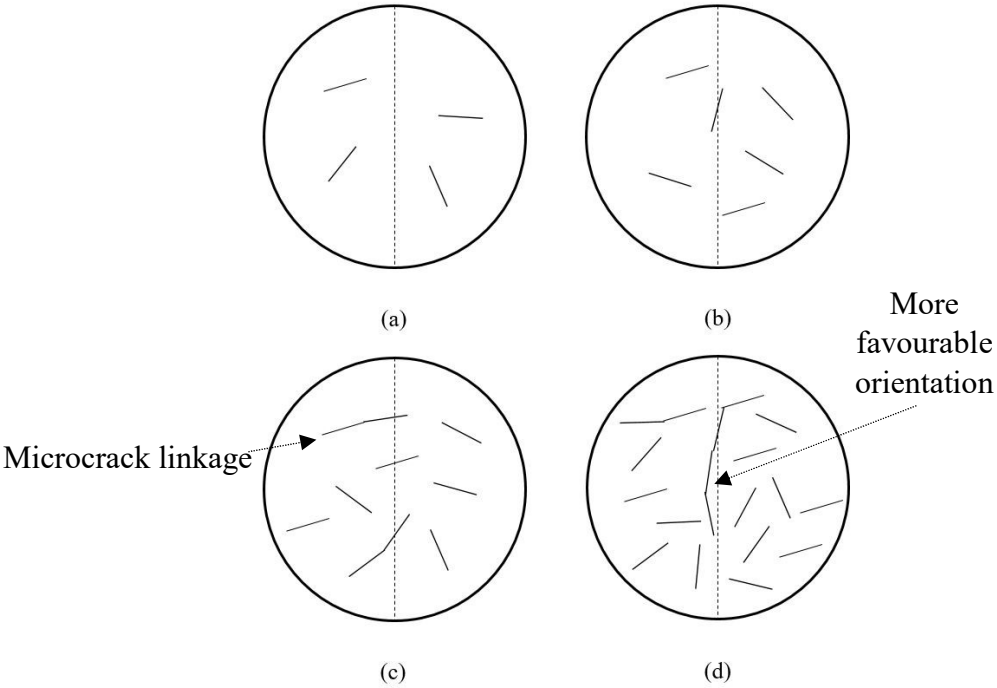

Fig. 4.6 Schematic illustration of possible positions and orientations of microcracks for (a) unheated rocks, (b) lightly heated rocks, (c) moderately heated rocks, and (d) heavily heated rocks

High speed camera footage of the Brazilian tensile tests taken at 20000 frames per second have also revealed a difference in the failure modes of the specimens that underwent different types of thermal treatment (Fig. 4.7). Specimens that were heated at 500 °C seem to develop ductile failure when compared to specimens that were heated at 200 °C, which failed in a more brittle manner accompanied by a loud cracking sound. It can be seen in Fig. 4.7 that for specimens that were heated at 500 °C, the amount of time needed for the central crack to fully develop in length is significantly longer than specimens that were unheated.

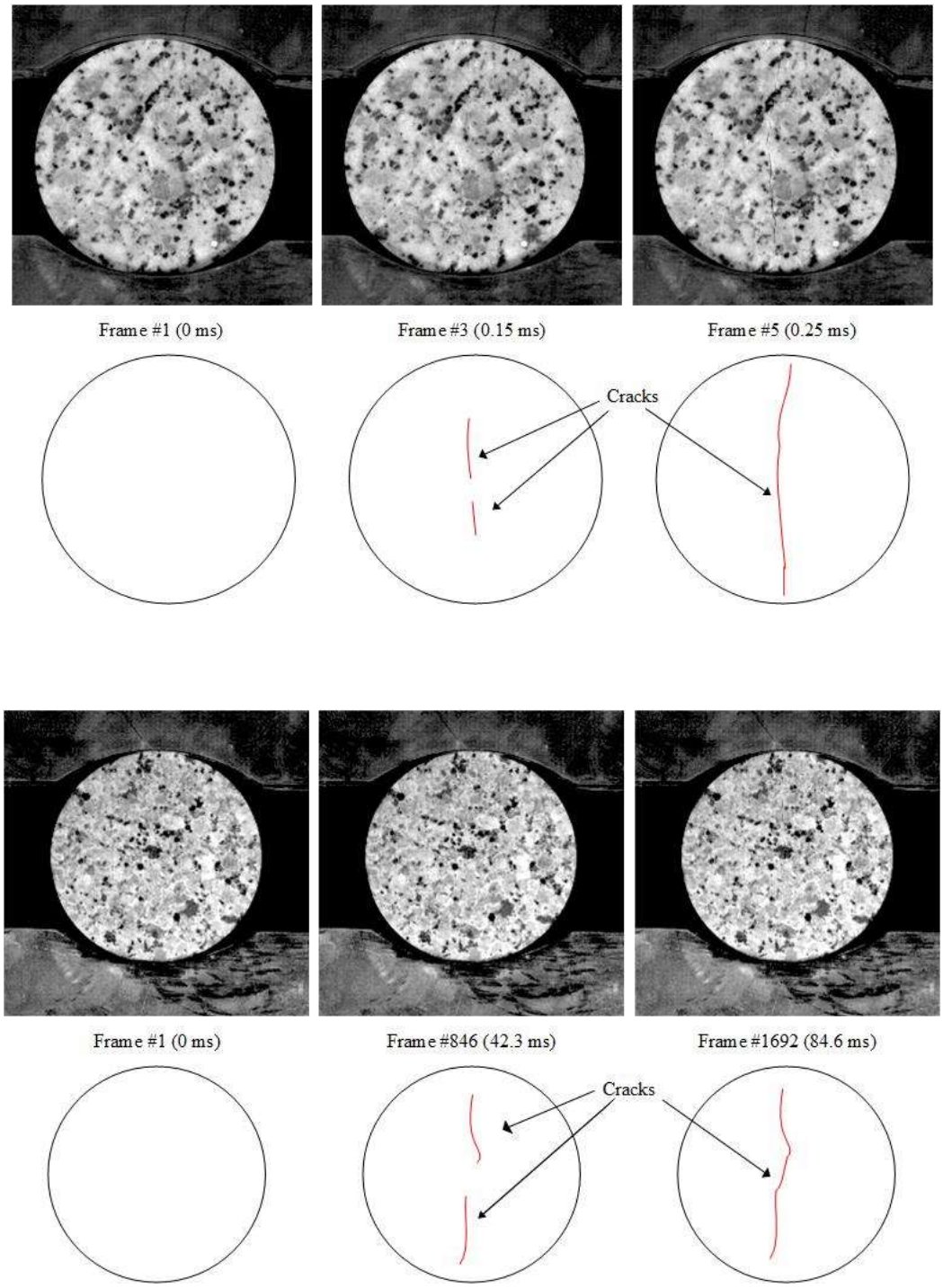

Fig. 4.7 High speed camera footage of Brazilian tensile test conducted for specimens heated at 500 °C (top) and 200 °C (bottom). Cracks highlighted for specimens heated at 500 °C and 200 °C in accompanying sketches. Labels indicate frame numbers of high speed camera footage and time after crack initiation, all specimens are of 50 mm diameter.

Brittleness has been used in different ways to characterize physical behavior of materials by various researchers in the past (Morley, 1944; Hetenyi, 1966; Obert and Duvall, 1967; Ramsay, 1967). Among them, Hucka and Das (1974) state the key features of materials possessing higher brittleness as below:

- Lower values of elongation
- Fracture failure
- Formation of fines
- Higher ratio of compressive to tensile strength
- Higher resilience
- Higher angle of internal friction
- Formation of cracks in indentation

In this chapter, at the end of the tests, the specimens heated at lower temperatures displayed a lower value of axial strain; failure modes that appear to be less ductile; as well as formation of fines and debris. It was also observed that the crack formed in specimens heated at a lower temperature is rougher and more jagged, as compared to specimens heated at a higher temperature. This may be similar to how perforated paper is torn, in which the tear will appear very straight. In contrast, unperforated paper will have a jagged tear upon tearing. In the case of the heated granite specimens, the microcracks generated by heating resemble the perforations.

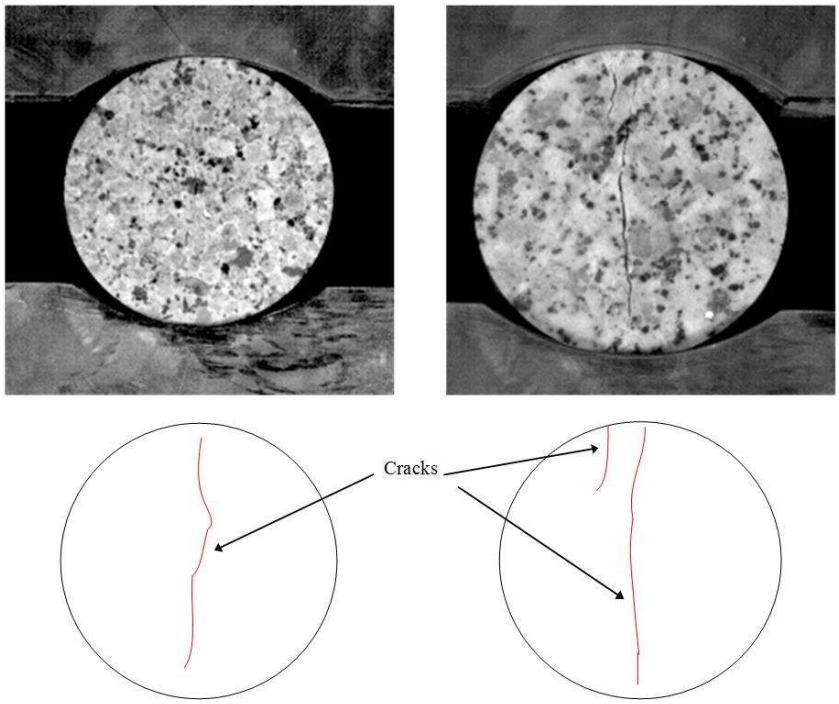

Fig. 4.8 Final frames from high speed camera footage of Brazilian tensile test conducted on specimen (50 mm diameter) heated at 500 °C (left), and 200 °C (right)

Fig. 4.8 shows snapshots taken at the end of the footage for both tests mentioned in Fig. 4.7. We can see that the 200 °C specimen has a larger crack width (wider aperture) as compared to the specimen heated at 500 °C. As the crack length of the specimen is constrained by the diameter of the specimen, the width of the crack developed in the specimen can provide insight into the amount of strain energy stored within the specimen during the test. It is likely that the 200 °C specimen possesses a greater amount of strain energy just before macro-crack initiation as compared to the 500 °C specimen. As the crack propagation time is longer for the 500 °C specimen as shown in Fig 4.7, it is likely that the strain energy within the 500 °C specimen has been significantly dispersed by the progressive coalescence of multiple closely-spaced microcracks separated by a short distance within the specimen (Fig. 4.6d). For the 200 °C specimen, since the microcracks are more distant from each other (Fig. 4.6a), it is likely that a greater amount of strain energy is stored within just before crack initiation. With a higher strain energy release rate, a larger crack width and the dispersion of strain energy in the form of a loud cracking sound seems likely.

4.2.5 P-wave velocity versus temperature

The reduction in the strength of the rock specimens may be due to many factors, including chemical changes in the minerals within the rock. However, heating induced microcracking will be a major contributing factor. Temperatures that may cause microcracking in granite can be as low as 60-70 °C (Yong and Wang, 1980). Temperatures beyond 573 °C would likely cause obvious disintegration of granite due to the α/β phase change of quartz. As such, the temperature range of interest in this chapter is between 200 °C to 500 °C

The P-wave measurement process (section 3.7) was performed before, and repeated after the heating process was completed. The ratio of the P-wave velocity after (V_a) and before (V_b) heating was plotted with respect to the heating temperature (Fig. 4.9).

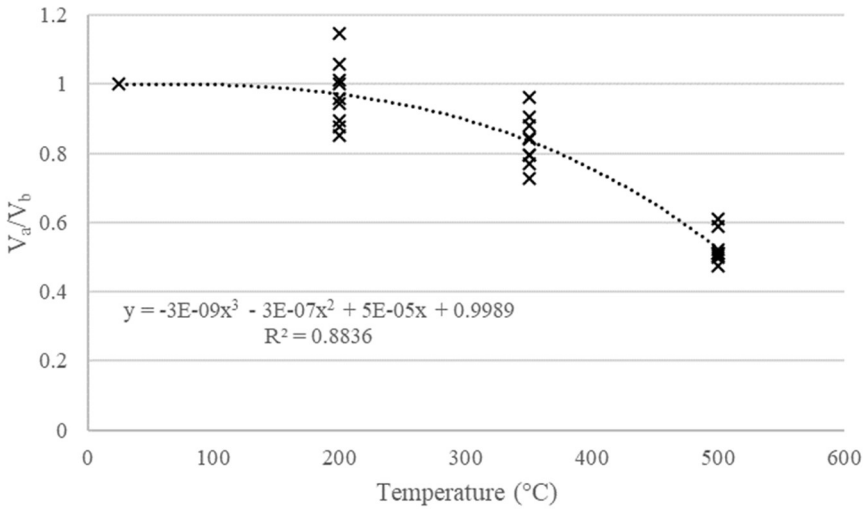

Fig. 4.9 Ratio of P-wave velocity after (V_a) and before (V_b) heating versus heating temperature

A negative correlation between the heating temperature and P-wave velocity of the rock specimens is obtained. The reduction of P-wave velocities of the rock specimens is a strong indication of the generation of microcracks within the specimens during the heating process, which in turn contributes to the reduction in the measured tensile strength.

The correlation of P-wave velocity of rocks with its physical properties such as tensile strength, porosity and elastic modulus has been investigated for different types of

rocks (Khandelwal, 2013; Kahraman and Yeken, 2008; Yagiz, 2011; Karakul and Urusay, 2013). The P-wave velocity is influenced by variables such as the density and porosity of the rock specimen (Blum, 1997) which also influences the strength of a rock specimen. Su et al. (2008) have found that not only is the P-wave velocity in brittle material correlated to the microcrack density, the average half crack length also contributes to the difference in the P-wave velocity changes.

4.2.6 Change in color values between the coated and uncoated side

A group of specimens had one flat side coated with high temperature grease after heating. This is to investigate the possible effects of soot and smoke on the reliability of the colorimetry process (section 3.5). Fig. 4.10 shows the coated sides of two specimens (top) versus the same sides of the specimens in their unheated state (bottom), while Fig. 4.11 shows the uncoated sides of two specimens (top) versus the same sides of the specimens in their unheated state (bottom).

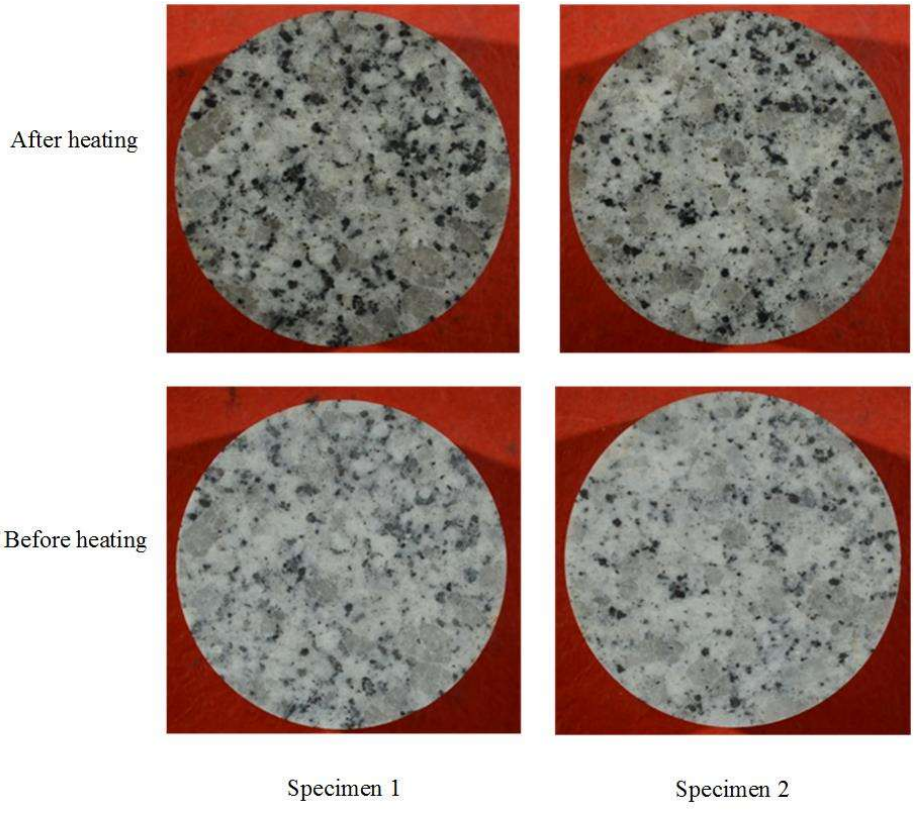

Fig. 4.10 Photos of specimens (50 mm diameter) heated at 200 ˚C coated with high temperature grease and cleaned off (top) and in the unheated state (bottom). Specimen 1 on the left, specimen 2 on the right.

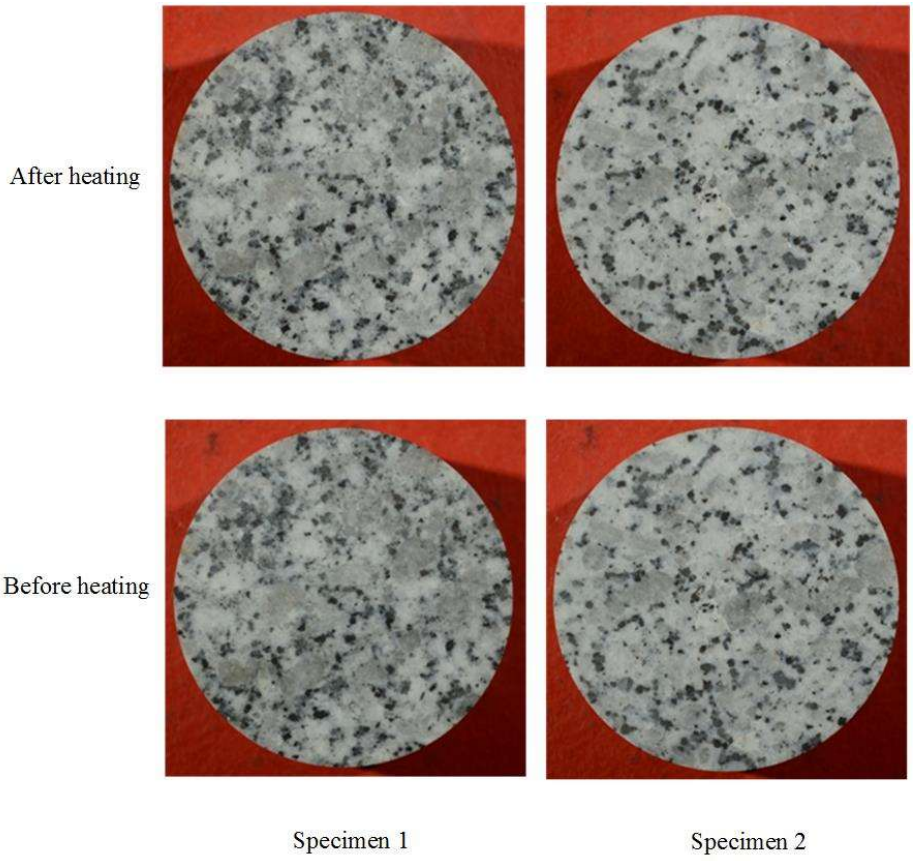

Fig. 4.11 Photos of the uncoated side of specimens (50 mm diameter) heated at 200 ˚C (top) and in the unheated state (bottom). Specimen 1 on the left, specimen 2 on the right.

Fig. 4.12 shows the changes in the L*, a* and b* color values for the uncoated side of the greased specimens, while Fig. 4.13 shows the results for the grease coated surfaces. As Fig. 4.13 shows, the specimens appeared to be more greenish and bluish as compared to the uncoated specimens, probably due to residue from the high temperature grease. However, we can see that there is still a trend of positive change for a* and b* color values with respect to heating temperature. Fig. 4.13c in particular shows the almost linear trend of changes of the a* against b* values with an increase in heating temperature that is also seen in Fig. 4c.

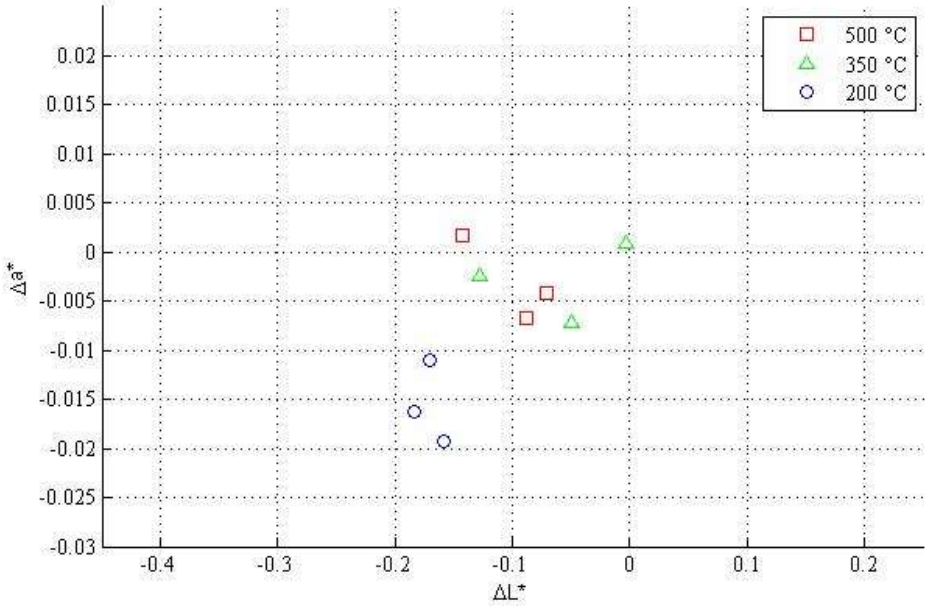
500 °C
350 °C
200 °C
Δa*
ΔL*
0.02
0.015
0.01
0.005
0
-0.005
-0.01
-0.015
-0.02
-0.025
-0.03
-0.4
-0.3
-0.2
-0.1
0
0.1
0.2

(a)

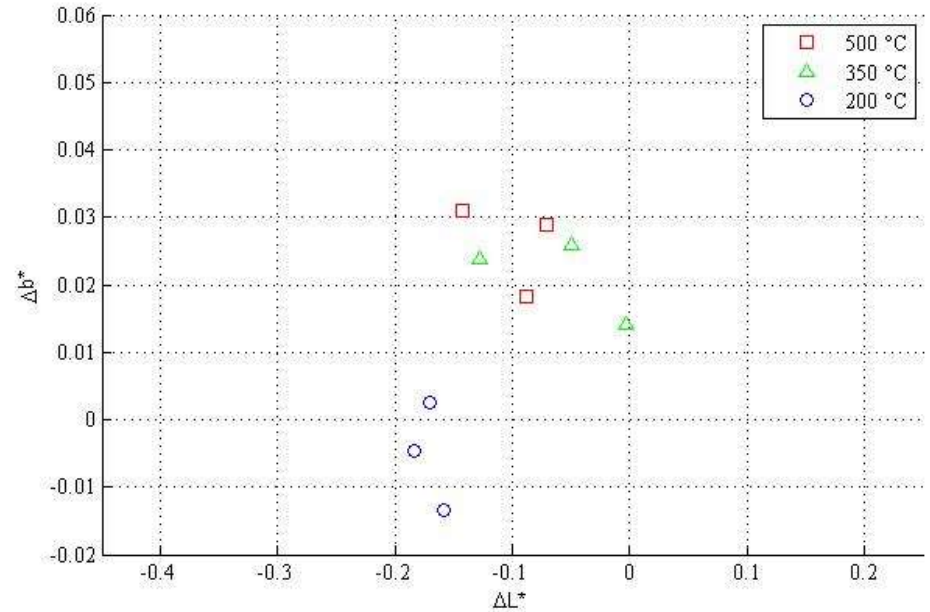
500 °C
350 °C
200 °C
Δb*
ΔL*
0.06
0.05
0.04
0.03
0.02
0.01
0
-0.01
-0.02
-0.4
-0.3
-0.2
-0.1
0
0.1
0.2

(b)

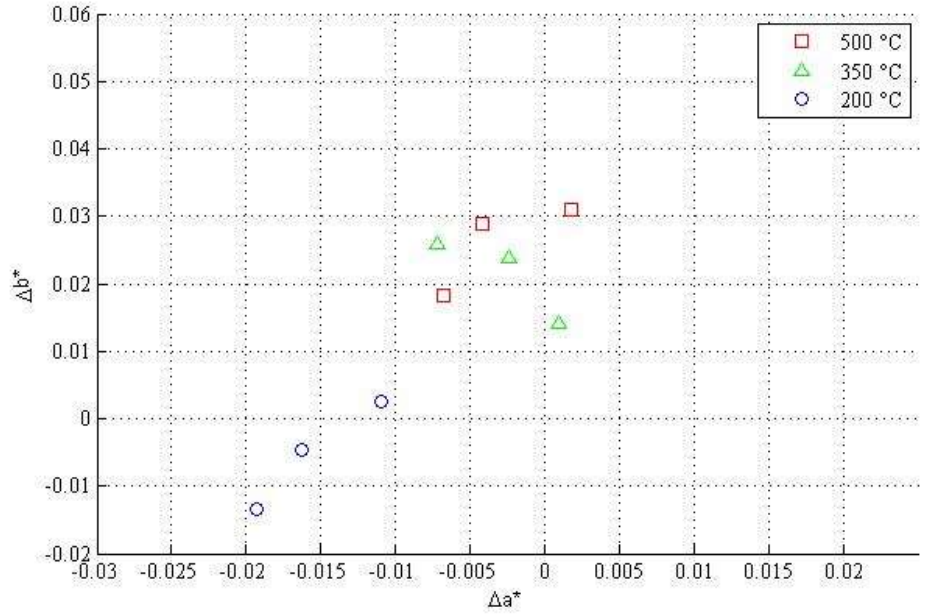

(c)

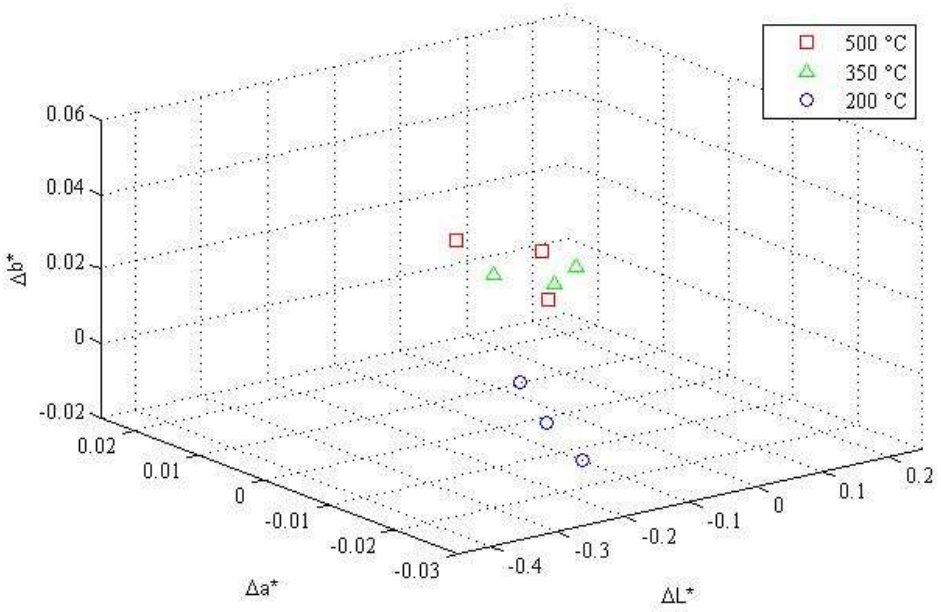

(d)

Fig. 4.12 Color changes (Δ) versus heating temperature of the granite specimens of the uncoated side for (a) ΔL* against Δa*, (b) ΔL* against Δb*, (c) Δa* against Δb*, (d) 3D plot of ΔL*, Δa* and Δb*

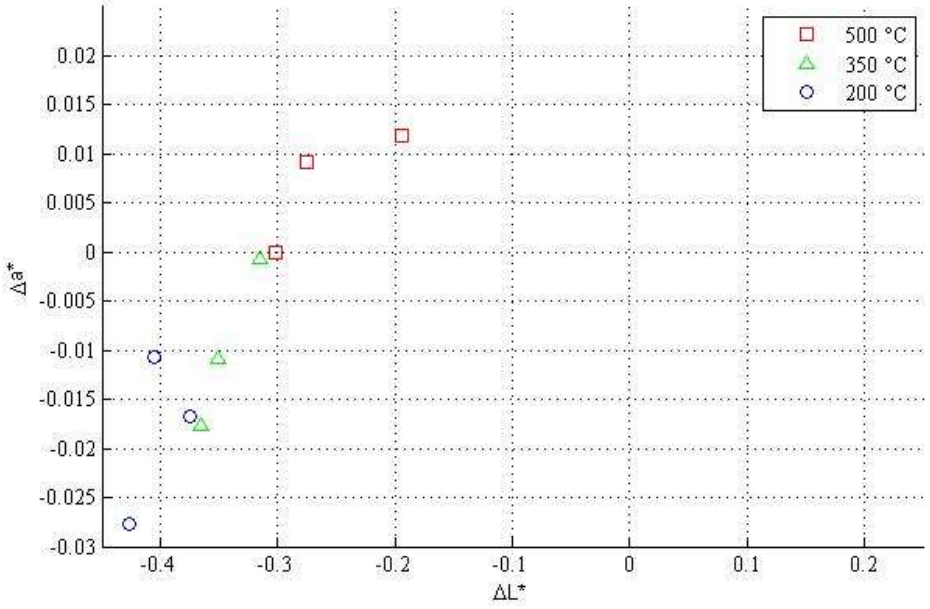
500 °C
350 °C
200 °C
Δa*
ΔL*
0.02
0.015
0.01
0.005
0
-0.005
-0.01
-0.015
-0.02
-0.025
-0.03
-0.4
-0.3
-0.2
-0.1
0
0.1
0.2

(a)

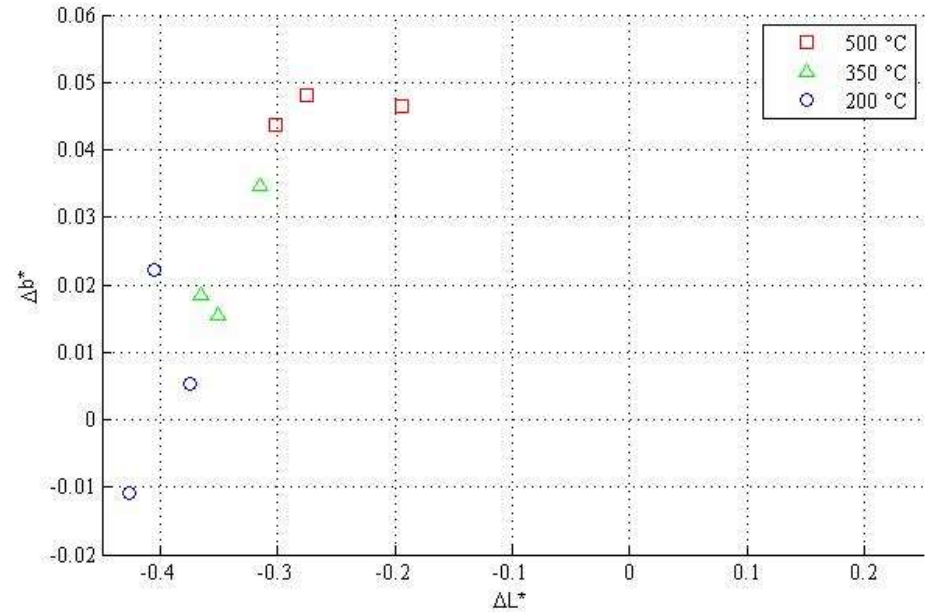
500 °C
350 °C
200 °C
Δb*
ΔL*
0.06
0.05
0.04
0.03
0.02
0.01
0
-0.01
-0.02
-0.4
-0.3
-0.2
-0.1
0
0.1
0.2

(b)

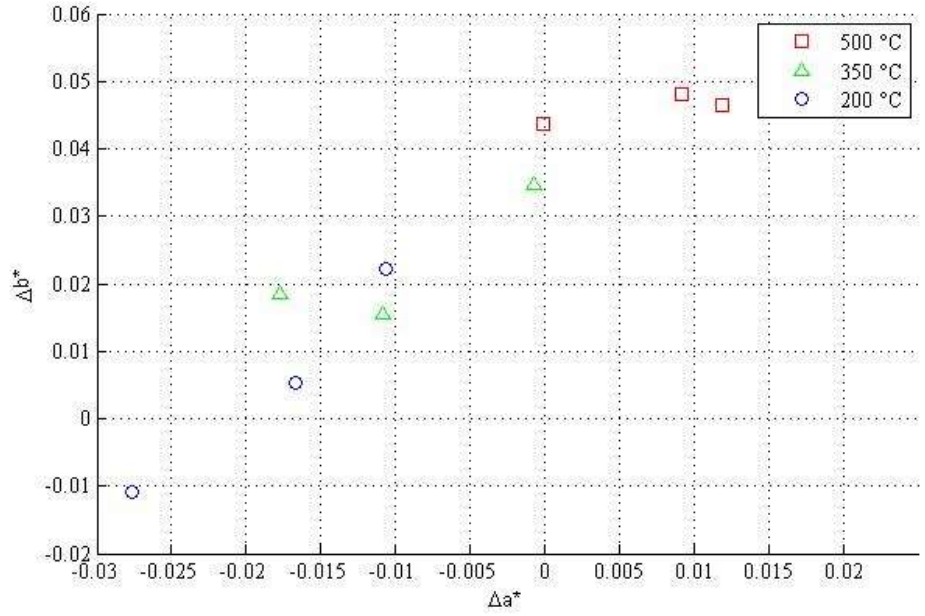

(c)

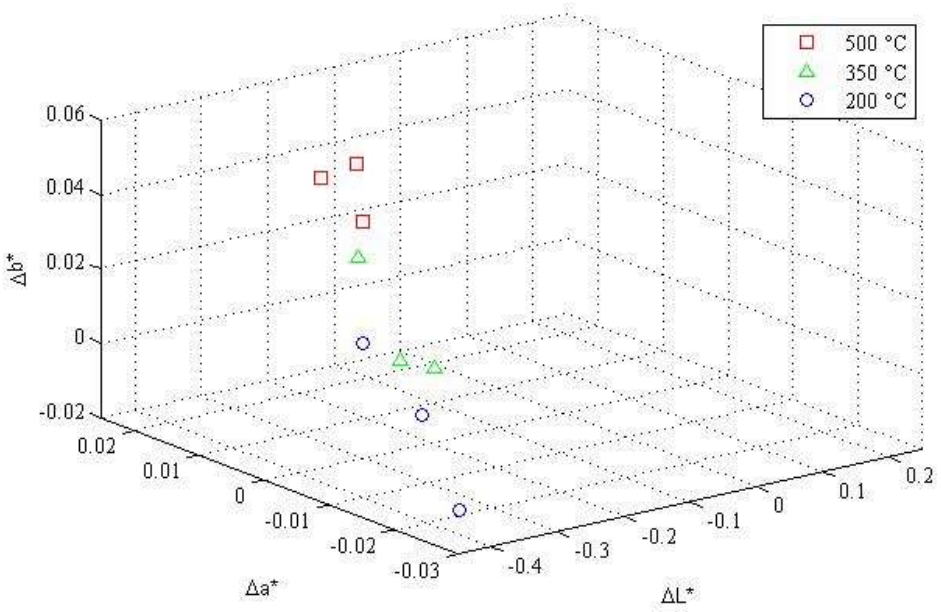

(d)

Fig. 4.13 Color changes (Δ) versus heating temperature of the granite specimens after cleaning off high temperature grease for (a) ΔL* against Δa*, (b) ΔL* against Δb*, (c) Δa* against Δb*, (d) 3D plot of ΔL*, Δa* and Δb*

The results for both the coated and uncoated sides are also summarized in Table 5. For specimens coated with high temperature grease, the percentage change of the a* value between the specimens heated at 200 °C was -1.83% while the percentage change for specimens heated at 500 °C was 0.70%. The percentage change of the b* value between the specimens heated at 200 °C was 0.56% while the percentage change for specimens heated at 500 °C was 4.61%. Similarly, for the sides that were uncoated with high temperature grease, the percentage change of the a* value for specimens heated at 200 °C was -1.55% while the percentage change for specimens heated at 500 °C was -0.11%. The percentage change of the b* value for specimens heated at 200 °C was -0.52% while the percentage change for specimens heated at 500 °C was 2.85%.

Table 4.1. Data of color value changes with respect to temperature for coated and uncoated specimens

	Heating temperature (°C)	**a* change**	**Δ of a* change**	**b* change**	**Δ of b* change**	**Ratio of b* change to a* change**
Coated	200	-1.83%	+1.13%	+0.56%	+4.05%	3.58
	500	+0.70%		+4.61%		
Uncoated	200	-1.55%	+1.44%	-0.52%	+3.37%	2.34
	500	-0.11%		+2.85%		

Note: Color changes of heated specimens calculated with respect to photos taken before heating (25 °C)

The results show that the high temperature grease used to simulate the effects of smoke and soot did have an effect on the absolute color values of the rock specimens. However, since the effects of heating on the a* and b* color values are similar at all temperatures, the difference in the a* and b* color values will still be similar, as seen from the similar gradient of the changes of the a* against b* values of Figs. 4.4c, 4.12c and 4.13c. We would still be able to estimate the heating temperature of the

specimens as the effect of the soot and smoke residue should be minimal. The linearity of the color changes with respect to heating temperature within the 200 °C to 500 °C range suggests that in a real world application, the scale would need to be calibrated by determining the color change of two points of known heating temperature in the affected area, which can be achieved via traditional fire forensic engineering techniques.

4.3 Discussion

In this chapter, granite specimens were photographed using a DSLR camera before and after heating, and the color changes of the specimens were quantified using a MATLAB script. Another set of specimens were prepared and coated with high temperature grease on one side to simulate the effects of smoke and soot on the reliability of colorimetry on rock surfaces that inevitably accompanies an actual fire. In both cases, it was found that the changes in the a* and b* values varied almost linearly with respect to heating temperature.

The above detailed method is a fast and cost effective method of determining the maximum temperature experienced by the rock. In the field, a portable frame can be built with suitable lighting integrated within it. Light Emitting Diodes (LEDs) seem to be ideal as they are bright, easy to transport and consume little power. LEDs are also readily available and easily replaced, enabling light sources with similar color temperature to be available. Integrating LEDs into a frame will also make it easier to transport, as well as fixes the position of the LEDs with respect to the area of the rock being photographed. This will ensure consistent lighting as the distance and the angle of the LEDs to the patch of rock being photographed will be fixed, thereby reducing any random error present. The resulting images taken can be easily analyzed as MATLAB can be run on almost any computer, such as a laptop at the site itself.

After a fire that occurs within a rock cavern\tunnel has been put out, the procedure for developing a preliminary thermal damage map of the cavern\tunnel can be as follows:

1. Use steel wool and rubbing alcohol to reveal the rock being photographed. The rock should be scrubbed for a minimum of 10 minutes, until no visible soot can be removed by wiping the rock with a piece of white paper.
2. Place portable frame with integrated LEDs over the area of interest to demarcate the area for analysis as well as to provide sufficient lighting.
3. Set up tripod with DSLR camera and take photographs of the rock.
4. Analyze the color of the rock with MATLAB.

As each set of color analysis takes around 10 minutes to complete, the mapping of the cavern\tunnel is essentially limited to the speed of the photo taking.

The photographs of the original rock for comparison purposes can be taken when construction of the project ends for an unlined cavern\tunnel portion, following the same procedure detailed above, with the exception of the first step. Alternatively, photos can be taken of any rock cores drilled as part of a routine site investigation.

For the estimation of the heating temperature to be of practical usage, the correlation between the heating temperature and the mechanical properties of the rock must be known. Common site investigation practice involves drilling rock cores for laboratory determination of the mechanical properties of the rock, such as its elastic modulus and uniaxial compressive strength at room temperature. A more comprehensive site investigation could also include testing for mechanical properties after exposure to high temperatures in a laboratory.

Another approach to correlate color changes of rocks with its mechanical properties is based on testing rock cores obtained from selected areas after a fire incident occurs. Once the correlation between rocks exposed to a known temperature and its mechanical properties is established, the structural integrity of the rest of the cavern\tunnel can be estimated. This can supplement traditional forensic fire engineering techniques such as correlating fire temperatures with melted items of known melting points. Using a two-pronged approach of traditional fire forensic engineering and the above-mentioned colorimetry technique also increases the level of confidence in the estimation of the fire temperature. Although the absolute color value change of the specimen may vary from different sets of photographs taken, the

ratio of a* to b* change has been shown to be almost consistent, provided the lighting conditions remain constant. This means as long as two localities of a rock cavern\tunnel of known heating temperature are available for calibration, a preliminary estimate of the fire damage can be quickly and cheaply mapped out. With a distribution map of the heating temperature, the integrity of various parts of a rock cavern\tunnel can be estimated and a decision to salvage the cavern\tunnel or to abandon it can be made.

The absolute color value changes in this chapter were found to vary, even though lighting conditions such as placement of lights and the type of light used were kept constant. A possible explanation is that even though the conditions were kept constant, the lights used were incandescent bulbs and subjected to lumen depreciation (section 2.4.6.2). Lumen depreciation is a phenomenon whereby the output of a light source gradually decreases over its lifespan and has a subtle effect on the lighting of the specimens (US Department of Energy, 2013). This is not expected to be significant in the field, as lumen depreciation is only significant if the lights were used over a long period on the scale of months.

The method outlined in this chapter is fairly robust, as smoke and soot damage caused by the fire can be mitigated by cleaning it off with rubbing alcohol to reveal the true color of the rock mass underneath. Although the smoke and soot still affects the readings after it has been cleaned off, the error does not affect the estimation of the heating temperature when compared to another point in the cavern\tunnel where similar smoke and soot damage has occurred. Another feasible method to remove the surface discoloration would be to chip off the surface layer of the rock.

The temperature tested has been capped at 500 °C, as granite has been known to disintegrate at 573 °C. It is obvious that the structural integrity of the rock mass is severely compromised at that point. The proposed technique is meant for use on granite that has been heated to a temperature where its mechanical properties have been compromised, but the degree of degradation is unknown.

This technique has been demonstrated for temperatures of 200 °C, 350 °C and 500 °C in this chapter. The data obtained may not be able to resolve the effects of temperature differences of 10 °C to 20 °C, depending on the sensitivity of the

equipment, and the lighting conditions. However, for the purpose of a preliminary evaluation, it is not necessary to be so precise, as the mechanical properties of the rock is unlikely to vary wildly over such a small temperature range.

Another potential problem is that some other rock types may not have a color change in response to heating, or the color change may be too subtle to be easily quantifiable. Other rocks may have a change in its appearance, but may manifest themselves in ways that are harder to quantify, such as a change in their luster or a change in the non-visible spectrum. The color of the rock is also affected by the amount of moisture on its surface, and in an underground cavern\tunnel, it may not be feasible to control the amount of surface moisture, especially after the fire-fighting efforts.

4.4 Conclusions

This chapter explores the feasibility of using relatively low cost DSLR cameras as a tool for quick and accurate colorimetry of heated and unheated rocks. The CIE L*a*b* color space is used in this chapter.

A correlation between the heating temperature of the specimens, and changes in the a* and b* color scales have been found. In general, heated Bukit Timah granite specimens have been found to be more “reddish” and “yellowish” than specimens that are unheated, or have been heated at a lower temperature. The variation in the a* and b* color values forms an almost linear relationship with the heating temperature.

High temperature grease was used to simulate smoke and soot damage that would result from a real fire as it has similar characteristics to actual smoke and soot, such as its color and greasiness. The high temperature grease that obscured the surface coloration of the heated specimens could be removed by rubbing alcohol and a scouring pad. Even though the high temperature grease affected the absolute color values of the rock specimens, it shifted the color values in the same direction of a similar magnitude for the specimens regardless of heating temperature. Since we are measuring the changes in the color values with respect to heating temperatures, the effect of the high temperature grease is minimal on the colorimetry process.

To conclude, colorimetry using DSLR cameras is a potentially useful tool to reveal the degradation of the structural integrity of rocks exposed to high temperatures. It

provides a relatively cheap and fast way in estimating the temperature that rocks have been exposed to. From this information, we can estimate the structural integrity of, and thermal damage done to the rock, provided corresponding site investigation was done previously. Although the data will only have a precision of around tens of degrees, it will be sufficient for a feasibility study on repairing the affected underground structure. From the color change, the mechanical properties such as the uniaxial compressive strength or the tensile strength of the rock can be estimated. The mechanical properties can then be used as input parameters for numerical simulations to determine the serviceability of the underground structure, as well as how effective will repair works be. Parts of the cavern\tunnel may also be selectively reinforced, based on the estimated weak spots. The cost of extensive testing to identify these areas will be prohibitive even considering the potential savings. A reliable yet faster and cheaper method of estimating the mechanical properties of fire damaged rock will be useful as it balances ease of use with accuracy.

Chapter 5 Dynamic compressive test of heated specimens

5.1. Introduction

This chapter deals with the effects of high temperatures on the dynamic compressive strength of rocks. The specimens that were tested in this chapter were manufactured from Carrara marble (CM) slabs and Bukit Timah Granite (BTG) rock cores. BTG was chosen as granite is a common rock that can be found globally. In a local context, the naturally high strength of BTG makes it desirable as a host rock for underground construction. CM, which is a metamorphic rock, was also used as it is often used as a medium to simulate carbonate rocks, due to it having the same chemical composition as other carbonate rocks such as limestone, and having very little impurities.

The experimental findings and the associated implications will be presented and discussed. The first half of this chapter will be dedicated to the dynamic compressive testing of CM, while the second half of this chapter will be dedicated to the dynamic compressive testing of BTG. The similarities and differences of CM and BTG will be discussed at the end of this chapter.

The effects of high temperatures on the dynamic properties of rock is critical to the understanding of rock behavior under scenarios not covered by current design approaches. Such scenarios include hazards associated with underground nuclear waste storage, explosions due to fires in underground coal mines or impact from traffic accidents during or after an outbreak of fire in an underground tunnel.

This chapter focuses on the behavior of rocks that are exposed to a dynamic load while being heated at high temperatures. This is useful in understanding the behavior of rocks during a fire, as explosions may happen as flammable material is heated to its flashpoint. This will be useful in estimating the damage suffered by rocks during a fire, and deciding on appropriate fire-fighting options.

5.2. Carrara marble

5.2.1. Dynamic compressive strength of marble with respect to testing pressure

Fig. 5.1 shows the relationship between the peak stress and strain rates for tests conducted under 4 temperatures: room temperature, 250 $^{\circ}$C, 500 $^{\circ}$C and 750 $^{\circ}$C. The

input energy of the impact bars is specified in terms of the pressure used to charge the gas gun (section 3.9). It can be seen from Fig. 5.1 that for the same amount of input energy, as determined in proxy by the pressure used, the strength of the specimen decreases as the heating temperature increases. Moreover, the strain rate also increases, implying increased ductility. Both observations can be explained with an increase in microcracking.

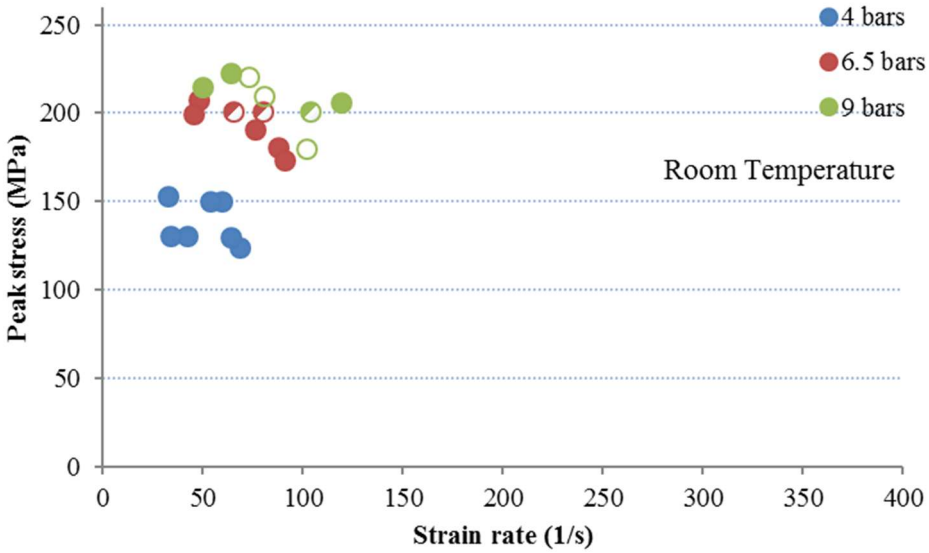

(a)

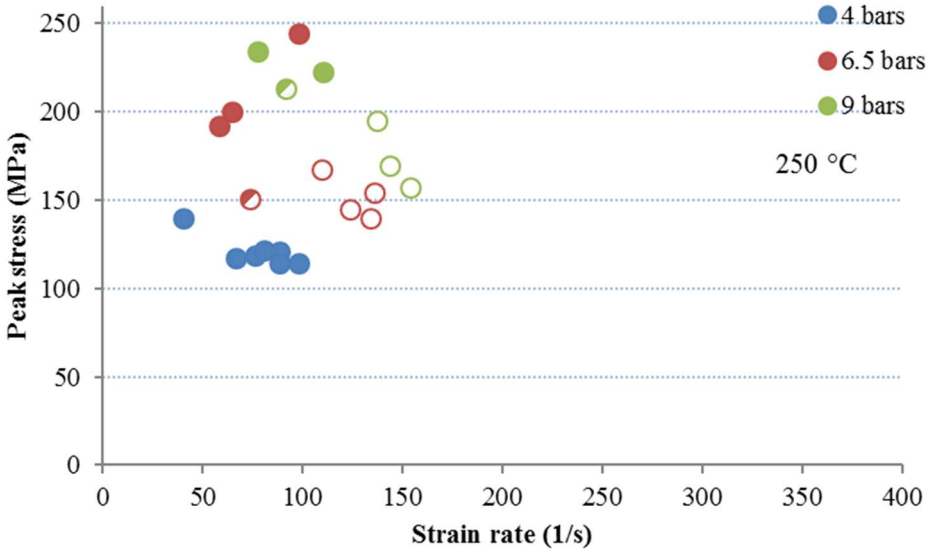

(b)

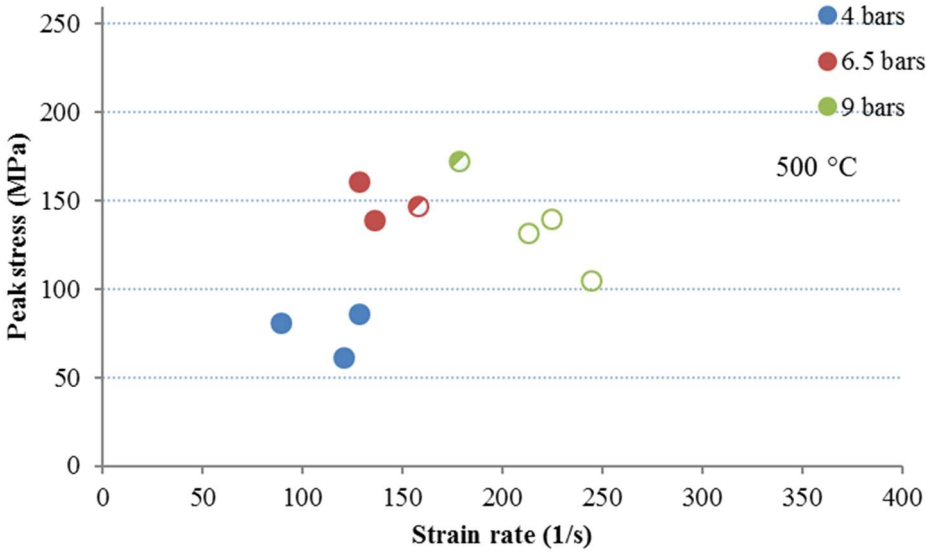

(c)

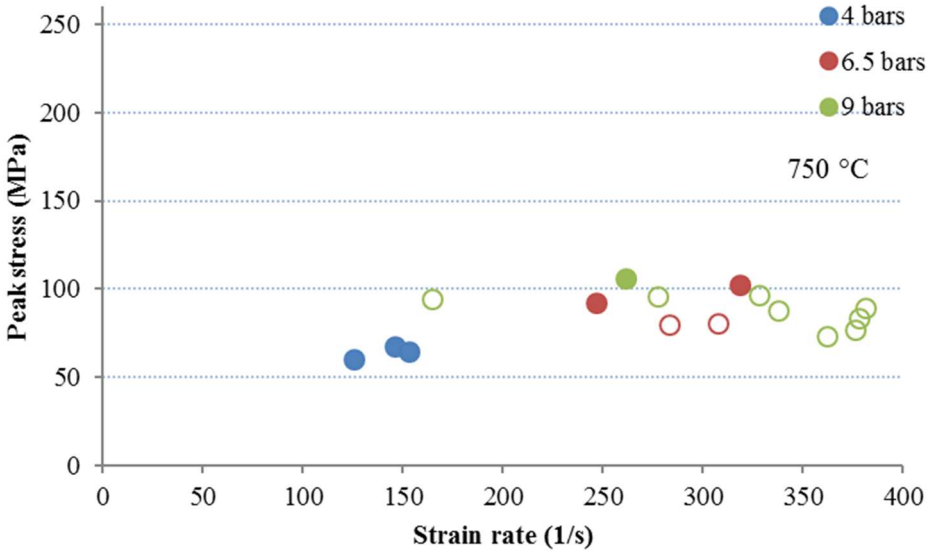

(d)

Fig. 5.1 Relationship between peak stress and heating temperature of marble for (a) room temperature, (b) 250 ˚C, (c) 500 ˚C and (d) 750 ˚C. Specimen failure types are represented by different symbols. Filled symbols indicate intact specimens, half-filled symbols indicate axial splitting, and empty symbols indicate pulverization.

Equation 2.1 (section 2.3) assumes plane strain conditions for a plate of infinite width being loaded at right angles to a single crack, of length 2α, where K_{1c} is the critical stress intensity factor for mode 1 cracking, σ is the stress applied (Fig. 2.1).

From equation 2.1 we can see that the strength of a material depends not only on the stress applied, but also the length of the microcrack. Thus, any variables that may increase the length of microcracks in a material would also weaken it. Another factor that may influence the strength of a material is the microcrack density of a material, as materials with high microcrack density may contain microcracks that are spaced closely enough with each other to interact (Ning et al. 2010).

As seen in Fig. 5.1, for all heating temperatures, a gas pressure of 4 bars does not provide enough energy to fail the specimen. At a temperature of 250 °C, the specimen may either remain intact under impact or it may fail by axial splitting or by pulverization. Two distinct trends are clearly observed in Fig. 5.1b (250 °C), as characterized by the failure type. For specimens that primarily failed via axial splitting or remained intact, a higher peak stress and a lower strain rate were observed. Whereas for specimens that failed via pulverization, a higher strain rate and lower peak stress was noted. This supports the hypothesis that the main mechanism was via microcrack generation due to heating, as the degree of pulverization suggests a large amount of heat-induced microcracks, which explains the lower peak stress and higher strain rate as compared with the specimens that remained intact or failed via axial splitting.

Another observation is how the strain rate effect is diminished or absent as heating temperature increases, regardless of failure mode. From Fig. 5.1, we can see that even though none of the specimens tested at 4 bars failed via axial splitting or pulverization, the peak stress recorded for the specimens tested at room temperature is higher than those tested at 750 °C, even though the latter experienced a higher strain rate.

From Fig. 5.1b (250 °C) and 5.1c (500 °C), we observe an increasing trend of specimen strength with respect to strain rate, until it reaches a critical point. Beyond this point, the strength of the specimens was observed to decrease with further

increase in the strain rate. In Fig. 5.1c (500 °C), we can observe that as the strain rate increases, there appears to be a zone where specimens fail via axial splitting between the intact specimens and the pulverized specimens. This is also noted by Doan and Billi (2011).

As shown in Fig. 5.1d (750 °C), both the specimens tested at 6.5 and 9 bars experience similar strain rate and peak stress. This could be due to the dynamic increase factor phenomenon being limited by the high microcrack density. Another reason may be due to more energy being used to increase the crack propagation velocity and reduce the average fragment size as explained in a later section of this chapter (section 5.2.4). According to Ravi-Chandar and Knauss (1984), the propagation of a crack is due to the linking up of many microcracks that are a function of the stress intensity factor and the amount of preexisting microcracks within the fracture process zone. The size of the fracture process zone is proportional to the stress intensity factor. As the stress intensity factor increases, the size of the fracture process zone also increases, causing a greater number of microcracks to interact and contribute to the crack growth. This process dissipates a greater amount of energy.

5.2.2. Dynamic compressive strength of marble with respect to heating temperature

Fig. 5.2 shows the same set of data as presented in section 5.2.1, but plotted in terms of testing pressure to further elucidate the relationship between heating temperature, testing pressure and the mechanical properties of the specimens.

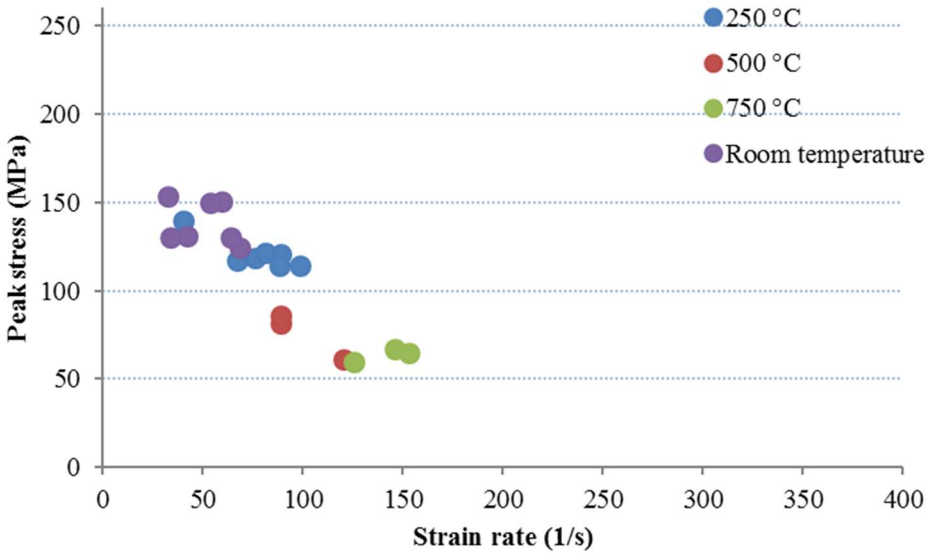
250 °C
500 °C
750 °C
Room temperature
Peak stress (MPa)
Strain rate (1/s)
0
50
100
150
200
250
300
350
400

(a)

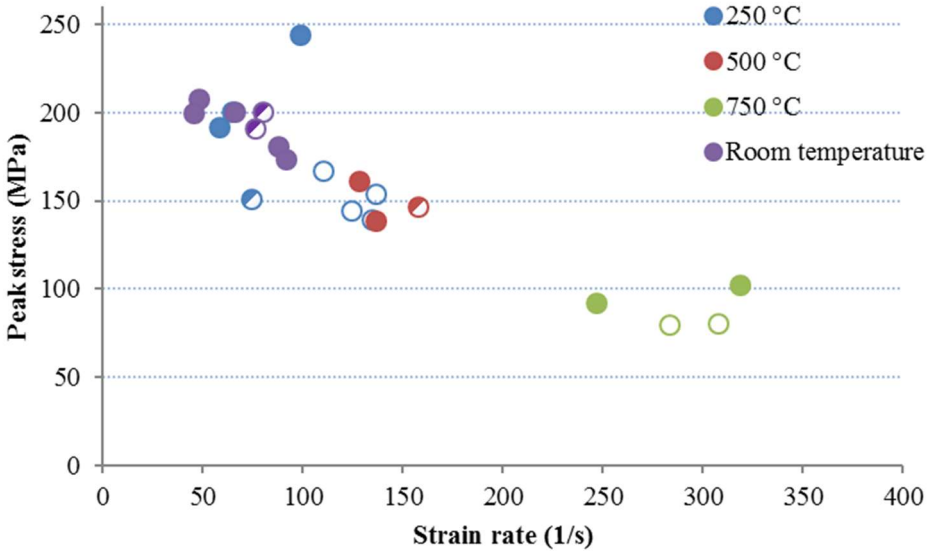
250 °C
500 °C
750 °C
Room temperature
Peak stress (MPa)
Strain rate (1/s)
0
50
100
150
200
250
300
350
400

(b)

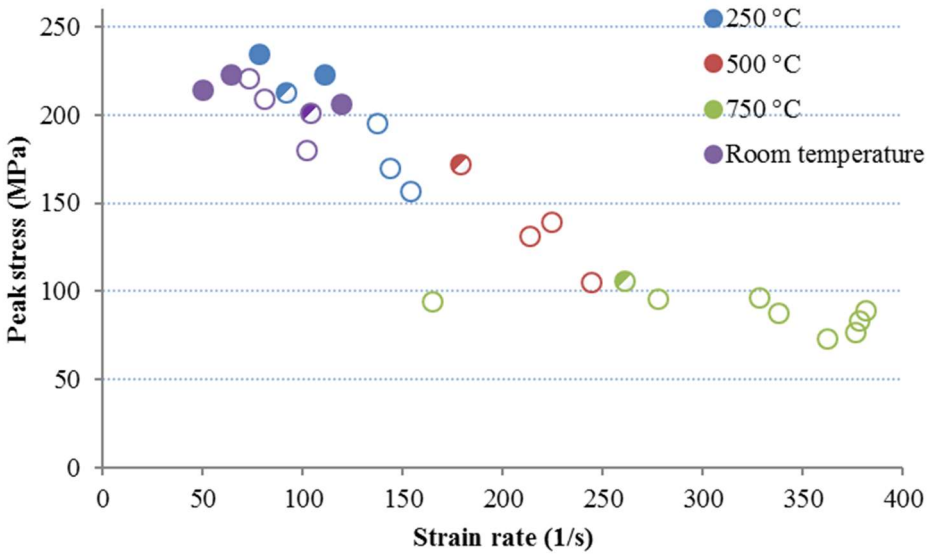

(c)

Fig. 5.2 Relationship between peak stress and testing pressure of marble for (a) 4 bars, (b) 6.5 bars and (c) 9 bars. Specimen failure types are represented by different symbols. Filled symbols indicate intact specimens, half-filled symbols indicate axial splitting, and empty symbols indicate pulverization.

From Fig. 5.2a (4 bar), we can see an obvious decrease in peak stress of the specimens with an increase in heating temperature; this is accompanied by a corresponding increase in the strain rate. This is most likely due to an increased microcrack formation in the specimen caused by the increased temperature. As none of the specimens have failed, it is reasonable to deduce that 4 bars of pressure does not provide sufficient energy to fail the marble specimen even if it is heated to 750 °C.

From Fig. 5.2b (6.5 bar) and 5.2c (9 bar), we can see a clear trend of the thermal damage done to the specimens. The variation of the strength of the specimens with temperature is quite similar for specimens tested at these two impact energies.

5.2.3. Dynamic compressive strength of marble with respect to maximum strain

Fig. 5.3 shows the variation of the peak stress with strain. For specimens tested at room temperature, Fig. 5.3a (25 °C) shows the measured strain at peak stress varies with applied gas pressure. For a gas pressure of 9 bar, the maximum strain was found

to be less than 2.5%. Increasing the specimen temperature brings about an increase in the strain at peak stress. For specimens tested at temperature of 750 °C and 9 bars of gas pressure, the peak strain was 5.5%, a nearly 2 fold increase when compared to that obtained for a specimen tested under room temperature. The increase in energy provided by higher testing pressure leads to a higher measured peak strain, but has lesser effect on the strength of the specimens as shown in Fig. 5.3c (500 °C) and 5.3d (750 °C). As the energy absorbed is calculated by the area under the stress-strain curve, this suggests that as the peak failure stress of the specimens remains similar; energy is mostly dissipated via plastic deformation of the specimens.

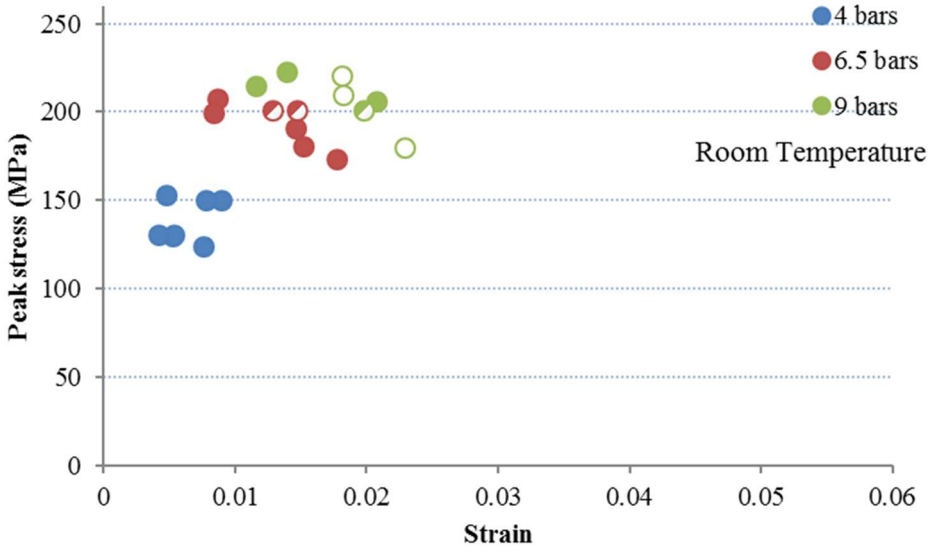

(a)

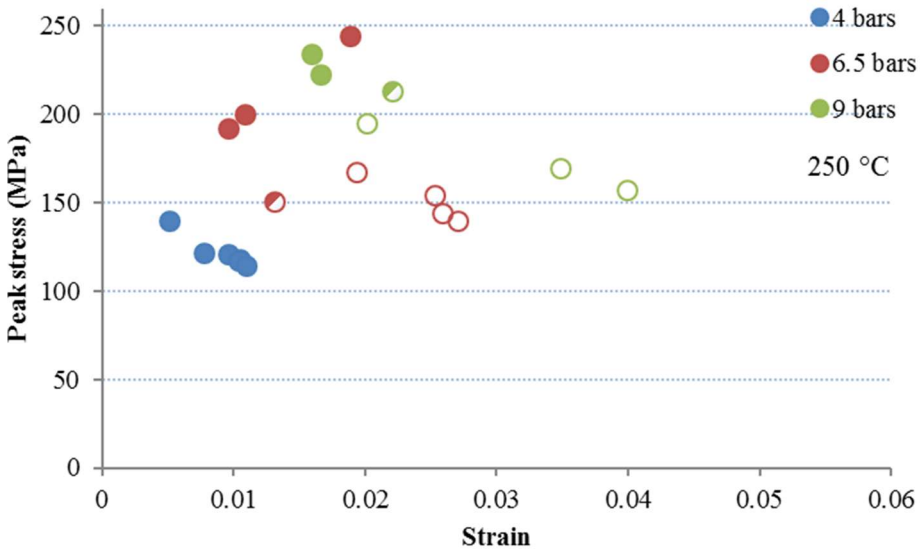
4 bars
6.5 bars
9 bars
250 °C
Peak stress (MPa)
Strain
0
50
100
150
200
250
0
0.01
0.02
0.03
0.04
0.05
0.06

(b)

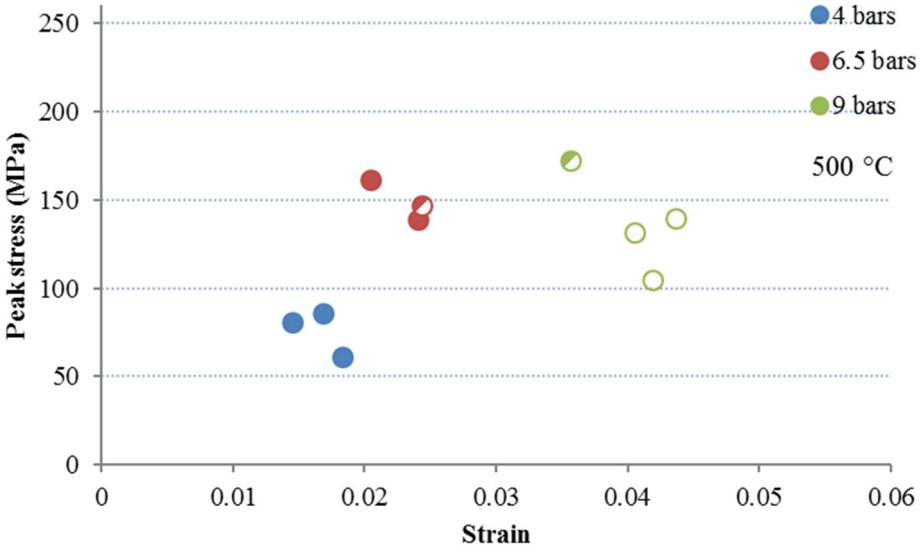
4 bars
6.5 bars
9 bars
500 °C
Peak stress (MPa)
Strain
0
50
100
150
200
250
0
0.01
0.02
0.03
0.04
0.05
0.06

(c)

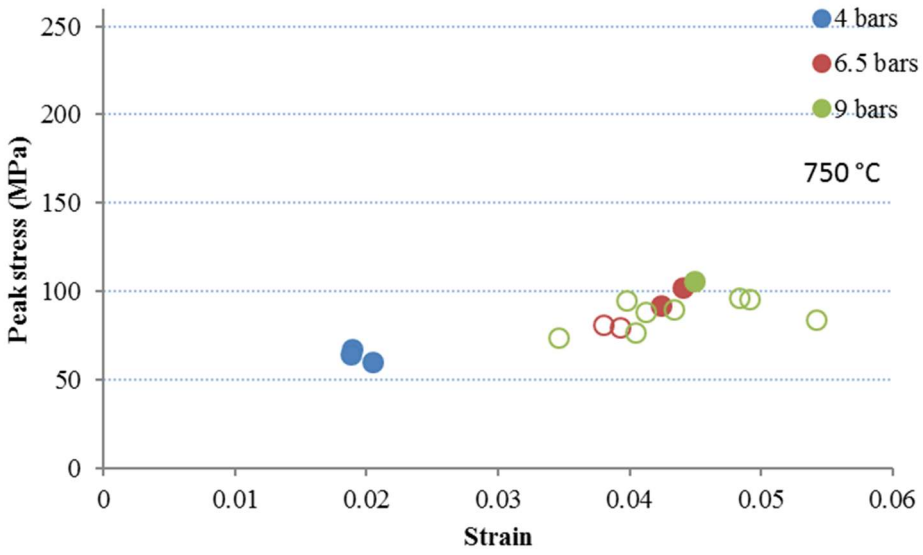

(d)

Fig. 5.3 Influence of gas pressure and temperature on strain for marble specimens tested at (a) room temperature, (b) 250 °C, (c) 500 °C and (d) 750 °C

The above phenomenon can be explained by equation 2.1 (section 2.3). As the generated microcrack length is dependent on the heating conditions, for a constant heating condition, the critical stress intensity and peak stress of a specimen should be constant.

5.2.4. Energy absorption per unit volume for marble

The Linear Elastic Fracture Mechanics (LEFM) theory is often used to account for the strength of a brittle material containing microcracks. This theory assumes that there is only a small plastic zone at the tip of the crack. This assumption is valid only when the material being tested is linear elastic, which is a reasonable assumption for materials that fail at a low strain level. From the tests, rocks that are heated show increasingly ductile behaviour under loading and it is likely that a significant amount of the input energy will be dissipated through plastic deformation of the specimen. For cases in which failure occurs at a high strain level, it will be more appropriate to adopt an Elastic-Plastic Fracture Mechanics (EPFM) based framework which takes into account plastic deformation within the rock. As we are interested in the performance of a rock cavern or tunnel in response to dynamic loading during and

after heating, we should take into account the dissipation of energy through plastic deformation of the rock.

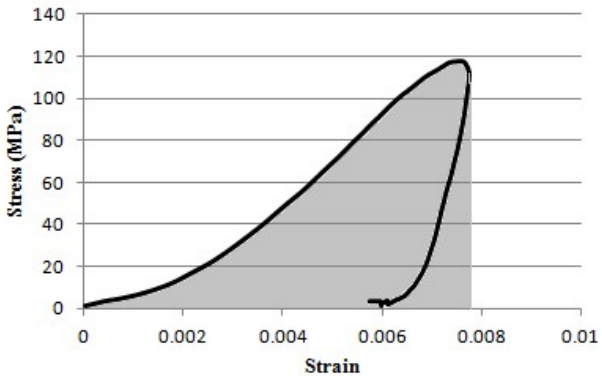

(a)

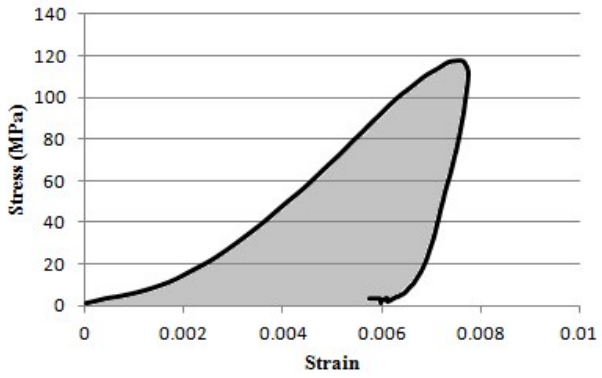

(b)

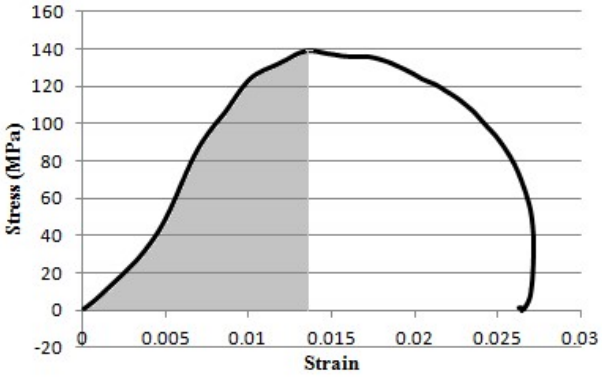

(c)

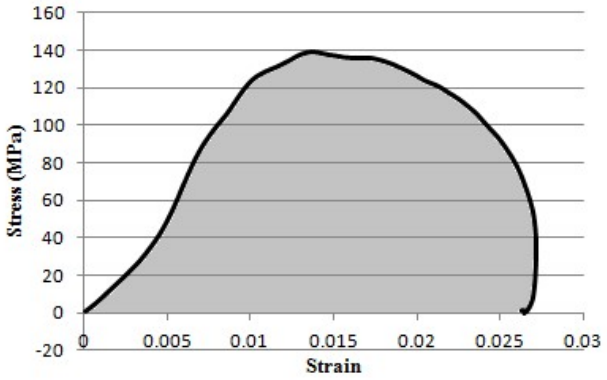

(d)

Fig. 5.4 (a) Energy at peak stress for intact specimens, (b) total energy absorbed for intact specimens, (c) energy at peak stress for fractured specimens, (d) total energy absorbed for fractured specimens.

A more comprehensive approach to compare the effects of different heating and loading conditions on the strength of the marble specimens would be to calculate the amount of energy needed to fail the specimens after heating as it takes into account energy used to deform the specimens as shown in Fig. 5.4. Similar approaches were also taken by Liu and Xu (2013), as well as Doan and Billi (2011). The energy absorbed, as shown by the shaded area, is calculated by integrating the area under the individual stress-strain curve using MATLAB.

In the following analysis, the total energy absorbed refers to the energy absorbed by the specimen as calculated from total area under the stress-strain curve, excluding any energy used for elastic deformation for cases where the specimen remained intact, as shown in Fig. 5.4b and 5.4d. The energy absorbed at peak stress refers to the amount of energy absorbed by the specimen from the start of the experiment to the point when the specimen reaches its peak stress. This is inclusive of any energy used to deform the specimen elastically, as shown in Fig. 5.4a and 5.4c.

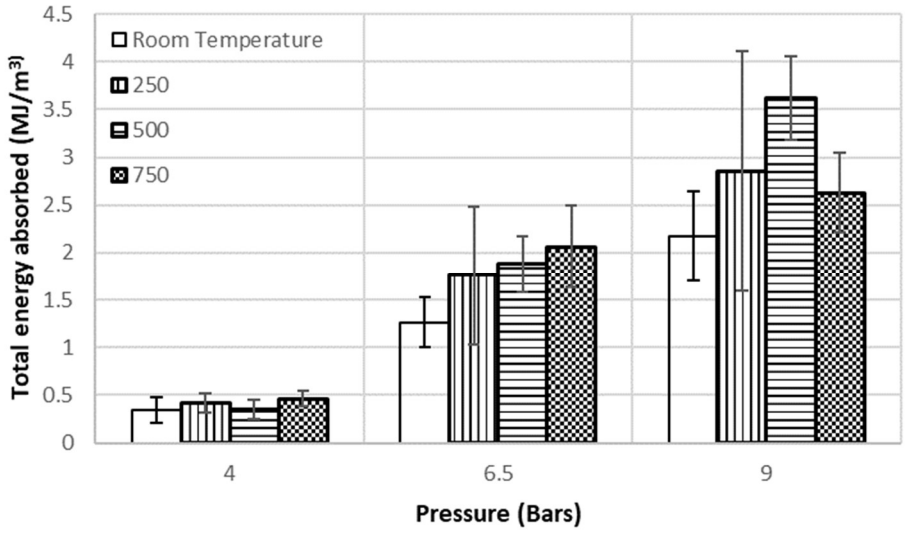

(a)

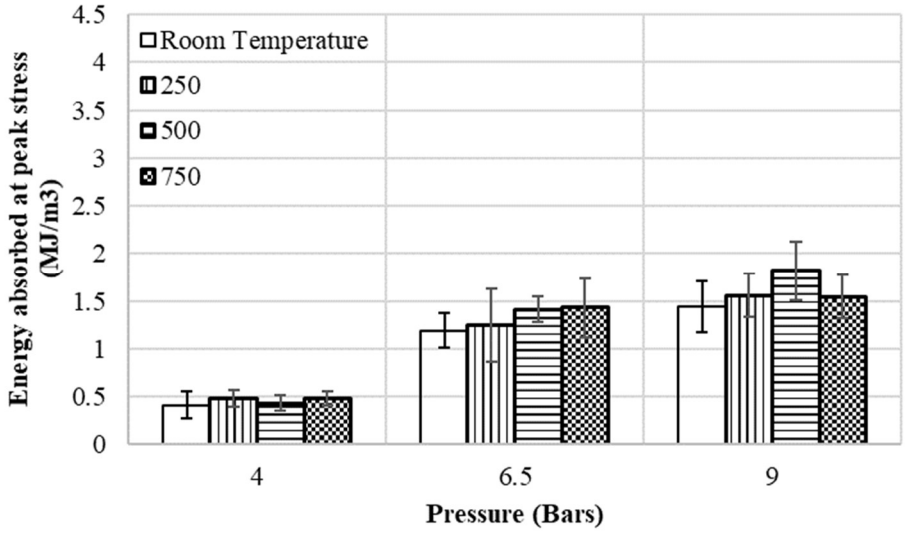

(b)

Fig. 5.5 Graph of (a) total energy absorption, (b) energy absorption for marble specimens at peak stress, error bars represents ±1 standard deviation.

The results of energies absorbed are shown in Fig. 5.5, clustered based on the gas pressure used. As seen in Fig. 5.5, for specimens tested at 4 bars of pressure, the total energy absorbed and energy absorbed at peak stress at all temperatures are similar, averaging about 0.5 MJ/m^3, with the latter being slightly higher. This shows that the energy absorbed by specimens tested at 4 bars of pressure is predominantly used to

generate new microcracks. The slightly lower total energy absorbed may be attributed to the release of elastic potential energy associated with the elastic deformation of the specimens, since none of the specimens failed when the applied gas pressure is 4 bars.

At higher temperatures, more heat induced microcracks developed in the specimen. With increased microcrack density, it is easier for material in the specimen to slide past each other, which is manifested as plastic deformation. For the specimens tested at 6.5 and 9 bars of pressure, there is an increase in the energy absorbed at peak stress as well. This may be due to additional energy dissipation due to increased plastic deformation as suggested by Fig. 5.3.

The total energy absorbed (Fig. 5.5a) is also significantly larger than the energy absorbed at peak stress (Fig. 5.5b). This implies that additional energy was consumed by the specimen to propagate cracks. The increased crack density caused by elevated temperatures could increase the amount of flaws initiated and result in a smaller average fragment size in the failed specimen. Therefore, the magnitude of the energy absorbed after the specimen failure can give us some insights into the fragmentation behavior of the specimens.

From Fig. 5.5b, we can see that the energy expended to fail the specimens at 6.5 and 9 bars of pressure is around 1.5 MJ/m^3, and the standard deviation is quite low compared to the data in Fig. 5.5a. While the total energy absorbed for the 6.5 and 9 bars specimens increased with the testing pressure used, it can be seen that the energy increase is mainly used for fragmenting the specimens after it reaches peak stress. While the energy needed for the specimens to reach peak stress remains somewhat consistent as shown by the smaller standard deviation, the energy needed to fragmentize the specimens fluctuates considerably as shown by the larger standard deviation. Furthermore, the energy requirements would vary with different failure modes as well as the fragment size distribution.

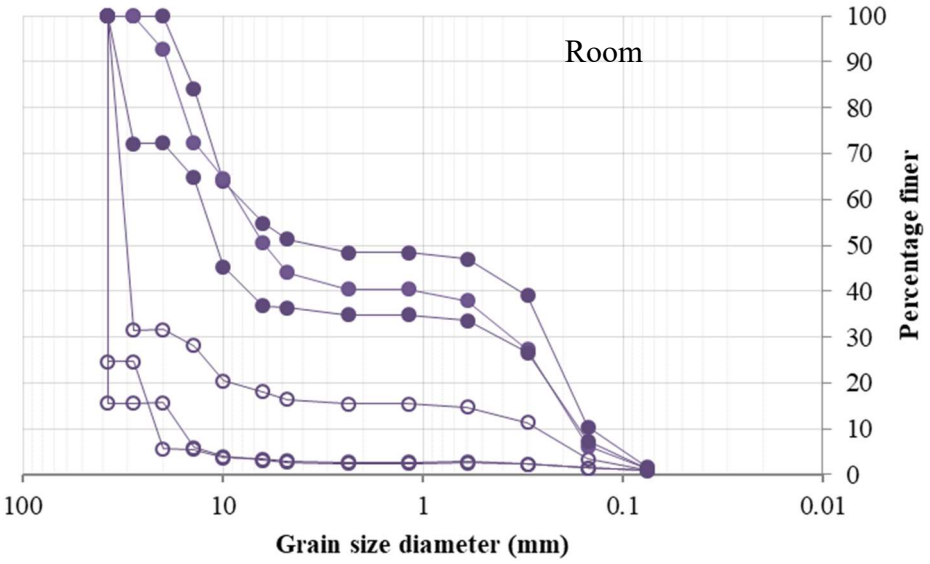
Room
100
90
80
70
60
50
40
30
20
10
0
Percentage finer
100
10
1
0.1
0.01
Grain size diameter (mm)

(a)

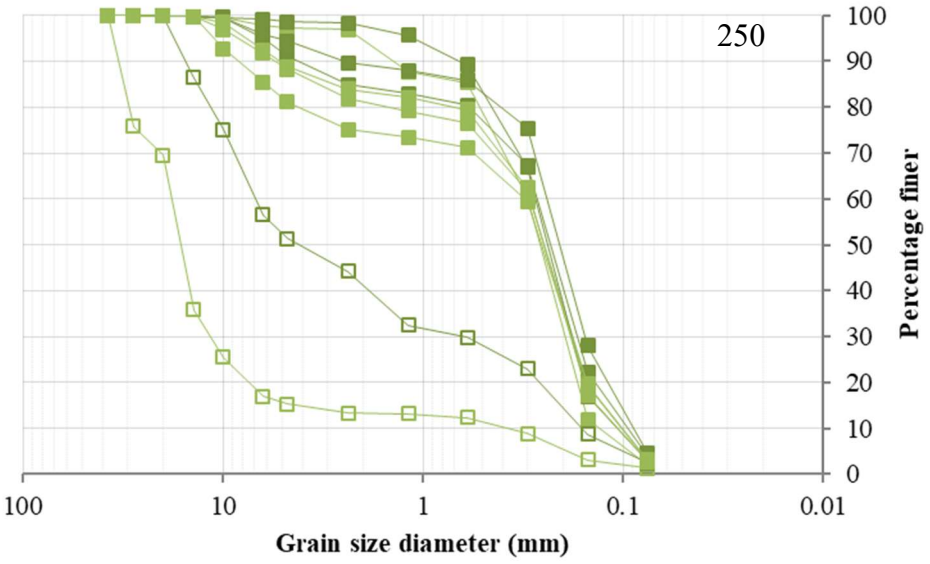
250
100
90
80
70
60
50
40
30
20
10
0
Percentage finer
100
10
1
0.1
0.01
Grain size diameter (mm)

(b)

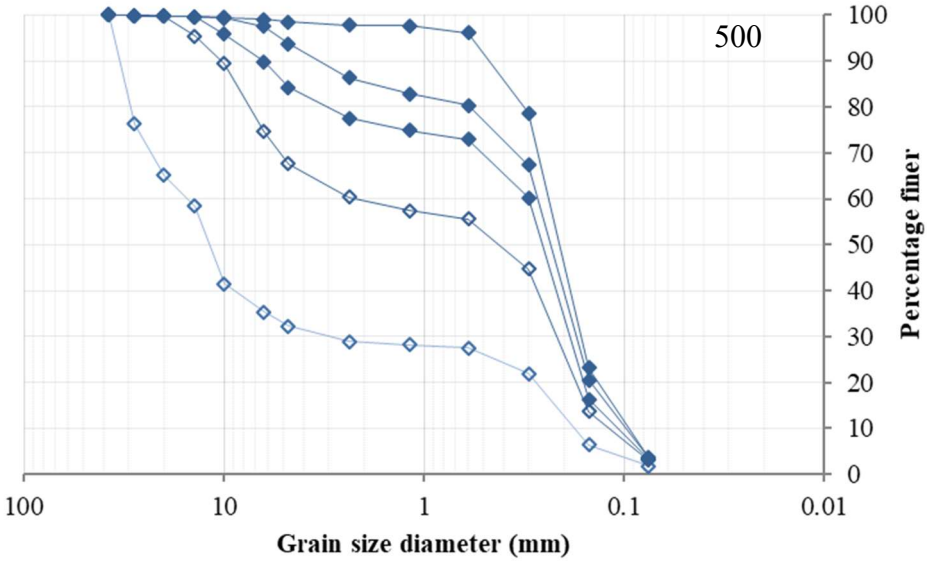

(c)

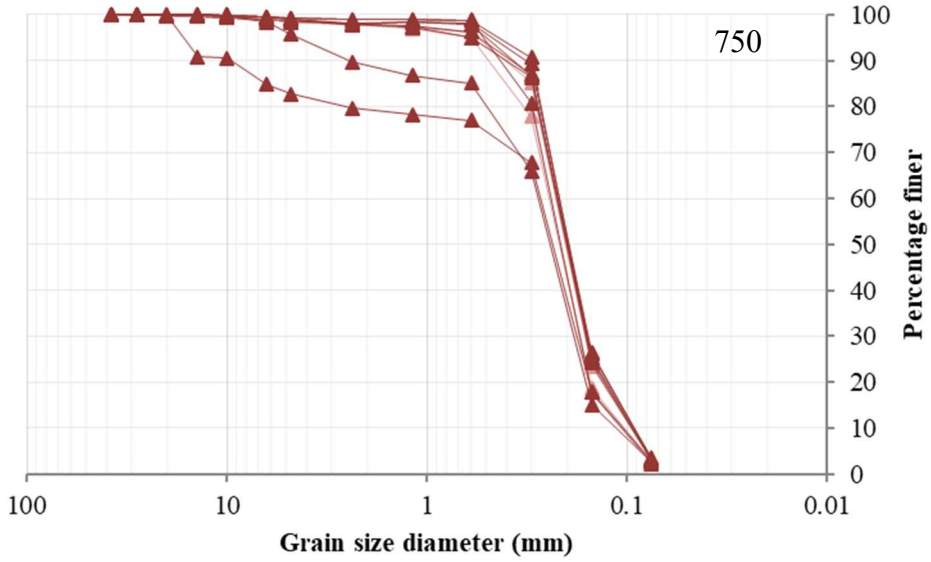

(d)

Fig. 5.6 Particle size distribution for marble specimens tested at (a) room temperature, (b) 250 °C, (c) 500 °C and (d) 750 °C, dark lines are for specimens tested at 9 bars, while light lines are for specimens tested at 6.5 bars. Open symbols indicate specimens that failed via axial splitting

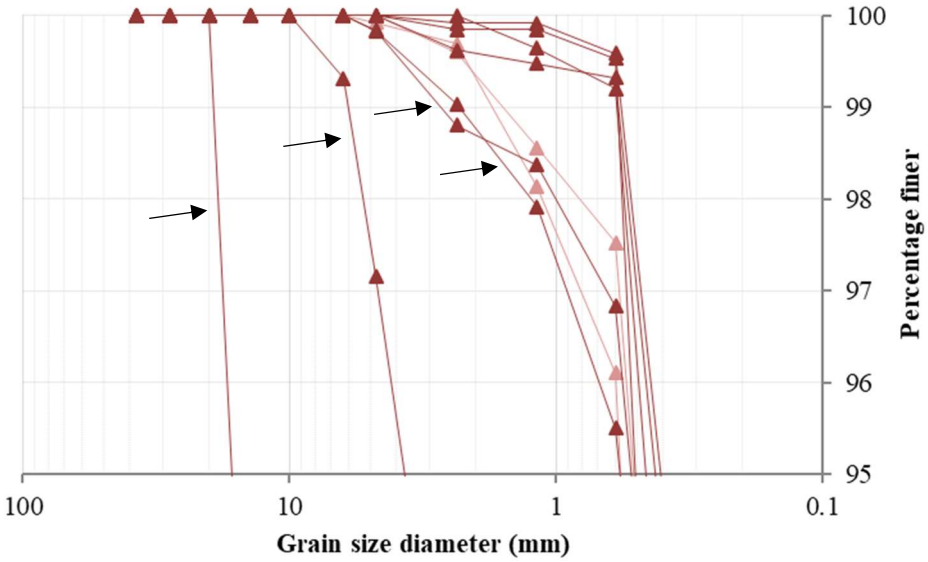

Fig. 5.7 Close up of the front part of the particle distribution curve of marble specimens tested at 750 °C, specimens in which stress shadowing occurred have been identified by arrows

The particle size distribution curves from the sieve analysis (section 3.9.2) are shown in Figs. 5.6 and 5.7. For the same failure mode, the specimens tested at higher temperatures result in finer fragment sizes. This observation can be explained by the increased heat-induced microcrack density in the specimen, which facilitates microcrack propagation and ultimately leading to smaller fragment size under a given impact. There is also a quantitative difference between the fragments of specimens that failed via axial splitting as compared to specimens that failed via pulverization. Although it is difficult to differentiate between axial splitting and pulverization by visual identification, sieve analysis shows that for heat treated specimens that failed via pulverization, the coefficient of uniformity, C_u, is below 5 and the coefficient of curvature, C_c, is generally below 5. For heat treated specimens that failed via axial splitting, C_u is above 5 and C_c is generally above 5. One exception is MDC 18 (Table 5.1), in which the C_c is 0.180.

Table 5.1 Coefficient of curvature, coefficient of uniformity and failure type of marble specimens

Specimen	Max temp (°C) – Gas gun pressure (bar)	Coefficient of curvature, C_c (1)	Coefficient of uniformity, C_u (2)	Failure type
MDC 38	250-6.5	16.690	18.000	Axial splitting
MDC 43	250-6.5	0.889	2.000	Pulverization
MDC 45	250-6.5	0.889	2.000	Pulverization
MDC 9	250-6.5	1.026	2.308	Pulverization
MDC 52	250-6.5	1.061	2.231	Pulverization
MDC 2	250-9	0.827	2.000	Pulverization
MDC 31	250-9	1.157	2.800	Pulverization
MDC 37	250-9	0.216	8.750	Axial splitting
MDC 41	250-9	1.237	2.556	Pulverization
MDC 23	500-6.5	9.888	53.500	Axial splitting
MDC 6	500-9	1.080	1.330	Pulverization
MDC 18	500-9	0.140	14.000	Axial splitting
MDC 27	500-9	1.178	2.270	Pulverization
MDC 30	500-9	1.350	2.400	Pulverization
MDC33	750-6.5	1.157	1.846	Pulverization
MDC49	750-6.5	1.543	2.100	Pulverization
MDC 51	750-9	1.219	2.100	Pulverization
MDC 20	750-9	1.543	2.100	Pulverization
MDC 28	750-9	0.992	2.150	Pulverization
MDC 44	750-9	0.860	1.867	Pulverization
MDC 53	750-9	1.409	2.300	Pulverization
MDC 54	750-9	1.281	2.091	Pulverization
MDC 55	750-9	1.409	2.300	Pulverization
MDC 56	750-9	0.939	1.533	Pulverization
MDC 61	Room temperature-6.5	0.0368	58.824	Axial splitting
MDC 62	Room temperature-9	87.604	106.667	Axial splitting

MDC 64	Room temperature-9	2.083	2.083	Pulverization
MDC 65	Room temperature-9	0.0756	50	Pulverization
MDC 68	Room temperature-9	0.04082	50	Pulverization
MDC 71	Room temperature-6.5	1.704	1.704	Axial splitting

Note: Formulas taken from ASTD D2487-11, where D_{10} is grain diameter at 10% passing, D_{30} is grain diameter at 30% passing and D_{60} is grain diameter at 60% passing

(1) $C_c = \frac{(D_{30})^2}{(D_{10})(D_{60})}$

(2) $C_u = \frac{D_{60}}{D_{10}}$

Another observation made is that the proportion of larger fragment sizes of MDC 28 and MDC 44 are significantly larger than the rest of the fragments collected of the specimens that were also tested at 750 °C with 9 bars of pressure. Also, the particle size distribution of MDC 27 and MDC 6 resembles the particle size distribution of specimens tested at 250 °C with 6.5 bars of pressure even though they were tested with 9 bars of pressure (Fig. 5.7).

This phenomenon was also observed by Liu and Xu (2013) and also Doan and Billi (2011), who explained it as a consequence of stress shadowing. As explained earlier, for similar failure modes, occasionally we can encounter a higher proportion of larger fragment sizes for specimens at high temperature tested at high pressures, such as those seen in Fig. 5.7. This increase in proportion of larger fragment sizes could be a product of stress shadowing. The larger fragments collected are also friable, and the presence of such weak fragments that survived dynamic loading further supports the presence of stress shadowing during the dynamic test.

5.2.5. Fracture behavior of marble

Wawersik and Fairhurst (1970) analyzed the post peak stress-strain behavior of rocks subjected to quasi-static uniaxial loading and found that most brittle failure of rocks

falls into two categories: Class 1 fracture, where additional energy is required to propagate the fracture after peak stress, and Class 2 fracture, where the strain energy within the specimen is enough to propagate the fracture of the specimen. The typical stress-strain curve for this experiment, Fig. 5.8, does not belong to either one of these two categories. It is a mixture of Class 1 and Class 2 fracturing. In region B of Fig. 5.8, we can see that the fracture type is a Class 1 fracture, which indicates that energy is being absorbed by the specimen.

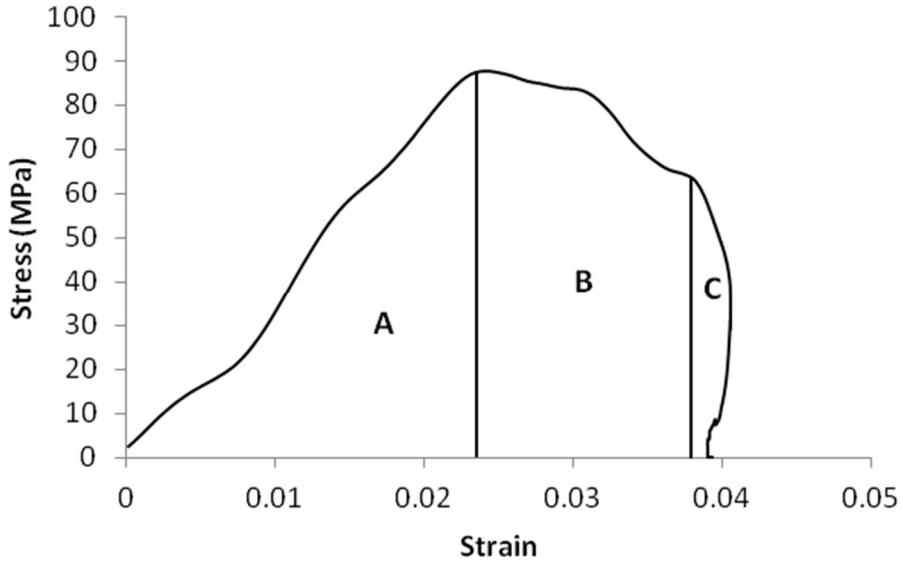

Fig. 5.8 Typical stress-strain curve for failed specimen

Wawersik and Fairhurst (1970) explained it as energy being taken in to propagate the fracture. However, the fracture proceeds into a Class 2 fracture in region C, which suggests that strain energy stored within the specimen was already sufficient to propagate the fracture without additional energy input.

For a specimen with a significant amount of microcracks present, the initial loading will provide enough energy for the primary crack to initiate and propagate. As strain energy is used up activating and propagating the primary crack, additional energy will be required to further activate the rest of the flaws within the specimen. Lastly, after the rest of the flaws in the specimen have been activated, the strain energy stored within the specimen would be enough to propagate the activated flaws and comminute the fragments.

This can be observed from Fig. 5.8. Loading that corresponds to region A provides enough energy to fail the specimen via propagation of a critical microcrack or coalescence of multiple microcracks, and an unstable fracture is formed. Region B represents an additional energy requirement to further activate remaining microcracks in the failed specimen and comminute the specimen fragments. In region C, the unstable fractures propagate themselves due to the stored elastic strain energy in the specimen.

5.2.6. Stress wave propagation velocity of marble

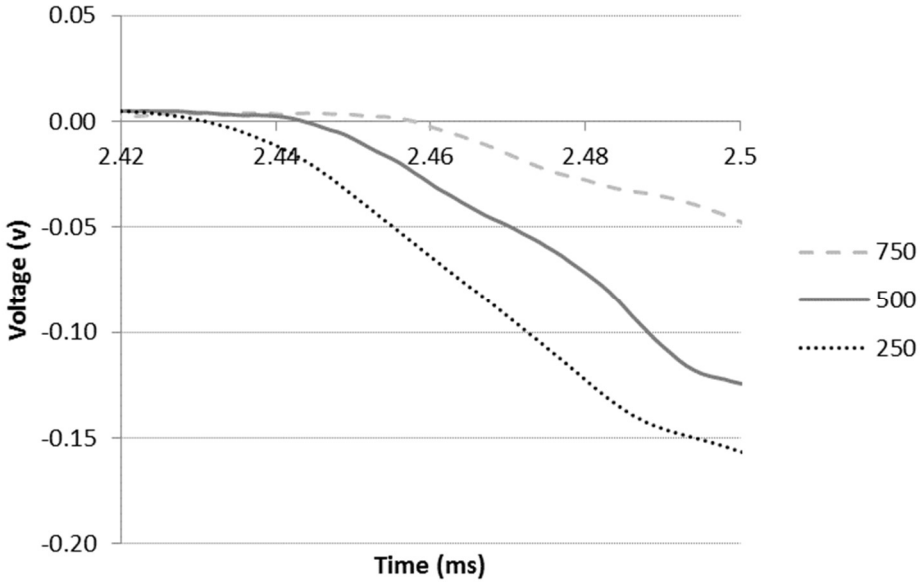

Fig. 5.9 Graph of the stress wave detected by strain gauge in output bar with respect to temperature (750 °C, 500 °C and 250 °C) for pulverized marble specimens tested at 9 bars of pressure

Stress shadowing only occurs when the crack propagation velocity is higher than the plastic wave propagation velocity. Fig. 5.9 shows the typical stress waves (voltage readings) detected in the output bar with respect to specimens tested at different temperatures. The oscilloscope used is programmed to start recording when a stress wave is detected within the input bar, which means the start time for all waves are the same. Since the elastic wave velocity of the stress wave within the metal bars are constant, any difference between the time needed for the stress wave to be detected in the output bar must be due to a difference in the plastic wave propagation velocity

in the marble specimens. We can see that there is a small difference between the peaks of the transmitted stress wave detected for the tests conducted at different temperatures.

It has been shown that the general trend of P-wave propagation velocity travelling through metamorphic rocks varies inversely to the temperature of the rock (Kern 1982; Punturo et al. 2005; Kern et al. 2001). This can be observed in Fig. 5.9 by how the stress wave for the specimens heated at a higher temperature is detected at a later time as compared to those heated at a lower temperature.

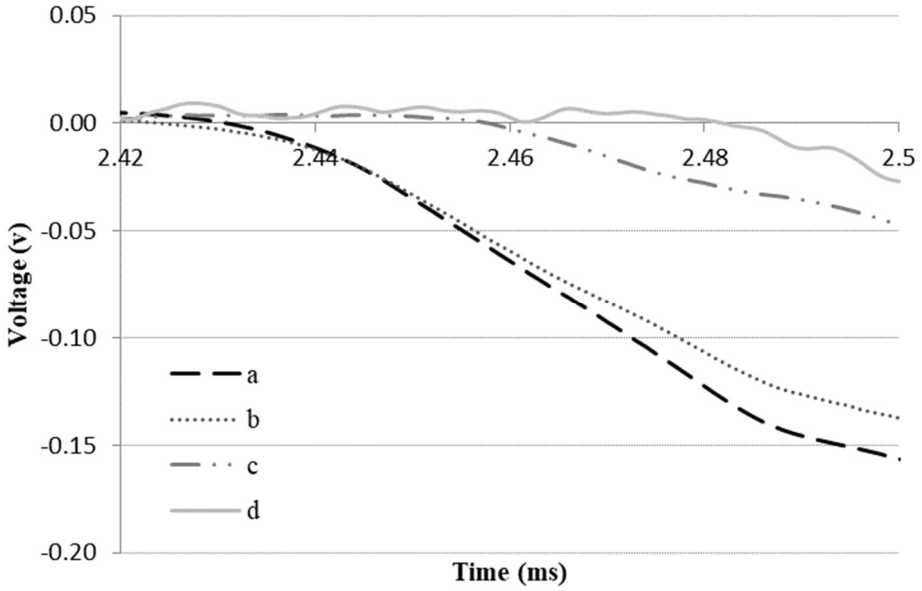

Fig. 5.10 Graph of stress wave detected within the output bar for pulverized marble specimens tested at (a) 250 °C and 9 bars of pressure, (b) 250 °C and 6.5 bars of pressure, (c) 750 °C and 9 bars of pressure, (d) 750 °C and 6.5 bars of pressure

As seen in Fig. 5.10, the effect of gas pressure on the wave propagation velocity within the specimen is subtler. The arrival time at which the peaks of the stress waves are detected for specimens with the same heating temperature but different gas pressure differs only by a small amount.

5.2.7. Crack propagation velocity of marble

The other variable is the crack propagation velocity. The variable affecting the crack propagation velocity in marble specimens is most probably the gas pressure used to

charge the gas gun of the SHPB system. For dynamic loading, the critical stress intensity factor as mentioned earlier is slightly different as now it needs to take into account the crack propagation velocity. Ravi-Chandar and Knauss (1984) showed that the crack propagation velocity of a brittle medium is affected by the initial critical stress intensity factor, which in turn, is dependent on the stress applied and microcrack length. This implies that the degree of microcracking and the loading conditions of the experiment would affect the crack propagation velocity.

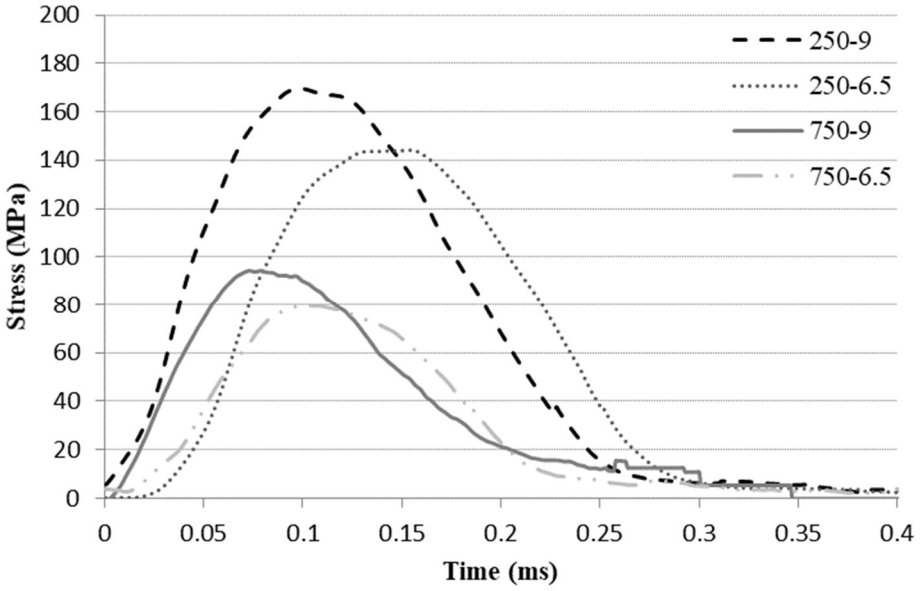

Fig. 5.11 Stress-time graph for marble specimens heated at 250 °C and 750 °C and tested at different pressures of 6.5 bars and 9 bars

As seen in Fig. 5.11, both the heating temperature and the gas pressure used to charge the gas gun affect the time to failure for the specimens tested. Assuming that the time at peak stress coincides with the time at which the cracks coalesce and fail the specimen, the time to failure will then be inversely proportional to the crack propagation velocity. This shows that the crack propagation velocity of the specimens tested increases in proportion to the gas pressure used as well as the heating temperature. Hence, we can view the time to peak stress as a reasonable proxy to the actual crack propagation velocity.

5.2.8. Stress shadowing in marble

We have seen that for a given gas pressure, specimens tested at higher temperatures will have a lower plastic wave propagation velocity, while the crack propagation velocity would increase, which favours the occurrence of stress shadowing. A temperature of 700 °C to 800 °C is likely to be the threshold when stress shadowing becomes significant. Liu and Xu (2013) noted that the anomaly regarding the fragment size started to occur at 800 °C, while stress shadowing is only noticeable at 750 °C in this experiment.

According to Doan and d'Hour (2012), rocks retrieved from fault zones typically crumble into powder when compressed by hand. They attributed this to the presence of stress shadowing during earthquakes and Rockwell et al. (2009) have shown that for these samples, a high degree of microfracturing is present.

The marble fragments collected from tests in which stress shadowing was identified also exhibited similar characteristics, in that a portion of the fragments fell apart during the course of the dry sieving process. When the fragments were dry sieved multiple times, it is noted that the proportion of larger to smaller fragments was reduced with each sieving. This lends credence to the explanation that the fragments collected during these tests are indeed products of stress shadowing.

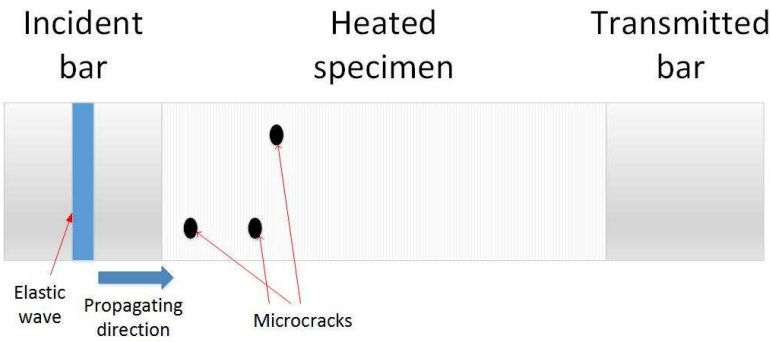

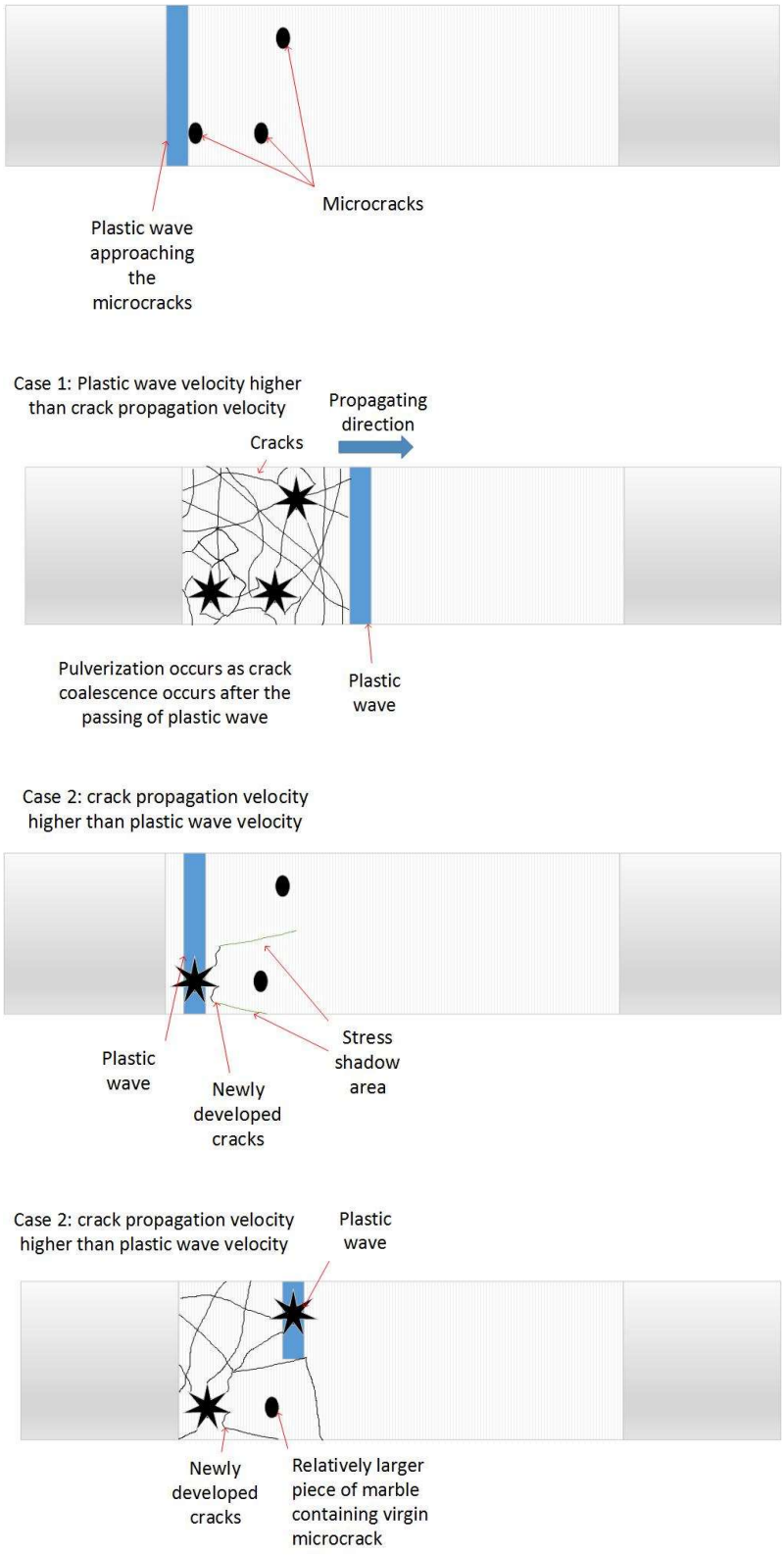

Fig. 5.12 Diagram showing the occurrence of stress shadowing

As Fig. 5.12 shows, as the rock specimen is loaded, two cases may happen. For the first case, the plastic wave velocity is higher than the crack propagation velocity. The plastic wave can travel further along the specimen and cause microcracks within the specimen to be activated. This causes the coalescence of cracks and a smaller overall fragment size.

For the second case, where the crack propagation velocity is higher than the plastic wave velocity, stress shadowing takes place. As the plastic wave travels through the specimen and activates microcracks closer to the loaded end, the activated microcracks start to extend outwards. This creates 'dead zones' behind the activated microcracks. Microcracks within these dead zones are shielded from the plastic wave that arrives later and will not experience the loading necessary for them to be activated.

5.3. Bukit Timah Granite

5.3.1. Dynamic compressive strength of granite with respect to testing pressure

Fig. 5.13 shows the relationship between the peak stress and strain rates for tests conducted under 4 temperatures: room temperature, 250 °C, 500 °C and 750 °C. The strength of the specimens in Fig. 5.13 are taken from the peak stress that the specimen experiences in the test, regardless of whether the specimen fails or not.

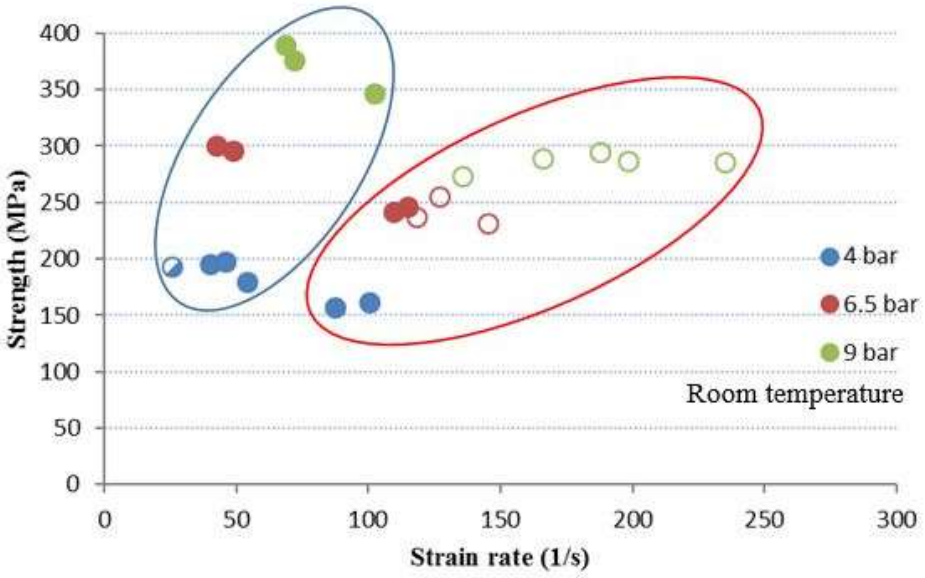

(a)

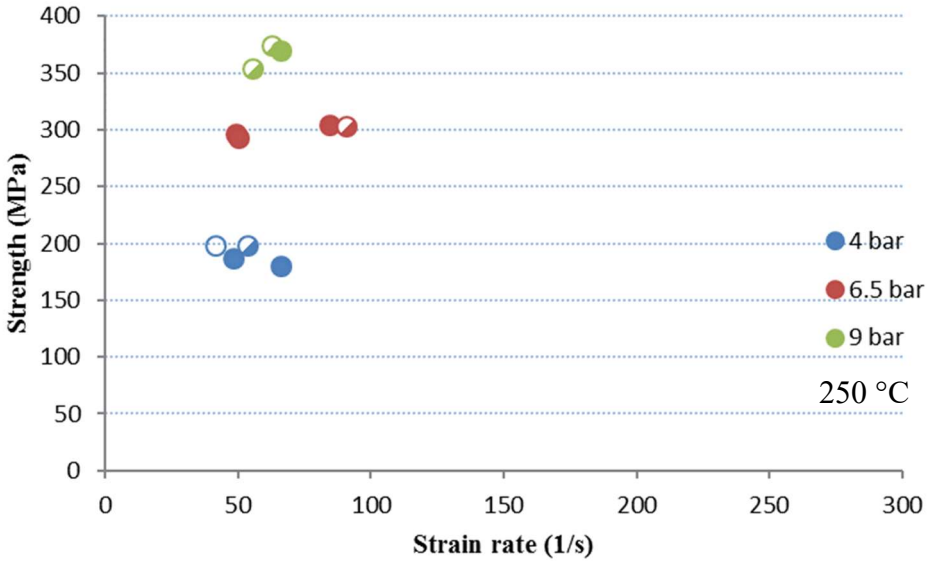
400
350
300
250
200
150
100
50
0
0
50
100
150
200
250
300
Strength (MPa)
Strain rate (1/s)
4 bar
6.5 bar
9 bar
250 °C

(b)

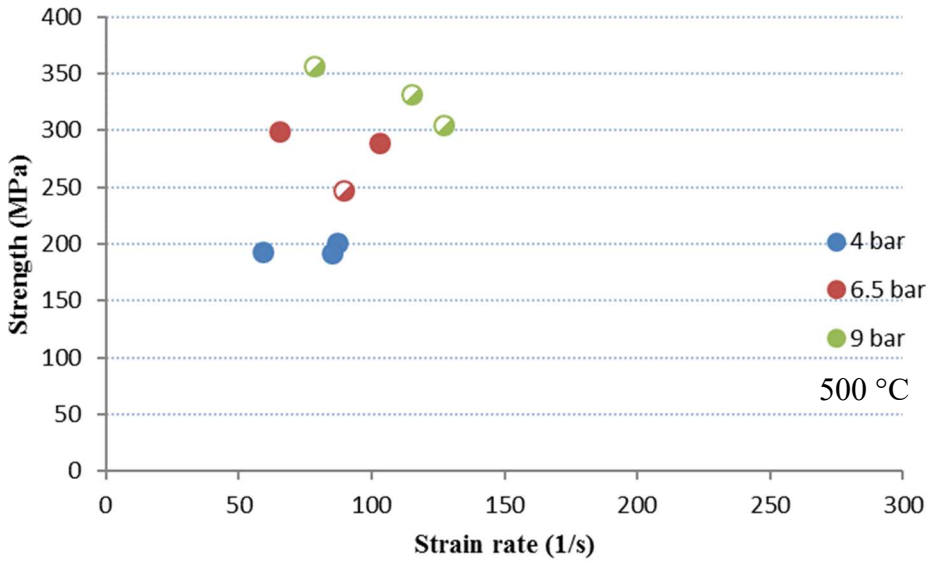
400
350
300
250
200
150
100
50
0
0
50
100
150
200
250
300
Strength (MPa)
Strain rate (1/s)
4 bar
6.5 bar
9 bar
500 °C

(c)

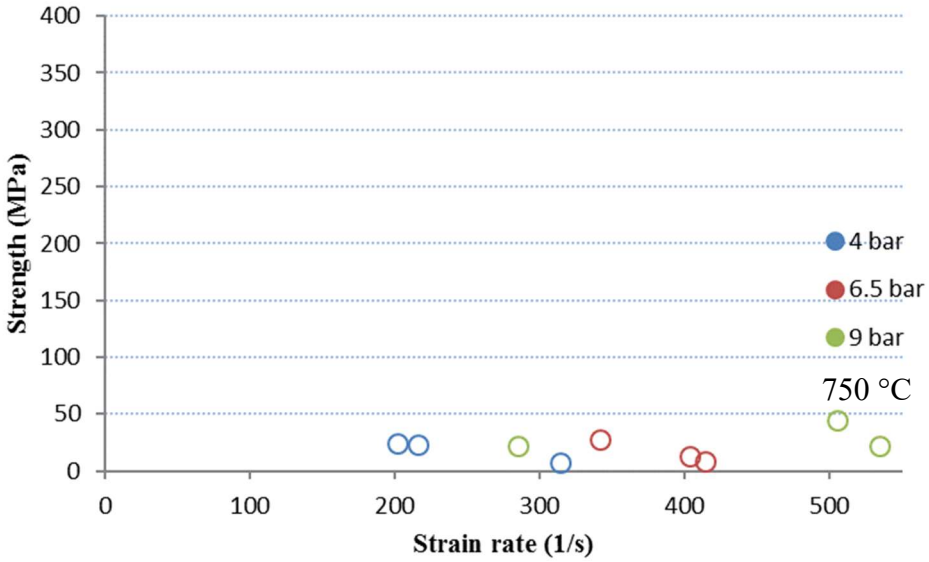

(d)

Fig. 5.13 Relationship between peak stress and heating temperature of granite for (a) room temperature, (b) 250 °C, (c) 500 °C and (d) 750 °C. Specimen failure types are represented by different symbols - filled symbols indicate specimens that remain more or less intact, half-filled symbols indicate axial splitting, and empty symbols indicate pulverization. (Scale changed for (d))

It can be seen that, below the heating temperature of 750 °C, the effects of heating on Bukit Timah Granite is limited. Only a minor strain rate increase and minor strength drop with increasing temperature were observed. However, the specimens heated at 750 °C showed a drastic increase in strain rate as well as a major drop in strength. During the test, when the customized oven was opened, it is possible to see cracks formed on the surface of the specimens (Fig. 5.14). This is likely due to the α/β phase transition of quartz, which occurs at 573 °C.

Fig. 5.14 Example of visible cracks forming on granite specimen at high temperatures.

The general increase in strain rate and drop in compressive strength of the specimens can be explained by the faces of the additional thermally-induced microcracks sliding past each other, which causes plastic deformation, and a reduction in strength. In contrast, intact rock requires additional energy to generate microcracks before sliding of adjacent crack surfaces can occur. Specimens at higher temperature will have more microcracks, which leads to increased plastic deformation, and lower strength.

Even though the number of additional thermally-induced microcracks would differ for specimens in Fig. 5.13a, 5.13b and 5.13c, the effects of such microcracks are limited. This can be explained through the presence of grain interlock along the microcracks. The microcracks formed during the heating process are not completely planar. Hence, there is significant shear resistance caused by the two faces of the microcracks sliding against each other. This is especially true in the dynamic compression test, in which the compressive forces applied to the specimen would help close up the microcracks and increase the compressive-shear strength of the specimens.

Another factor which may contribute to the small degree of strength drop and strain rate increase is that the specimens were tested in a heated state. Even though the specimens would contain thermally induced microcracks from heating, but because the specimens were tested while remaining in a heated state, thermal expansion of the specimen would have caused the microcracks to remain closed or have a small

microcrack width even after a microcrack has formed. This results in the two faces of the microcracks that better match with each other (Barton, 2007).

From Fig. 5.13a, we can see two distinct trends within the data. The first group (enclosed by blue ellipse) has a lower strain rate increase and higher strength increase with respect to gas pressure. The second group (enclosed by red ellipse) has a higher strain rate increase and lower strength increase with respect to gas pressure.

The specimens tested at room temperatures fail in two distinct failure modes: axial splitting and pulverization. The distinguishing characteristic between the two failure modes is the extent of fragmentation of the residual fragments of the specimen post test. The appearance of two different failure modes under the same testing conditions indicates that the failure modes is likely to be influenced by the specimen.

Wang et al. (2016) found that the orientation of a flaw bisecting a dynamic compression specimen affected both the strain rate and the strength of the artificial gypsum-sand specimen, giving rise to two distinct trends, similar to the results seen in Fig. 5.13a. The lack of such a trend in Figs. 5.13b, 5.13c and 5.13d is probably due to the initiation of randomly orientated thermal induced microcracks, which reduced the impact of any pre-existing microcracks that may have a specific orientation.

5.3.2. Dynamic compressive strength of granite with respect to heating temperature

Fig. 5.15 shows the same set of data as presented in section 5.3.1, but plotted in terms of testing pressure to further elucidate the relationship between heating temperature, testing pressure and the mechanical properties of the specimens.

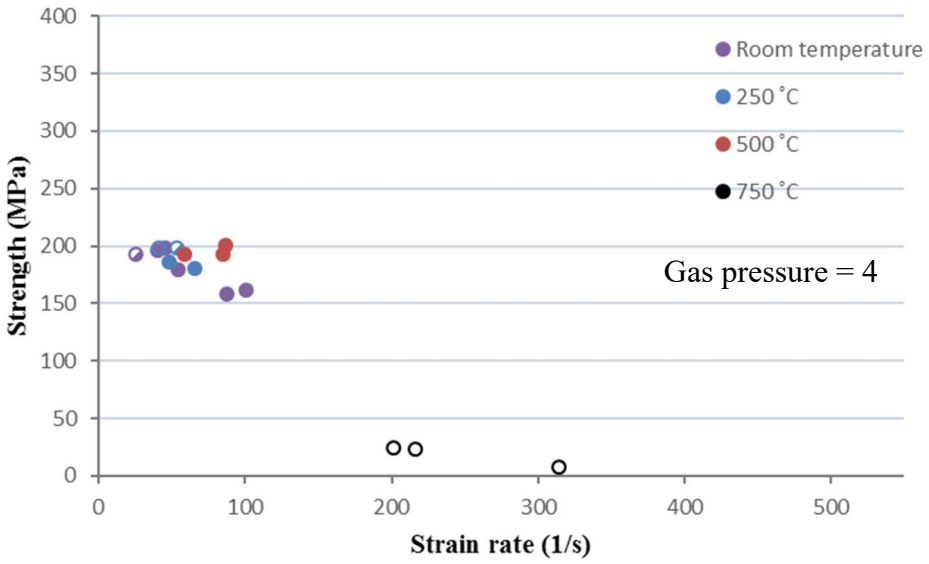
Strength (MPa)
Strain rate (1/s)
Room temperature
250 ˚C
500 ˚C
750 ˚C
Gas pressure = 4

(a)

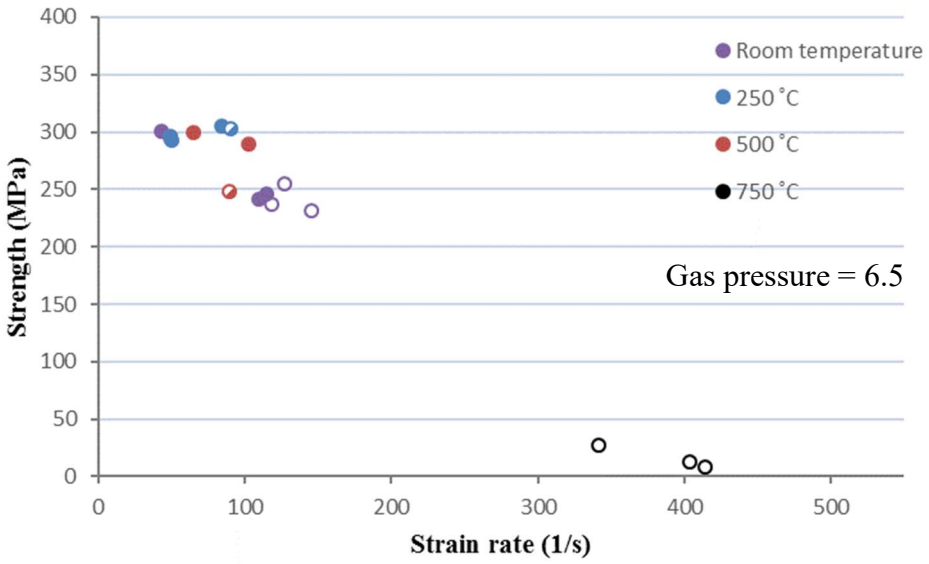
Strength (MPa)
Strain rate (1/s)
Room temperature
250 ˚C
500 ˚C
750 ˚C
Gas pressure = 6.5

(b)

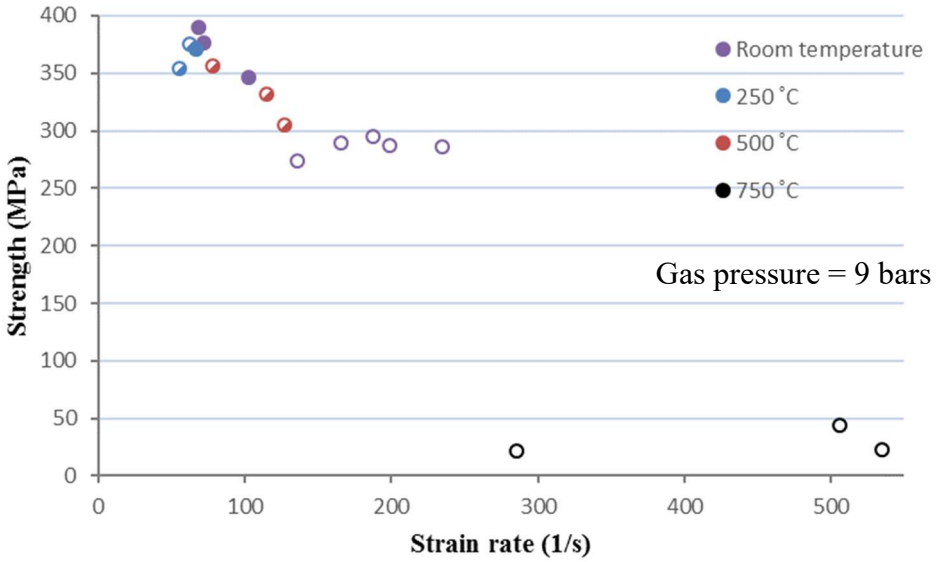

(c)

Fig. 5.15 Relationship between peak stress and gas gun pressure of granite for (a) 4 bars, (b) 6.5 bars and (c) 9 bars. Specimen failure types are represented by different symbols - filled symbols indicate specimens that remain more or less intact, half-filled symbols indicate axial splitting, and empty symbols indicate pulverization.

We can see from Fig. 5.15 that temperatures of up to 500 °C do not significantly affect the dynamic compressive strength of the granite being tested, as the data points for specimens tested between room temperature to 500 °C are clustered together. With an increase in gas pressure, we generally see an increase in strain rate, as well as strength, with the exception of specimens heated at 750 °C, which showed an extremely high strain rate and negligible strength as compared to the other specimens.

Although Figs. 5.15b and 5.15c show that the specimens tested at room temperature have a lower mean strength then the heated specimen, we can see that the unheated specimens form two distinct groups. The first group has higher strength, with a lower strain rate. The second group has lower strength with a higher strain rate. This is explained in section 5.3.1 as being due to randomly orientated microcracks. As the specimens are heated, the impact that any pre-existing microcracks may have are reduced, and only one failure mode dominates. This reduces data scattering.

The failure mode of the specimen is seen to depend on both the heating temperature as well as the testing pressure. As Figs. 5.13 and 5.15 show, for specimens tested at 750 °C, pulverization occurred for specimens tested at all gas pressure. This is probably due to the α/β phase transition of quartz at 573 °C, causing its significantly larger magnitude of expansion as compared to the rest of the constituent minerals, and hence producing more microcracks in these specimen.

From Fig. 5.15, we can see that as the testing pressure increases, the number of specimens that failed also increases. However, the higher temperature specimens were more likely to fail as compared to specimens that were heated at a lower temperature. An example of this is Fig. 5.15c, where all specimens that were heated at 500 °C experienced axial splitting, while only two specimens heated at 250 °C experienced axial splitting.

5.3.3. Dynamic compressive strength of granite with respect to maximum strain

Fig. 5.16 shows no noticeable trend between the maximum strain experienced by the specimen and the failure mode. The strength of the specimens heated at all temperatures was comparable except for specimens heated at 750 °C. This suggests that even though microcracks were generated, various factors limited the strength loss that such microcracks were supposed to cause.

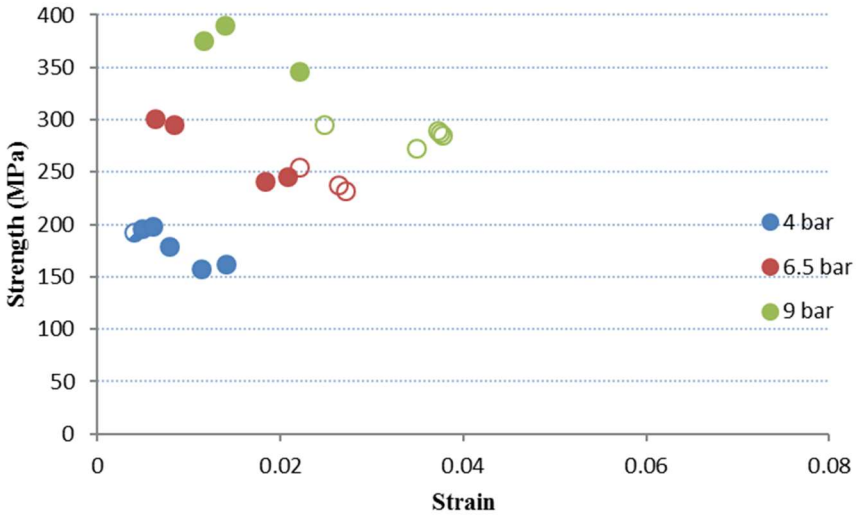

(a)

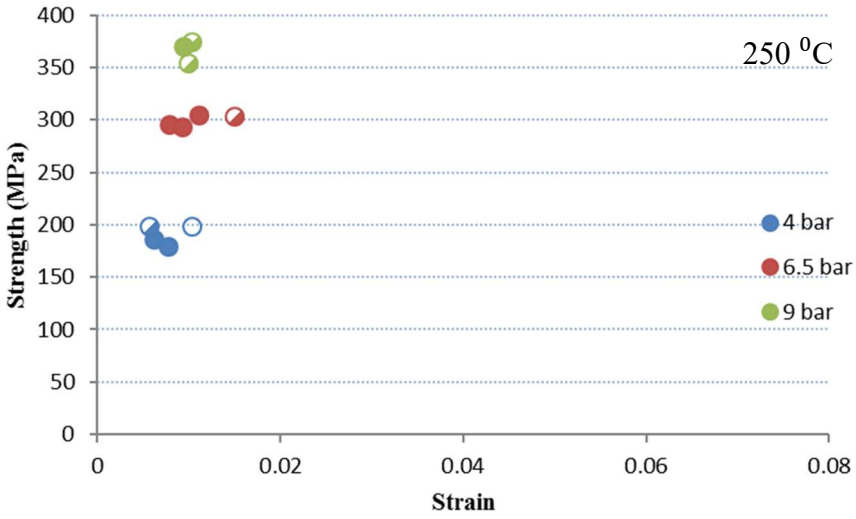
250 ^{0}C
Strength (MPa)
Strain
4 bar
6.5 bar
9 bar
0
50
100
150
200
250
300
350
400
0
0.02
0.04
0.06
0.08

(b)

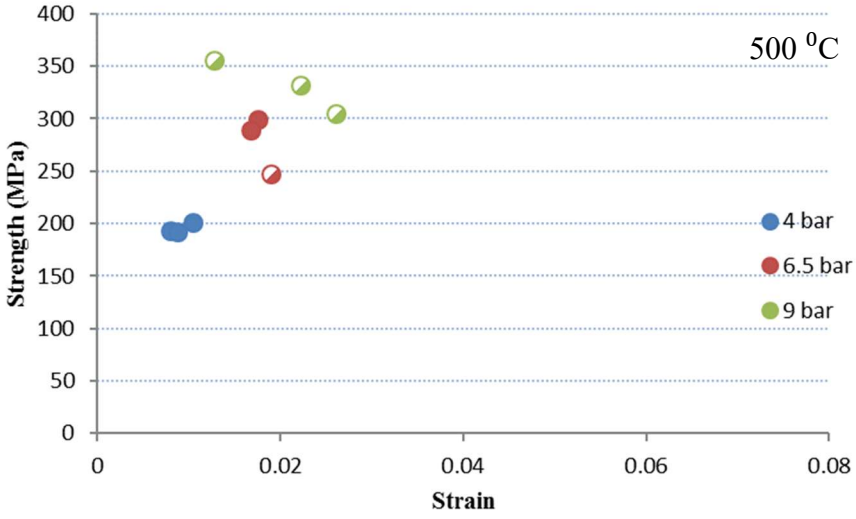
500 ^{0}C
Strength (MPa)
Strain
4 bar
6.5 bar
9 bar
0
50
100
150
200
250
300
350
400
0
0.02
0.04
0.06
0.08

(c)

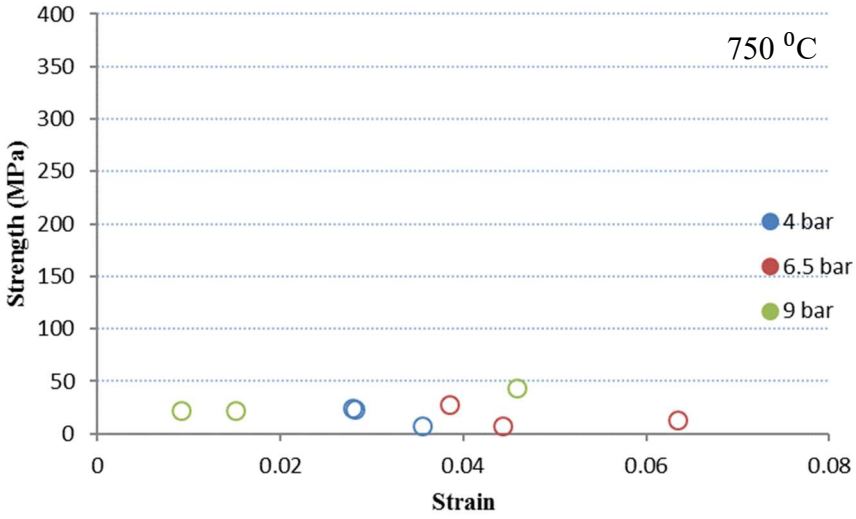

(d)

Fig. 5.16 Influence of gas pressure and temperature on strain for granite specimens tested at (a) room temperature, (b) 250 °C, (c) 500 °C and (d) 750 °C

One such factor is the friction between the microcrack faces. Irwin's (1957) refinement of Griffith's (1921) work focuses on the stress field near the microcrack tip. The stress intensity factor formulas that were developed assume no frictional effect between the microcrack faces, and that the stress intensity factor depends on crack and specimen geometry. The ISRM suggested methods for determining mode I and mode II fracture toughness involve creating open flaws into specimens (Backers and Stephansson, 2012; Kuruppu et al., 2014). The difference between open flaws and closed flaws is that the walls of the closed flaws are touching each other, which generates frictional shear resistance upon loading. Studies involving closed flaws have shown that friction does play a part in limiting strength loss from microcrack generation (Bieniawski, 1967; Hoek, 1965; Park and Bobet, 2009, 2010; Shen et al., 1995). It is likely that the applied stress to the specimen needs to overcome such frictional shear resistance before crack propagation is possible. With the expansion of the constituent minerals providing a tighter fit (higher normal stress) onto the microcrack faces, the effect of friction between the microcrack faces is more pronounced. It thus severely limits the effects of microcrack generation on the strength loss of the specimen.

5.3.4. Energy absorption per unit volume for granite

Fig. 5.17 shows the energy absorbed by the specimen during the dynamic impact test. A comparison of Fig. 5.17a with 5.17b showed almost no change of energy absorbed for specimens heated at 750 °C and tested at all pressures. This could be due to a loss of integrity of the specimen following the heating process.

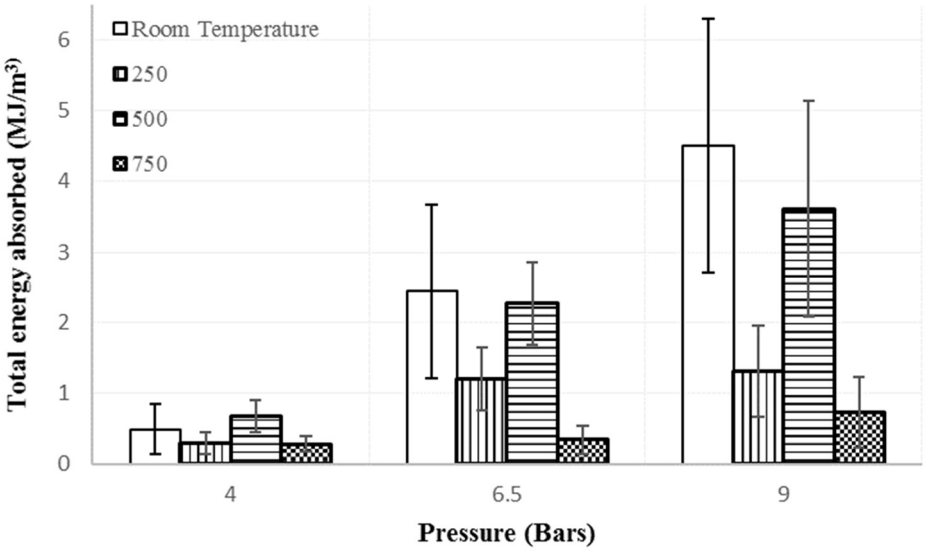

(a)

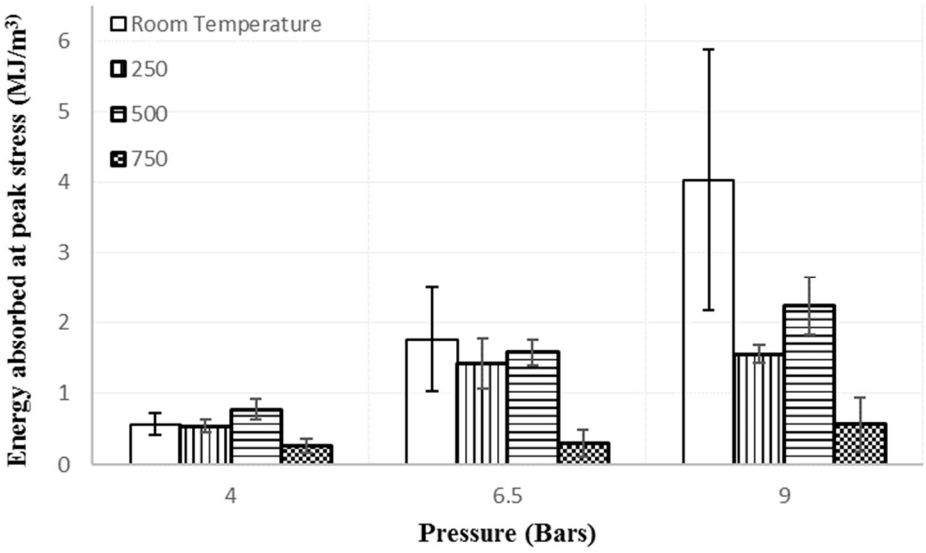

(b)

Fig. 5.17 Graph of (a) average total energy absorption, (b) average energy absorption for granite specimens at peak stress, each error bar represents ±1 standard deviation.

Fig 5.17b shows that similar amounts of energy are consumed by specimens to reach peak stress except for specimens that are unheated and those heated at 750 °C. An increase of energy used with testing pressure is seen with the exception of specimens heated at 750 °C. The energy absorbed at peak stress for specimens heated at 750 °C shows almost no increase with respect to gas pressure. This is probably due to the specimen having disintegrated during the heating phase. The energy used by the 750 °C specimens is just to overcome the residual strength left in the specimens.

The specimens tested at 250 °C shows a lower level of energy absorbed at peak stress and lower total energy absorbed. In such specimens, the peak stress experienced by the specimens tested were similar to other specimens (Fig 5.16), but undergone a smaller maximum strain. This is likely due to the temperature not being high enough to generate a large amount of microcracks, while the slight expansion of minerals allowed the microcracks to close up and the faces of the microcracks to be in tighter contact with each other. This reduced the deformation of the specimens and hence reducing the total energy absorbed and energy absorbed at peak stress.

Good contact between the microcrack faces would help increase the efficiency of energy transmission through the specimen, similar to how grease applied to the SHPB specimen helps increase the efficiency of energy transmission. Fig 5.17b shows that the energy absorption for unheated specimens is very high compared to the other specimens. This is because the unheated specimens have greater microcrack widths compared to the heated specimens, which allows energy to be dissipated through overcoming frictional resistance. Although the amount of microcracks for the unheated specimens is lower than the heated specimens, the displacement of the microcrack faces dissipates a lot of energy due to the high friction attributed to the rough microcrack faces.

The small difference in energy absorbed by the unheated specimens in Fig 5.17a and 5.17b indicates that only a small proportion of energy was needed to propagate secondary microcracks in the specimens that exhibited pulverization. As a result, less

energy may be needed to propagate the primary microcrack and fail the specimen. It is likely that most of the energy absorbed by the unheated specimen shown in Fig 5.17b is expended in other processes such as overcoming frictional resistance of the microcracks rather than microcrack propagation.

More energy seems to have been absorbed by specimens tested at room temperature as compared with the heated specimens. The free energy requirement for the generation of new microcracks in heated specimens is already partially provided by the thermal energy as well as the internal strain of the specimen caused by thermal expansion mismatch of the constituent minerals. As Fig. 5.17 is calculated from the stress-strain curve of the dynamic compression test, the energy supplied by the heating and thermal expansion is not taken into account.

Unheated specimens contain inherent microcracks as a result of the release of in-situ stresses during the coring process, tectonic stresses, or natural variations in temperature due to the diurnal cycle. In dynamic compression tests, energy applied to the specimen during the impact is partially consumed in work done by closing the microcracks. Some evidence can be adduced from Fig. 5.16a, where the average strain of the unheated specimens is higher than that of the heated specimens in Fig. 5.16b and 5.16c. When the specimens were heated to 750 °C (Fig. 5.16d), the average strain during impact are higher as the specimens have already suffered a major loss of integrity and hence cannot provide much resistance to the impact loading.

Fig. 5.18 shows the particle size distribution of the tested specimens. The specimens were collected after the dynamic compressive test and dry sieved to show any possible connection between the particle size distribution and the energy absorbed by the specimens.

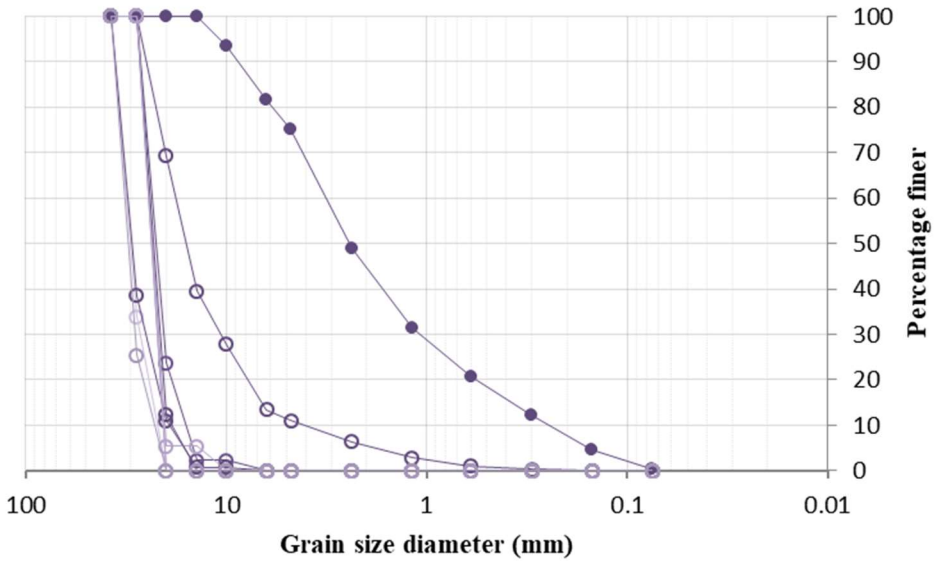
100
90
80
70
60
50
40
30
20
10
0
Percentage finer
100
10
1
0.1
0.01
Grain size diameter (mm)

(a)

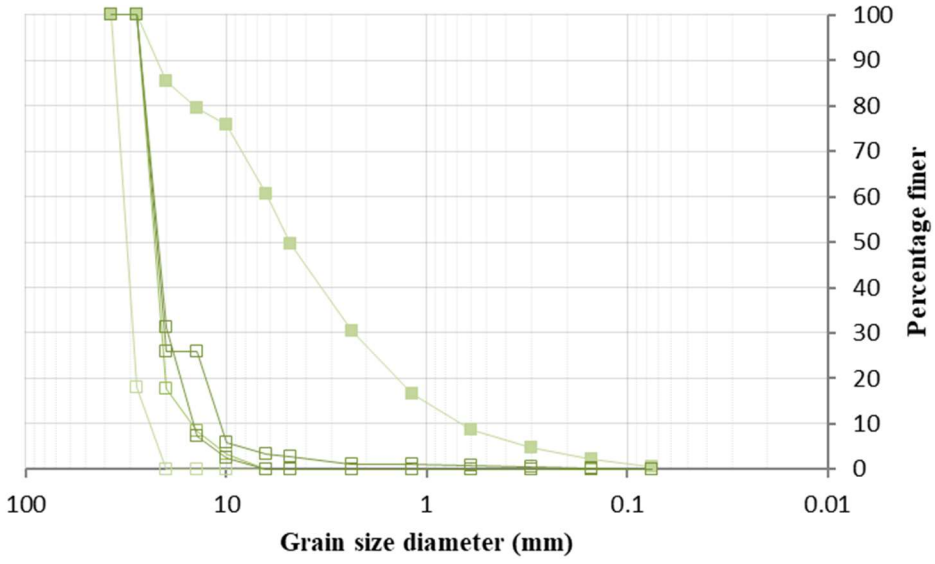
100
90
80
70
60
50
40
30
20
10
0
Percentage finer
100
10
1
0.1
0.01
Grain size diameter (mm)

(b)

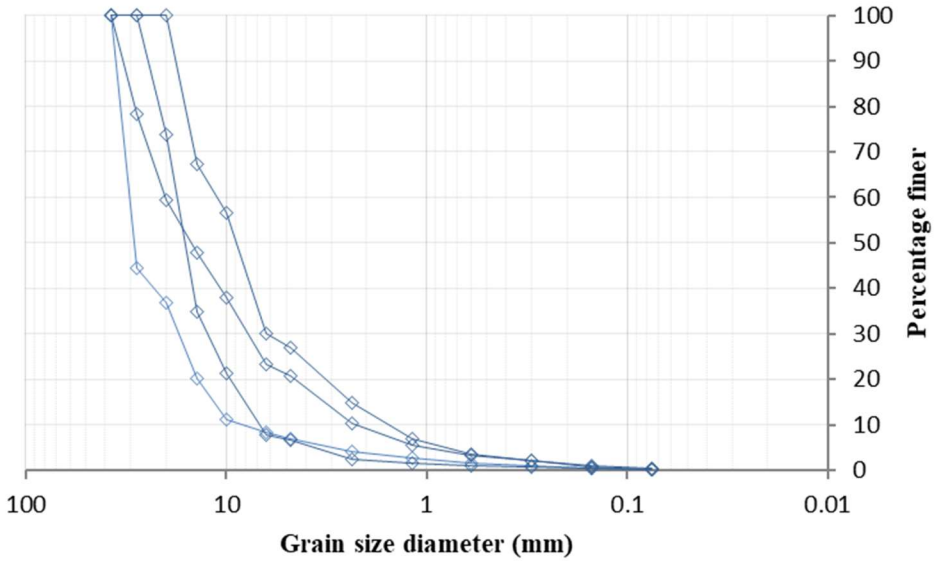

(c)

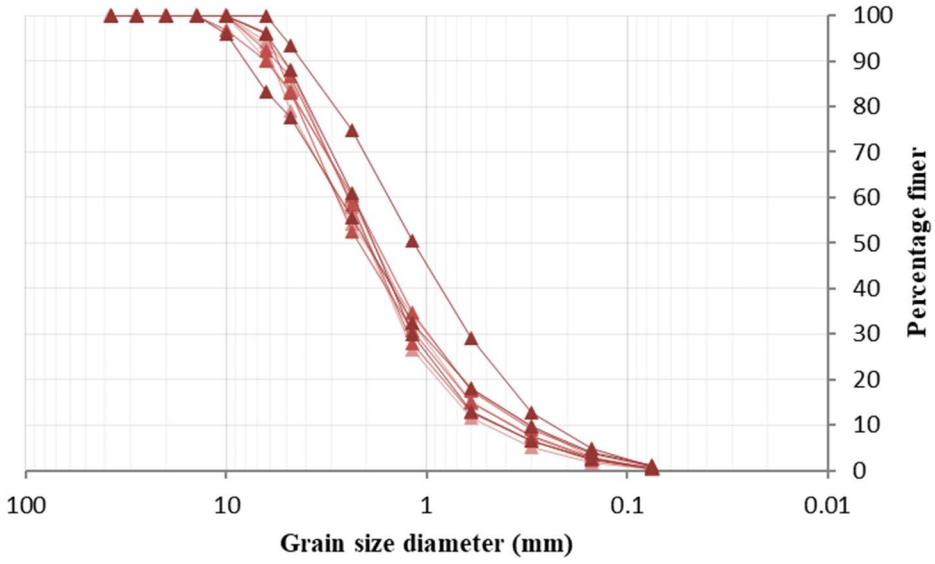

(d)

Fig. 5.18 Particle size distribution for granite specimens tested at (a) room temperature, (b) 250 °C, (c) 500 °C and (d) 750 °C, dark lines are for specimens tested at 9 bars, while light lines are for specimens tested at 6.5 bars. Open symbols indicate specimens that failed via axial splitting.

As Fig. 5.18 shows, specimens tested at higher gas pressures tend to show a smaller average particle size, except for Fig. 5.18d. Fig. 5.18d shows the particle size

distribution of specimens that were heated at 750 °C. The particle size distribution of specimens heated at 750 °C show a consistent particle size distribution regardless of the magnitude of applied gas pressure. This is possible if the heating already caused a large amount of microcracks to coalesce and the dynamic compression test simply provided enough energy to cause the specimen to fall apart. The consistent particle size distribution of Fig. 5.18d, consistent and low value of energy absorbed at peak stress and total energy absorbed of Fig. 5.17 supports this theory.

Figs. 5.18a and 5.18b show only minor difference between the particle size distribution between the specimens tested at 6.5 bars of pressure and exhibited axial splitting. This supports the theory that the difference in the energy absorbed is due to increased efficiency in energy transmission caused by tighter contact.

Fig. 5.18c shows that the average particle size of specimens tested at 500 °C is smaller than those shown in Figs. 5.18a and 5.18b. From Fig. 5.17, we can see that the energy required to fail the specimen is similar for the specimens heated at 250 °C and 500 °C, while the total energy absorbed for the specimen heated at 500 °C is significantly higher than for the specimen heated at 250 °C. This shows that the smaller average particle size is likely related to the increased total energy absorption due to more microcracks forming. The energy requirement is higher for specimens with more microcracks to propagate post-failure.

The sudden jump in the difference between energy absorbed at peak stress and total energy absorbed can be explained by how microcracks only start forming once a certain temperature threshold has been reached (Hasselman, 1969; Yong and Wang, 1980; Wang et al., 1989).

5.3.5. Comparison with quasi-static tests on granite specimens

The minor strength loss with respect to increasing heating temperature has also been observed on uniaxial compressive strength tests (UCS) conducted on Bukit Timah Granite using cylindrical specimens measuring 100 mm in length and 50 mm in diameter. Both the UCS test and the Brazilian tensile test were conducted with the MTS 815 rock testing system. The cylinders were heated to the target temperature in 30 minutes. The temperature was then maintained for another 30 minutes before

being left to cool before testing. This process is believed to promote thermal shock and to induce more microcracking so as to make the effects of heating more obvious. The UCS test was conducted using a loading rate of 1 kN/sec.

Fig. 5.19 shows the uniaxial compressive strength versus temperature. The tests conducted at 200 °C show very significant scatter. The scatter for specimens tested at 375 °C is smaller but still significant. The mean trend line of the UCS with temperature show only small decrease with temperature.

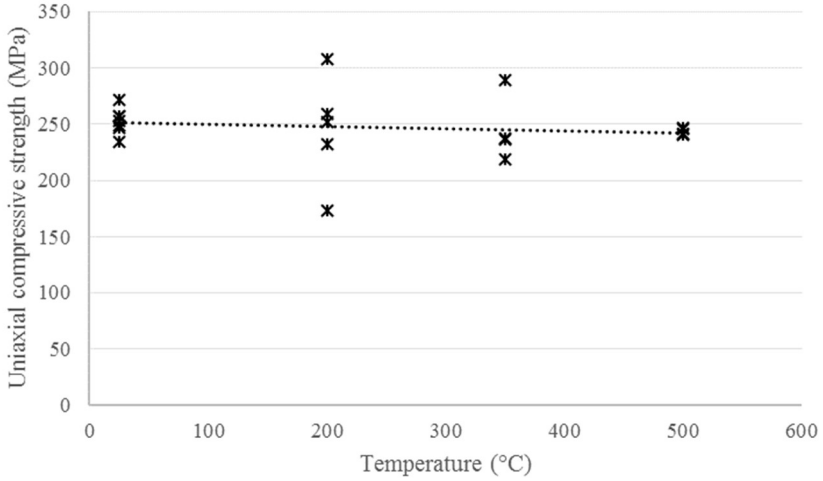

Fig. 5.19 Quasi-static uniaxial compressive strength of Bukit Timah Granite with respect to heating temperature.

Brazilian tensile strength data on Bukit Timah Granite heated to different temperature can be found in section 4.2.4 (Fig 4.5). Bukit Timah Granite Brazilian tensile test specimens of 50 mm diameter and 25 mm thickness were heated according to the same scheme and temperatures used for the UCS test. The specimens were then tested with the same MTS 815 rock testing system as the UCS test.

In comparison to uniaxial compressive strength (Fig 5.19), the decrease in tensile strength due to temperature is much more pronounced. As the same heating procedure was applied to both sets of test specimens, it is reasonable to attribute the percentage differences in strength reduction to the nature of tests.

A possible explanation for the difference in strength reduction is that the microcracks induced within the uniaxial compressive test specimens still have shear resistance

along the microcrack faces. Although the tests were conducted after the specimens were cooled, the compression during the test would gradually, either completely or partially, close the microcracks and increase the shear strength of the microcracks (Persson et al., 1993).

Another contributing factor that may explain the small strength degradation shown in both dynamic and quasi-static is due to the way the microcracks were formed. Thermally induced microcracks are mostly induced by tensile stresses generated within the rock specimen (Meredith and Atkinson, 1985; Homand-Etienne and Houpert, 1989; Jansen et al., 1993). Microcracks initiated by tension tend to have a rougher surface then those formed via shearing (Barton, 1973). The faces of the thermally induced microcracks can be expected to be rougher than microcracks formed via mechanical means, and hence, provide greater frictional resistance to shearing. The Brazilian tensile test induces tension within most parts of the specimen. The local tension would cause the faces of favorably orientated microcracks to move apart from each other; it would also cause other microcracks to experience a tensile component. Consequently, frictional resistance is reduced. This potentially explains the larger percentage decrease of tensile strength compared to that observed in the UCS of Bukit Timah Granite.

Using Barton and Choubey's (1977) semi-empirical shear strength criterion (eq. 7) as an analogy, we can see that the shear strength of a microcrack may be related to several factors, which include the roughness of the joint, or microcrack, and the normal stress applied.

$$\tau_p = \sigma_n \left[\tan\left(\varphi_b + JRC \cdot \log\left(\frac{JCS}{\sigma_n}\right)\right)\right] \quad (7)$$

where τ_p is the peak shear strength of the joint

σ_n is the normal stress

φ_b is the basic friction angle

JCS is the joint wall compressive strength

This potentially means that microcracks generated during a fire in an underground rock tunnel may have a higher than expected shear strength during a fire than when

the fire has been extinguished. The elevated temperature causes the differential expansion of various minerals in the rocks, hence increasing the normal stress applied to the microcracks (Yin et al., 2015). This can cause a further reduction in shear strength within a rock mass after it has cooled down. An even more drastic reduction in shear strength is possible considering that water is very likely used to extinguish the fire, and water is known to reduce the shear strength of rocks via a variety of mechanisms (Barton, 1973; Barton et al., 1974, Wong et al., 2016).

5.4. Differences with dynamic compressive tests conducted between Bukit Timah Granite and Carrara marble

As the CM and BTG specimens underwent the same treatment and testing process, any differences between the experimental results of the two can be attributed to the difference in test material.

Firstly, the granite specimens exhibited a non-linear strength drop when compared to the marble specimens tested. Fig. 5.13 shows very minor strength reduction for granite specimens tested up to 500 °C, while a drastic strength reduction was seen in granite specimens tested at 750 °C. This is probably due to the difference in mechanisms for the strength degradation. The thermal expansion of marble exhibits a strong anisotropy, as shown in Fig 5.20. Calcite grains have a difference in thermal expansion of almost 8 times along different crystallographic axis, and the expansion of calcite is relatively linear up to 600 °C. As Fig. 5.1 showed, the peak stress of heated marble specimens undergoing the dynamic compression test steadily decreases with respect to temperature. As the material used (CM) is extremely pure and consists mainly of calcite, a mismatch in thermal expansion coefficients between different constituent minerals is not a likely reason for the decrease in dynamic compressive strength. A more plausible explanation for the strength decrease of heated marble is the anisotropy of thermal expansion in different directions of calcite (Fredrich and Wong, 1986).

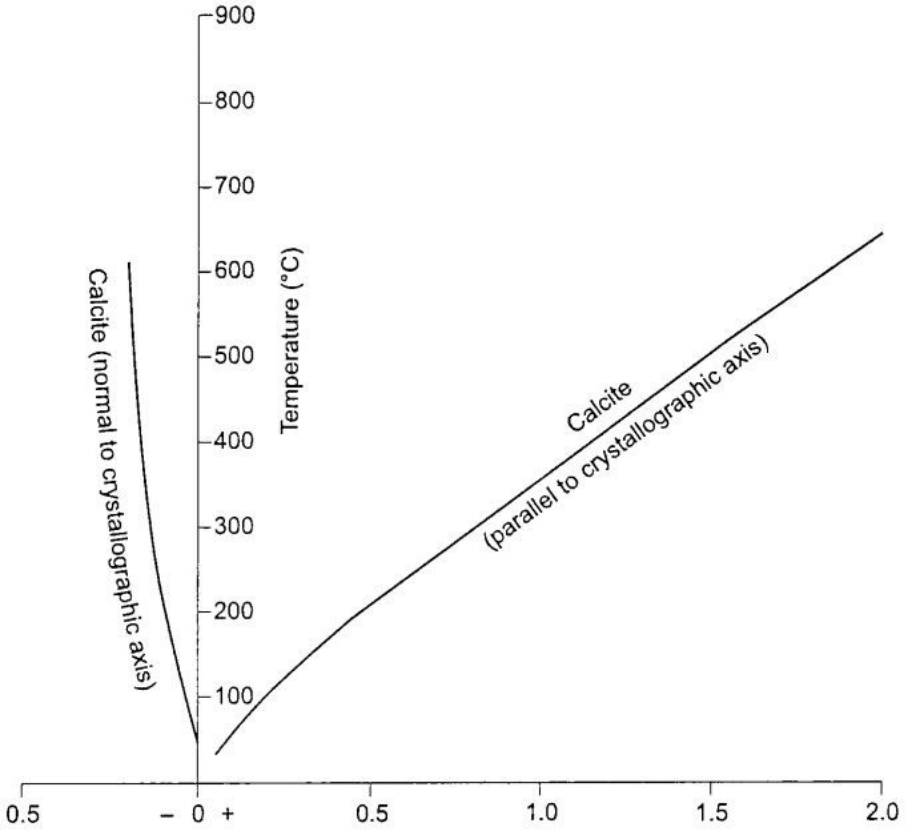

Fig. 5.20 Thermal expansion of marble, both parallel and perpendicular to crystallographic axis (after Goudie and Viles, 2000).

The strong anisotropy in thermal expansion of marble would also likely cause the microcrack apertures to widen as temperature increases, as noted by microscopic observations of heated marble by Yavuz et al. (2010) and Goudie and Viles (2000). This could explain the decrease in stress wave propagation velocity, which is a factor in stress shadowing, as well as the decrease in dynamic compressive strength.

As microcrack apertures widen, the faces of the microcracks that were thermally induced would likely move further apart. With lesser contact between the microcrack faces, the stress wave propagation efficiency across microcracks decreases. This potentially leads to a decrease in the stress wave propagation velocity. Another effect of wider microcrack apertures is that the shear resistance of the microcracks will decrease. Less energy is consumed by the frictional resistance caused by the faces of the microcracks sliding across each other, thus, more energy is available for microcracks to propagate.

As marble specimens are known to thermally decompose, specimens were heated to determine the effects of heating on the chemical decomposition of the marble specimens. The heating protocol used is the same one used in this chapter. Marble, chemically known as calcium carbonate, is susceptible to thermal decomposition starting at 550 °C. Since only the specimens heated at 700 °C showed a change in mass (Fig. 5.21), it is very likely that thermal decomposition does not play a key part in the strength degradation of specimens heated at 250 °C and 500 °C. As significant strength degradation was seen at 250 °C and 500 °C for marble specimens (Fig. 5.1), it is likely that the strength degradation at those temperatures is due to the anisotropy in thermal expansion of the calcite grains, rather than thermal decomposition. The strength degradation at 550 °C is likely to be caused by microcracking generated by a combination of thermal decomposition and anisotropic thermal expansion.

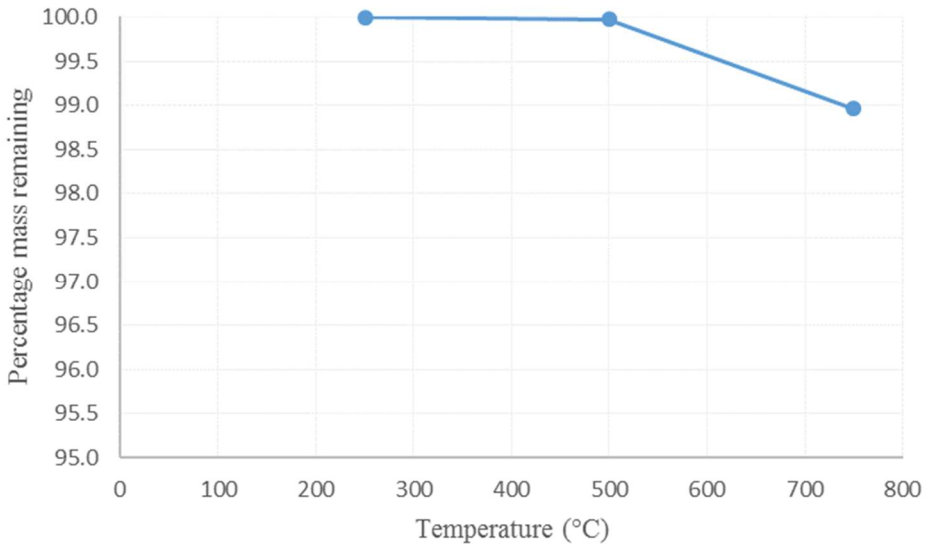

Fig. 5.21 Percentage remaining of marble after heating

In contrast, the mechanism behind the generation of microcracks in granite is mainly due to the mismatch in thermal expansion of the constituent minerals of granite (Wang et al., 1989; Yong and Wang, 1980; Richter and Simmons, 1974).

Due to the expansion of the calcite grains in Carrara marble, there is likely to be little shear resistance between the thermally generated microcracks in the rock as it is heated. Han et al. (2007) also noted that another factor contributing to low friction is that even in cases where significant friction occurs between marble faults, the

frictional sliding generates sufficient heat to thermally decompose the marble locally, leading to ultra-fine particles which subsequently lower the friction between the marble faults. This factor should be taken into account when marble is heated above 550 °C. Granite is mainly composed of quartz and feldspar, amongst which, quartz has a larger thermal coefficient of expansion that is about 3.5 times that of feldspar (Jeong et al., 1993; Table 7.2). As such, most of the internal stress within thermally treated granite can be attributed to the expansion of quartz. The thermal expansion anisotropy of quartz is not as severe as that of feldspar (Amatuni and Shevchenko, 1966), and it is likely that the microcracks that form in granite are not as wide as those in marble.

Second, the overall strength of marble is lower than that of granite. According to the Barton shear strength criteria (eq. 7), shear strength is correlated to the joint wall compressive strength. With a weaker material, it is easier for asperities to be worn down through shearing. This could be another reason accounting for the difference in the dynamic compressive strength between granite and marble despite the same heating and testing conditions.

Lastly, for specimens tested at 750 °C, the mechanisms for the strength degradation is also different between marble and granite. Granite shows an almost complete strength loss primarily due to the α/β phase transition of quartz, which caused an abrupt, large expansion, while the rest of the constituent minerals of granite did not show any such behavior. For marble, the strength degradation is attributed to the strong anisotropy of thermal expansion, as well as the partial thermal decomposition that marble will experience at temperatures above 550 °C (Lide, 2005). Also, ultra-fine particles may be produced at this stage, which leads to reduced friction, as stated earlier.

In section 5.2.8, the occurrence of stress shadowing in marble specimens at high temperatures upon subjected to the dynamic compression tests was deduced by the recovery of large, friable marble fragments after the tests. A sieve analysis was conducted, which revealed that the average residual particle size of marble specimens showing stress shadowing were larger.

However, stress shadowing was not observed in Bukit Timah Granite as the average particle size of the specimens tested was found to be inversely proportional to the gas pressure used to charge the SHPB setup. Cases whereby specimens tested at a higher pressure left fragments of larger sizes did not occur. This may possibly be due to the more heterogeneous nature or the higher microcrack shear resistance of Bukit Timah Granite. As the occurrence of stress shadowing is determined by the crack propagation velocity and the stress wave propagation velocity, the test material used have an effect on these two variables. Being heterogeneous in nature, cracks may not propagate as easily through Bukit Timah Granite, as propagating cracks may be slowed down or hindered by minerals with a higher strength in their path.

The higher microcrack shear resistance of Bukit Timah Granite may cause a lower crack propagating velocity as more energy will be consumed to overcome the frictional resistance between the faces of the microcracks. Since the crack propagation velocity of a brittle medium is affected by the initial critical stress intensity factor (Ravi-Chandar and Knauss, 1984), lesser energy to propagate existing cracks would cause a decrease in the crack propagation velocity. A medium of higher strength will require a higher stress to reach its critical stress intensity factor, while the increased frictional resistance means a higher energy threshold for the cracks to propagate, as propagation can only occur when the faces of the microcracks move past each other.

Figs. 5.9 and 5.10 observed a discrepancy in the time that the transmitted stress wave was detected in the output bar of the SHPB setup, which showed that the stress wave propagation time through Carrara marble sandwiched between the steel bars is affected by heating. However, as shown in Fig. 5.22, no significant variations in the detection time of the transmitted wave in the output bar in the present tests on Bukit Timah Granite.

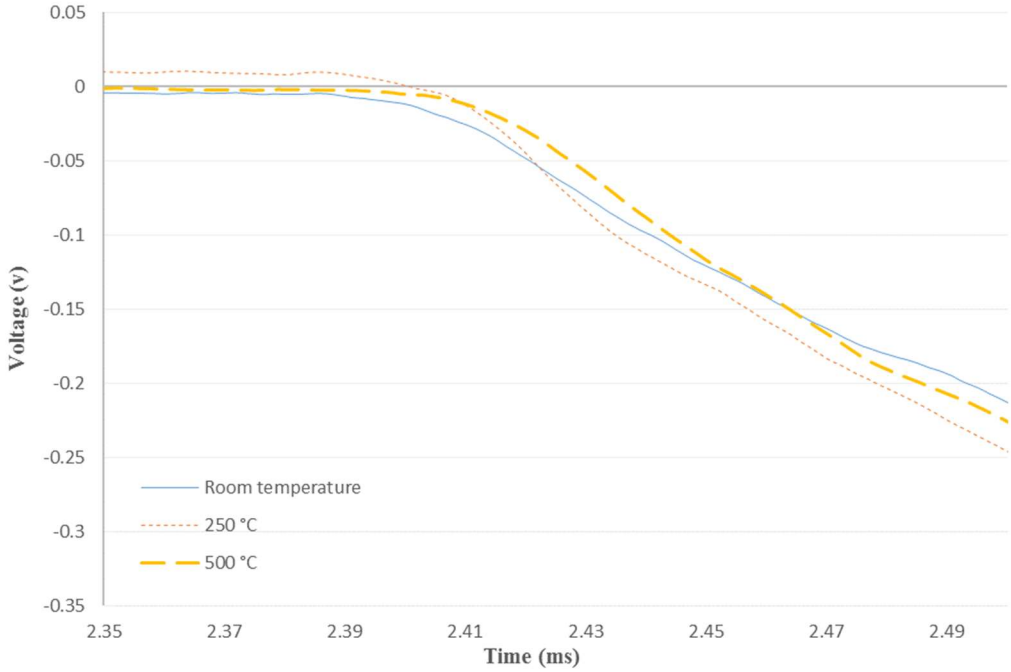

Fig. 5.22 Timing of stress waves detected in output bar for granite specimens

It implies that the stress wave propagation velocity was not adversely affected by the heating. This could possibly be due to the expansion of the constituent minerals within Bukit Timah Granite, which tightened the contact between the faces of the microcracks for a more efficient transmission of stress wave. Although microcracks with a higher friction coefficient, such as those created by tension, are known to cause stress wave attenuation, this is assuming that the wave energy is mainly dissipated through the movement of the microcrack faces relative to each other. In a situation where the minerals around the microcrack undergo expansion, the rough surface of the microcracks are pressed tighter against each other and experiences greater interlock. This increases the amount of energy required for the microcrack faces to slip along each other. Stress waves which do not meet this energy threshold is likely to be transmitted across the microcrack with lesser attenuation instead.

5.5. Conclusions

In this chapter, the uniaxial dynamic compressive strength of CM and BTG specimens were tested using a SHPB setup. The specimens were first heated up in a customized oven to various temperatures. The specimen was held at the target

temperature and impact loading using the SHPB was carried out. Tests were carried out for different temperatures and different gas charging pressures in the SHPB setup. The dynamic stress-strain curves of the specimens were analyzed to obtain the stress versus strain rate relationship. The energy absorption characteristics of the specimens were calculated and correlated with the particle size distribution of the collected fragments.

5.5.1. Dynamic compressive strength and failure mode

The dynamic strength of the marble specimen was found to decrease with heating temperature. This is probably due to the increase in microcrack density and length within the marble specimen caused by heating. For the granite specimens, dynamic compressive strength degradation is minimal up to 500 °C, beyond which, the α/β phase transition of quartz significantly degraded the rock integrity.

There is a very minor decrease in the dynamic compressive strength of Bukit Timah Granite with respect to heating temperature. The same phenomenon was also observed in quasi-static uniaxial compression tests on cylindrical granite specimens but was absent in quasi-static Brazilian tensile tests on BTG. As a similar density of thermally generated microcracks should have developed in both tensile and compression test specimens following heating with the same procedure, it is likely that the difference in behaviour is due to the nature of the tests and the generated microcracks. The thermally generated microcracks in Bukit Timah Granite are likely to be tensile cracks (Meredith and Atkinson, 1985; Homand-Etienne and Houpert, 1989; Jansen et al., 1993) generated by a mismatch in thermal expansion between the constituent minerals (Wang et al., 1989; Yong and Wang, 1980; Richter and Simmons, 1974). As such, the faces of the microcracks would tend to be rougher (Barton, 1973) than compression-induced shear microcracks generated by mechanical loading. The dynamic compression test would then reveal only a minor loss in strength as a large proportion of the energy imparted by the SHPB striker bar is resisted by frictional forces along the microcracks.

Specimens tested at 750 °C showed an almost complete loss of integrity during the heating process, as shown by the extremely low amount of energy absorbed by the specimen leading to failure (Fig. 5.17). While preparing the SHPB setup, long cracks

were noted in the specimens heated at 750 °C even before the tests were performed (Fig. 5.14). This is likely due to the abrupt, large expansion of the quartz grains within Bukit Timah Granite as a result of the α/β phase transition that occurred at 573 °C.

The strain rate effect was observed for the tests performed on both types of specimens, however, the point at which the strain rate effect no longer applies is influenced by the heating temperature. At lower temperatures, two distinct strain rate effects can be observed for both axial splitting and pulverization failure modes and both failure modes are common. At higher temperatures, failure via pulverization dominates and axial splitting was rarely seen.

5.5.2. Particle size distribution and stress shadowing

The particle size distribution curves of the collected marble fragments revealed that specimens that failed via axial splitting have a larger proportion of fragments of size larger than 0.4 mm than those that failed via pulverization. The fragment size distribution for all failure modes tends towards a larger proportion of smaller fragments with increases in loading force and heating temperature as observed in the post failure fragments shown in Fig. 5.23. In some cases, the fragments of specimens tested at higher temperatures and higher gas pressures, have been found to show a higher proportion of larger fragment sizes. This can possibly be explained by the stress shadowing phenomenon.

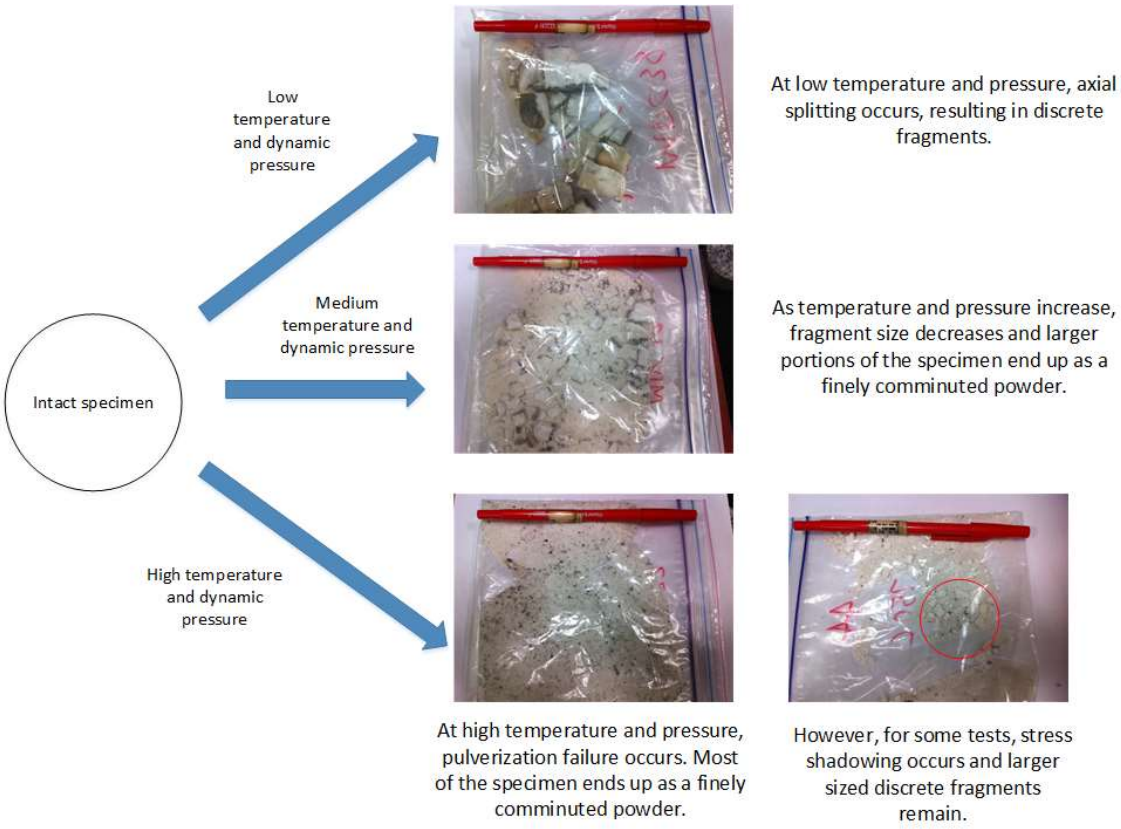

Fig. 5.23 Marble fragment size with respect to temperature and pressure

As shown in Figs. 5.9 and 5.11, the plastic wave propagation velocity decreases, while the crack propagation velocity increases slightly with an increase in heating temperature. The crack propagation velocity is also proportional to the loading force and hence, gas charging pressure, as shown in Fig. 5.10.

This increase in crack propagation velocity and decrease in plastic wave propagation velocity produce an effect called stress shadowing, which becomes significant when cracks propagate within the specimen and forms zones that are shielded from the plastic stress wave travelling within the specimen. When this happens relatively larger fragments remain at the end of the loading test, and these fragments will be friable due to the high microcrack density. Since the total energy absorbed increases with a decrease in the average collected fragment size, it may be that lesser energy will be absorbed by the specimens in cases where stress shadowing is present. This implies that for an explosive impact within an underground structure at high temperatures, an explosion that is higher in force, yet shorter in duration, may cause more damage to the underground structure. For a short duration, high force explosion,

stress shadowing may occur, leading to lesser energy being used to comminute the rock material, and more energy being used to generate microcracks further within the rock itself.

In contrast to the same tests performed on Carrara marble specimens, obvious signs of stress shadowing were not observed in Bukit Timah Granite. This is likely due to a smaller stress intensity at the crack tips of microcracks associated with increased frictional forces within microcracks found in the granite specimens, as compared to microcracks in marble. This could potentially affect the crack propagation velocity within granite. Also, due to the expansion of the constituent minerals of granite, the faces of the microcracks are likely to be pressed tightly together. This could present an environment where the stress wave is transmitted more efficiently in granite than in marble even after heating (Fig. 5.22). The decreased crack propagation velocity and increased stress wave propagation velocity could reduce the likelihood of stress shadowing.

5.5.3. Implications

At lower temperatures, the amount of strain that the marble specimen undergoes is limited and Linear Elastic Fracture Mechanics is generally applicable to explain the behavior of the marble specimen. However, at higher temperatures, the amount of thermally induced microcracks is high enough that significant plastic deformation takes place during the experiment, which can be accounted for by Elastic-Plastic Fracture Mechanics.

For an example of a real world application, we can take a traffic accident happening inside a rock tunnel. As the accident happens, a fire is started and heats up the rock tunnel. As the fire rages on, the fuel tanks of the vehicles involved are heated up to the flashpoint of the petrol within, and an explosion happens. The shockwave from the explosion, as well as the shrapnel from the explosion would impart a dynamic loading to nearby heated rock. As our results have shown, although an increase in the heating temperature leads to a drop in the dynamic compressive strength of the rock specimens, the fragment size of the rock specimens tested is reduced, while the energy absorbed by the specimens is increased. This is similar to the ‘crumple zone’ in modern automobiles, where the front and the back of the car are specially

engineered to crumple upon impact and absorb energy so as to protect the occupants of the car. The current school of thought is that the damage sustained by the tunnel is proportionate to the magnitude of the loading, however, phenomenon such as stress shadowing also has an effect on the magnitude of damage suffered by the rock tunnel. The fragment size distribution and the calculated energy absorbed by the specimen reveals that the area affected by the loading and the magnitude of damage within the affected zone is not always directly related.

The integrity of Bukit Timah Granite is unlikely to be severely compromised at temperatures below 573 °C, especially with the minimization of local tensile stress concentration with proper tunnel or cavern design. Microcracks generated from the heating would be mostly tensile cracks, which are rougher than compression-induced shear microcracks. Such microcracks would have a higher peak shear strength, and the stress applied would have to overcome the shear resistance of the microcrack before crack initiation can take place. Loading in cases of fires would likely be explosions caused by temperatures increasing past the flashpoint of flammable materials and debris from such explosions, which was simulated by the dynamic compression tests. The test results indicate that, in such an event, Bukit Timah Granite would likely be able to resist the loading due to its high resistance to strength degradation. The mechanism behind the minimal strength degradation during a fire is likely to be frictional forces within the microcracks, which is enhanced by the tighter contact between the microcrack faces caused by expansion of the constituent minerals of the rock.

At temperatures higher than 573 °C, it is likely that Bukit Timah Granite would disintegrate, even without external loading. During a fire, the rock mass surrounding the fire would most likely be above 750 °C, which is the highest temperature tested in this thesis. The rock mass nearest to the fire will likely disintegrate during the fire due to being heated above 573 °C and will not be able to resist loading of any kind.

In real world applications, granite cavern or tunnel sections that collapse during a fire would have likely been exposed to temperatures above 573 °C and will need extensive repair works that may not be economically feasible, while sections that do not show obvious signs of damage after a fire is put out would not suffer as much

damage and may be repaired in a safe and economic manner. As long as the section in question does not show obvious signs of spalling and other damage, it may be possible that the thermal microcracking induced may not have a detrimental effect on the integrity of the section, provided that the shape of the tunnel/cavern section was not altered significantly and the surrounding rock mass is still under compression.

More attention needs to be paid to the tunnel/cavern after the fire has been put out, as the lower temperature may cause the aperture of microcracks to widen, reducing the compressive strength of the rock by a reduction of the frictional forces within the microcracks. Water that was used to put out the fire will also contribute to the reduction in frictional resistance of the microcracks. The present findings indicate that sections of the granite tunnel/cavern that do not collapse during the fire may be salvaged or reinforced with little loss of strength. Expanding rock bolts would be ideal in such an operation, as it mimics the effects of the expanding constituent minerals. The expanding rock bolts would tighten the contact between the microcrack faces and increase shear resistance.

Chapter 6 Microscopic observation of heated granite

6.1. Introduction

The current understanding of the weakening mechanisms of rocks upon exposure to high temperatures attributes it mainly to chemical changes within the rock and the generation of microcracks. An understanding of how microcrack generation evolves due to exposure to high temperatures would help in formulating guidelines governing fire safety regulations in underground structure construction.

This chapter explores the microcrack length and orientation of specimens exposed to different heating temperatures. The microcrack length distribution with respect to temperature was plotted to reveal connections between the individual microcrack length and the heating temperature. The overall cumulative microcrack density was also plotted as a line chart and as a rose diagram to discern any pattern in the microcrack orientation.

A better understanding on possible mechanisms behind the strength degradation of rocks when exposed to high temperatures can help us predict the severity of the strength degradation of different types of rocks, and fill in existing gaps about the factors influencing strength degradation when exposed to high temperatures.

6.2. Bi-exponential curve fitting

The microcrack data obtained using the process mentioned in section 3.6 were further processed for ease of analysis. The pre-processed microcrack length, count and orientation data were found to conform to a bi-exponential curve as expressed in the following equation:

$$y = ae^{\alpha\bar{x}} + be^{\beta\bar{x}} \tag{6.1}$$

Where y = microcrack count

$\bar{x}$ = normalized microcrack length, $\frac{x}{D}$

x = microcrack length in μm

D = average grain size (taken as 2000 μm in this thesis)

The numerical values of the constants a, b, α and β were determined by using the Microsoft Excel solver function to minimize the error, E, between the experimental microcrack count and the value obtained from equation 6.1 (Fig. 6.1). The values of the constants a, b, α and β are given in Table 6.1.

$$E = (y_C - y)^2 \tag{6.2}$$

where y_c = experimental microcrack count

y = microcrack count from equation 6.1

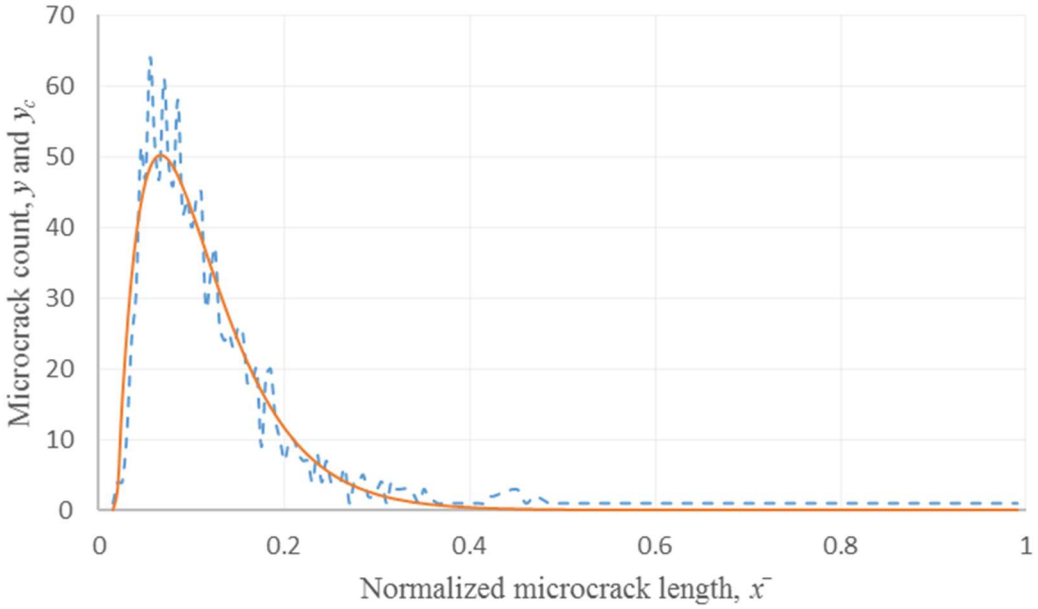

Fig. 6.1 Comparison of experimental microcrack length data (dashed line) and the bi-exponential curve (solid line), data taken from U200, mechanically unloaded specimen heated at 200 °C

Table 6.1. a, b, α, β values for bi-exponential curve obtained by curve fitting.

Specimen*	a	α	b	β
U025	2042.01	-26.54	-2207.50	-31.60
L025-N	5681.89	-31.50	-5994.36	-34.74
L025-F	4598.05	-23.04	-4731.28	-24.52
U200	1767.08	-19.88	-1847.95	-22.24
L200-N	1770.86	-21.42	-1856.95	-24.05
L200-F	1696.05	-18.33	-1806.84	-21.00
U350	2323.15	-25.60	-2748.80	-38.83
L350-N	2090.82	-24.21	-2291.39	-29.64
L350-F	2025.38	-23.34	-2192.91	-28.06
U500	331.63	-11.87	-461.33	-20.48
L500-N	754.29	-16.52	-905.57	-25.06
L500-F	1470.31	-18.77	-1755.87	-26.40

*Note: U = mechanically unloaded specimens, L = mechanically loaded specimens, numerals represent heating temperature, N represents rock segments adjacent to the fractured plane, F represents rock segments further from the fractured plane. Refer to Table 3.1 and Fig. 3.7 for nomenclature and schematic sketch.

The steps for obtaining the a, b, α and β values are as follows:

1. Plot the pre-processed data to show the microcrack count against the normalized microcrack length.
2. Enter suitable starting values for a, b, α and β to generate a bi-exponential curve using equation 6.1.
3. Sum up the error, E, for all data points using equation 6.2.
4. Use the Microsoft Excel solver function to generate the ideal values of a, b, α and β with the ending criteria of minimizing the sum of E.

6.3. Cumulative microcrack length

The following results were obtained from microphotographs taken in accordance with section 3.10. The results of the microcrack length with respect to orientation are shown as rose diagrams in Fig. 6. The loading direction and orientation of the failure plane is along the 0° to 180° plane (Fig. 3.7). For mechanically unloaded specimens (group 1, Table 3.1) which were not loaded, the segment selected for microcrack observation were chosen at random. The 0° to 180° plane was arbitrarily assigned. The individually recorded microcrack lengths were grouped into intervals of 5°, and the cumulative microcracks of the same orientation were summed up. The cumulative microcrack lengths were then normalized by dividing the observed cumulative crack lengths with the longest cumulative microcrack length present (U350, Table 3.1) to construct the rose diagrams (Fig. 6.2).

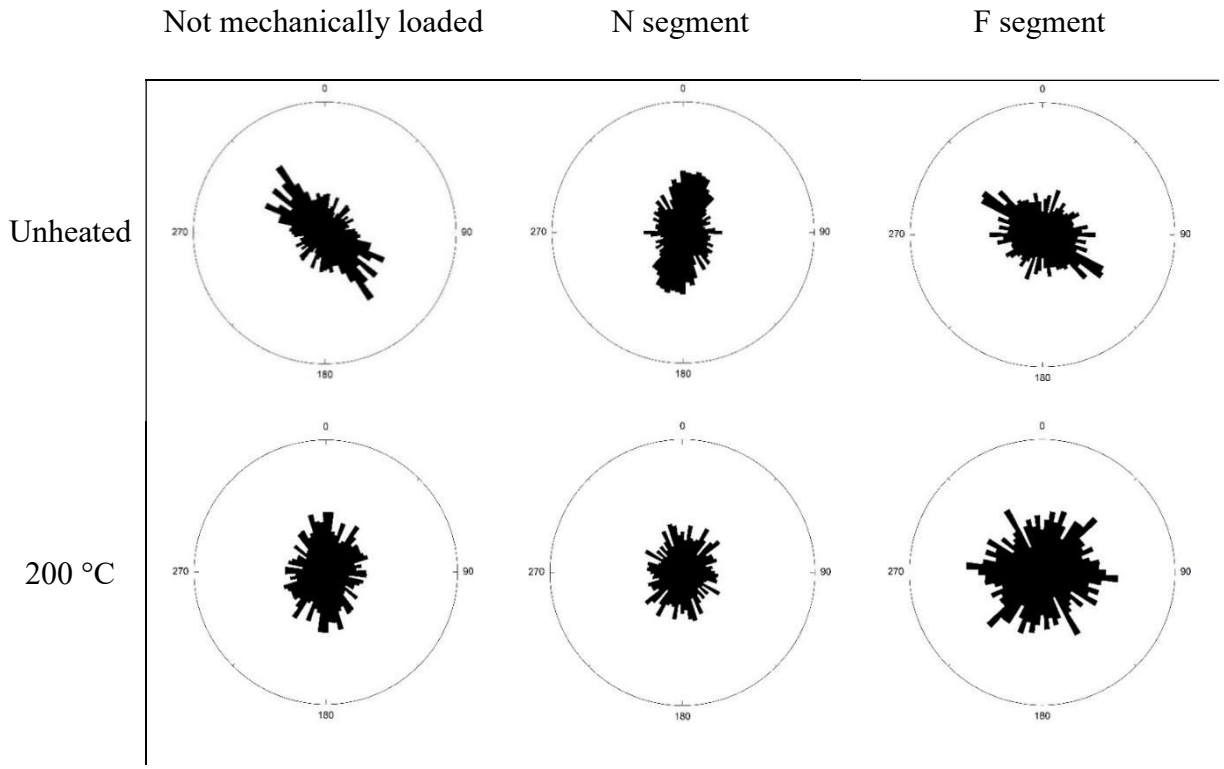

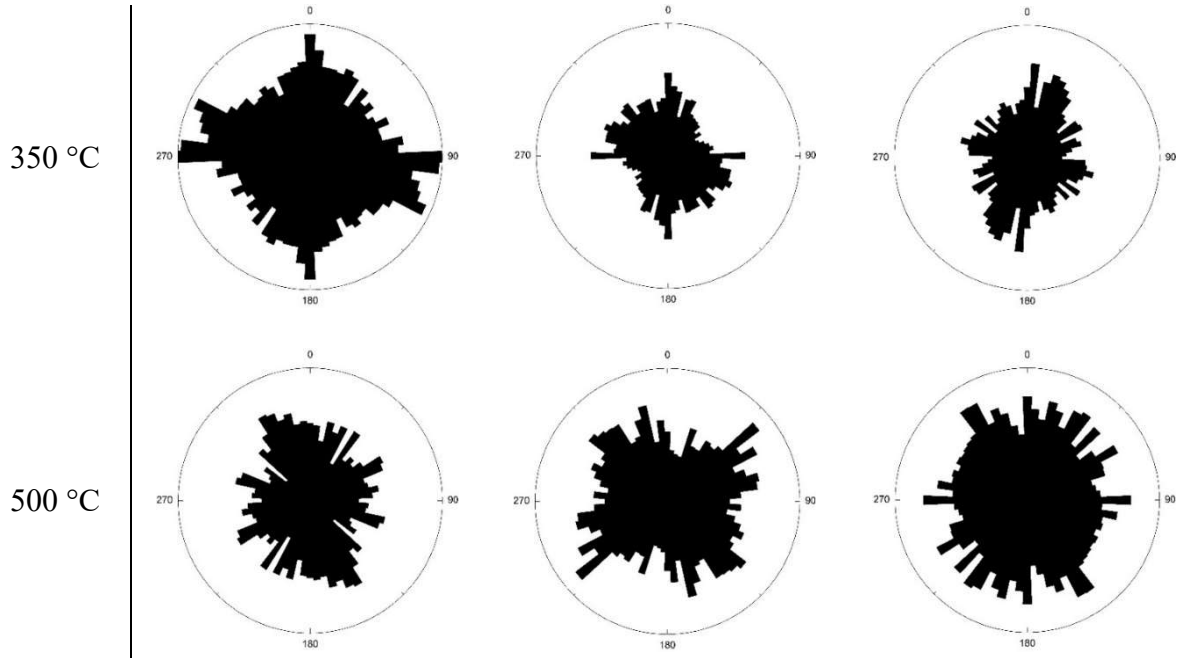

Fig. 6.2 Cumulative microcrack length with respect to orientation. Shaded area represents total normalized microcrack length in that particular direction. Each bar represents microcracks in a 5° angular sector.

The resolution of the microcrack using the fluorescent epoxy method is within the micrometer scale, which is similar to what Nishiyama and Kusuda (1994) achieved. The shortest recorded crack for this chapter is 10 μm.

Assuming no major deviation in microcrack widths, the crack density of a segment is proportionate to its cumulative microcrack length. A general trend of increasing crack density with respect to heating temperature can be observed as an increase in the shaded area of the rose diagrams as well as the plots of the cumulative microcrack length of the specimens (Figs. 6.2 and 6.3). The microcrack length was normalized as $\overline{x}$ against the average grain size of 2 mm of the test rock.

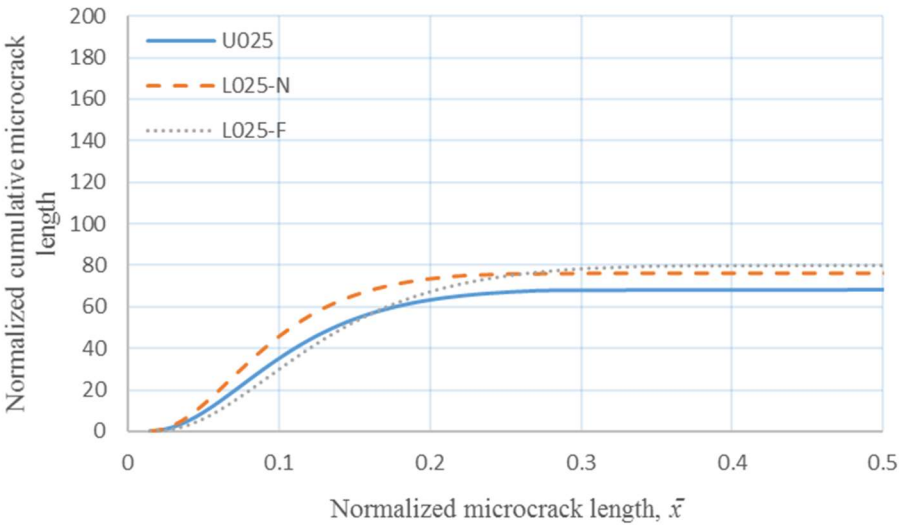
U025
L025-N
L025-F
Normalized cumulative microcrack length
Normalized microcrack length, $\bar{x}$
0
20
40
60
80
100
120
140
160
180
200
0
0.1
0.2
0.3
0.4
0.5

(a)

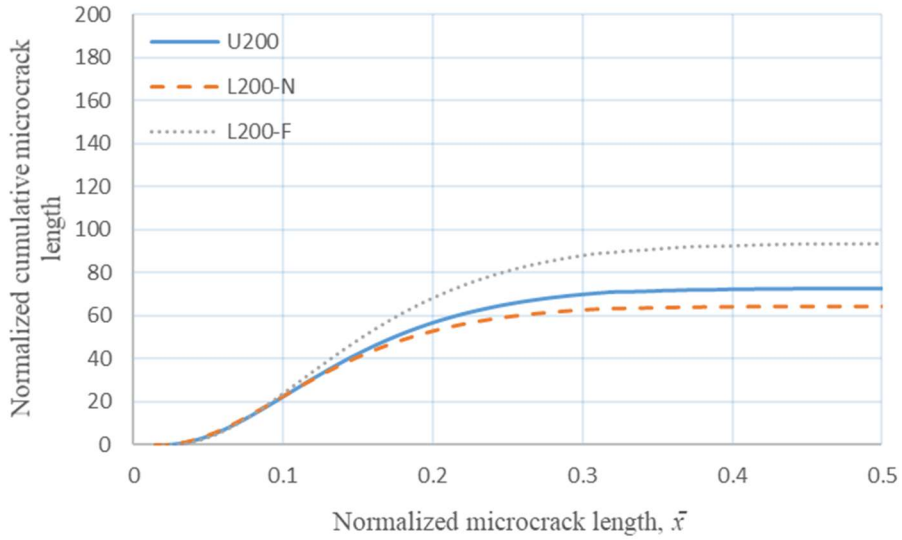
U200
L200-N
L200-F
Normalized cumulative microcrack length
Normalized microcrack length, $\bar{x}$
0
20
40
60
80
100
120
140
160
180
200
0
0.1
0.2
0.3
0.4
0.5

(b)

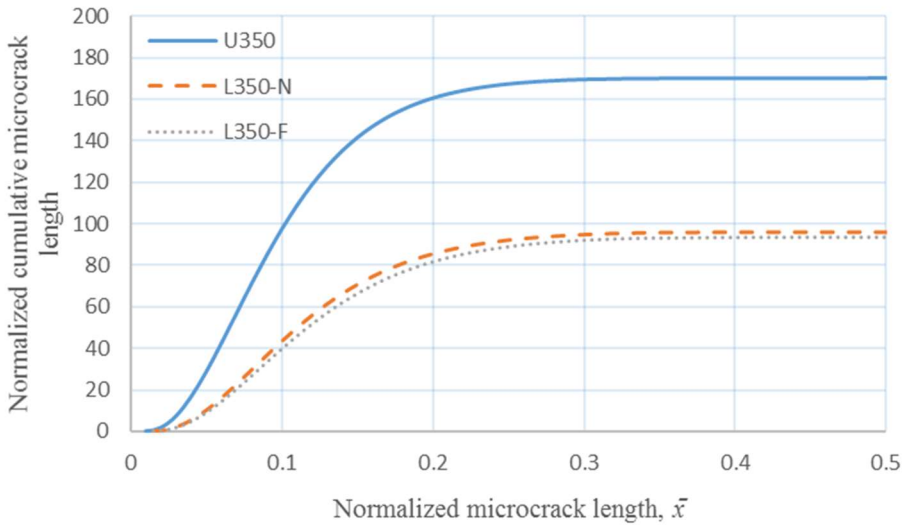

(c)

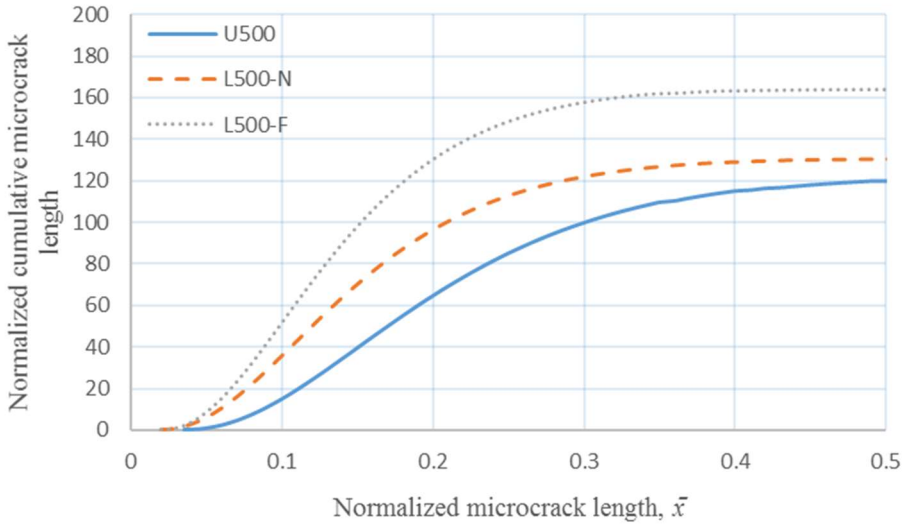

(d)

Fig. 6.3 Normalized cumulative microcrack length plotted against normalized microcrack length for specimens, irrespective of orientation, at (a) room temperature, (b) 200 °C, (c) 350 °C and (d) 500 °C.

A plausible explanation for the correlation between microcrack density and heating temperature is due to a mismatch in the coefficient of thermal expansion between the constituent minerals (Devore, 1969). These are around $6x10^{-6}$ °C^{-1} to $14x10^{-6}$ °C^{-1} for quartz (Kosinski et al., 1991) and around $2.5x10^{-6}$ °C^{-1} to $6.125x10^{-6}$ °C^{-1} for

plagioclase and orthoclase (Huotari and Kukkonen, 2004), which are the major constituent minerals of Bukit Timah Granite (BTG). As the specimens were heated, certain minerals would expand more than the others, leading to uneven localized tensile and compressive stresses throughout the specimen, which ultimately results in the formation of microcracks. The expansion and thus, the magnitude of the stress, is determined by the heating temperature.

For U025, the segment that was neither heated nor mechanically loaded, we can see that the microcracks are preferentially orientated along the 45° to 135° plane. This is probably due to microcracks generated as a result of the release of in-situ stresses during the coring process, tectonic stresses, or natural variations in temperature due to the diurnal cycle, as no noticeable mineralogical anisotropy is observed. L025-N showed a strong anisotropy in the microcracks observed. A large majority of the microcracks aligned along the 0° - 180° plane, which is also the major alignment orientation of the primary cracks as well. The microcracks of L025-F, however, showed an anisotropy along the 135° - 315° plane. Fig. 6.3a revealed that the cumulative microcrack length of the unheated segments (U025, L025-F and L025-N) were similar despite the difference in mechanical loading. It is possible that the tension experienced by the specimen causes microcracks that make up the primary cracks to propagate and coalesce before significant amounts of microcracks were formed elsewhere.

The specimens heated to 200 °C do not show such a strong preferential orientation (Fig. 6.2), probably due to the random orientation of the heat generated microcracks, which would mask the pre-existing microcracks that existed before heat treatment and those generated during the coring process. Fig. 6.3b shows that the cumulative microcrack lengths of the specimens were all similar, with L200-F possessing a slightly higher cumulative microcrack length.

When the specimens were not mechanically loaded, the segment heated to 350 °C (U350) appear to have a larger number of microcracks compared to the segments heated to 500 °C (U500, L500-F and L500-N) (Fig. 6.3). The cracks show a slight preferential orientation that correspond to the cleavage angles of alkali feldspar and plagioclase (Fig. 6.2). The grains of the tested specimens showed some variations in

the grain sizes, otherwise the grains were orientated randomly and showed no noticeable anisotropy. As most of the intragranular cracks within the individual plagioclase or feldspar grain follow a consistent pattern due to the presence of cleavage planes, a larger grain would contain slightly more microcracks aligned perpendicular to each other. It was observed that for the mechanically unloaded specimen heated at 350 °C (U350), a significantly larger proportion of quartz was present, as compared to other specimens. During the heating process, stresses induced by the thermal expansion mismatch between the various minerals caused local crushing of the alkali feldspar and plagioclase grains (Fig. 6.4). Intragranular microcracking that developed within the quartz grains were smaller in number but larger in width as implied by the difference in the brightness of the fluorescence.

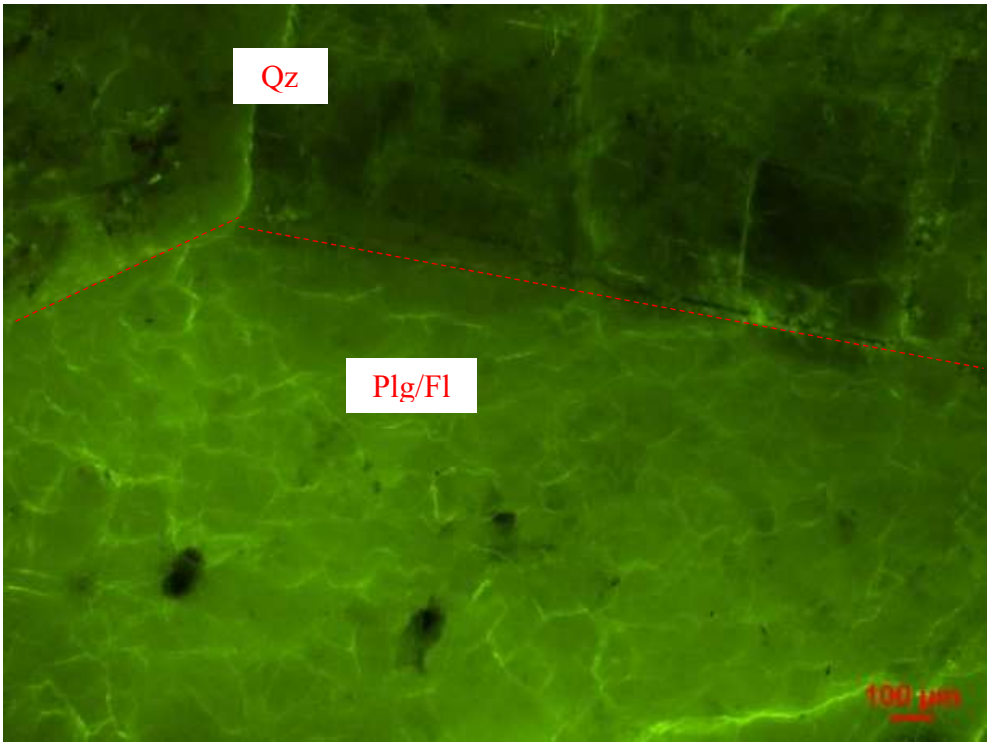

(a)

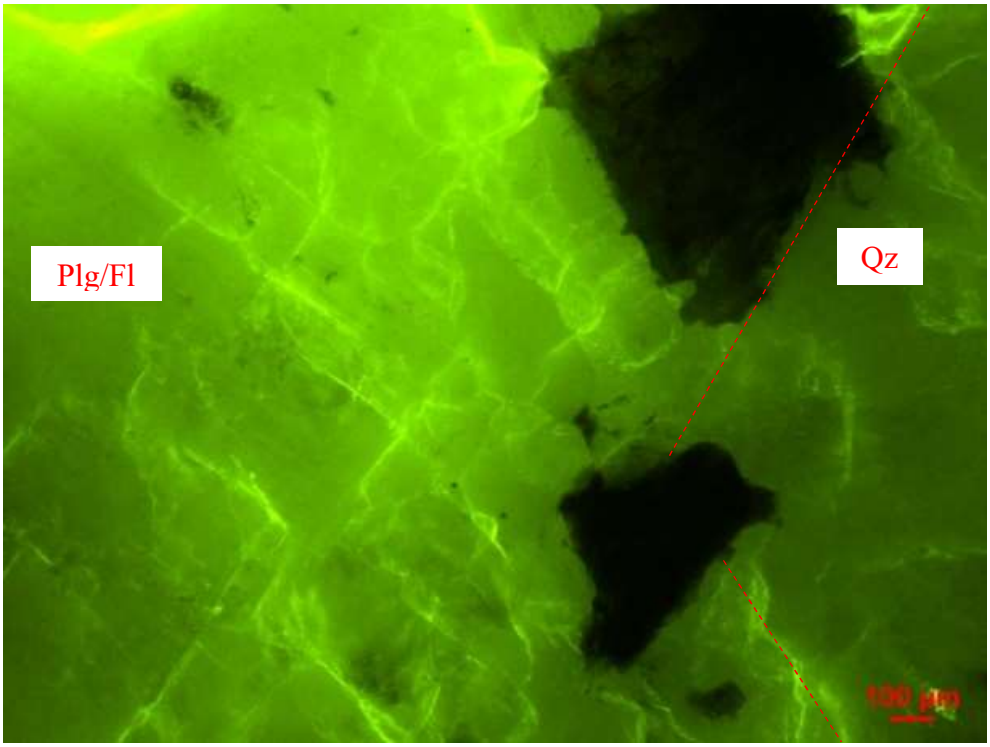

(b)

Fig. 6.4 Microscopic images (at 4X magnification) of specimens that exhibited (a) crushing, and (b) no crushing, both images taken from different specimens heated at 350 °C. Brightness level of the digital photos, which is not subjected to any post-treatment, indicates the extent of the microcracks. The brighter cracks indicate wider and deeper cracks. Dotted line denotes observed grain boundaries between quartz (Qz) and plagioclase or alkali feldspar (Plg/Fld).

Among all the specimens tested, the 500 °C segments (U500, L500-F and L500-N) have the longest cumulative crack length except for U350. Fig. 6.2 shows no discernable anisotropy in segments heated to 500 °C, regardless of mechanical loading. Fig. 6.3d shows a longer cumulative microcrack length for L500-F as compared to L500-N.

The above findings suggest that microcrack formation is strongly dependent on the mineralogical composition and proportion of those minerals within the rock in question, at least with regards to heat generated microcracks. As the quartz grains have a higher coefficient of thermal expansion (Bass, 1995), and a higher strength (Passchier & Trouw, 2005) as compared to alkali feldspar and plagioclase, in

specimens where there is a disproportional amount of quartz present, the expansion of the specimen and stresses experienced by other minerals will be higher than specimens that contain smaller quantities of quartz. Since the locations where microcracks are likely to be generated (alkali feldspar or plagioclase) are reduced, dissipation of strain energy would be concentrated in a smaller area. The density of generated microcracks within the reduced alkali feldspar or plagioclase areas will be correspondingly increased, to dissipate the larger amount of strain energy. This is supported by the presence of crushed alkali feldspar and plagioclase grains, which does not appear even in the 500 °C specimens.

Another trend observed is that the microcrack density for Type-N segments is generally lower than that of Type-F segments. An exception is seen for unheated specimens where the microcrack density of the N segment is slightly higher than the F segment. This observation is counter-intuitive as one would expect a larger number of microcracks being formed closer to the fracture process zone, as compared to regions further from the fracture process zone.

6.4 Microcrack length distribution

As the individual length of the microcracks has been carefully recorded, an analysis of the distribution of microcrack lengths was also conducted.

The abnormally high microcrack count in Fig. 6.5c for the unloaded specimen heated to 350 °C is probably due to the higher quartz content in that particular specimen, which caused a higher degree of crushing of the alkali feldspar and plagioclase grains (Fig. 6.4). Despite the unusually high microcrack count, the modal crack length does not change much. This supports the claim that the modal crack length is related to energy requirement for the formation and propagation of microcracks. The energy requirement for crack formation is a material property and is not significantly dependent on the loading magnitude.

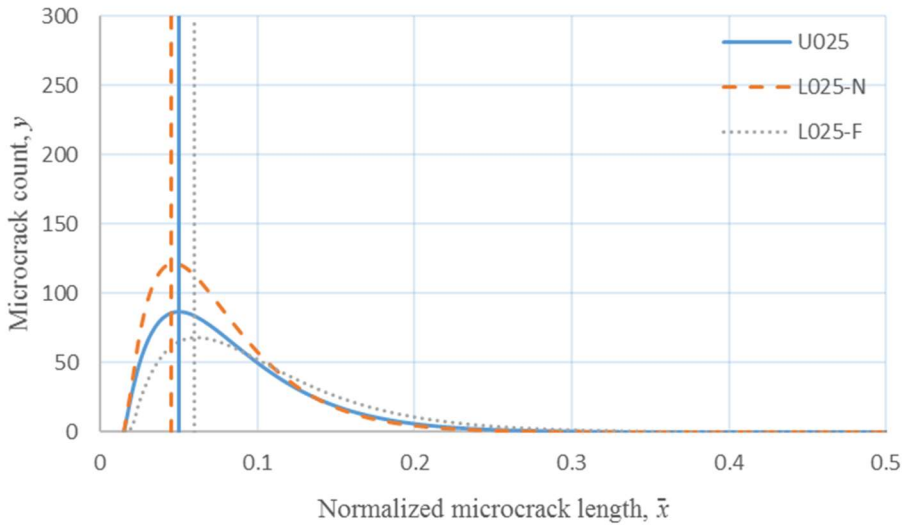
300
250
200
150
100
50
0
Microcrack count, y
0
0.1
0.2
0.3
0.4
0.5
Normalized microcrack length, $\bar{x}$
U025
L025-N
L025-F

(a)

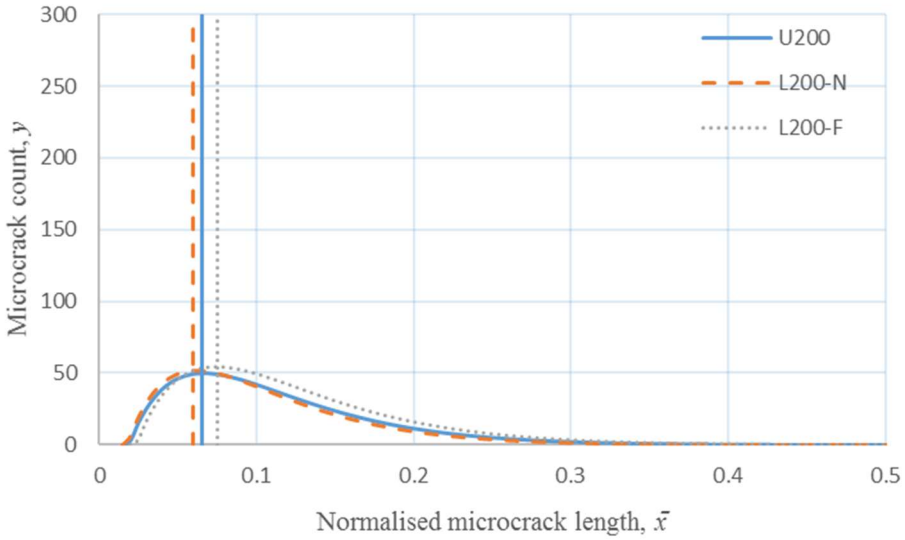
300
250
200
150
100
50
0
Microcrack count, y
0
0.1
0.2
0.3
0.4
0.5
Normalised microcrack length, $\bar{x}$
U200
L200-N
L200-F

(b)

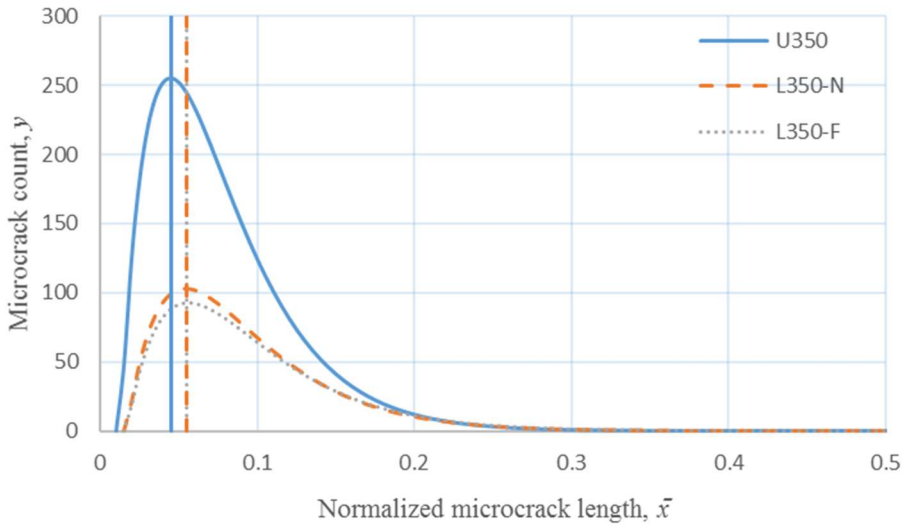

(c)

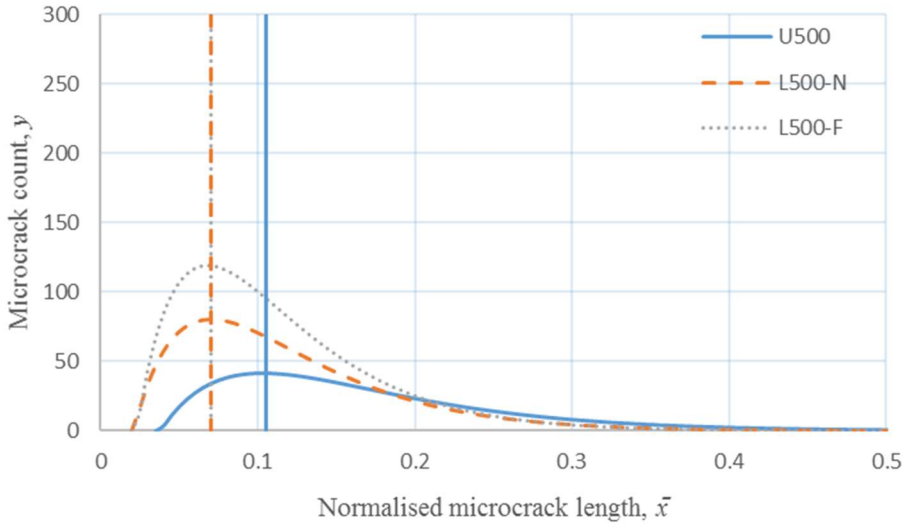

(d)

Fig. 6.5 Normalized microcrack length distribution for specimens at (a) room temperature, (b) 200 °C, (c) 350 °C and (d) 500 °C.

It appears that the thermal treatment and the microcrack count shows a weak correlation. This could be due to the coalescence of multiple microcracks into a single long crack. A coalescence of multiple small cracks will result in a significant reduction of the microcrack count. Furthermore, besides increasing the crack length,

energy input from thermal and mechanical loading can also be dissipated by the grains rolling and sliding past each other or by widening of pre-existing cracks.

6.5 Relationship between microcrack characteristics and rock texture

The two common types of microcracks are intergranular cracks, which propagate along the grain boundaries; and the intragranular cracks, which are commonly bound within the confines of the grain boundaries. The intragranular cracks show a tendency to develop along the cleavage planes of the specific mineral within the grain itself, and terminate when they reach the grain boundary.

The relatively large grain size of the coarse-grained Bukit Timah Granite may potentially increase the probability of intragranular crack formation as compared with its finer-grained counterparts. This is because coarse-grained rocks have shorter total grain boundary lengths as compared to finer-grained rocks, thus limiting the intergranular crack lengths. This will lead to an increase in the ratio of intragranular to intergranular cracks.

It can be seen that there is very little variation in the modal crack length (Fig. 6.5) is similar for both heated and unheated specimens. The modal microcrack length for most segments observed is about 0.05 to 0.08 of the average grain size, it is consistent with the observation that most microcracks observed in this chapter are intragranular cracks. Intragranular cracks were rarely seen in quartz and platy biotite grains, and were mostly formed within plagioclase and alkali feldspar grains. This could be due to the unfavorable (parallel to plane of observation) cleavage orientation of the platy biotite. Another reason is the higher strength of quartz as compared to alkali feldspar and plagioclase.

As for the intergranular cracks, even though the grain sizes are quite large, the subhedral and anhedral nature of the grains inhibits the growth of the intergranular crack to any considerable length in a relatively straight line. The dotted line in Fig. 6.6b is an example of a typical grain boundary crack observed. In this chapter, cracks that deviate by more than 10° is deemed as a separate crack. Although the grain boundary cracks highlighted by the dotted line in Fig. 6.6b may look like a straight line without magnification, it is composed of multiple straight short cracks.

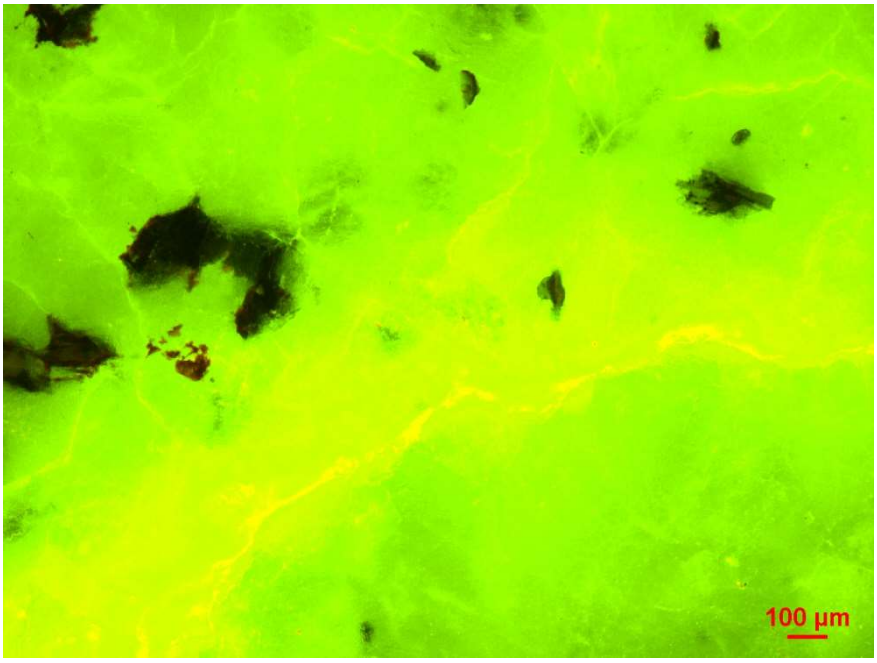

(a)

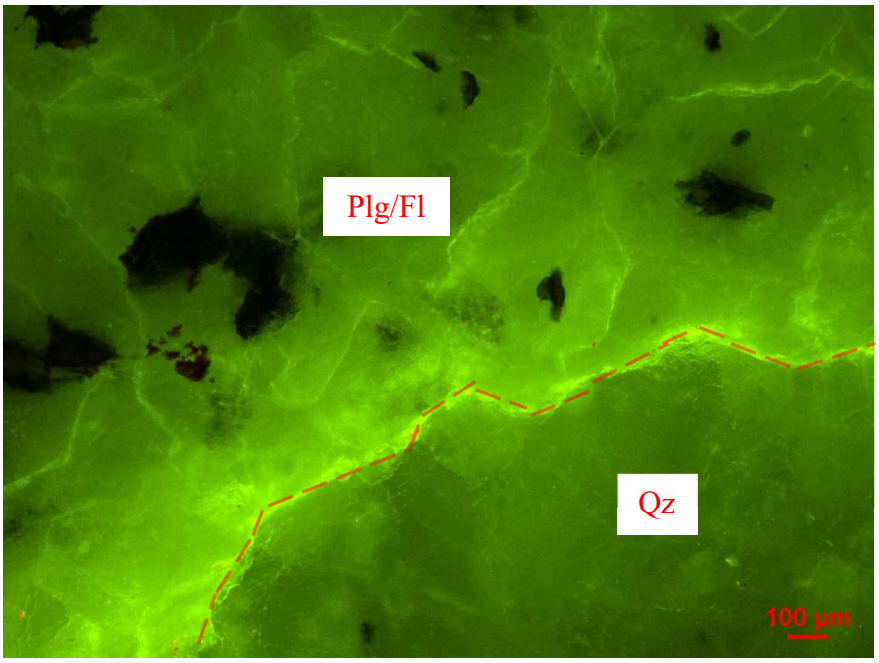

(b)

Fig. 6.6 Microscopic images of specimen heated to 500 °C, 4X magnification, (a) at original brightness, (b) at 30% brightness. The brightest crack forms along the grain boundary (dotted line) between the quartz grain (Qz) and the alkali feldspar/plagioclase grain (Plg/Fld).

6.6 Microcrack width

Microcrack width is not quantified in this thesis. It is observed that the microcrack width is affected by heating temperature (Figs. 6.4 and 6.6). In this method using fluorescent epoxy, the width of the microcracks can be inferred from the brightness of the microcracks. The fluorescent dye in the epoxy glows when excited with blue light, and the brightness of the fluorescence will increase with the amount of dye trapped within the microcrack.

Fig. 6.6a shows that the brightness level of the microcracks in specimens heated at 500 °C is a lot higher as compared with those of a specimen heated at 350 °C (Fig. 6.4). Fig. 6.6b is the same image as Fig. 6.6a but with the brightness level reduced to 30%, so as to better show the wider crack aperture. It is observed that the intergranular crack (dotted line) has a wider aperture and that it was impregnated with more yellow fluorescent dye. The widening of cracks can be another variable that determines the strength of rocks other than microcrack counts and crack lengths.

6.7. Discussion

6.7.1. Microcrack length

From the test data, we can see that the key attributes of microcracks generated in this chapter are dependent on factors such as the temperature of the specimens, the petrography of the rock, as well as the texture of the mineral grains.

The amount of microcracks generated in the specimen is generally proportional to the heating temperature. Increased heating temperature increases the differential volumetric expansion of the different minerals becomes greater, and results in more microcracks. While the cumulative microcrack length of all specimens varies (Fig. 6.3), the modal microcrack length shows only a small variation, regardless of the thermal and mechanical loading conditions (Fig. 6.5.) A possible explanation is that the strain energy from heating and mechanical loading is relieved periodically by microcrack formation. Due to the periodic release of potential energy in the form of crack initiation and propagation, the potential energy does not get a chance to form microcracks of a significantly longer length.

The modal microcrack length is likely a material property. The strain energy would initiate new cracks when it exceeds the free surface energy requirement, which is determined by the material.

As the modal microcrack length is influenced by the energy requirement for microcrack formation, it tends to be similar for all specimens and segments. Thus, crack initiation occurs when the threshold temperature has been passed, and crack propagation stops when the stored strain energy drops below a lower threshold. Since the upper and lower thresholds are dependent on material properties, the modal crack length could be expected to be similar for a given material.

Homand-Etienne and Houpert (1989) also observed that the microcrack initiation and characteristics is at least partially dependent not only on material properties, but also grain geometry and microstructures of the constituent minerals in the rock.

Another possible explanation is that strain energy was expended in widening the induced microcracks. Although the width of the microcracks were not quantitatively measured in this thesis, the increasing brightness of the fluorescent epoxy impregnated microcracks for specimens treated at higher temperatures suggests greater crack widths in specimens that were heated at a higher temperature (Fig. 6.6). Lin (2002), who adopted the mercury intrusion porosimetry method, had also observed that the modal width for microcracks increases with heating temperature.

No observable differences were detected between the crack densities at the rim and at the center of the segments. This may be because the localized thermal gradient induced near the rim of the specimen was not high enough to produce significantly more microcracks.

6.7.2. Petrological and geometrical factors

Petrological factors influencing the microcrack count and distribution include the mineralogical composition of the specimens. Most of the intragranular damage observed in this chapter occurs within alkali feldspar or plagioclase grains. The cleavages of alkali feldspar and plagioclase are preferential sites for intragranular cracking, in contrast to quartz which has no discernible cleavages. Bauer and Johnson (1979), Homand-Etienne and Houpert (1989), and Schild et al. (2001), had also

observed similar microcracking pattern in alkali feldspar which comprised of one or two sets of cleavage cracks. Concurrently, while the intragranular and intergranular cracks in quartz showed no preferred orientation. Similar cases of microcrack generation and propagation along the cleavage planes had also been reported by other researchers (Bandini et al., 2012; Freire-Lista et al., 2016; Rigopoulos et al., 2011). Fredrich and Wong (1986) as well as Lin (2002) observed that intergranular cracks formed mostly between quartz-feldspar boundaries and that the number for intragranular cracks was much higher for feldspar than in quartz.

The majority of intragranular damage occurs within alkali feldspar and plagioclase rather than quartz, because quartz is stronger (Passchier & Trouw, 2005). Besides, quartz is the main "driver" of thermally induced microcrack formation by reason of its larger coefficient of thermal volumetric expansion. Microcracks may form more easily in rocks that contain a disproportionally high amount of quartz, as compared to rocks that have a more balanced proportion of these minerals.

Besides petrological factors, the grain geometry also influences the ratio of intragranular versus intergranular cracks. The relatively large grain size of the Bukit Timah Granite increased the probability of intragranular crack formation. The coarse-grained rocks have shorter total grain boundary lengths as compared to finer-grained rocks, which restricts the intergranular crack lengths, resulting in an increase in the ratio of intragranular to intergranular crack count.

As Fig. 6.5 shows, the modal crack length of all specimens examined is below the average grain size of Bukit Timah Granite. This is partly due to the large number of cleavage cracks generated within the alkali feldspar and plagioclase. Another factor is the subhedral or anhedral nature of the mineral constituents. As the grains of the minerals do not have perfectly straight faces, the perimeter of the grains in the micrographs are broken up into jagged linear sections much smaller in dimension than the average grain size (2 mm, Fig. 2.13). In this chapter, the discontinuous intergranular cracks of the grains were counted as distinct, separate cracks.

Eberhardt et al. (1999) suggested that rocks with a larger grain size tends to be weaker as the larger grain size allows for a longer path of weakness for cracks to propagate. However, this mechanism does not consider the texture of the grains. Grains with a

subhedral or anhedral texture may suppress the crack propagation along the potential long paths of weaknesses. Shorter crack lengths, or a reduction in 2α, may mean lesser strength degradation due to a lower stress intensity factor (equation 2.1, section 2.3).

Intergranular cracks measured in this chapter are jagged due to the subhedral or anhedral texture of the minerals. The jagged nature of the intergranular cracks limits the strength degradation of the granite primarily by increasing the degree of grain interlock. The increased degree of grain interlock arising from mineral textures enhances the shear resistance for microcracks that develop. With an increased frictional shear resistance, the localized stress at the crack tip, σ, in equation 2.1, would also be reduced, leading to a lower stress intensity factor.

6.8 Conclusions

In this chapter, Brazilian tensile tests were performed on Bukit Timah Granite specimens which had been prepared and subjected to a variety of thermal and mechanical loading conditions. The tested specimens were then impregnated with a fluorescent dye for the observation of the generated microcracks. The microcracks were then visually counted. The length and orientation of each microcrack were also recorded and compiled with the aid of a computer program.

The overall orientation and amount of the microcracks has been found to be influenced by the mineralogy of the rock. Intragranular cracks tend to propagate along planes of weaknesses such as the cleavage planes of the minerals. An example of how mineralogy can affect the microcrack characteristics is having an abundance of quartz in the specimen. As quartz expands the most, for each unit increase in temperature, rocks that contain a higher proportion of quartz would lead to a greater amount of internal stresses. This may favor the development of microcracks in other constituent mineral grains such as feldspar and plagioclase.

The modal intragranular crack lengths within the plagioclase and alkali feldspar appear to be independent of all loading and heating conditions. This implies that the length of the intragranular microcracks may be a function of the material. At a micro level, a mineral grain can be visualized as a homogenous brittle material subjected to mechanical loading due to the stresses caused by the confining material around the

grain. The mineral grain would gain elastic strain energy until a certain threshold is reached, at which point, a microcrack is initiated and propagated using the stored elastic strain energy. Since this threshold is likely to be a function of the material property, the length of the microcrack being created would likely be similar.

Previous studies correlate the length of microcracks within a rock to the average grain size. This may appear to be valid at a macroscopic scale. A closer examination reveals that the texture of the mineral grains has a strong influence on the average length of the intergranular microcracks. As intergranular microcracks tend to propagate along the grain boundary, for subhedral or anhedral crystals, the microcrack lengths will be shorter, and appear more jagged after coalescence. It is likely that the energy requirements, and stress required, for a crack to propagate in a straight line is vastly lesser than that of a crack propagating in a jagged line, assuming that the crack propagation is due to in-plane shearing.

Chapter 7 Conclusions and future work

7.1 Introduction

As the global population increases, competition for land usage has increased significantly. Such usage includes agriculture and recreational purposes. One promising method of expanding the current usable land supply for construction is underground construction. Underground construction is attractive as it exploits land that are unattractive for other usages. However, there exists fire hazards within underground rock tunnels or caverns. Hence, there is a need to understand the influence of thermal loading on rocks.

The influence of thermal loading on rocks is one of the major topics of study in rock mechanics. The usefulness of such studies range from fire engineering to thermal fracking (Ezzedine et al., 2015). Although the effects of thermal loading can range from microcrack generation to chemical changes of constituent minerals within the rocks, this study mainly focuses on microcrack generation as it is widely applicable to many different rock types.

7.2 Conclusions

The mechanisms behind microcrack generation, the microcrack characteristics in response to different thermal and mechanical loading conditions and the effects of microcrack density on the visual properties of the rock are among some of the areas explored within this study. The conclusions drawn from the previous chapters of this thesis are summarized below.

I. Color change of Bukit Timah Granite (BTG) with respect to heating temperature

1) The cooling rate that the Brazilian tensile test specimens were exposed to had no significant effect on both the Brazilian tensile strength of the specimens and the color changes of the specimens.

2) The color changes of the specimens were found to be correlated to the heating temperature of the specimen. In particular, specimens that were heated at a higher temperature were found to be more reddish and yellowish.

3) The color scheme used in this thesis is the CIE L*a*b* color space

4) The ratio of the a* and b* change was found to be consistent regardless of the heating temperature. Even though the a* and b* values change with respect to the heating temperature, the magnitude of the change for the two values are similar.

5) The colorimetry method used in this study has been shown to be reliable even in cases where the surface of the rock specimen suffered soot and smoke damage. After the simulated soot and smoke was cleaned off using a combination of rubbing alcohol and a scouring pad, the changes in a* and b* values were found to be mostly linear and similar in magnitude, as in point 4.

6) The colorimetry method used in this study was found to be sensitive to lighting conditions. Care should be taken to ensure similar lighting conditions when taking photos of specimens before and after heating. Lumen depreciation should be taken into account if the photo taking period is relatively long.

7) The color changes within the rock may be due to light scattering, which is a function of the generated microcrack length, as well as microcrack density. Colorimetry seems to be a suitable indirect measurement method for estimating the remaining integrity of rock mass after exposure to high temperatures.

II. Dynamic compression test of heated Carrara marble (CM) specimens

1) The dynamic compressive strength of marble is inversely proportionate to the heating temperature that the marble specimens were heated at. At higher temperature, there seems to be a limit on the dynamic compressive strength, regardless of the strain rate or the gas pressure used to charge the gas gun.

2) At lower temperatures (250 °C), there seems to be two distinct trends of increasing peak dynamic compressive stress with respect to strain rate. Each trend corresponds to a different failure type (pulverization vs axial splitting).

3) Average particle size of the residual fragments is inversely correlated with the heating temperature and gas pressure used to charge the gas gun for the SHPB setup, except in cases where stress shadowing occurred. Stress shadowing produced relatively larger fragments that crumble easily during the dry sieving process.

4) The stress wave propagation speed travelling through the marble specimen is affected by the temperature of the marble specimen, and to a smaller extent, the gas pressure used to charge the gas gun of the SHPB setup.

5) Both the heating temperature and gas pressure used to charge the gas gun affect the time to failure for the specimens tested. Assuming that completion of the fracture initiation of the primary crack coincides with the peak stress sustained by the specimen tested, the crack propagation velocity is inversely correlated with both the heating temperature and the gas pressure used to charge the gas gun.

6) Analysis of the energy absorbed by the specimens revealed that specimens tested at 6 and 9 bars of pressure required similar amounts of energy to initiate fracture of the primary crack regardless of the temperature that the specimens were heated at. However, specimens that were heated at a higher temperature absorbed a larger amount of energy in total, with the exception of specimens heated at 750 °C.

III. Dynamic compression of heated granite specimens

1) The dynamic compressive strength of granite does not vary much with the heating temperature until the specimens were heated at 750 °C. Specimens tested at 750 °C exhibited an almost complete loss of integrity even before the tests were conducted. Cracks visible to the naked eye were seen on the specimens heated at 750 °C.

2) At room temperature, there seems to be two distinct trends of increasing peak dynamic compressive stress with respect to strain rate. Each trend may correspond to a different failure type (pulverization vs axial splitting).

3) Sieve analysis revealed that the particle size distribution of the residual fragments was similar regardless of the heating temperature, although higher gas pressures tend to produce smaller fragments. The exception were specimens heated at 750 °C, which produced fragments of a consistent size regardless of the testing pressure. This implies that the fragments were produced as a result of the heating, and that the dynamic compression test merely separated them.

4) Analysis of the energy absorbed revealed that specimens heated at 750 °C showed an almost loss of integrity due to the extremely low energy needed to fail the specimen. Unheated specimens absorbed an extremely high amount of energy, but this is likely due to energy needed to close the microcracks.

5) The decrease in dynamic compressive strength is likely resisted by the frictional shear resistance of the microcracks induced in the granite specimens.

6) Expansion of the constituent minerals causes a tighter matching between the faces of the microcracks. This leads to more efficient propagation of the stress wave and lesser energy dissipation through closure of the microcracks. This tighter matching also increases the frictional shear resistance of the microcrack.

7) The mechanisms behind microcrack generation is different between BTG and CM. Microcracks in BTG are likely generated by a mismatch in the coefficient of thermal expansion of the constituent minerals (quartz, alkali feldspar, plagioclase, biotite). However, at 573 °C, a large amount of microcracks are generated when α/β phase change of quartz occurs. Microcracks in CM are likely to be generated by an anisotropy of thermal expansion with respect to direction, until 550 °C, when thermal decomposition starts to occur.

8) Stress shadowing is not apparent in dynamic compression of BTG. This is most likely due to reduced crack propagation velocity as a result of high frictional shear resistance of the microcracks, as well as increased stress wave

propagation velocity due to an expansion in the constituent minerals of the rock.

IV. Microscopic observations of heated granite

1) The modal crack length of granite is similar despite different heating temperatures used. This supports the idea that the length of the microcracks generated via heating is a material property. When the stored strain energy is sufficient to overcome the strength of the material, microcracks are formed and the strain energy is dissipated. As the length of the microcrack is dependent on the amount of energy available to fulfill the free energy requirement of producing new surfaces, the strength of the material controls the length of the microcracks generated.

2) The texture of the minerals within a rock affects the individual length of microcracks generated. In this thesis, connecting microcracks that deviated by more than 10° are deemed as multiple cracks. For subhedral and anhedral grains, the contorted nature of the grain boundaries limits the length of intergranular cracks that may form. With shorter microcrack lengths, more stress to be applied to the specimen before a microcrack reaches its critical stress intensity.

3) Unheated specimens show a preferential orientation for microcracks. As heating temperature increases, the degree of anisotropy of the microcracks decreases. The overall microcrack density is mostly proportionate to the heating temperature.

4) The variation of microcrack width can be another way for rock materials to dissipate strain energy. Qualitative observations show that specimens heated at higher temperatures have wider crack apertures.

5) The length of thermally induced microcracks forms a bi-exponential distribution.

7.3 Limitations

- Lack of triaxial testing

The experiments that were conducted within this thesis are either dynamic uniaxial compressive tests, quasi-static uniaxial compressive tests, or Brazilian tensile tests. This limits application of the test data within this thesis to real world scenarios. Field scale excavations are typically conducted at depths that have significant overburden stress and in situ horizontal stress. This means that the rock mass at those depths are more similar to specimens undergoing triaxial compressive tests, rather than uniaxial compressive tests.

The scenarios in this thesis are of accidents happening in shallow tunnels near the surface that leads to deeper tunnels or caverns. The confining pressure that the rock mass experiences at deeper depths may suppress microcrack propagation, similar to the mineral expansion as discussed in chapter 5.

- Long term creep deformation

Besides catastrophic collapse of underground rock structures, another way for underground rock structures to be rendered unusable is due to exceeding of serviceability limits due to long term creep deformation. Long term creep deformation can be exacerbated by exposure to high temperatures.

Research in this direction can help understand the potential risks of operating geothermal power plants in underground rock caverns, or using underground rock caverns to house fossil fuel generators.

7.4 Future work

- Exploration of failure modes with respect to strength

Chapter 5 reports that, at low to moderate temperatures, there appears to be two trends for BTG and CM specimens tested with the Split Hopkinson Pressure Bar (SHPB). One was of higher strength, lower strain and lower strain rate. The other was with lower strength, higher strain and higher strain rate. However, one of the trends does not appear after heating at high or moderate temperatures.

It is likely that the two trends are related to the anisotropy of specimens that were unheated or heated at a low temperature. But the specimens may also be affected in some other way by the heating. An experiment to see if the two trends are related to

the heating would be to mechanically induce microcracks in BTG and CM specimens in such a way as to produce isotropic microcracks and anisotropic microcracks in different specimens.

- Experiments at low temperatures

Besides being heated at high temperatures, another condition that rocks may be exposed to is cooling to low temperatures. Underground rock caverns are currently being used to store liquefied natural gas and other petroleum products around the world. It is common to cool liquefied natural gas to prevent evaporation. The rock mass in contact with the liquefied natural gas would also likely be cooled to a similar temperature.

Similar to how exposure to high temperatures causes mismatches in thermal expansion of the constituent minerals within a rock, exposure to low temperatures may cause a mismatch in thermal contraction of the constituent minerals within a rock. This may potentially cause more damage to the rocks. As minerals contract, they tend to pull apart from each other. This causes the grain boundaries to experience a local tensile force.

References

Adams, F. D., & Nicolson, J. T. (1900). XI. An experimental investigation into the flow of Marble. Phil. Trans. R. Soc. Lond. A, 195(262-273), 363-401.

Adobe Systems Incorporated, (2004). CIE color standard general information, Document 310662

Afshari-Jouybari, H. and Farahnaky, A., (2011). Evaluation of Photoshop software potential for food colorimetry, Journal of Food Engineering, vol 106, issue 2, pages 170-175

Akcaoglu, T (2017) Determining aggregate size & shape effect on concrete microcracking under compression by means of a degree of reversibility method. Construction and Building Materials 143, 376-386

Akesson, U., Hansson, J., & Stigh, J. (2004). Characterisation of microcracks in the Bohus granite, western Sweden, caused by uniaxial cyclic loading, Engineering Geology, 72(1), 131-142.

Allison, R. J., & Bristow, G. E. (1999). The effects of fire on rock weathering: some further considerations of laboratory experimental simulation. Earth Surface Processes and Landforms, 24(8), 707-713.

Alter, B.E.K., Curtis C.W. (1956) Effect of strain-rate on the propagation of a plastic pulse along a lead bar. Jnl. Appl. Phys., 27, 1097

Amelinckx, S., Van Dyck, D., van Landuyt, J., & Van Tendeloo, G. (Eds.). (2008a). Handbook of Microscopy, Handbook of Microscopy: Applications in Materials Science, Solid-State Physics, and Chemistry. Methods II. John Wiley & Sons.

Amelinckx, S., Van Dyck, D., Van Landuyt, J., & Van Tendeloo, G. (Eds.). (2008b). Electron microscopy: principles and fundamentals. John Wiley & Sons.

Annarel, E. and Taerwe, L., 2009. Revealing the temperature history in concrete after fire exposure by microscopic analysis, Cement and Concrete Research, vol 39, 1239-1249.

Annarel, E. and Taerwe, L., 2011. Methods to quantify the colour development of concrete exposed to fire, Construction and Building Materials, vol 25, 3989-3997

Arndt N. (2011) Geothermal Gradient. In: Gargaud M. et al. (eds) Encyclopedia of Astrobiology. Springer, Berlin, Heidelberg

Ashby, M. F., Ferreira, P., & Schodek, D. L (2009). Nanomaterials, nanotechnologies and design: an introduction for engineers and architects. Butterworth-Heinemann.

Ashby, M. F., Shercliff, H., & Cebon, D. (2013). Materials: engineering, science, processing and design. Butterworth-Heinemann.

ASTM, (2008a). Standard test method for splitting tensile strength of intact rock core specimens.

ASTM, (2008b). Standard test method for fundamental transverse, longitudinal and torsional resonant frequencies of concrete specimens

ASTM, (2009). Standard test method for pulse velocity through concrete

Atkinson, B. K. (1979, February). Fracture toughness of Tennessee sandstone and Carrara marble using the double torsion testing method. International Journal of Rock Mechanics and Mining Sciences & Geomechanics Abstracts (Vol. 16, No. 1, pp. 49-53). Pergamon.

Atkinson, B. K., & Meredith, P. G. (1987). The theory of subcritical crack growth with applications to minerals and rocks. Fracture mechanics of rock, 2, 111-166.

Backers, T., & Stephansson, O. (2012). ISRM suggested method for the determination of mode II fracture toughness. The ISRM Suggested Methods for Rock Characterization, Testing and Monitoring: 2007-2014 (pp. 45-56). Springer International Publishing.

Bakai, A.S., Bakai, S.A., Neklyudov, I.M., Stoev, P.I., Eckert, J., Macht, M.-P., (2007). On the Kaiser effect in bulk metallic glasses, Journal of Non-Crystalline Solids, 353, pages 3769-3771.

Baldridge, W.S. and Simmons, G., (1971). Thermal expansion of lunar rocks, Proceedings of the Second Lunar Science Conference, vol 3, pg 2317-2321, The M.I.T Press.

Bandini, A., Berry, P., Bemporad, E., & Sebastiani M. (2012) Effects of intra-crystalline microcracks on the mechanical behavior of a marble under indentation. International Journal of Rock Mechanics and Mining Sciences, 54, 47-55

Barton, N. (1973). Review of a new shear-strength criterion for rock joints. Engineering geology, 7(4), 287-332.

Barton, N. (2007). Thermal over-closure of joints and rock masses and implications for HLW repositories. Proc. of 11th ISRM congress (pp. 109-16).

Barton, N., & Choubey, V. (1977). The shear strength of rock joints in theory and practice. Rock Mechanics and Rock Engineering, 10(1), 1-54.

Barton, N., Lien, R., & Lunde, J. (1974). Engineering classification of rock masses

Bass, J.D. (1995) Elasticity of minerals, glasses, and melts. Mineral physics & crystallography: a handbook of physical constants

Batzle, M. L., Simmons, G., & Siegfried, R. W. (1980). Microcrack closure in rocks under stress: direct observation. Journal of Geophysical Research: Solid Earth, 85(B12), 7072-7090.

Bauer, S.J. and Handin, J., (1983). Thermal expansion and cracking of three confined, water-saturated igneous rocks to 800˚C, Rock Mechanics and Rock Engineering, 16, 181-198.

Bauer, S.J., & Johnson, B. (1979) Effects of slow uniform heating on the physical properties of the Westerly and Charcoal granites. 20th US Symposium on Rock Mechanics (USRMS). American Rock Mechanics Association

Bell, J.F. (1956) Plastic wave propagation in rods subjected to longitudinal impact. Johns Hopkins University Tech. Rep. No. 4, Army Contract No. DA-36-034-ORD 1363

Bieniawski, Z. T. (1967). Mechanism of brittle fracture of rock: part I—theory of the fracture process. International Journal of Rock Mechanics and Mining Sciences & Geomechanics Abstracts (Vol. 4, No. 4, pp. 395).

Blum, P., (1997). Physical properties handbook: A guide to the shipboard measurement of physical properties of deep-sea cores by the ocean drilling program

Brantut, N., Schubnel, A., & Guéguen, Y. (2011). Damage and rupture dynamics at the brittle-ductile transition: The case of gypsum. Journal of Geophysical Research: Solid Earth, 116(B1).

Breunese, I. A., Both, I. C., & Wolsink, I. G. (2008). Fire testing procedure for concrete tunnel linings. Efectis-R0695, 25.

British Broadcasting Corporation (1999) World: Europe Mont Blanc tunnel systems 'inefficient'. Retrieved from http://news.bbc.co.uk/2/hi/europe/305821.stm

Bunger AP, Cardella DJ (2015) Spatial distribution of production in a Marcellus Shale well: Evidence for hydraulic fracture stress interaction. Journal of Petroleum Science and Engineering, 133, 162-166

Caner, A., Zlatanic, S., & Munfah, N. (2005). Quantitative assessment of structural fire endurance of concrete and shotcrete tunnel liners. Underground Space Use: Analysis of the Past and Lessons for the Future, Erdem & Solak (eds), 585-590.

Carvel, R. O., Beard, A. N., Jowitt, P. W., & Drysdale, D. D. (2004). The influence of tunnel geometry and ventilation on the heat release rate of a fire. Fire Technology, 40(1), 5-26.

Chakrabarti, B., Yates, T., Lewry, A., (1996). Effect of fire damage on natural stonework in buildings, Construction and Building Materials, vol 10, no. 7, pages 539-544

Chen, L., Fang, Q., Jiang, X., Ruan, Z., Hong, J. (2015) Combined effects of high temperature and high strain rate on normal weight concrete. Int J Impact Eng 86:40–56

Chen, G., Li, T., Zhang, G., Yin, H., & Zhang, H. (2014). Temperature effect of rock burst for hard rock in deep-buried tunnel. Natural hazards, 72(2), 915-926.

Chen, C. S., Pan, E., & Amadei, B. (1998). Determination of deformability and tensile strength of anisotropic rock using Brazilian tests. International Journal of Rock Mechanics and Mining Sciences, 35(1), 43-61.

Chen, S., Yang, C., & Wang, G. (2017). Evolution of thermal damage and permeability of Beishan granite. Applied Thermal Engineering, 110, 1533-1542.

Cheng, Y., & Wong, L. N. Y. (2017). Microscopic characterization of tensile and shear fracturing in progressive failure in marble. Journal of Geophysical Research: Solid Earth, vol 123, issue 1, pg 204-225

Cheng, Y., Wong, L. N. Y., & Maruvanchery, V. (2016). Transgranular Crack Nucleation in Carrara Marble of Brittle Failure. Rock Mechanics and Rock Engineering, 49(8), 3069-3082.

Christensen, R. J., Swanson, S. R., & Brown, W. S. (1972). Split-Hopkinson-bar tests on rock under confining pressure. Experimental Mechanics, 12(11), 508-513.

Colombo, M., & Felicetti, R. (2007). New NDT techniques for the assessment of fire-damaged concrete structures. Fire Safety Journal, 42(6), 461-472.

Cooper, R.C., Bruno, G., Wheeler, M.R., Pandey, A., Watkins, T.R., & Shyam, A. (2017) Effect of microcracking on the uniaxial tensile response of β-eucryptite ceramics: Experiments and constitutive model. Acta Materialia 135, 361-371

Covey-Crump, S. J. (1997). The high temperature static recovery and recrystallization behaviour of cold-worked Carrara marble. Journal of Structural Geology, 19(2), 225-241.

Dai, F., Huang, S., Xia, K., & Tan, Z. (2010). Some fundamental issues in dynamic compression and tension tests of rocks using split Hopkinson pressure bar. Rock mechanics and rock engineering, 43(6), 657-666.

Dan, D. Q., Konietzky, H., & Herbst, M. (2013). Brazilian tensile strength tests on some anisotropic rocks. International journal of rock mechanics and mining sciences, (58), 1-7.

Danilatos, G. D. (2009). Optimum beam transfer in the environmental scanning electron microscope. Journal of microscopy, 234(1), 26-37.

Dengler, L. (1976). Microcracks in crystalline rocks. Electron microscopy in mineralogy (pp. 550-556). Springer Berlin Heidelberg.

Devore, G.W., 1969. Differential thermal contractions and compressibilities as a cause for mineral fracturing and annealing, Rocky Mountain Geology, vol 8, 21-36.

Doan, M., & Billi, A. (2011) High strain rate damage of Carrara marble. Geophysical Research Letters, vol 38, L19302

Doan, M., d'Hour, V. (2012) Effect of initial damage on rock pulverization along faults. Journal of Structural Geology, 45, 113-124

DSO National Laboratories (2016) Engineering land systems. Singapore: Ministry of Defence

Dwivedi, R. D., Goel, R. K., Prasad, V. V. R., & Sinha, A. (2008). Thermo-mechanical properties of Indian and other granites. International Journal of Rock Mechanics and Mining Sciences, 45(3), 303-315.

Eberhardt, E., Stimpson, B., & Stead, D. (1999). Effects of grain size on the initiation and propagation thresholds of stress-induced brittle fractures. Rock Mechanics and Rock Engineering, 32(2), 81-99.

Erdakov, P., & Khokhryachkin, D. (2005). Impact of fire on the stability of tunnels.

Ezzedine, S., Rubenchik, A., & Yamamoto, R. (2015). Laser-Enhanced Drilling and Laser Assisted Fracturing for Subsurface EGS Applications. Proceedings, Fourtieth Workshop on Geothermal Reservoir Engineering.

Fairbairn, E.M.R., Ulm, F.J., (2002). A tribute to Fernando L. L. B. Carneiro (1913-2001) engineer and scientist who invented the Brazilian test, Materials and Structures, volume 35, issue 3, pages 195-196.

Fairhurst, C., (1964). On the validity of the 'Brazilian' test for brittle materials, Int. J. Rock Mech. Mining Sci., vol 1, pages 535-546.

Ferrero, A. M., & Marini, P. (2001). Experimental studies on the mechanical behaviour of two thermal cracked marbles. Rock Mechanics and Rock Engineering, 34(1), 57-66.

Frantz, C. E., Follansbee, P. S., & Wright, W. J. (1984, June). New experimental techniques with the split Hopkinson pressure bar. 8th International conference on high energy rate fabrication (pp. 17-21). San Antonio, TX, June.

Fredrich, J. T., Evans, B., & Wong, T. F. (1990). Effect of grain size on brittle and semibrittle strength: Implications for micromechanical modelling of failure in compression. Journal of Geophysical Research: Solid Earth, 95(B7), 10907-10920.

Fredrich, J. T., Menendez, B., & Wong, T. F. (1995). Imaging the pore structure of geomaterials. Science, 268(5208), 276-279.

Fredrich, J. T., & Wong, T. F. (1986). Micromechanics of thermally induced cracking in three crustal rocks. Journal of Geophysical Research: Solid Earth, 91(B12), 12743-12764.

Freire-Lista, D.M., Fort, R., & Varas-Muriel, M.J. (2015) Freeze–thaw fracturing in building granites. Cold Regions Science and Technology, 113, 40-51

Freire-Lista, D.M., Fort, R., & Varas-Muriel, M.J. (2016) Thermal stress-induced microcracking in building granite. Engineering Geology, 206, 83-93

Freire-Lista, D.M., & Fort, R. (2017) Exfoliation microcracks in building granite. Implications for anisotropy. Engineering Geology, 220, 85-93

Frew, D. J., Forrestal, M. J., & Chen, W. (2001). A split Hopkinson pressure bar technique to determine compressive stress-strain data for rock materials. Experimental mechanics, 41(1), 40-46.

Frew, D. J., Forrestal, M. J., & Chen, W. (2002). Pulse shaping techniques for testing brittle materials with a split Hopkinson pressure bar. Experimental mechanics, 42(1), 93-106.

Gilat, A., Schmidt, T. E., & Walker, A. L. (2009). Full field strain measurement in compression and tensile split Hopkinson bar experiments. Experimental Mechanics, 49(2), 291-302.

Glover, P. W. J., Baud, P., Darot, M., Meredith, P., Boon, S. A., LeRavalec, M., ... & Reuschle, T. (1995). α/β phase transition in quartz monitored using acoustic emissions. Geophysical Journal International, 120(3), 775-782.

Gómez-Robledo, L., López-Ruiz, N., Melgosa, M., Palma, A. J., Capitán-Vallvey, L. F., & Sánchez-Marañón, M. (2013). Using the mobile phone as Munsell soil-colour sensor: An experiment under controlled illumination conditions. Computers and electronics in agriculture, 99, 200-208.

Goudie, A.S., McLaren, S.J., Allison, R.J., (1992). The relations between modulus of elasticity and temperature in the context of the experimental simulation of rock weathering by fire, Earth Surface Processes and Landforms, 17, pages 605-615

Goudie, A. S., & Viles, H. A. (2000). The thermal degradation of marble. Acta Universitatis Carolinae, Geographica, 35, 7-16.

Gray, G. T. (2000). Classic Split-Hopkinson pressure bar testing. ASM Handbook, Mechanical testing and evaluation, 8, 462-476.

Gray, G. T., & Blumenthal, W. R. (2000). Split-Hopkinson Pressure Bar Testing of Soft Materials. Materials Park, OH: ASM International, 2000., 488-496.

Griffith, A. A. (1921). The phenomena of rupture and flow in solids. Philosophical transactions of the Royal Society of London. Series A, containing papers of a mathematical or physical character, 221, 163-198.

Griggs, D. T., Turner, F. J., & Heard, H. C. (1960). Deformation of Rocks at 500° to 800° C. Geological Society of America Memoirs, 79, 39-104.

Hager, I., 2014. Colour change in heated concrete, Fire Technology, vol 50, 945-958

Hajpal, M., 2002. Changes in sandstones of historical monuments exposed to fire or high temperature, Fire Technology, vol 38, 373-382

Hajpál, M., & Török, A. (2004). Mineralogical and colour changes of quartz sandstones by heat. Environmental Geology, 46(3-4), 311-322.

Hall, K., & Hall, A. (1991). Thermal gradients and rock weathering at low temperatures: some simulation data. Permafrost and Periglacial Processes, 2(2), 103-112.

Hall, K. (1997). Rock temperatures and implications for cold region weathering. I: New data from Viking Valley, Alexander Island, Antarctica. Permafrost and Periglacial Processes, 8(1), 69-90.

Hall, K. (1999). The role of thermal stress fatigue in the breakdown of rock in cold regions. Geomorphology, 31(1), 47-63.

Han, R., Shimamoto, T., Hirose, T., Ree, J. H., & Ando, J. I. (2007). Ultralow friction of carbonate faults caused by thermal decomposition. Science, 316(5826), 878-881.

Haney, M.G., Shakoor, A. (1994) The relationship between tensile and compressive strengths for selected sandstones as influenced by index properties and petrographic characteristics. Proceedings of 7th International IAEG Congress, Lisbon, Portugal, September 5–9, 1994. Vol. II, 1994. p. 493–500

Hao, X. J., Yuan, L., & Zhao, Y. X. Influence of initial microcrack on the physic-mechanical properties of rock with slaty cleavage. Geotechnical and Geological Engineering, 1-10.

Hassan, A. M. T., Jones, S. W., & Mahmud, G. H. (2012). Experimental test methods to determine the uniaxial tensile and compressive behaviour of ultra high performance fibre reinforced concrete (UHPFRC). Construction and building materials, 37, 874-882.

Hasselman, D. P. H. (1969). Unified theory of thermal shock fracture initiation and crack propagation in brittle ceramics. Journal of the American Ceramic society, 52(11), 600-604.

Hatzor, Y. H., & Palchik, V. (1997). The influence of grain size and porosity on crack initiation stress and critical flaw length in dolomites. International Journal of Rock Mechanics and Mining Sciences, 34(5), 805-816.

Heap, M.J., Baud, P., & Meredith, P.G. (2009) Influence of temperature on brittle creep in sandstones. Geophysical Research Letters, 36(19)

Hettema, M. H. H., Wolf, K. A., & De Pater, C. J. (1998). The influence of steam pressure on thermal spalling of sedimentary rock: theory and experiments. International Journal of Rock Mechanics and Mining Sciences, 35(1), 3-15.

Heuze, F. E. (1983, February). High-temperature mechanical, physical and thermal properties of granitic rocks—a review. International Journal of Rock Mechanics and Mining Sciences & Geomechanics Abstracts (Vol. 20, No. 1, pp. 3-10). Pergamon.

Hetenyi, M. I. (1966). Handbook Of Experimental Stress Analysis.

Hild, F., Denoual, C., Forquin, P., Brajer, X. (2003) On the probabilistic-deterministic transition involved in a fragmentation process of brittle materials. Computers and Structures, 81, 1241-1253

Hoek, E. (1965). Rock fracture under static stress conditions, Doctoral dissertation, University of Cape Town.

Hoffman, G., (2013). CIELab color space

Holcomb, D.J. and Stevens, J.L., (1980). The reversible Griffith crack: a viable model for dilatancy, Journal of Geophysical Research, vol 85, no. B12, pages 7101-7107.

Homand-Etienne, F., & Houpert, R. (1989, March). Thermally induced microcracking in granites: characterization and analysis. International Journal of Rock Mechanics and Mining Sciences & Geomechanics Abstracts (Vol. 26, No. 2, pp. 125-134). Pergamon.

Homand-Etienne, F., & Troalen, J. P. (1984). Behaviour of granites and limestones subjected to slow and homogeneous temperature changes. Engineering Geology, 20(3), 219-233.

Hondros, G. (1959). The evaluation of Poisson's ratio and the modulus of materials of low tensile resistance by the Brazilian (indirect tensile) test with particular reference to concrete. Australian J. Appl. Sci., 10(3), 243-268.

Hortolà, P. (2005). SEM examination of human erythrocytes in uncoated bloodstains on stone: use of conventional as environmental-like SEM in a soft biological tissue (and hard inorganic material). Journal of microscopy, 218(2), 94-103.

Howarth, D. F., & Rowlands, J. C. (1986). Development of an index to quantify rock texture for qualitative assessment of intact rock properties. Geotechnical Testing Journal, 9(4), 169-179.

Howarth, D. F., & Rowlands, J. C. (1987). Quantitative assessment of rock texture and correlation with drillability and strength properties. Rock Mechanics and Rock Engineering, 20(1), 57-85.

Hucka, V., & Das, B. (1974, October). Brittleness determination of rocks by different methods. International Journal of Rock Mechanics and Mining Sciences & Geomechanics Abstracts (Vol. 11, No. 10, pp. 389-392). Pergamon.

Hugman III, R. H. H., & Friedman, M. (1979). Effects of texture and composition on mechanical behavior of experimentally deformed carbonate rocks. AAPG Bulletin, 63(9), 1478-1489.

Inada, Y., Kinoshita, N., Ebisawa, A., & Gomi, S. (1997). Strength and deformation characteristics of rocks after undergoing thermal hysteresis of high and low temperatures. International Journal of Rock Mechanics and Mining Sciences, 34(3-4), 140-e1.

Ingham, J.P., (2009). Application of petrographic examination techniques to the assessment of fire-damaged concrete and masonry structures, Materials Characterization, 60, 700-709

Iphar, M. & Goktan, R.M., (2003). The effect of liquids on mechanical strength and abrasiveness of rocks, Eng.&Arch.Fac.Osmangazi University, Vol.XVII, No: 1, 2003

Irwin, G. R. (1956). Onset of fast crack propagation in high strength steel and aluminum alloys (No. NRL-4763). Naval Research Lab Washington DC.

Irwin, G. R. (1957). Analysis of stresses and strains near the end of a crack traversing a plate. Journal of applied mechanics, 24(3), 361-364.

ISRM. (1978). Suggested methods for determining tensile strength of rock materials. International Journal of Rock Mechanics and Mining Sciences & Geomechanics Abstracts, 15(3), 99-103.

Jansen, D. P., Carlson, S. R., Young, R. P., & Hutchins, D. A. (1993). Ultrasonic imaging and acoustic emission monitoring of thermally induced microcracks in

Lac du Bonnet granite. Journal of Geophysical Research: Solid Earth, 98(B12), 22231-22243.

Jeong, G. C., Ichikawa, Y., & Kawamoto, T. (1993). Direct observation of microcracking and subsequent failure in quartz–feldspar rock (bisphere) under uniaxial compression. Proceedings of international symposium on assessment and prevention of failure phenomena in rock engineering. Istambul, Balkema, Rotterdam (pp. 335-41).

Joblove, G.H. and Greenberg, D., (1978). Color spaces for computer graphics, SIGGRAPH '78 Proceedings of the 5th Annual Conference on Computer Graphics and Interactive Techniques, pages 20-25

John, D. S. (1990). The use of large-area thin sectioning in the petrographic examination of concrete. Petrography Applied to Concrete and Concrete Aggregates. ASTM International.

Kahraman, S. and Yeken, T., (2008). Determination of physical properties of carbonate rocks from P-wave velocity, Bulletin of Engineering Geology and the Environment, vol 67, issue 2, pages 277-281.

Karakul, H. and Ulusay, R., (2013). Empirical correlations for predicting strength properties of rocks from P-wave velocity under different degrees of saturation, Rock Mech. Rock Eng., 46, pages 981-999

Kennard, I. G., & Howell, D. H. (1941). Types of coloring in minerals. Am. Mineral., 26, 405-421.

Kern, H. (1982) Elastic-wave velocity in crustal and mantle rocks at high pressure and temperature: the role of the high-low quartz transition and of dehydration reactions. Phys Earth Planet Inter 29:12–23

Kern, H., Popp, T., Gorbatsevich, F., Zharikov, A., Lobanov, K.V., Smirnov, Y.P. (2001) Pressure and temperature dependence of VP and VS in rocks from the superdeep well and from surface analogues at Kola and the nature of velocity anisotropy. Tectonophysics 338:113–134

Kerr, D.A., (2010). The CIE XYZ and xyY color spaces, issue 1

Khandelwal, M., (2013). Correlating P-wave velocity with the physico-mechanical properties of different rocks, Pure and Applied Geophysics, vol 170, issue 4, pages 507-514.

Kim, D. S., & McCarter, M. K. (1998). Quantitative assessment of extrinsic damage in rock materials. Rock mechanics and rock engineering, 31(1), 43-62.

Knapek, M., Húlan, T., Minárik, P., Dobroň, P., Štubňa, I., Stráská, J., & Chmelík, F. (2016). Study of microcracking in illite-based ceramics during firing. Journal of the European Ceramic Society, 36(1), 221-226.

Kojima, T. and Matsuki, K., (1994). A fundamental study on the use of the Kaiser effect for tectonic stress measurement, NDT and E International, volume 27, no. 1, 1994.

Kolaříková, I., Přikryl, R., Hanus, R., & Jelínek, E. (2005). Thermal loading of smectite-rich rocks: natural processes vs. laboratory experiments. Applied clay science, 29(3-4), 215-223.

Kolay, E., & Baser, T. (2017). The effect of the textural characteristics on the engineering properties of the basalts from Yozgat region, Turkey. Journal of the Geological Society of India, 90(1), 102-110.

Kolsky, H. (1949) An investigation of the mechanical properties of materials at very high rates of loading. Proceedings of the Royal Society A: Mathematical, Physical and Engineering Sciences, B62 (11), pg 676-700

Kolsky, H. (1964) Stress wave in solids. J. Sound Vib., I, 88-110

Kolsky, H., Douch, L.S. (1962) Experimental studies in plastic wave propagation. J. Mech. Phys. Solids, Vol 10, pgs 195-223

Konecny, P., Kozusnikova, A., Goel, R. K., Dwivedi, R. D., Swarup, A., & Prasad, V. V. R. (2005, May). A comparative study of influence of temperature on granites from India and Czech Republic. Proceedings of EUROCK (pp. 265-267).

Kuruppu, M. D., Obara, Y., Ayatollahi, M. R., Chong, K. P., & Funatsu, T. (2014). ISRM-suggested method for determining the mode I static fracture toughness using semi-circular bend specimen. Rock Mechanics and Rock Engineering, 47(1), 267-274.

Kusuda, H., Nishiyama, T., & Saito, T. (1995). Observation and evaluation of microcrack propagation in granite fractured by uniaxial compression test using fluorescent resins. Journal-Society Of Materials Science Japan, 44, 851-851.

Lanaro, F., Sato, T., Stephansson, O., (2009). Microcrack modeling of Brazilian tensile tests with the boundary element method, International Journal of Rock Mechanics and Mining Sciences, 46, pages 450-461.

Landa, E.L. and Fairchild, M.D., (2005). Charting color from the eye of the beholder, American Scientist, 93, pages 436-443

Larsson, K. (2006). Fires in tunnels and their effect on rock: a review.

Lavrov, A., (2001). Kaiser effect observation in brittle rock cyclically loaded with different loading rates, Mechanics of Materials, 33, pages 669-677.

Lavrov, A., (2003). The Kaiser effect in rocks: principles and stress estimation techniques, International Journal of Rock Mechanics and Mining Sciences, vol 40, issue 2, pages 151-171.

Lawn, B. (1993). Fracture of brittle solids. Cambridge university press.

Leckie, F.A. and Dal Bello, D.J., (2008). Strength and stiffness of engineering systems.

Lee, S. E., Kim, M. I., Park, J. H., Park, C. K., Kang, M., & Jeong, G. C. (2006). Damage process of intact granite under uniaxial compression: microscopic observations and contact stress analysis of grains. Geosciences Journal, 10(4), 457-463.

Lee, K. W., & Zhou, Y. (2009). Geology of Singapore. Singapore: Defence Science and Technology Agency

Lehtonen, A., Cosgrove, J.W., Hudson, J.A., Johansson, E., (2012). An examination of in situ rock stress estimation using the Kaiser effect, Engineering Geology, 124, pages 24-37.

Leon, K., Mery, D., Pedreschi, F., Leon, J., (2006). Color measurement in L*a*b* units from RGB digital images, Food Research International, 39, pages 1084-1091

Li D, Wong LNY (2013) The Brazilian Disc Test for Rock Mechanics Applications: Review and New Insights. Rock Mech Rock Eng 46:269-287

Li, X. B., Lok, T. S., Zhao, J., & Zhao, P. J. (2000). Oscillation elimination in the Hopkinson bar apparatus and resultant complete dynamic stress–strain curves for rocks. International Journal of Rock Mechanics and Mining Sciences, 37(7), 1055-1060.

Lide, D.R., (2005). CRC handbook of chemistry and physics, 86th edition.

Lin, W., (2002). Permanent strain of thermal expansion and thermally induced microcracking in Inada granite, Journal of Geophysical Research: Solid Earth, vol 107, issue B10, pages ECV 3-1 – ECV 3-16

Liu, D., Li, X., & Yang, X. (1996). An approach for controlling oscillation in dynamic stress-strain measurement. Transactions of the Nonferrous Metals Society of China, 6(2), 144-147.

Liu, J., Chen, L., Wang, C., Man, K., Wang, L., Wang, J., & Su, R. (2014). Characterizing the mechanical tensile behavior of Beishan granite with different experimental methods. International Journal of Rock Mechanics and Mining Sciences, 69, 50-58.

Lockner, D. A., Moore, D. E., & Reches, Z. E. (1992, January). Microcrack interaction leading to shear fracture. The 33th US Symposium on Rock Mechanics (USRMS). American Rock Mechanics Association.

Lok, T. S., Li, X. B., Zhao, P. J., Liu, D. S., & Lim, C. H. (2001). A large diameter split Hopkinson pressure bar for testing rocks. Frontiers of rock mechanics and

sustainable development in the 21st century, 1st edn. CRC Press, Boca Raton, 97-100.

Lubliner J (1964) A generalized theory of strain-rate-dependent plastic wave propagation in bars. J. Mech. Phys. Solids, Vol 12, pgs 59-65

Lyakhovsky, V., Hamiel, Y., Ampuero, P., Ben-Zion, Y., (2009). Non-linear damage rheology and wave resonance in rocks, Geophys. J. Int., 178(2), pages 910-920

Lynn, W.C. and Pearson, M.J., (2000). The color of soil, Science Teacher, vol 67, no. 5, pages 20-23

Mamtani, M. A., Vishnu, C. S., & Basu, A. (2012). Quantification of microcrack anisotropy in quartzite—a comparison between experimentally undeformed and deformed samples. Journal of the Geological Society of India, 80(2), 153-166.

Markides, C.F., Pazis, D.N., Kourkoulis, S.K., (2011). Influence of friction on the stress field of the Brazilian tensile test, Rock Mech. Rock Eng., 44, pages 113-119.

Markides, C.F. and Kourkoulis, S.K., (2012). The stress field in a standardized Brazilian disc: the influence of the loading type acting on the actual contact length. Rock Mech. Rock Eng., 45(2), pages 145-158.

McCabe, S., Smith, B. J., & Warke, P. A. (2007). Sandstone response to salt weathering following simulated fire damage: a comparison of the effects of furnace heating and fire. Earth Surface Processes and Landforms, 32(12), 1874-1883.

Mellor, M., & Hawkes, I. (1971). Measurement of tensile strength by diametral compression of discs and annuli. Engineering Geology, 5(3), 173-225.

Meredith, P. G., & Atkinson, B. K. (1985). Fracture toughness and subcritical crack growth during high-temperature tensile deformation of Westerly granite and Black gabbro. Physics of the Earth and Planetary Interiors, 39(1), 33-51.

Ministry of Defence, Singapore (2010) Factsheet – Underground Ammunition Storage. Retrieved from

https://www.mindef.gov.sg/imindef/press_room/official_releases/nr/1999/aug/12aug99_nr/12aug99_fs.html

Mohr, D., Gary, G., & Lundberg, B. (2010). Evaluation of stress–strain curve estimates in dynamic experiments. International Journal of Impact Engineering, 37(2), 161-169.

Morley, A. (1944) Strength of Materials, Longman, Green, London, p.35

Nemat-Nasser, S., & Isaacs, J. B. (1997). Direct measurement of isothermal flow stress of metals at elevated temperatures and high strain rates with application to Ta and TaW alloys. Acta Materialia, 45(3), 907-919.

Nemat-Nasser, S., Isaacs, J. B., & Starrett, J. E. (1991, November). Hopkinson techniques for dynamic recovery experiments. Proceedings of the Royal Society of London A: Mathematical, Physical and Engineering Sciences (Vol. 435, No. 1894, pp. 371-391). The Royal Society.

The New York Times (2001) 128 Missing in Swiss Tunnel Fire; 11 Confirmed Dead. Retrieved from http://www.nytimes.com/2001/10/26/world/128-missing-in-swiss-tunnel-fire-11-confirmed-dead.html

Ning, J., Fang, M., Ren, H., (2010). An interacting micro-cracks damage constitutive model for alumina ceramics under uniaxial compression, International Journal of Nonlinear Sciences and Numerical Simulation, 11, 183-188.

Nishiyama, T., & Kusuda, H. (1994). Identification of pore spaces and microcracks using fluorescent resins. International journal of rock mechanics and mining sciences & geomechanics abstracts, Vol. 31, No. 4, pp. 369-375

Nishiyama, T., & Kusuda, H. (1996). Application of a fluorescent technique to the study of the weathering process. Engineering Geology, 43(4), 247-253

Nordlund, E., Zhang, P., Dineva, S., Saiang, D., & Mainali, G. (2015). Impact of fire on the stability of hard rock tunnels in Sweden.

Obert, L., & Duvall, W. I. (1967). Rock mechanics and the design of structures in rock.

O'Connell, R.J. and Budiansky, B., (1974). Seismic velocity in dry and saturated cracked solids, Journal of Geophysical Research, vol 79, issue 35, pages 5412-5426

Odedra, A., Ohnaka, M., Mochizuki, H., & Sammonds, P. (2001). Temperature and pore pressure effects on the shear strength of granite in the Brittle-Plastic Transition Regime. Geophysical research letters, 28(15), 3011-3014.

Oestmo, S. (2013). Digital imaging technology and experimental archeology: a methodological framework for the identification and interpretation of fire modified rock (FMR). Journal of Archaeological Science, 40(12), 4429-4443.

Ojo, O. and Brook, N., (1990). The effect of moisture on some mechanical properties of rock. Mining science and technology, vol 10, 1990, pg 145-156.

Olsson, W. A. (1974). Grain size dependence of yield stress in marble. Journal of Geophysical Research, 79(32), 4859-4862.

Onishi, C. T., & Shimizu, I. (2005). Microcrack networks in granite affected by a fault zone: Visualization by confocal laser scanning microscopy. Journal of structural geology, 27(12), 2268-2280.

Onodera TF, Asoka Kumara HM. Relation between texture and mechanical properties of crystalline rocks. Bull Int Assoc Eng Geol 1980;22:173–7

Osczevski, R.J., (1995). The basis of wind chill, Arctic, vol 48, no. 4, pages 372-382.

Paliwal, B., & Ramesh, K. T. (2008). An interacting micro-crack damage model for failure of brittle materials under compression. Journal of the Mechanics and Physics of Solids, 56(3), 896-923.

Park, C. H., & Bobet, A. (2009). Crack coalescence in specimens with open and closed flaws: a comparison. International Journal of Rock Mechanics and Mining Sciences, 46(5), 819-829.

Park, C. H., & Bobet, A. (2010). Crack initiation, propagation and coalescence from frictional flaws in uniaxial compression. Engineering Fracture Mechanics, 77(14), 2727-2748.

Passchier, C.W., & Trouw, R.A.J. (2005). Microtectonics. Berlin: Springer

Peirs, J., Verleysen, P., Van Paepegem, W., & Degrieck, J. (2011). Determining the stress–strain behaviour at large strains from high strain rate tensile and shear experiments. International Journal of Impact Engineering, 38(5), 406-415.

Perkins, R. D., Green, S. J., & Friedman, M. (1970, September). Uniaxial stress behavior of porphyritic tonalite at strain rates to 103/second. International Journal of Rock Mechanics and Mining Sciences & Geomechanics Abstracts (Vol. 7, No. 5, pp. 527IN5529-528IN6535). Pergamon.

Persson, P. A., Holmberg, R., & Lee, J. (1993). Rock blasting and explosives engineering. CRC press.

Pierron, F., & Forquin, P. (2012). Ultra-High-Speed Full-Field Deformation Measurements on Concrete Spalling Specimens and Stiffness Identification with the Virtual Fields Method. Strain, 48(5), 388-405.

Postiglione, G., Colombo, A., Dragonetti, C., Levi, M., Turri, S., & Griffini, G. (2017). Fluorescent probes based on chemically-stable core/shell microcapsules for visual microcrack detection. Sensors and Actuators B: Chemical, 248, 35-42.

Přikryl, R. (2006). Assessment of rock geomechanical quality by quantitative rock fabric coefficients: limitations and possible source of misinterpretations. Engineering Geology, 87(3-4), 149-162.

Přikryl, R., Lokajíček, T., Li, C., & Rudajev, V. (2003). Acoustic emission characteristics and failure of uniaxially stressed granitic rocks: the effect of rock fabric. Rock Mechanics and Rock Engineering, 36(4), 255-270.

Promat (2017a) Fire protection. http://www.promat-international.com/en/fpi/tunnel

Promat (2017b) Fire curves. http://www.promat-tunnel.com/en/advices/fire-protection/fire%20curves

Punturo, R., Kern, H., Cirrincione, R., Mazzoleni, P., Pezzino, A. (2005) P- and S-wave velocities and densities in silicate and calcite rocks from the Peloritani Mountains, Sicily (Italy): the effect of pressure, temperature and the direction of wave propagation. Tectonophysics 409:55–72

Ramesh, K.T. (2008) High strain rate and impact experiments. In: Sharpe WN (ed) Springer handbook of experimental solid mechanics, 2008 ed. Springer, New York, pp 929–960

Ramsay, J. (1967). Folding and fracturing of rocks.

Ravi-Chandar K, Knauss WG (1984) An experimental investigation into dynamic fracture: III. On steady-state crack propagation and crack branching. International Journal of Fracture, 26, pg 141-154

Ree, J. H., Ando, J. I., Han, R., & Shimamoto, T. (2014). Coseismic microstructures of experimental fault zones in Carrara marble. Journal of Structural Geology, 66, 75-83.

Richter, D., & Simmons, G. (1974, October). Thermal expansion behavior of igneous rocks. International Journal of Rock Mechanics and Mining Sciences & Geomechanics Abstracts (Vol. 11, No. 10, pp. 403-411). Pergamon.

Rigopoulos, I., Tsikouras, B., Pomonis, P., & Hatzipanagiotou, K. (2011) Microcracks in ultrabasic rocks under uniaxial compressive stress. Engineering geology, 117(1), 104-113

Robbins, M. (1994). Fluorescence: gems and minerals under ultraviolet light. Geoscience Press.

Rockwell, T., Sisk, M., Girty, G., Dor, O., Wechsler, N., Ben-Zion, Y. (2009) Chemical and physical characteristics of pulverized Tejon lookout granite adjacent to the san Andreas and garlock faults: implications for earthquake physics. Pure Appl Geophys 166:1725–1746

Rossana, B., & Paola, M., (2012). The effect of water on the strength of building stones. American journal of environmental sciences, 8 (2), pg 158-161

Saiang, C., & Miskovsky, K. (2011, January). Effect of heat on the mechanical properties of selected rock types–a laboratory study. 12th ISRM Congress. International Society for Rock Mechanics.

Sassoni, E., Graziani, G., Ridolfi, G., Bignozzi, M. C., & Franzoni, E. (2017). Thermal behavior of Carrara marble after consolidation by ammonium phosphate, ammonium oxalate and ethyl silicate. Materials & Design, 120, 345-353.

SCDF (2012) Standard for Fire Safety in Rapid Transit Systems, 2012 edition. Singapore Civil Defence Force.

Schild, M., Siegesmund, S., Vollbrecht, A., & Mazurek, M. (2001) Characterization of granite matrix porosity and pore-space geometry by in situ and laboratory methods. Geophysical Journal International, 146(1), 111-125.

Shan, R., Jiang, Y., & Li, B. (2000). Obtaining dynamic complete stress–strain curves for rock using the split Hopkinson pressure bar technique. International Journal of Rock Mechanics and Mining Sciences, 37(6), 983-992.

Shen, B., Stephansson, O., Einstein, H. H., & Ghahreman, B. (1995). Coalescence of fractures under shear stresses in experiments. Journal of Geophysical Research: Solid Earth, 100(B4), 5975-5990.

Siegesmund, S., Kern, H., & Vollbrecht, A. (1991). The effect of oriented microcracks on seismic velocities in an ultramylonite. Tectonophysics, 186(3-4), 241-251.

Smith, A. G., & Pells, P. J. N. (2008). Impact of fire on tunnels in Hawkesbury sandstone. Tunnelling and Underground Space Technology, 23(1), 65-74.

Song, B., & Chen, W. (2004). Loading and unloading split Hopkinson pressure bar pulse-shaping techniques for dynamic hysteretic loops. Experimental Mechanics, 44(6), 622-627.

Song, Y. K., Lee, K. H., Hong, W. S., Cho, S. Y., Yu, H. C., & Chung, C. M. (2012). Fluorescence sensing of microcracks based on cycloreversion of a dimeric anthracene moiety. Journal of Materials Chemistry, 22(4), 1380-1386.

Song, Y. K., Lee, K. H., Kim, D. M., & Chung, C. M. (2016). A microcapsule-type fluorescent probe for the detection of microcracks in cementitious materials. Sensors and Actuators B: Chemical, 222, 1159-1165.

Sprunt, E. S., & Brace, W. F. (1974). Direct observation of microcavities in crystalline rocks. International Journal of Rock Mechanics and Mining Sciences & Geomechanics Abstracts (Vol. 11, No. 4, pp. 139-150). Pergamon.

Sternglass, E.J., Stuart, D.A. (1953) Experimental study of propagation of transient longitudinal deformations in elastoplastic media. J. App. Mech., 20, 427–34

Stutzman, P. E. (1990). Serial sectioning of hardened cement paste for scanning electron microscopy. Center for Building Technology, National Institute of Standards and Technology.

Suzuki, E. (2002). High-resolution scanning electron microscopy of immunogold-labelled cells by the use of thin plasma coating of osmium. Journal of Microscopy, 208(3), 153-157.

Sweet, J. M. (1961). Ultraviolet Guide to Minerals. A Complete Working Manual for the Use of Ultraviolet Light in Locating and Recognizing Minerals Including Field Identification Charts. Mineralogical Magazine, 32, 743-744.

Swift, J. A., & Brown, A. C. (1970). An environmental cell for the examination of wet biological specimens at atmospheric pressure by transmission scanning electron microscopy. Journal of physics E: Scientific instruments, 3(11), 924.

Taghichian, A., Zaman, M., Devegowda, D. (2014) Stress shadow size and aperture of hydraulic fractures in unconventional shales. Journal of Petroleum Science and Engineering, 124, 209-221

Tapponnier, P., & Brace, W. F. (1976). Development of stress-induced microcracks in Westerly granite. International Journal of Rock Mechanics and Mining Sciences & Geomechanics Abstracts (Vol. 13, No. 4, pp. 103-112). Pergamon.

The Mathworks Inc, (2014). Color-based segmentation of fabric using the L*a*b* color space, Mathworks Documentation Center

Thirumalai, K. and Demou, S.G., (1974). Thermal expansion behavior of intact and thermally fractured mine rocks, AIP conference proceedings, 17, 60.

Timoshenko, S. (1953). History of strength of materials: with a brief account of the history of theory of elasticity and theory of structures. Courier Corporation.

Todd, T.P., (1973). Effect of cracks on elastic properties of low porosity rocks, Ph.D. thesis, Mass. Inst. Of Technol., Cambridge.

Tullis, J. and Yund, R.A., (1977). Experimental deformation of dry Westerly granite, Journal of Geophysical Research, vol 82, no 36, pg 5705-5718.

US Department of Energy, 2013. Lumen maintenance and light loss factors: Consequence of current design practices for LEDs.

Vásárhelyi, B., & Ván, P. (2006). Influence of water content on the strength of rock. Engineering Geology, 84(1-2), 70-74.

Vasarhelyi, B., (2004). Statistical analysis of the influence of water content on the strength of Miocene limestone. Rock mechanics and rock engineering, 2005, vol 38, issue 1, pg 69-76

Vasarhelyi, B., and Van, P., (2006). Influence of water content on the strength of rock, Engineering Geology, 84, pages 70-74.

Vidya Sagar, R., Raghu Prasad, B.K., Singh, R.K., (2014). Kaiser effect observation in reinforced concrete structures and its use for damage assessment, Archives of Civil and Mechanical Engineering, article in press, 2014.

Vishal, V., Pradhan, S. P., & Singh, T. N. (2011). Tensile strength of rock under elevated temperatures. Geotechnical and Geological Engineering, 29(6), 1127.

Wang, H. F., Bonner, B. P., Carlson, S. R., Kowallis, B., & Heard, H. C. (1989). Thermal stress cracking in granite. Journal of Geophysical Research: Solid Earth, 94(B2), 1745-1758.

Wang, P., Cai, M., & Ren, F. (2018). Anisotropy and directionality of tensile behaviours of a jointed rock mass subjected to numerical Brazilian tests. Tunnelling and Underground Space Technology, 73, 139-153.

Wang, J., Li, Y., Han, J., Xu, Q. and Guo, Y. (2011). Evaluating subsurface damage in optical glasses, Journal of the European Optical Society – Rapid Publications, vol 6.

Warren, T. S. (1995). Ultraviolet light and fluorescent minerals: understanding, collecting, and displaying fluorescent minerals. Gem Guides Book Co.

Wawersik WR, Fairhurst C (1970) A study of brittle rock fracture in laboratory compression experiments. Int. J. Rock Mech. Min. Sci., vol 7, pp 561-575

Wei, W., Zhao, D., & Xu, J. (2013). P-wave anisotropic tomography in Southeast Tibet: New insight into the lower crustal flow and seismotectonics. Physics of the Earth and Planetary Interiors, 222, 47-57.

Wong, R. H., Chau, K. T., & Wang, P. (1996). Microcracking and grain size effect in Yuen Long marbles. International journal of rock mechanics and mining sciences & geomechanics abstracts (Vol. 33, No. 5, pp. 479-485). Pergamon.

Wong, L. N. Y., & Einstein, H. (2006, January). Fracturing behavior of prismatic specimens containing single flaws. Golden Rocks 2006, The 41st US Symposium on Rock Mechanics (USRMS). American Rock Mechanics Association.

Wong, L. N. Y., & Einstein, H. H. (2007, January). Coalescence behavior in Carrara marble and molded gypsum containing artificial flaw pairs under uniaxial compression. 1st Canada-US Rock Mechanics Symposium. American Rock Mechanics Association.

Wong, L. N. Y., & Einstein, H. H. (2008). Using high speed video imaging in the study of cracking processes in rock. Geotechnical Testing Journal, 32(2), 164-180.

Wong, L. N. Y., & Einstein, H. H. (2009a). Crack coalescence in molded gypsum and Carrara marble: part 1. Macroscopic observations and interpretation. Rock Mechanics and Rock Engineering, 42(3), 475-511.

Wong, L. N. Y., & Einstein, H. H. (2009b). Crack coalescence in molded gypsum and Carrara marble: part 2—microscopic observations and interpretation. Rock Mechanics and Rock Engineering, 42(3), 513-545.

Wong, L. N. Y., & Einstein, H. H. (2009c, November). Process zone development associated with cracking processes in Carrara marble. The 9th International Conference on Analysis of Discontinuous Deformation: New Developments and Applications, Singapore (pp. 581-588).

Wong, L. N. Y., & Einstein, H. H. (2009d). Systematic evaluation of cracking behavior in specimens containing single flaws under uniaxial compression. International Journal of Rock Mechanics and Mining Sciences, 46(2), 239-249.

Wong, L. N. Y., & Jong, M. C. (2014). Water saturation effects on the Brazilian tensile strength of gypsum and assessment of cracking processes using high-speed video. Rock mechanics and rock engineering, 47(4), 1103-1115.

Wong, L.N.Y., & Maruvanchery, V. (2016) Different Lithological Varieties of Bukit Timah Granite in Singapore: a Preliminary Comparison Study on Engineering Properties. Rock Mech Rock Eng 49:2923-2935

Wong, L. N. Y., Maruvanchery, V., & Oo, N. N. (2015). Engineering properties of a low-grade metamorphic limestone. Engineering Geology, 193, 348-362.

Wong, L. N. Y., Zou, C., & Cheng, Y. (2014). Fracturing and failure behavior of Carrara marble in quasistatic and dynamic Brazilian disc tests. Rock mechanics and rock engineering, 47(4), 1117-1133.

Xia, K., & Yao, W. (2015). Dynamic rock tests using split Hopkinson (Kolsky) bar system–A review. Journal of Rock Mechanics and Geotechnical Engineering, 7(1), 27-59.

Xia, K., Nasseri, M. H. B., Mohanty, B., Lu, F., Chen, R., & Luo, S. N. (2008). Effects of microstructures on dynamic compression of Barre granite. International Journal of Rock Mechanics and Mining Sciences, 45(6), 879-887.

Yagiz, S., (2011). P-wave velocity test for the assessment of some geotechnical properties of rock materials, Bulletin of Materials Science, 34, 943-957

Yam, K.L. and Papadakis, S.E., (2004). A simple digital imaging method for measuring and analyzing color of food surfaces, Journal of Food Engineering, 61, pages 137-142

Yatsu, E. (1988). Nature of Weathering, The; An Introduction. Sozosha.

Yin, T., Li, X., Cao, W., & Xia, K. (2015). Effects of thermal treatment on tensile strength of Laurentian granite using Brazilian test. Rock Mechanics and Rock Engineering, 48(6), 2213-2223.

Yin TB, Li XB, Xia K, Huang S (2012) Effect of thermal treatment on the dynamic fracture toughness of Laurentian granite. Rock Mech Rock Eng 45(6):1087–1094

Yong, C. and Wang, C., (1980). Thermally induced acoustic emission in Westerly granite, Geophysical Research Letters, vol 7, no. 12, pages 1089-1092

Yoshioka, S., & Kitano, Y. (1985). Transformation of aragonite to calcite through heating. Geochemical Journal, 19(4), 245-249.

Yu, Y., Yin, J., Zhong, Z., (2006). Shape effects in the Brazilian tensile strength test and a 3D FEM correction, Int. J. Rock Mech. Min. Sci., 43(4), 623-627.

Yu, Y., Zhang, J., Zhang, J., (2009). A modified Brazilian disk tension test, International Journal of Rock Mechanics and Mining Sciences, 46, pages 421-425.

Yuan, R. and Li, Y., (2008). Theoretical and experimental analysis on the mechanism of the Kaiser effect of acoustic emission in brittle rocks, Journal of University of Science and Technology Beijing, Mineral, Metallurgy, Material, Vol 15, Issue 1, pages 1-4.

Yuryeva, T.V. and Yuryev, V.A., 2014. Degradation and destruction of historical blue-green glass beads: a study using microspectroscopy of light transmission, Journal of Optics, vol 16.

Zangeneh, N., Eberhardt, E., Bustin, R.M. (2014) Investigation of the influence of stress shadows on horizontal hydraulic fractures from adjacent lateral wells. Journal of Unconventional Oil and Gas Resources, 9, 54-64

Zhang, J.J. and Bentley, L.R., (2005). Factors determining Poisson's ratio, Consortium for Research in Elastic Wave Exploration Seismology Research Report, vol 17

Zhang, L., Mao, X., & Lu, A. (2009). Experimental study on the mechanical properties of rocks at high temperature. Science in China Series E: Technological Sciences, 52(3), 641-646.

Zhao, J. (1998). Rock mass hydraulic conductivity of the Bukit Timah granite, Singapore. Engineering geology, 50(1-2), 211-216.

Zhao, H., & Gary, G. (1996). On the use of SHPB techniques to determine the dynamic behavior of materials in the range of small strains. International Journal of Solids and structures, 33(23), 3363-3375.

Zhou, Y. X., Xia, K., Li, X. B., Li, H. B., Ma, G. W., Zhao, J., Zhou, Z. L. & Dai, F. (2012). Suggested methods for determining the dynamic strength parameters and

mode-I fracture toughness of rock materials. International Journal of Rock Mechanics and Mining Sciences, 49, 105-112.

Zhu, Z. D., Ni, X. H., Wang, W., Li, S. B., Zhao, J., & Wu, Y. Q. (2008). Dynamic experimental study on rock meso-cracks growth by digital image processing technique. Journal of Central South University of Technology, 15(2), 114-120.

Zinke, J. C. (1999). The relationship between open, dry microcracks and P wave velocity of crystalline rocks: Application to in situ stress estimates on KTB drill cores after stress relaxation. Journal of Geophysical Research: Solid Earth, 104(B5), 10863-10881.

Zou, C., & Wong, L. N. Y. (2016a). Different Compressive and Tensile Strength of Moulded Gypsum Under Various Strain Rates from Quasi-Static to Dynamic Regime. Geotechnical Testing Journal, 39(4), 596-607.

Zou, C., & Wong, L. N. Y. (2016b). Size and Geometry Effects on the Mechanical Properties of Carrara Marble Under Dynamic Loadings. Rock Mechanics and Rock Engineering, 49(5), 1695-1708.

Zou, C., Wong, L. N. Y., Loo, J. J., & Gan, B. S. (2016). Different mechanical and cracking behaviors of single-flawed brittle gypsum specimens under dynamic and quasi-static loadings. Engineering Geology, 201, 71-84.

Zunino, F., Castro, J., & Lopez, M. (2015) Thermo-mechanical assessment of concrete microcracking damage due to early-age temperature rise. Construction and Building Materials, 81, 140-153

Appendix I - Summary of previous studies on the effects of high temperatures on rocks

Type 1 - Tests conducted while specimen is held at high temperatures

Author	**Rock type**	**Heating conditions**	**Heating method**	**Tests conducted/equipment used***	**Parameters determined***
Adams and Nicholson (1900)	Marble and limestone	25 ˚C, 300 ˚C and 450 ˚C (deformed as specimen is heated)	iron tube heated by hot gas	petrographic microscope	qualitative observation about microstructures
Griggs et al. (1960)	various (peridotite, pyroxenite, basalt, granite, dolomite, marble, quartz)	Held at 25 ˚C, 300 ˚C, 500 ˚C, 600 ˚C and 800 ˚C Confining pressures used are 250 MPa, 500 MPa, 1000 MPa and 2000 MPa	split furnace or external furnace	triaxial compression test, triaxial tension test, shear strength test, petrographic microscope	triaxial compressive strength, triaxial tension test, shear strength, qualitative observations about microstructures

Author	Rock type	Heating conditions	Heating method	Tests conducted/equipment used*	Parameters determined*
Baldridge and Simmons (1971)	lunar rocks	-100 ˚C to 200 ˚C (strain measured as specimen is heated)	not stated	Brinkmann TD IX Dilatometer	thermal strain
Griffin and Demou (1972)	various (basalt, dacite, obsidian, pumice, tuff, rhyolite, gabbro, dunite, granodiorite, serpentine	-140 ˚C to 950 ˚C (strain measured as specimen is heated)	heating via tube furnace	Direct Current Differential Transformer strain gages	thermal strain
Richter and Simmons (1974)	granite, gabbro, diabase	25 ˚C to 550 ˚C (strain measured as specimen is heated)	heating via tube furnace	LVDT	thermal strain

Author	Rock type	Heating conditions	Heating method	Tests conducted/equipment used*	Parameters determined*
Thirumalai and Demou (1974)	granite	30 ˚C to 400 ˚C (Strain measured as specimen is heated)	heating via tungsten mesh heating element	microscopic observation of acetate peels, LVDT	thermal strain, microcrack density

Author	Rock type	Heating conditions	Heating method	Tests conducted/equipment used*	Parameters determined*
Tullis and Yund (1977)	granite	25 ˚C, 200 ˚C, 300 ˚C, 400 ˚C, 500 ˚C, 600 ˚C, 700 ˚C, 900 ˚C and 1000 ˚C Confining pressures used are 1.5 kilobar, 5 kilobar, 7.5 kilobar, 10 kilobar and 15 kilobar (specimens deformed while specimen is heated)	heated via a modified Griggs hot creep tester with sodium chloride as confining medium	transmission electron microscope, petrographic microscope	qualitative observations about microstructures

Author	Rock type	Heating conditions	Heating method	Tests conducted/equipment used*	Parameters determined*
Yong and Wang (1980)	granite	20 ˚C to 120 ˚C (measurements taken as specimen was heated) Heating rates used are 0.4 ˚C/min, 1.1 ˚C/min, 2.5 ˚C/min, 5 ˚C/min, 7.5 ˚C/min, 10 ˚C/min, 12.5 ˚C/min	heating via furnace	PZT transducer	AE rate and AE events

Author	Rock type	Heating conditions	Heating method	Tests conducted/equipment used*	Parameters determined*
Bauer and Handin (1983)	granite, Andesite, Basalt	100 ˚C to 800 ˚C (strain measured while specimen was heated) Confining pressures used are 5 MPa, 50 MPa and 100 MPa	heating coils wrapped around copper jacket	Direct Current Differential Transformer strain gages	thermal strain
Homand-Etienne and Troalen (1984)	granite, crystalline limestone, oolitic limestone	200 ˚C, 400 ˚C, 500 ˚C, 600 ˚C and 700 ˚C	heating via furnace	SEM, ultrasonic tester, French Institute of Petroleum permeameter	P-wave velocity, permeability changes, qualitative observations about microstructures
Homand-Etienne and Houpert (1989)	granite	20 ˚C, 200 ˚C, 400 ˚C, 500 ˚C and 600 ˚C	not stated	SEM, UCS test, direct tensile test, indirect tensile test	crack density, crack length, crack width, porosity, stress-strain curve for specimens

Author	Rock type	Heating conditions	Heating method	Tests conducted/equipment used*	Parameters determined*
Wang et al. (1989)	granite	20 ˚C, 100 ˚C, 200 ˚C, 250 ˚C, 300 ˚C, 350 ˚C at 7 MPa, 28 MPa and 55 MPa confining pressure (measurements taken as pressure is increased)	not stated	Custom built AE and P-wave velocity tester, SEM, Differential Strain Analysis	thermal strain, P-wave velocity, microcrack density, AE events
Goudie et al. (1992)	various (gabbro, slate, white marble, granite, white granite, York stone, limestone)	50 ˚C, 100 ˚C, 200 ˚C, 300 ˚C, 400 ˚C, 500 ˚C, 600 ˚C, 700 ˚C, 800 ˚C, and 900 ˚C	heating via furnace	Grindoscopic apparatus	modulus of elasticity

Author	Rock type	Heating conditions	Heating method	Tests conducted/equipment used*	Parameters determined*
Allison and Bristow (1999)	various (dolerite, wehrlite, gabbro, chalk, serpentinite)	500 ˚C	furnace	ultrasonic tester	dynamic modulus of elasticity
Odedra et al. (2001)	granite	25 ˚C, 100 ˚C, 200 ˚C, 300 ˚C and 480 ˚C with 70 MPa to 480 MPa confining pressure	heat transfer fluid used as confining medium	triaxial shear test	shear strength
Lin (2002)	granite	20 ˚C, 100 ˚C, 200 ˚C, 300 ˚C, 400 ˚C, 500 ˚C and 600 ˚C	heating via furnace	LVDT, petrographic microscope, ultrasonic tester	P-wave velocity, permanent strain, qualitative observations about microstructures

Author	Rock type	Heating conditions	Heating method	Tests conducted/equipment used*	Parameters determined*
McCabe et al. (2007)	sandstone	500 ˚C	heating via furnace and wood fire	Munsell color chips	qualitative observation about color change, and weathering resistance
Smith and Pells (2008)	sandstone	250 ˚C, 500 ˚C, 750 ˚C and 950 ˚C	heating via electric and charcoal fire	UCS test	UCS, qualitative observations about spalling
Brantut et al. (2011)	gypsum	70 ˚C with 2 MPa, 5 MPa, 10 MPa, 20 MPa, 50 MPa and 95 MPa confining pressure	heating wire wrapped around pressure vessel	AE sensors, ultrasonic tester, petrographic microscope, triaxial compressive test	thermal strain, triaxial compressive strength, qualitative observations about microstructures, P-wave velocity, acoustic emission location and waveform

Author	Rock type	Heating conditions	Heating method	Tests conducted/equipment used*	Parameters determined*
Saiang and Miskovsky (2011)	diabase, granite, quartzitic schist	20 ˚C, 400 ˚C, 750 ˚C and 1100 ˚C	heating via furnace	petrographic microscope, SEM, UCS test, indirect tensile test	UCS, tensile strength, microcrack length and density

Type 2 - Tests conducted after specimen is cooled

Author	Rock type	Heating conditions	Heating method	Tests conducted/equipment used*	Parameters determined*
Clark et al. (1981)	quartzite and sandstone	25 ˚C, 300 ˚C, 485 ˚C, 575 ˚C and 675 ˚C for quartzite, 25 ˚C, 40 ˚C, 50 ˚C, 60 ˚C, 80 ˚C, 10(˚C, 150 ˚C for sandstone	not stated	Vibrating bar method	seismic quality factor Q
Chakrabarti et al. (1996)	various (limestone, sandstone, magnesian limestone, granite, marble)	200 ˚C, 250 ˚C, 300 ˚C, 400 ˚C, 600 ˚C, 800 ˚C and 1000 ˚C	not stated	qualitative observation, UCS test	UCS, qualitative observations about color changes and damage

Author	Rock type	Heating conditions	Heating method	Tests conducted/equipment used*	Parameters determined*
Hettema et al. (1998)	sandstone, siltstone, shale	350 ˚C, 400 ˚C, 500 ˚C, 600 ˚C, 700 ˚C, 800 ˚C, 900 ˚C, 1000 ˚C and 1200 ˚C	heating via tube furnace	presence of spalling	qualitative observation about the occurrence of spalling
Hajpal (2002)	sandstones	20 ˚C, 150 ˚C, 300 ˚C, 450 ˚C, 600 ˚C, 750 ˚C and 900 ˚C	heating via furnace	petrographic microscope, x-ray diffractometry, SEM, ultrasonic tester, indirect tensile test, UCS test, Duroskop	qualitative observations of microstructures, chemical composition, specific and bulk density, porosity, P-wave velocity, tensile strength, UCS, hardness
Hajpal and Torok (2004)	sandstones	22 ˚C, 150 ˚C, 300 ˚C, 450 ˚C, 600 ˚C, 750 ˚C and 900 ˚C	heating via furnace	SEM, x-ray diffractometry, spectral analyser	CIEL*a*b* color change, chemical composition, qualitative observations about microstructures, porosity

Appendix II - Summary of experimental studies where strength increases were observed after heating

Author	Mechanism	Material	Heating source	Results	Test conditions
Heuze (1983)	Not stated, higher triaxial compressive strength correlated with higher composition of quartz and feldspar, may be due to increased confining pressure (1kbar to 5 kbar)	Granite	Not stated	Triaxial compressive strength increase (18% to 167% increase in deviatoric stress)	150 °C and 500 °C

Author	Mechanism	Material	Heating source	Results	Test conditions
Inada et al. (1997)	Microcracking	Granite and tuff	Thermal cycle apparatus	No change in Poisson ratio, drop in tensile strength with respect to temperature, slight increase of compressive strength (about 1%) at 5th cycle of 15 °C to 100 °C compared to 4th cycle	15 °C to 100 °C and 15 °C to -160 °C cycles
Ferrero and Marini (2001)	Strength increase not explained	Marble	Not mentioned	Increase in compressive strength at moderate temperatures (2% - 17%), decrease of tensile strength, similar crack length distribution to our results	230 °C, 400 °C, 470 °C, 500 °C and 600 °C

Author	Mechanism	Material	Heating source	Results	Test conditions
Konecny et al. (2005)	Not stated	Granite	oven	Triaxial compressive strength increase up to 100 °C	25 °C, 100 °C, 200 °C, 300 °C, 400 °C, 500 °C and 600 °C
Dwivedi et al. (2008)	Not stated	Granite	High temperature chamber	UCS increase up to 12% at 150 °C	30 °C, 65 °C, 100 °C, 125 °C and 160 °C, other data also obtained from lit review
Zhang et al. (2009)	Hot-melt effect of some minerals caused microcrack healing	Marble, limestone, sandstone	Oven	Sandstone UCS increases by up to 17% at 700 °C, marble UCS increases by up to 20% at 100 °C	28 °C, 100 °C, 200 °C, 300 °C, 400 °C, 500 °C, 600 °C, 700 °C and 800 °C
Vishal et al. (2011)	Strain hardening of minerals	Khondalitic rocks	Not mentioned	Tensile strength increased up to 50% at 90 °C	30 °C, 50 °C, 70 °C, 90 °C, 110 °C, 130 °C, 150 °C, 170 °C, 190 °C, 210 °C, 230 °C and 250 °C

Author	Mechanism	Material	Heating source	Results	Test conditions
Chen et al. (2014)	Temperature effect was found to be uncertain, brittleness increases up to 60 °C before decreasing due to increased elastic strain energy	Granite	Oven	Minor strength increase (3% – 15%), but only 1 specimen per temperature	20°C, 40 °C, 60 °C, 90 °C, 130°C, loading rate of 0.1 mm/min until yield stage, 0.03 mm/min until failure
Yin et al. (2015)	Increased microcracking, increase in strength due to evaporation of water and dilation of minerals which reduced porosity	Granite	furnace	Quasi-static tensile strength decrease, slight increase in dynamic tensile strength at 100 °C (4.5%)	25 °C, 100 °C, 250 °C, 450 °C, 600 °C, 850 °C at 2 °C/min

Author	Mechanism	Material	Heating source	Results	Test conditions
Chen et al. (2017)	Strength drop due to α/β phase transition	Granite	Furnace	Increase in UCS up to 2% at 500 °C	100 °C, 200 °C, 300 °C, 400 °C, 500 °C, 600 °C, 700 °C and 800 °C. Heating rates of 1 °C/min, 3 °C/min, 5 °C/min, 8 °C/min, 12 °C/min and 15 °C/min

*Note

- AE stands for acoustic emission
- SEM stands for scanning electron microscope
- UCS stands for uniaxial compressive strength

Appendix III – Color values for heated Bukit Timah Granite specimens

Before heating									
Specimen				Background			Correction factor		
Name	L*	a*	b*	L*	a*	b*	L*	a*	b*
3	171.26	127.29	136.91	157	190.31	179.46	1.007702	1.006186	1.009734
5	151.99	127.33	134.41	155.07	191.51	181.07	1.032767	1.008637	1.014455
7	174.21	127.35	137.72	154.57	192.29	181.87	0.989058	1.013546	1.022029
8	173.97	127.25	135.62	156.57	190.62	181.07	1.004942	1.00538	1.021263
10	171.29	127.27	135.69	156.98	190.31	180.05	1.014673	0.999947	1.010892
11	170.4	127.35	135.43	154.7	191.65	181.08	1.024843	1.009109	1.01582
12	140.36	127.68	134.22	152.86	192.16	181.97	0.991696	1.007286	1.015571
13	162.52	127.38	136.62	157.28	190.01	179.8	1.019577	1.004759	1.013586
15	171.44	127.23	135.16	157.22	190.11	179.73	1.008079	1.002849	1.012392
17	170.41	127.28	136.34	156.83	190.41	179.75	0.998408	1.004325	1.013076
21	158.33	127.45	136.08	154.41	191.58	180.73	0.990252	1.011563	1.01791
22	145.63	127.46	134.49	153.25	192.26	182.58	0.981177	1.009345	1.020627
25	174.38	127.24	135.71	157.07	190.19	179.96	1.014926	0.999737	1.008801
26	172.91	127.29	135.11	157.71	189.65	179.35	1.005098	0.997475	1.004874
28	145.58	127.47	134.87	154.14	191.89	181.96	1.015817	1.008196	1.016707
29	176.25	127.21	135.32	157.52	189.84	179.47	1.003952	1.000896	1.011669
30	166.81	127.28	135.24	153.46	192.1	182.25	1.02334	1.009088	1.017418
31	175.49	127.19	135.68	157.55	189.8	179.27	1.053705	1.000105	1.005328
33	157.92	127.35	134.1	157.74	189.62	178.98	1.068554	0.999578	1.002184
35	161.16	127.44	135.28	155.19	191.63	180.99	1.002002	1.009801	1.018285
37	176.06	127.3	135.23	157.87	189.52	179.09	1.032437	0.998998	1.005164
38	169.75	127.2	134.76	155.86	191.24	180.55	1.056678	1.007162	1.009844
41	165.16	127.29	135.2	155.74	190.98	180.67	1.023999	1.009621	1.01872
47	166.17	127.35	135.33	154.95	191.72	181.12	1.044349	1.011075	1.016443
48	168.53	127.36	135.19	156.56	190.62	180.78	1.023937	1.008145	1.021183
51	170.16	127.29	135.21	156.18	190.95	180.63	0.984307	1.011816	1.017118

Name	L*	a*	b*	L*	a*	b*	L*	a*	b*
54	165.54	127.37	135.08	153.18	191.79	181.91	1.025713	1.024793	1.044259

After heating							
Specimen				Background			
Name	L*	a*	b*	Name	L*	a*	b*
3	178.85	130.17	142.88	3	155.8	189.14	177.73
5	165.8	130.08	142.07	5	150.15	189.87	178.49
7	183.36	129.86	142.74	7	156.28	189.72	177.95
8	185.64	127.57	138.44	8	155.8	189.6	177.3
10	183.96	129.53	140.85	10	154.71	190.32	178.11
11	172.79	128.51	138.34	11	150.95	189.92	178.26
12	164.84	127.88	136.04	12	154.14	190.77	179.18
13	177.11	129.45	141.17	13	154.26	189.11	177.39
15	176.75	128.51	138.23	15	155.96	189.57	177.53
17	186.17	127.32	138.07	17	157.08	189.59	177.43
21	178.74	129.36	140.79	21	155.93	189.39	177.55
22	170.53	127.53	136.06	22	156.19	190.48	178.89
25	180.13	128.39	138.31	25	154.76	190.24	178.39
26	182.22	128.27	138.63	26	156.91	190.13	178.48
28	162.61	128.91	139.4	28	151.74	190.33	178.97
29	189.68	127.51	136.6	29	156.9	189.67	177.4
30	179.26	127.46	135.94	30	149.96	190.37	179.13
31	178.37	129.19	140.1	31	149.52	189.78	178.32
33	154.57	128.9	138.1	33	147.62	189.7	178.59
35	169.91	128.51	137.94	35	154.88	189.77	177.74
37	178.57	128.49	138.47	37	152.91	189.71	178.17
38	181.22	129.34	140.77	38	147.5	189.88	178.79
41	179.04	127.95	136.41	41	152.09	189.16	177.35
47	178.87	127.61	136.02	47	148.37	189.62	178.19
48	164.12	127.31	132.88	48	152.9	189.08	177.03
51	157.67	127.9	134.82	51	158.67	188.72	177.59
54	174.96	128.22	136.03	54	149.34	187.15	174.2

Before heating									
Specimen				Background			Correction factor		
Name	L*	a*	b*	L*	a*	b*	L*	a*	b*
200-1a	145.83	125.43	129.08	86.45	175.09	168.26	0.730646	0.96874	0.975138
200-1b	140.48	125.47	129.7	96.01	175.91	168.62	0.865735	0.98175	0.985045
200-2a	148.88	125.56	129.59	91.47	176.29	169.79	0.769626	0.980424	0.991996
200-2b	145.85	125.56	129.4	90.48	176.14	169.66	0.814695	0.985399	0.99414
200-3a	148.97	125.43	128.75	94.59	177.03	170.37	0.758784	0.984211	1.000294
200-3b	147.68	125.57	129.3	93.86	176.86	170.06	0.841869	0.990868	0.998532
350-1a	146.29	125.32	128.72	98.95	177.54	170.31	0.734105	0.974959	0.98891
350-1b	142.17	125.27	129.42	103.19	178.01	170.24	0.955463	1.001575	1.00265
350-2a	145.86	125.41	128.58	90.96	175.87	169.2	0.809829	0.983668	0.991968
350-2b	146.86	125.4	129.09	95.11	177.44	170.75	0.857542	1.001467	1.012032
350-3a	139.72	125.32	128.43	92.59	176.26	169.58	0.867841	0.992008	0.999705
350-3b	136.09	125.33	128.95	91.83	175.75	169.36	0.855346	0.975143	0.976138
500-1a	148.1	125.32	128.35	91.52	176.04	169.33	0.851349	0.994352	1.001656
500-1b	145.08	125.37	129.02	91.64	177.18	170.87	0.764622	0.989888	1.006065
500-2a	141.08	125.31	128.83	94.47	176.44	169.42	0.852694	0.991682	0.999764
500-2b	146.18	125.29	128.71	104.16	177.82	170.11	0.939055	1.00107	1.005022
500-3a	147.96	125.33	128.56	95.27	177.84	171.32	0.89835	0.996582	1.002164
500-3b	142.88	125.34	128.88	91.7	176.57	170.13	0.839282	0.984609	0.990683

After heating (greased side)							
Specimen				Background			
Name	L*	a*	b*	Name	L*	a*	b*
200-1a	114.51	125.9	130.94	200-1a	118.32	180.74	172.55
200-2a	120.87	125.93	131.34	200-2a	118.85	179.81	171.16
200-3a	116.79	126.08	131.57	200-3a	124.66	179.87	170.32
350-1a	126.5	126.26	132.58	350-1a	134.79	182.1	172.22
350-2a	116.83	126.11	131.62	350-2a	112.32	178.79	170.57
350-3a	110.31	126.24	132.91	350-3a	106.69	177.68	169.63
500-2b	125.35	126.65	134.03	500-2b	110.92	177.63	169.26
500-1b	132.42	126.64	133.84	500-1b	119.85	178.99	169.84
500-3a	119.28	126.91	134.44	500-3a	106.05	178.45	170.95

After heating (clean side)							
Specimen				Background			
Name	L*	a*	b*	Name	L*	a*	b*
200-1b	136.46	125.33	129.91	200-1b	110.9	179.18	171.18
200-2b	146.23	125.35	129.57	200-2b	111.06	178.75	170.66
200-3b	145.62	125.34	129.81	200-3b	111.49	178.49	170.31
350-1b	150.65	125.6	131.54	350-1b	108	177.73	169.79
350-2b	150.64	125.61	131.55	350-2b	110.91	177.18	168.72
350-3b	150.63	126.15	133.34	350-3b	107.36	180.23	173.5
500-2a	155.3	126.37	133.3	500-2a	110.79	177.92	169.46
500-1a	148.29	126.51	132.25	500-1a	107.5	177.04	169.05
500-3b	153.68	126.39	132.54	500-3b	109.26	179.33	171.73

Appendix IV – Brazilian tensile test data for Bukit Timah Granite specimens

Specimen	Treatment	Force (N)	Length (mm)	Diameter (mm)	t/d ratio	Strength (MPa)	Deformation (mm)	Strain
3	500sc	9224.9258	21.35	51.2	0.42	5.375209416	0.6914764	0.013505
5	500sc	11540.198	22.13	47.52	0.47	6.989655352	0.639325	0.013454
7	500sc	6848.4658	23.35	47.31	0.49	3.948696965	0.7649465	0.016169
8	200fc	18852.906	21.85	47.38	0.46	11.59930991	0.630367	0.013304
10	500fc	10721.751	23.34	47.33	0.49	6.181995839	0.642313	0.013571
11	350fc	12496.887	21.05	47.31	0.44	7.992766804	0.787579	0.016647
12	200fc	19933.572	22.57	47.12	0.48	11.938469	0.600605905	0.012746
13	500fc	7530.437	21.33	51.16	0.42	4.395407409	0.5709877	0.011161
15	350fc	16936.137	22.36	47.3	0.47	10.19956772	0.54106541	0.011439
17	200sc	17946.424	18.9	51.16	0.37	11.82186326	0.5604553	0.010955
21	500fc	6265.2212	17.8	51.18	0.35	4.380427256	0.3481822	0.006803
22	200fc	19279.668	22.06	47.15	0.47	11.80626952	0.593926	0.012597
25	350sc	14238.591	21.87	47.3	0.46	8.767129852	0.399828	0.008453
26	350ac	17584.371	22.92	47.22	0.49	10.34871888	0.646107	0.013683
28	350ac	13059.435	23.14	47.12	0.49	7.628797716	0.531901	0.011288
29	200ac	20603	26.53	47.3	0.56	10.45760947	0.7393584	0.015631
30	200sc	15268.632	21.37	47.26	0.45	9.62946671	0.713087	0.015089
31	500ac	10835.737	24.32	47.29	0.51	6.001031666	0.458136	0.009688
33	350sc	11346.547	16.85	47.11	0.36	9.104394224	0.663003	0.014074
35	350fc	12843.822	17.64	47.24	0.37	9.817166483	0.392241	0.008303
37	350ac	14061.603	18.5	47.27	0.39	10.24183675	0.406091	0.008591
38	500ac	7736.8682	19.88	47.32	0.42	5.238469627	0.7629526	0.016123
41	200ac	21623.76	29.31	47.35	0.62	9.924205722	0.6541428	0.013815
47	200ac	26776.061	31.35	47.35	0.66	11.48919255	0.6837187	0.01444
48	200sc	25452.267	23.47	47.32	0.50	14.59718098	0.63421458	0.013403
51	350sc	15446.892	19.01	47.35	0.40	10.93048311	0.58192641	0.01229
54	500ac	8385.1175	20.04	47.35	0.42	5.628488716	0.51060307	0.010784

Appendix V – P-wave velocity for Bukit Timah Granite specimens

Before			After		
Specimen	Length (m)	Average value (m/s)	Specimen	Length (m)	Average value
3	0.02135	5474.359	3	0.02135	3335.938
5	0.02213	5674.359	5	0.02213	3353.03
7	0.02335	5306.818	7	0.02335	2715.116
8	0.02185	5161.417	8	0.02185	5161.417
10	0.02334	5304.545	10	0.02334	2724.514
11	0.02105	5397.436	11	0.02105	4295.918
12	0.02257	5978.808	12	0.02257	6045.536
13	0.02133	5613.158	13	0.02133	2882.432
15	0.02236	5081.818	15	0.02236	4272.611
17	0.0189	5770.992	17	0.0189	6096.774
21	0.0178	5884.298	21	0.0178	2781.25
22	0.02206	5656.41	22	0.02206	6488.235
25	0.02187	4970.455	25	0.02187	4374
26	0.02292	5414.173	26	0.02292	4167.273
28	0.02314	6089.474	28	0.02314	5142.222
29	0.02653	5604.93	29	0.02653	4912.963
30	0.02137	5660.927	30	0.02137	5342.5
31	0.02432	5744.882	31	0.02432	2861.176
33	0.01685	5810.345	33	0.01685	5265.625
35	0.01764	5386.26	35	0.01764	5188.235
37	0.0185	5781.25	37	0.0185	4204.545
38	0.01988	5266.225	38	0.01988	2650.667
41	0.02931	5556.398	41	0.02931	4967.797
47	0.03135	5548.673	47	0.03135	5313.559
48	0.02347	5831.056	48	0.02347	4958.451
51	0.01901	5431.429	51	0.01901	4320.455
54	0.02004	5566.667	54	0.02004	2904.348

Appendix VI – Dynamic compressive test data for Carrara marble specimens

Specimen	Strain rate (1/s)	Strength (MPa)	Max strain	Energy at peak stress (MJ/m^3)	Total energy absorbed (MJ/m^3)	Temperature (°C)	Pressure (Bars)
MDC22	318.3245269	102.35054	0.0440836	1.8751	2.6327	750	6.5
MDC15	261.0270048	106.04615	0.0449428	1.7712	2.9719	750	9
MDC17	246.8327582	92.096318	0.0423822	1.3752	2.1599	750	6.5
MDC19	146.0959009	67.341760	0.0188695	0.543	0.4714	750	4
MDC20	165.0876913	94.438596	0.0397669	1.1981	2.212	750	9
MDC26	125.1487602	60.044548	0.0204611	0.3947	0.3772	750	4
MDC28	328.545103	96.137933	0.0484150	1.7122	3.0371	750	9
MDC33	307.6175839	80.483058	0.0380126	1.2791	1.7295	750	6.5
MDC35	152.6643845	64.552001	0.0188145	0.5133	0.5453	750	4
MDC44	277.6446049	95.518707	0.0491221	1.483	2.7615	750	9
MDC49	283.6048815	79.626012	0.0393203	1.1942	1.7259	750	6.5
MDC51	378.4630599	83.496104	0.0541873	1.5755	2.1651	750	9
MDC16	136.2910297	138.49380	0.0241014	1.2609	1.6906	500	6.5
MDC18	178.7502115	172.17262	0.0356671	2.1844	3.9525	500	9
MDC1	128.29	86.040728	0.0168430	0.5261	0.3856	500	4
MDC23	157.8301159	146.63365	0.0243495	1.5125	2.2205	500	6.5
MDC6	224.4519669	139.47131	0.0437423	1.4641	3.984	500	9
MDC21	128.1940156	161.29043	0.0204514	1.4657	1.7249	500	6.5
MDC24	88.99332345	80.943311	0.0144508	0.357	0.2329	500	4
MDC25	120.5318908	61.461038	0.0183359	0.4194	0.4275	500	4
MDC27	213.2448733	131.40250	0.0406249	1.9217	3.4807	500	9
MDC30	244.3885354	104.77228	0.0419504	1.7035	3.0608	500	9
MDC7	77.6443541	234.50287	0.0159106	1.439	1.8133	250	9
MDC9	110.0681479	166.97034	0.0194309	1.4141	1.859	250	6.5
MDC10	88.70618799	121.00153	0.0095856	0.534	0.3624	250	4
MDC2	137.3681172	194.87640	0.0201832	1.9677	2.3604	250	9

Specimen	Strain rate (1/s)	Strength (MPa)	Max strain	Energy at peak stress (MJ/m^3)	Total energy absorbed (MJ/m^3)	Temperature (°C)	Pressure (Bars)
MDC29	98.16669791	244.41789	0.0188254	1.9749	2.2701	250	6.5
MDC31	143.7945999	169.53382	0.0349286	1.4045	3.8408	250	9
MDC32	58.34171915	192.05269	0.0095445	0.7989	0.7406	250	6.5
MDC36	40.24024177	139.60673	0.0050597	0.3206	0.2675	250	4
MDC37	91.71347578	212.85103	0.0221213	1.6792	3.0956	250	9
MDC38	74.26303158	150.61608	0.0131051	0.8512	1.1597	250	6.5
MDC39	75.95077309	118.42652	0.0104845	0.5228	0.4949	250	4
MDC40	64.67954658	200.44420	0.0109017	1.0263	1.0964	250	6.5
MDC41	153.8679227	156.87319	0.0399591	1.3489	3.9733	250	9
MDC42	80.94291167	121.63499	0.0113359	0.5591	0.5395	250	4
MDC43	124.3197452	144.21601	0.0259518	1.4544	2.3428	250	6.5
MDC45	134.4488493	139.49467	0.0271188	1.144	2.6061	250	6.5
MDC46	66.91614571	117.34790	0.0077461	0.3908	0.3342	250	4
MDC47	110.4087653	222.79943	0.0165728	1.5251	2.0418	250	9
MDC48	88.12899834	114.19103	0.0103794	0.5285	0.4787	250	4
MDC50	98.24446427	114.14898	0.0109110	0.5135	0.4666	250	4
MDC52	136.3435021	153.77137	0.0253609	1.2779	1.9849	250	6.5
MDC57	63.78286217	222.94067	0.0139319	1.4563	1.9621	25	9
MDC62	103.610468	200.82901	0.0198391	1.2296	2.0947	25	9
MDC64	101.9655773	179.76553	0.0229575	1.8976	2.8266	25	9
MDC59	47.6478033	207.67088	0.0086636	0.9664	0.9531	25	6.5
MDC61	80.06012924	200.49394	0.0147952	1.4999	1.5965	25	6.5
MDC63	45.55451012	199.67627	0.0083899	0.9874	0.9479	25	6.5
MDC60	59.63811539	150.30828	0.0089084	0.6098	0.5177	25	4
MDC58	53.67088624	150.20083	0.0078037	0.5983	0.5319	25	4
MDC66	32.2197521	153.25684	0.0047528	0.393	0.273	25	4
MDC65	80.98925936	209.24590	0.0182509	1.4244	2.3655	25	9

Specimen	Strain rate (1/s)	Strength (MPa)	Max strain	Energy at peak stress (MJ/m^3)	Total energy absorbed (MJ/m^3)	Temperature (°C)	Pressure (Bars)
MDC67	50.01307642	214.45523	0.0116579	1.0625	1.5124	25	9
MDC68	73.45347605	220.46724	0.0181628	1.4205	2.6496	25	9
MDC69	119.1498519	206.02212	0.0207071	1.6281	1.798	25	9
MDC70	65.61352357	200.72175	0.0129185	1.1645	1.1249	25	6.5
MDC71	76.02856967	190.72456	0.0146352	1.2725	1.5198	25	6.5
MDC72	87.67233806	180.64781	0.0152321	1.1894	1.2533	25	6.5
MDC73	91.26484277	173.44010	0.0177906	1.2454	1.4236	25	6.5
MDC74	68.05720371	124.29916	0.0075530	0.4	0.3522	25	4
MDC75	63.72859328	130.18971	0.0052245	0.3042	0.2834	25	4
MDC76	42.17181055	130.67410	0.0053655	0.3345	0.2527	25	4
MDC77	33.53977753	130.39054	0.0041589	0.2541	0.1727	25	4

Appendix VII – Dynamic compressive test for Bukit Timah Granite specimens

Specimen	Strain rate (1/s)	Strength (MPa)	Max strain	Energy at peak stress (MJ/m^3)	Total energy absorbed (MJ/m^3)	Temperature (°C)	Pressure (bars)
GDCS9	48.007578	186.67306	0.0061502	0.591132	0.370109	250	4
GDCS13	41.529046	197.89772	0.0103439	0.500953	0.286803	250	4
GDCS26	65.954081	180.06033	0.0076959	0.64238	0.444084	250	4
GDCS4	53.822186	197.56327	0.0056522	0.43726	0.090285	250	4
GDCS10	48.963884	296.04719	0.0078246	1.12508	0.726272	250	6.5
GDCS15	90.711847	302.81410	0.0150562	1.89664	1.802413	250	6.5
GDCS30	49.95582	292.96601	0.0092150	1.189881	1.156148	250	6.5
GDCS3	84.481848	304.97072	0.0110534	1.5028	1.092524	250	6.5
GDCS12	62.686663	374.31101	0.0103439	1.69749	1.800541	250	9
GDCS18	55.650918	353.88876	0.0099304	1.51219	1.546657	250	9
GDCS8	66.177832	370.38210	0.0094003	1.46062	0.571529	250	9
GDCS11	58.939906	192.90611	0.0079709	0.63417	0.451488	500	4
GDCS19	86.93019	200.97272	0.0103807	0.93438	0.894052	500	4
GDCS24	85.046011	192.34780	0.0088075	0.76955	0.658342	500	4
GDCS16	65.219427	299.21205	0.0176023	1.76832	1.727446	500	6.5
GDCS22	89.830799	247.08095	0.0190456	1.42039	2.891525	500	6.5
GDCS28	102.82034	289.31448	0.0167148	1.55686	2.160483	500	6.5
GDCS17	115.39123	331.47406	0.0222709	2.56486	3.702519	500	9
GDCS23	78.502728	355.82461	0.0128494	1.77625	2.029467	500	9
GDCS29	127.21221	304.49739	0.0260840	2.385466	5.092603	500	9
GDCS14	216.48806	22.937911	0.0281554	0.3037	0.312653	750	4
GDCS25	314.83247	7.1143059	0.0355362	0.148427	0.15296	750	4
GDCS32	201.82636	23.713378	0.0279476	0.343188	0.357426	750	4
GDCS20	414.53356	7.5488839	0.0444104	0.1006	0.135132	750	6.5
GDCS27	403.54864	12.476975	0.0634980	0.31642	0.351379	750	6.5
GDCS33	342.19263	27.174825	0.0385659	0.485064	0.529081	750	6.5

Specimen	Strain rate (1/s)	Strength (MPa)	Max strain	Energy at peak stress (MJ/m^3)	Total energy absorbed (MJ/m^3)	Temperature (°C)	Pressure (bars)
GDCS21	285.53069	21.368421	0.0151382	0.134412	0.15707	750	9
GDCS31	535.07964	21.683320	0.0092150	0.816672	0.916786	750	9
GDCS34	505.93465	43.734598	0.0458589	0.74053	1.096476	750	9
GDCS5	25.951508	192.32456	0.0040723	0.35583	0.069332	25	4
GDCS2	39.921035	195.65799	0.0048892	0.40717	0.155531	25	4
GDCS43	87.345752	157.75203	0.0113504	0.67803	0.800574	25	4
GDCS44	53.929257	179.34845	0.0078475	0.614506	0.584884	25	4
GDCS39	100.31701	162.08269	0.0140307	0.75497	0.94488	25	4
GDCS6	45.837248	198.10631	0.0060040	0.604604	0.340945	25	4
GDCS7	42.642727	301.03559	0.0063358	0.9129	0.303108	25	6.5
GDCS45	48.837185	295.55372	0.0083749	1.23124	1.151982	25	6.5
GDCS46	114.85870	246.19315	0.0208232	1.511908	2.999583	25	6.5
GDCS48	109.43295	241.81209	0.0182969	1.411638	2.565326	25	6.5
GDCS49	118.59723	236.89165	0.0264167	2.816150	3.352561	25	6.5
GDCS40	145.66945	231.36377	0.0271746	2.711218	3.556429	25	6.5
GDCS41	127.11581	254.28723	0.0221054	1.775703	3.150488	25	6.5
GDCS1	188.03947	294.73012	0.024899	1.787157	4.605524	25	9
GDCS35	102.13560	346.42167	0.0220045	2.986955	4.452476	25	9
GDCS36	68.542155	389.83742	0.0139293	2.34607	1.898189	25	9
GDCS37	71.777072	376.12094	0.0116502	2.213405	1.792018	25	9
GDCS50	235.16778	285.16636	0.0377046	5.651256	5.337108	25	9
GDCS42	166.02817	288.80931	0.0371916	5.449520	5.430696	25	9
GDCS47	135.97165	272.84755	0.0348593	5.591903	6.833081	25	9
GDCS51	198.74517	286.50566	0.0374823	6.154483	5.720272	25	9